ELECTROCHEMICAL AND ELECTRICAL CONDUCTIVITY STUDIES OF REDOX MOLECULES AND NANOMATERIALS IN SOME SELF-ORGANISED SYSTEMS

by

P. Suresh Kumar

Thesis submitted to the

Jawaharlal Nehru University

for the degree of
Doctor of Philosophy

June 2009

Raman Research Institute

Bangalore 560 080
India

CERTIFICATE

This is to certify that the thesis entitled **Electrochemical and electrical conductivitiy studies of redox molecules and nanomaterials in some self-organised systems** submitted by P. Suresh Kumar for the award of the degree of DOCTOR OF PHILOSOPHY of Jawaharlal Nehru University is his original work. This has not been published or submitted to any other University for any other Degree or Diploma.

Prof. Ravi Subrahmanyan
Director
Raman Research Institute
Bangalore 560 080 INDIA

Prof. V. Lakshminarayanan
(Thesis Supervisor)

DECLARATION

I hereby declare that this thesis is composed independently by me at Raman Research Institute, Bangalore, under the supervision of Prof. V. Lakshminarayanan. The subject matter presented in this thesis has not previously formed the basis for the award of any degree, diploma, membership, associateship, fellowship or any other similar title of any university or institution.

(Prof. V. Lakshminarayanan) (P. Suresh Kumar)

Raman Research Institute

Bangalore 560 080 - INDIA

ACKNOWLEDGEMENTS

I am greatly indebted to my thesis supervisor Prof. V. Lakshminarayanan for his invaluable and inspiring guidance throughout my research work. I am grateful to him for revealing me the richness of electrochemistry and science in general. It was a memorable experience to work with and learn so many things from him both as a scientist and as a human being. I thank him for the constant help and thought provoking discussions. It has been a great pleasure for me to work with him.

I thank Prof. Sandeep Kumar, for his providing many of the materials that are used in this study and also for the many valuable discussions with him throughout my research period.

I thank Raman Research Institute for giving an opportunity to work towards my PhD degree.

I would like to express my gratitude to Prof. N. Kumar and Prof. Ravi Subrahmanyan for their keen interest in my research work.

Thanks are also due to Dr. B. Ramesh, Prof. K. A. Suresh, Prof. B. K. Sadashiva, Dr. V. A. Raghunathan, Dr. R. Pratibha and Dr. D. Vijayaraghavan for many valuable discussions. I also thank the students academic affairs committee for their helps.

I thank all the staff members of SCM group for their help at various stages of my research works. I would like to thank Mr. Jayadevaiah for his help in STM studies, Dr. Santanu Kumar Pal for his help in the synthesis of some of the compounds that are used in this work and also for the help in polarising optical microscopic images.

I would like to thank Mr. N. Ravi Sankar, for his valuable help in my experiments. I would also like to thank Mr. A. Dhason for fabricating many of the glass apparatus and electrodes used in the experiments, Mr. H. Subramonyam Ram for preparing the evaporated gold samples; Mr. Mani for constructing various accessories for the experimental set up; Mrs. K.N. Vasudha for her help in the X-ray, conductivity and spectroscopic measurements,

Shashidhara and Srinivasa for many technical helps. I also acknowledge with thanks the help of our secretary Mr. K. Radhakrishna for his valuable and timely help throughout my research work.

It is a pleasure to thank all the library staffs of RRI who have provided an excellent and timely help during my research. I would like to thank various other departments of RRI like the Administration, Computer, Accounts, Workshop, Security, Transport, Canteen, Hostel and Clinic for their constant support throughout my research.

I am enriched by many useful discussions both academic and non-academic matters with my lab-mates Ganesh, Mohanapriya, Rakesh, Nagaraju and Kavitha. I thank Bharat, Bibhu, Hari and Radhakrishnan for their constant support and encouragement during my research period. I thank Sajal for several discussions on X-ray scattering studies. I also thank Srikanth, Arun, Amit, Anija, Brindaban, Alpana, Sandeep, Rahul, Tripta, Satyam, Jayakumar, Radhika, Madhu and Santosh for their help and several discussions.

I would like to thank my beloved parents, my sister and family members for being a constant source of encouragement, support and help throughout my research work.

Finally I thank Indian Tax payer with whose money I have carried out my research works.

Contents

ABBREVIATIONS

H1: Lyotropic columnar hexagonal liquid crystalline phase

H2: Lyotropic reverse columnar hexagonal liquid crystalline phase

Col_h: Thermotropic columnar hexagonal liquid crystallin phase

HAT6: Hexahexyloxytriphenylene

HHTT: Hexahexylthiotriphenylene

GNP: Gold nanoparticle

SAM: Self-assembled monolayer

BAu: Bare gold

HDT: Hexadecanethiol

DS8: 4'-{[8-({8-[(4'-Cyano[1,1'-biphenyl]-4yl)oxy]hexyl}-disulphanyl)hexyl]oxy}[1,1'-biphenyl]-4-carbonitrile

DS9: 4'-{[9-({9-[(4'-Cyano[1,1'-biphenyl]-4yl)oxy]hexyl}-disulphanyl)hexyl]oxy}[1,1'-biphenyl]-4-carbonitrile

DS10:4'-{[10-({10-[(4'-Cyano[1,1'-biphenyl]-4yl)oxy]hexyl}-disulphanyl)hexyl]oxy}[1,1'-biphenyl]-4-carbonitrile

DS12:4'-{[12-({12-[(4'-Cyano[1,1'-biphenyl]-4yl)oxy]hexyl}-disulphanyl)hexyl]oxy}[1,1'-biphenyl]-4-carbonitrile

TP6: 6-{[3,6,7,10,11-pentakis(hexyloxy)-2-triphenylenyl]oxy}-1-hexanethiol

TP10: 10-{[3,6,7,10,11-pentakis(hexyloxy)-2-triphenylenyl]oxy}-1-decanethiol

TP12: 12-{[3,6,7,10,11-pentakis(hexyloxy)-2-triphenylenyl]oxy}-1-dodecanethiol

$Fe[(CN)_6]^{4-|3-}$:ferocyanide/ferricyanide

$[Ru(NH_3)_6]^{2+|3+}$: HexaammineruthenimII/III

Bq: 4-benzoquinone

Qh: 1,4-benzenediol

mv: Methylviologen

Fc: Ferrocene

FcTFB: Ferrocenium tetrafluoroborate

NaF: Sodium fluoride

$LiClO_4$: Lithium perchlorate

TBATFB: Tetrabutylammonium tetrafluoroborate

$HClO_4$: Perchloric acid

$HAuCl_4$: Chloroauric acid

CV: Cyclic voltammetry

EIS: Electrochemical impedance spectroscopy

POM: Polarising optical microscopy

DSC: Differential scanning calorimetry

SAXS: Small angle X-ray scattering

FTIR: Fourier transform infrared

STM: Scanning tunneling microscopy

$E_{1/2}$: Half-peak potential

R_u: Uncompensated resistance

C_{dl}: Double layer capacitance

R_{ct}: Charge transfer resistance

Z_W: Warburg impedance

SYNOPSIS

Electrochemical and electrical conductivity studies of redox molecules and nanomaterials in some self-organised systems

This thesis describes the electrochemical and electrical conductivity studies of redox probes and nanoparticles in self-organised systems. Self-organisation finds a key role in many fields of science as can be seen from the example of protein folding and the functioning of all the biological systems, the formation of colloids, crystals, liquid crystals and so on. In the present thesis work, we have used three different self-organised systems, *viz*, lyotropic liquid crystals, thermotropic liquid crystals and self-assembled monolayers formed by different organic thiol molecules on gold surface.

Liquid crystals are considered to be the fourth state of matter and the properties of these phases are between crystalline and liquid phases. More precisely liquid crystals possess the orientational order of crystalline phase and the dynamic nature of liquid phase. This special feature of the liquid crystalline phases makes them interesting in many fields. Broadly the liquid crystals are classified into two types, lyotropic liquid crystals and thermotropic liquid crystals. Lyotropic liquid crystals are normally formed by the amphiphilic molecules or surfactants in a solvent phase. The aggregation of these molecules in a solvent results in the formation of micelles above a particular concentration, which is known as the critical micellar concentration (CMC). The shape of the micelles depends upon the nature and concentration of the surfactant molecules. At higher concentration of the surfactants, the micelles further get aggregated to form 2-dimensional networks which is known as lyotropic liquid crystals. There are several types of lyotropic liquid crystalline phases. Nematic, smectic, cubic, lamellar and columnar hexagonal phases are some of the common liquid crystalline phases formed by the surfactants. The lamellar phase has a significant role in biological systems as

many of the lipids form the lamellar phase in biological media. In our studies, we have used the columnar hexagonal phase, that are formed by the aggregation of cylindrical micelles in the aqueous medium.

Thermotropic liquid crystals may be defined as liquid crystalline phases, when the substance passes between the solid, liquid crystal and liquid state and *vice versa* as a function of temperature and in the absence of solvent. Similar to the lyotropic liquid crystalline phases, thermotropic liquid crystals also have several different phases, including nematic, smectic, cholesteric and columnar phases. In the present thesis, we have extensively used columnar hexagonal phase formed by triphenylene based discotic molecules. This phase is well-known for their quasi-one-dimensional electron transport properties through the columns due to the strong $\pi - \pi$ interactions between the electron rich triphenylene cores within the columns. In the pure state, due to the large band gap, these discotic materials are insulators while addition of a small amount of electron deficient or electron rich dopants have shown to enhance the electrical conductivity by several orders of magnitude with retaining the liqud crystalline order.

Self-assembled monolayers (SAMs) are formed by the spontaneous adsorption of certain molecules on the surface resulting in the formation of a single layer of the molecules. SAMs of organic thiol molecules on the gold surface are of special interest among all SAMs due to the long-term stability and the potential applications of these monolayers in different fields.

Electrochemistry in the lyotropic liquid crystalline phases is attracting attention in recent years as these phases can be explored for many of the biological studies. On the other hand, the electrical conductivity studies on the thermotropic discotic liquid crystals are of fundamental interest with several potential applications, mainly due to their unique quasi-one-dimensional electronic transport mechanism in the liquid crystalline phase. This particular property of the discotic systems can find applications in the field of molecular electronics, photovoltaics, solar cells and sensors. The self-assembled monolayers are important in the surface science studies due to the wide variety of possible applications using simple fabrication methods.

In the following, a brief description of the contents of the chapters are presented.

Chapter 1: Introduction

This chapter gives a brief introduction to different topics covered in the thesis. This chapter contains two parts. First part deals with the materials and methods used in the thesis. This includes a description about the lyotropic liquid crystals, thermotropic liquid crystals, gold nanoparticles and self-assembled monolayers. The second part of the chapter deals with the different experimental techniques that have been used in the thesis. We have extensively used electrochemical techniques like cyclic voltammetry and electrochemical impedance spectroscopy for the characterisation of different systems. This section also deals with other experimental techniques like polarising optical microscopy, differential scanning calorimetry, grazing angle FTIR spectroscopy, small angle X-ray scattering and scanning tunneling microscopy. This chapter also provides the aims and scope of the present thesis.

Chapter 2: Electron transfer studies of redox probes in the columnar hexagonal phase of Triton X-100/water system

This chapter deals with the experimental results on the electron transfer studies of different redox probes in the lyotropic liquid crystalline phase (H1 phase) of Triton X-100/water system. We have used a variety of redox probes like ferrocyanide|ferricyanide, hexaammineruthenium (II|III), benzoquinone|hydroquinone, methylviologen, ferrocene|ferrocenium and ferrocenemethanol systems. Using polarising optical microscopy and small angle X-ray scattering techniques, we have confirmed that the liquid crystalline phase is retained even after the addition of redox probes and supporting electrolyte.

The cyclic voltammetric studies show that the half-peak potentials of the redox probes have shifted significantly in the H1 phase compared to the solvent phase as shown in Figure 1. The peak currents have decreased in the H1 phase for all the redox systems. The nature and extent of the potential shifts have been explained on the basis of the interaction between the redox probe and the surrounding H1 phase. For the hexaammineruthenium (II/III) redox system, we have observed that there is only a negligible shift in the half-peak potential, which

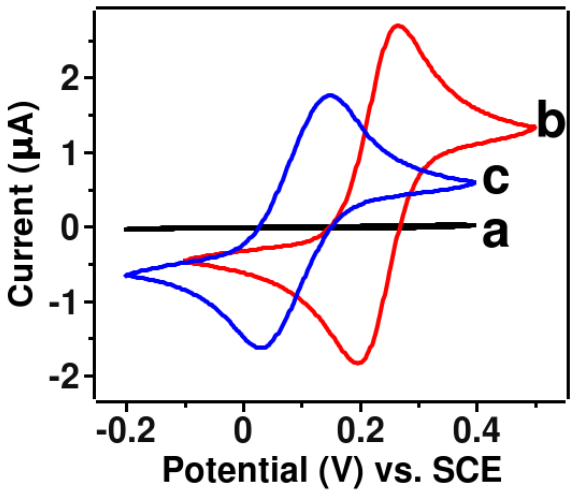

Figure 1: Cyclic voltammogram in a) the presence of only supporting electrolyte, 0.1 M TBATFB in the H1 phase b) 1 mM $Fe[(CN)_6]^{4-|3-}$/0.1 M NaF in the aqueous phase and c) 1 mM $Fe[(CN)_6]^{4-|3-}$ 0.1 M TBATFB in the H1 phase at a scan rate of 20 mV/s

has been attributed due to the outer-sphere electron transfer mechanism. On the other hand, the diffusion coefficient of all the redox probes have decreased in the H1 phase compared to the solvent phase. The extent of decrease was observed to be dependent on the nature of the redox probes. Comparison of the cyclic voltammetric and electrochemical impedance spectroscopic results indicate that the linear diffusion characteristics of the redox probes are still valid in the liquid crystalline phase even in the presence of columnar arrangement of the cylindrical micelles in the medium.

Chapter 3: Dispersion of nanoparticles in the lyotropic liquid crystalline phases

This chapter describes a novel method of dispersion of thiol-protected gold nanoparticles in two different lyotropic liquid crystalline phases *viz*, the columnar hexagonal phase (H1 phase) of Triton X-100/water system and the reverse columnar hexagonal phase (H2 phase) of AOT system. We find that the dispersion of the nanoparticles retains the columnar hexagonal structure with an increase in the liquid crystalline order both in the H1 phase and in the H2 phase. These types of dispersions of the nanoparticles in the liquid crystalline matrix are interesting as they possess an ordered structure of the liquid crystalline phase while retaining the unique properties of the nanomaterials.

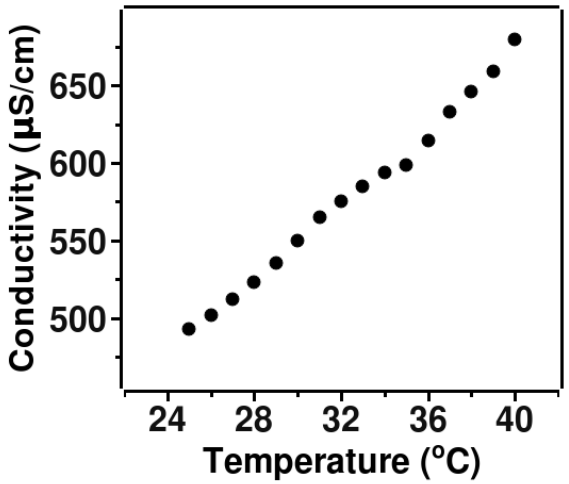

Figure 2: Ionic conductivity of the H1 phase of Triton X-100/water system as a function of temperature

This chapter also discusses the results of the ionic conductivity studies of the H1 phase formed by Triton X-100/water system. Surprisingly the ionic conductivity values of these systems are very high even though the phase is formed by the nonionic surfactant, Triton X-100 (Figure 2). We find that the addition of gold nanoparticles increases the liquid crystalline order and also the ionic conductivity of the medium. On the other hand, the addition of chaotropic agents like urea results in a decrease in the ionic conductivity. Based on these observations, the high ionic conductivity of these systems has been explained on the basis of Grotthus mechanism, which rely on the proton transfer pathways by the water clusters. The ionic conductivity of these systems resembles the proton conductivity in proteins as there are several similarities in the conductivity mechanism in these two systems.

Chapter 4: Electrical conductivity studies on the discotic liquid crystals and its composites

This chapter explores the quasi-one-dimensional electron transport properties of the discotic liquid crystalline phases. We have carried out the electrical conductivity studies on the thermotropic columnar hexagonal liquid crystalline phases formed by triphenylene based discotic molecules and some of its composites. The discotic composites are prepared using two different acceptor systems, ferrocenium tetrafluoroborate and chloroauric acid, while hexahexyloxytriphenylene and hexahexylthiotriphenylene were used as the discotic materials. The electrical conductivity studies of a series of pyridinium tethered triphenylene derivatives which form ionic liquid crystals form a part of this chapter.

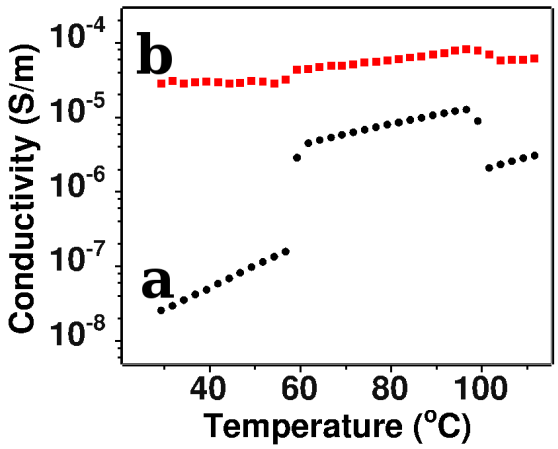

Figure 3: DC electrical conductivity plots for the composites a) 0.1 % $HAuCl_4$/HAT6 and b) 1 % $HAuCl_4$/HAT6 as a function of temperature

The composite materials have been characterised by polarising optical microscopy, differential scanning calorimetry and small angle X-ray scattering studies. The results from these studies show that lower concentration of the dopants do not alter the columnar structure of the discotic molecules. The UV-visible spectral studies show that the ferrocenium ions form charge-transfer complex with the electron rich discotic molecules while the chloroaurate oxidises the triphenylene core of the discotic molecules resulting in the formation of triphenylene radical cations. Both the dopants have enhanced the DC conductivity of the discotic phase by almost million times due to the formation of donor-acceptor pairs. In

addition to high electrical conductivity as shown in Figure 3, chloroaurate-discotic composites also show very high ionic conductivity, due to the formation of radical cations. The chloroaurate-discotic composites show a significant absorption in the entire visible and NIR region, which indicates that these composites can find potential applications in the field of solar cells. The DC conductivity of these composites have decreased in the isotropic phase, indicating that the high electronic conductivity of these composites is due to the quasi-one-dimensional electronic transport through the columns. The ionic conductivity of the pyridinium tethered triphenylene systems show enhancement in the electrical conductivity by almost million times, indicating that functionalising the triphenylenes with ionic groups can also be used as a method for preparing highly conducting discotic materials.

Chapter 5: Self-assembled monolayers of liquid crystalline disulphides and thiols on gold surface

This chapter describes the formation and electrochemical characterisation of cyanobiphenyl functionalised disulphides and triphenylenethiols on gold surface, where the disulphides show nematic phase and the triphenylenethiols show columnar hexagonal phase in the bulk. The electron transfer barrier properties, double layer capacitance and the ionic permeability of these monolayer modified surfaces are discussed in this chapter.

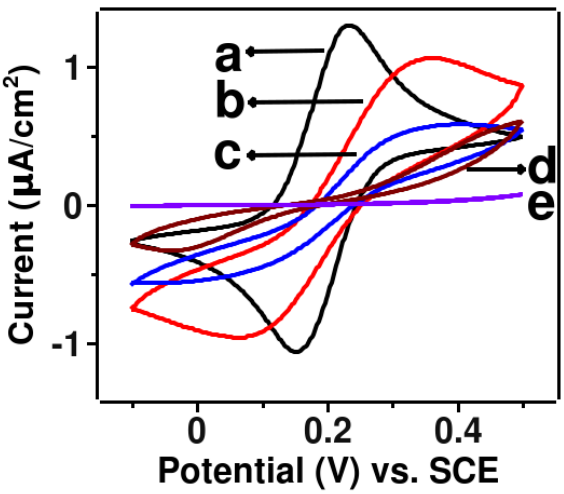

Figure 4: Cyclic voltammogram in ferocyanide/ferricyanide using a) bare gold electrode and b) DS8, c) DS9, d) DS10 and e) DS12 modified electrodes

The studies show that the cyanobiphenyl substituted disulphides show good barrier to electron transfer process for the ferrocyanide|ferricyanide reaction (Figure 4), while for the hexaammineruthenium(II/III) system, they show poor blocking behaviour. The facile electron transfer for the hexaammineruthenium(II/III) system has been explained on the basis of outer-sphere electron transfer reaction mechanism. The poor blocking ability of the disulphides arises due to polar terminal cyano groups. However the higher chain disulphide modified monolayers show better barrier to electron transfer process due to more compact organisation of the monolayers on the surface by the hydrophobic-hydrophobic interactions. On the other hand, the triphenylenethiol modified monolayers show very poor blocking behaviour and the blocking ability decreases for higher chain length. This has been explained on the basis of the disorganised structure of the longer chain length monolayers resulting from the $\pi - \pi$ interaction between the electron rich triphenylene cores.

Chapter 6: Summary and future works

This chapter summarises the results and conclusions of the experimental works in the present investigation. This chapter also proposes scope and further work that can be carried out for a better understanding of some of the topics discussed in the thesis.

List of Publications

1. Electron-transfer studies in a lyotropic columnar hexagonal liquid crystalline medium;

P. Suresh Kumar and V. Lakshminarayanan;

Langmuir 2007, **23**, 1548.

2.Dispersion of thiol stabilized gold nanoparticles in lyotropic liquid crystalline systems;

P. Suresh Kumar; Santanu Kumar Pal; Sandeep Kumar and V. Lakshminarayanan

Langmuir 2007, **23**, 3445.

3.Novel conducting nanocomposites: synthesis of triphenylene-covered gold nanoparticles and their insertion into a columnar matrix;

Sandeep Kumar; Santanu Kumar Pal; P.Suresh Kumar and V. Lakshminarayanan

Soft Matter 2007, **3**, 896.

4.Electrical conductivity studies on discotic liquid crystal-ferrocenium donor-acceptor systems;

P. Suresh Kumar; Sandeep Kumar and V. Lakshminarayanan

J. Phys. Chem. B 2008, **112**, 4865.

5.Electrochemical studies of redox probes in self-organized lyotropic liquid crystalline systems;

P. Suresh Kumar and V. Lakshminarayanan;

J. Chem. Sci. (*accepted*)

6.Electrochemical redox reactions in the micellar and liquid crystalline media;

P. Suresh Kumar and V. Lakshminarayanan

J. Indian Inst. Sci. (*accepted as review*)

7.Supramolecular nanocomposites as a quasi-one-dimensional semiconductor under ambient conditions;

P. Suresh Kumar, Sandeep Kumar and V. Lakshminarayanan;

(Communicated)

Chapter 1

Introduction

This thesis describes the electrochemical and electrical conductivity studies of redox probes and nanoparticles in some self-organised systems. In general self-organisation plays a key role in soft matter as can be seen from the example of protein folding and the functioning of all the biological systems, the formation of colloids, crystals, liquid crystals and so on. We have used three different self-organised systems, *viz*, lyotropic liquid crystals, thermotropic liquid crystals and self-assembled monolayers formed by different organic thiol molecules on gold surface. Electrochemistry in the lyotropic liquid crystalline phases is attracting importance in recent years as these phases can be explored for many of the biological studies. On the other hand, the electrical conductivity studies on the thermotropic discotic liquid crystals are of fundamental interest with several potential applications, mainly due to the unique quasi-one-dimensional electronic transport mechanism in the liquid crystalline phase. This particular property of the discotic systems can find applications in the field of molecular electronics, photovoltaics, solar cells and sensors. The self-assembled monolayers are important in the surface science due to the wide variety of applications by using simple fabrication methods.

In brief the thesis consists of three parts. The first part deals with the electrochemical redox reactions of different redox probes in a lyotropic columnar hexagonal liquid crystalline phase of Triton X-100/water system. The second part deals with the electrical conductivity studies in lyotropic and thermotropic columnar hexagonal liquid crystalline phases where

the lyotropic phase is formed by Triton X-100/water system, whereas thermotropic liquid crystalline phase was formed by triphenylene based organic molecules. The third part describes the electrochemical characterisation of self-assembled monolayers on the gold surface, formed by different organic thiol molecules that show liquid crystalline phases in the bulk.

The present chapter gives an overview of different topics covered in the thesis and is divided into two sections. The first section describes the materials and methodology used in the thesis, including lyotropic and thermotropic liquid crystals, gold nanoparticles as well as self-assembled monolayers. The second part provides a brief introduction to the theory and setup of different experimental techniques used in the present studies. This includes electrochemical techniques like cyclic voltammetry and electrochemical impedance spectroscopy, bulk characterisation techniques like polarising optical microscopy, small angle X-ray scattering, differential scanning calorimetry and spectroscopic techniques as well as scanning tunneling microscopy.

1.1 Materials

1.1.1 Liquid Crystals

Liquid crystalline phases are considered to be the fourth state of matter. They are also known as mesophases, which means intermediate phases. As the names indicate the properties of these phases are between that of crystalline phase and the liquid phase, which means that they have the orientational order of crystalline phase and the dynamic nature of liquid phase [1]. This makes the liquid crystals very interesting in many respects. The liquid crystals may be classified as of two types: thermotropic and lyotropic liquid crystals. Thermotropic liquid crystals may be defined as liquid crystalline phases, when the substance passes between the solid, liquid crystal and liquid state and *vice versa* as a function of temperature and in the absence of solvent [2]. Lyotropic liquid crystals are formed by amphiphilic molecules in solvents, typically in aqueous medium, or may be in a mixture of solvents [3]. The different

lyotropic phases are formed as a function of the concentration of the surfactant as well as the temperature. In lyotropic liquid crystals, the concentration of the surfactant has a more specific role on the formation of different phases than the temperature. The following sections provides an introduction to both lyotropic and thermotropic liquid crystals. We have carried out the experiments in lyotropic columnar hexagonal liquid crystalline phase as well as thermotropic columnar hexagonal phase and the following section deals with the general discussion of these two classes of liquid crystals.

1.1.1.1 Lyotropic Liquid Crystals

Lyotropic liquid crystals are generally formed by the self-organisation of micelles, that are aggregates of surfactants in a solvent medium.

Surfactants: Surface active agents or surfactants are amphiphilic molecules, having a hydrophilic head group and a hydrophobic tail group as shown in Figure 1.1(a). Depending upon the head group, they may be classified as cationic, anionic, neutral or zwitterionic surfactants. The tail group normally consists of alkyl or substituted aromatic chains. A cationic surfactant has a positively charged head group with anionic counterions. Cetyltrimethylammonium bromide (CTAB) is an example for cationic surfactant, while sodium dodecyl sulphate (SDS) is an anionic surfactant where the amphiphilic part is anionic with Na^+ as the cationic counterion. There are surfactants that have neither cationic nor anionic groups but a neutral group as the hydrophilic group and they are known as neutral surfactants. Polyethylene glycol p-(1,1,3,3-tetramethylbutyl)-phenyl ether, which is popularly known as Triton X-100 is one example for such a surfactant. Here the polyethoxy chain acts as the hydrophilic part and the alkyl substituted phenyl group acts as hydrophobic part. The zwitterionic surfactants have both anionic and cationic groups in the same molecule that together act as the hydrophilic part. The structure of some of the common surfactants are shown in the Figure 1.1.

Micelles: The surfactants in a solvent, for example in water, at very low concentrations behave like a salt solution. At high concentrations, however the surfactant molecules in-

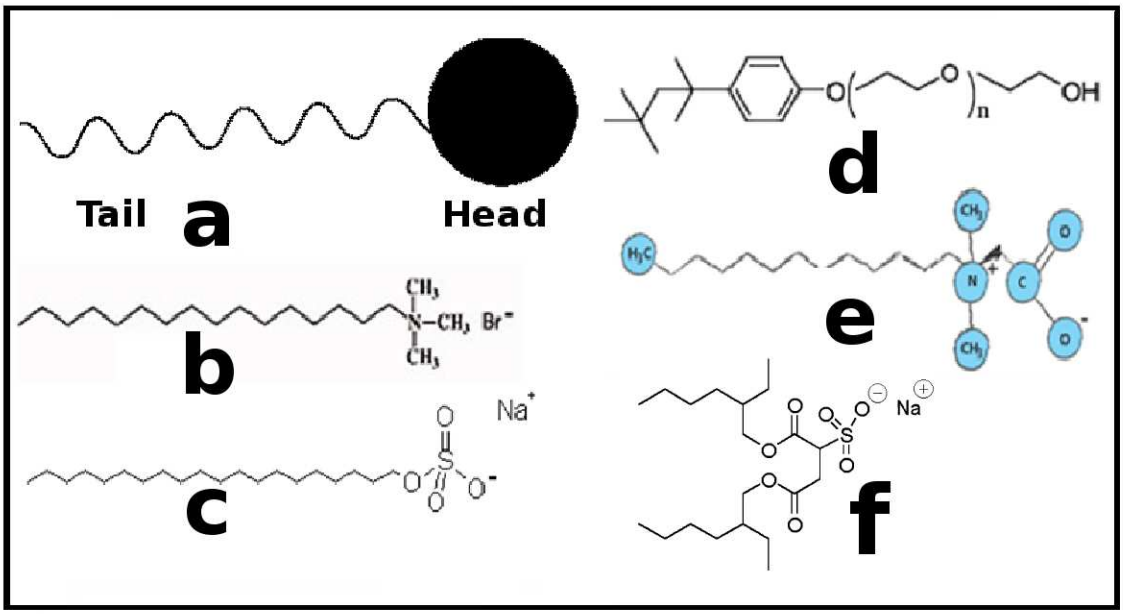

Figure 1.1: Schematic diagram of a) an amphiphilic molecule and the structures of some of the common surfactants b) cationic CTAB, c) anionic SDS, d) non-ionic Triton X-100, e) zwitterionic tridecyl betaine and f) Aerosol OT (AOT)

teract together and deviate far away from the properties that characterise the ideal solution. These intermolecular forces arise due to the electrostatic, polar-polar as well as hydrophobic-hydrophobic interactions which leads to the aggregation of surfactants. Above a particular concentration, known as the critical micellar concentration (cmc), they form the micelles. The micelles may be defined as small aggregated structures of surfactants with the solvent molecules, having uniform shape and size. The cmc depends on the nature of surfactant as well as the solvent. The shape of the micelles depends on the structure of the surfactant molecules. Spherical and cylindrical micelles are the most common shapes. Bilayer structure is very common with lipids and similar surfactants in aqueous solutions [3, 4].

The shape of the micelles can be predicted by knowing the interfacial energies between the hydrocarbon chain and water (γ), the area of the head group of the surfactant (a), the maximum effective length of the alkyl chain of the surfactant that may be assumed as the critical chain length (l_c) and the hydrocarbon volume of the surfactant (v). The critical chain length and the hydrocarbon volume can be approximately calculated by knowing the number

of carbon atoms (n) in the alkyl chain of the surfactant using the equations [3]:

$l_c \leq l_{max} \approx (0.154 + 0.1265n)$ nm and

$v \approx (27.4 + 26.9n) \times 10^{-3}$ nm^3

It is observed that for large n values, $\frac{v}{l_c} \approx 0.21$ nm^2 and is constant, which is close to the minimum cross sectional area of a hydrocarbon chain. The optimal hydrophilic area of the surfactant with minimum energy configuration corresponds to a_0 and the dimensionless packing parameter or the shape factor (s) can be defined as

$$s = \frac{v}{a_o l_c}$$

From this shape factor, the shape of the micelles may be predicted as:

$(\frac{v}{a_o l_c}) < \frac{1}{3}$ corresponds to spherical micelles,

$\frac{1}{3} < (\frac{v}{a_o l_c}) < \frac{1}{2}$ corresponds to non-spherical micelles or cylindrical micelles,

$\frac{1}{2} < (\frac{v}{a_o l_c}) < 1$ corresponds to vesicles or bilayers and

$(\frac{v}{a_o l_c}) > 1$ corresponds to inverted structures or reverse micelles.

It may be noted that for a given alkyl chain length, different micellar shapes may be formed depending on the hydrophilic head group area of the molecules. For the reverse micelles, for example, the hydrophilic area should be very less so that the shape factor is more than 1. This is important as in the reverse micelles, the hydrophobic part exposes outside and the hydrophilic part stays inside the micelles so that the hydrophilic part has to be close packed inside the micelles.

Lyotropic Liquid Crystalline Phases: The different types of micelles, as explained above, may aggregate further at higher concentration of the surfactants, leading to a 2-dimensional network of the micelles to form the liquid crystalline phase. Nematic, smectic, lamellar, cubic and columnar hexagonal phases are some of the examples of liquid crystalline phases formed by the surfactant molecules in the aqueous medium. A general discussion on these phases may be found elsewhere [5]. Among all these, the nematic phases are the simplest from point of view of their structure. They are formed by the rod-like or disc-like micelles and they orient in the same direction as that of the director. They have no positional order

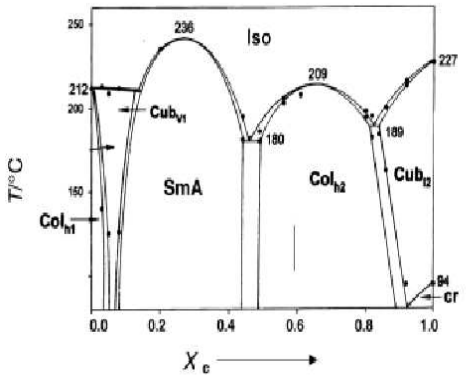

(a) A typical phase diagram for surfactant-water mixture

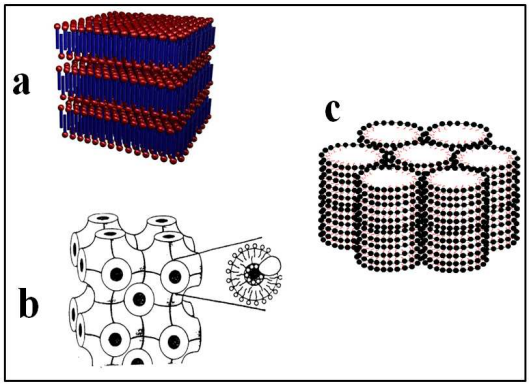

(b) Schematic representation of a) lamellar, b) cubic and c) columnar hexagonal liquid crystalline phases

Figure 1.2: Schematic representation for a phase diagram and lyotropic liquid crystalline phases

in the nematic phase. Smectic phases are structurally close to nematic order, with additional layered structure perpendicular to the director. The bicontinuous cubic phases are the first type of lyotropic liquid crystalline phases, and were reported in the 1960's [6, 7]. The lamellar phases are very common in the living systems, where the lipids form the bilayer structure in the biological environment. The columnar hexagonal phases are formed by the aggregation of cylindrical micelles. A plot of temperature vs. concentration of surfactant is usually represented for the properties of the binary mixture of surfactant and the solvent. Such a plot indicates the different liquid crystalline phases that can be formed by the binary mixture and is known as phase diagram and a typical phase diagram is shown in Figure 1.2(a). Phase diagram of ternary systems are also common. A schematic representation of some of the lyotropic liquid crystalline phases are shown in Figure 1.2(b).

Nematic phase: Nematic liquid crystals are common in the lyotropic phases and are formed mainly by the disc-shaped micelles. One of the example of such phase comes from the perfluorosurfactant/water systems where the surfactant is rubidium, potassium or tetramethyl ammonium salt of perfluorocarboxylic acids [8]. SDS has shown to form discotic nematic and a calamatic nematic phases [9]. In this phase the micelles orient in the same direction as

that of the director $\hat{n}$ without any positional order for the micelles.

Cubic phases: As the name indicates, the cubic phases have the cubic symmetry and physically they are highly viscous in nature. They have the most complex structure among all the lyotropic liquid crystalline phases with different symmetric structures. Three different symmetry groups have been identified in the cubic phases namely P($Im\bar{3}m$), D($Pn\bar{3}m$) and the G($Ia\bar{3}d$) phases. The G phase is a bicontinuous phase. The different symmetry forms can be interchanged with a small change in the composition or temperature and the enthalpy change for this transformation has been estimated to be very less ($<$0.01 kJ.mol^{-1}). Due to the cubic symmetry possessed by these phases, they are optically isotropic and hence they do not show any characteristic birefringence under cross-polarised light. This makes them very difficult to identify. The most common way of identification is by small-angle X-ray scattering studies. The three different cubic systems have their own characteristic ratio of the scattering vectors and from this, the symmetry group of the mesophase can be identified [5].

Lamellar Phases: The lamellar phase is one of the most common mesophase in the surfactant based systems and also in the biological environment that makes the phase very important. Many of the lipids are shown to form lamellar phase or the bilayer phase in living systems. The calculations show that for a bilayer structure, the shape factor s (defined by $v/a_o l_c$) should be close to 1 which is almost 2-3 times greater than that for a spherical micelles. This shows that bilayer structures are possible with the surfactants and lipids that have very small head group area or very long hydrophobic chains. The bilayer structures are common in surfactants and lipids that have double chain hydrophobic groups. It is also observed that due to the high hydrophobic volume of the surfactants, the critical micellar concentration (cmc) is very less for these surfactants and are less dynamic in nature.

A close analogue of the lamellar structure is the vesicles, which are closed spherical bilayers. When s=1, it can form only a planar bilayer structure. For the formation of vesicle, s should be less than 1, but following the condition that $\frac{1}{2} < \frac{v}{a_o l_c} < 1$. The minimum radius of the vesicle is given by

$$R_c \approx \frac{l_c}{(1 - v/a_o l_c)}$$

which is the critical radius to form the vesicle without strain on the surfactant or lipid molecules.

Columnar phases: The columnar phases are formed by the aggregation of cylindrical micelles in the medium. For a normal cylindrical micelle, the shape factor should be $\frac{1}{3} < \frac{v}{a_o l_c} < \frac{1}{2}$. Several ionic as well as non-ionic surfactants are known to form cylindrical micelles. One of the most common example is Triton X-100/water system. The columnar phases may also be formed by reverse micelles, for example AOT/water system. Here the ratio $\frac{v}{a_o l_c}$ is more than 1, so that it forms reverse micelles and reverse hexagonal phase. A general discussion on the columnar hexagonal phase is described below.

1.1.1.2 Lyotropic Columnar Hexagonal Phase

The lyotropic columnar phases are formed by the hexagonal arrangement of the cylindrical micelles. They belong to the symmetry group of p6mm. This mesophase is classified into two types, the columnar hexagonal phase or the H1 phase and reverse columnar hexagonal phase or the H2 phase. H1 phase is formed by the aggregation of normal cylindrical micelles in hexagonal order with their hydrophilic groups projecting outside the micelle and hydrophobic groups inside the core of the micelle. In H2 phase, the hydrophobic groups project outside with the hydrophilic core inside, where the micelles are known as reverse micelles. The columnar phase formed by the non-ionic surfactant Triton X-100 in aqueous medium is an example for the H1 phase [10] while the surfactant Aerosol OT (AOT) forms the H2 phase [11, 12].

1.1.1.3 Thermotropic liquid crystals

Thermotropic liquid crystals may be defined as liquid crystalline phases, when the substance passes between the solid, liquid crystal and liquid state and *vice versa* as a function of temperature and in the absence of solvent. The different phases shown by these materials are smectic, nematic, cholesteric, columnar phases. A schematic representation of some of these phases are shown in Figure 1.3.

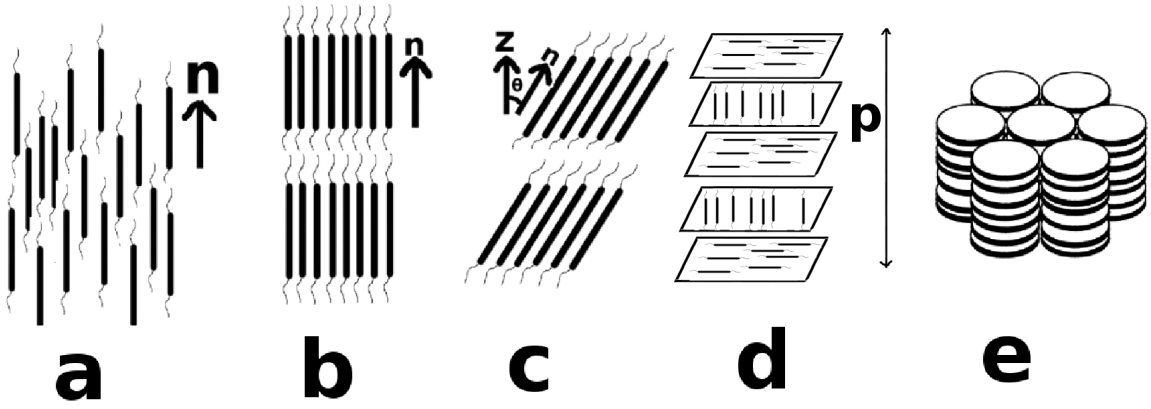

Figure 1.3: Schematic representation of a) nematic, b) smectic A, c) smectic C, d) cholesteric and e) columnar hexagonal liquid crystalline phases

Nematic Liquid Crystal: These are structurally the simplest among all the liquid crystalline phases. In this phase, the molecules have only orientational order without any positional order. The direction in which the molecules are oriented is called the director $\hat{n}$. This phase is generally observed with rod like molecules or calamatic molecules. Nematic phase formed by disc shaped molecules are known as discotic nematic phase (n_D phase). The name, nematic has the origin from the Greek word, which means thread, as these phases show a thread like texture between crossed polarisers.

Smectic Phase: Smectic phases possess an additional layered order compared to the nematic phase. Smectic phases are also formed mainly by the rod-like molecules. They have the layered order either 90°or at an angle θ with respect to the directer $\hat{n}$. If the layered order is perpendicular to the director, they are called Smectic A phases, commonly abbreviated as SmA phases. On the other hand, if it is at an angle other than 90°, they are called Smectic C (SmC) phase. A schematic representation of these two phases are shown in the Figure 1.3.

Cholesteric Phase: This was the first liquid crystalline phase reported by Friedrich Reinitzer in 1888 [13]. He observed that cholesteryl benzoate has two different melting points and later studies showed that the intermediate phase between the two melting points corresponds to a liquid crystalline order which currently termed as chiral nematic phase. The term cholesteric liquid crystals is also used for the phase as cholesteryl derivatives were the most common

compounds that exhibit this phase. All these compounds are chiral in nature and hence the name chiral nematic. Chiral structures are also reported in other liquid crystalline phases. A model structure of the chiral nematic phase is represented in Figure 1.3.

Columnar Phases: The thermotropic columnar liquid crystalline phase was first reported by Chandrasekhar *et al.* in 1977 with a hexasubstituted benzene derivative [14]. These phases are generally formed by molecules having an aromatic core with flexible alkyl substitution which resembles a disc like shape. Some of the most common core groups are benzene, anthracene, triphenylene, hexabenzocoronene and anthraquinone [2]. The phase is formed by the aggregation of different columns of the discotic molecules forming different architectures like columnar hexagonal, rectangular, oblique and plastic phases. These different columns are formed due the $\pi - \pi$ interactions between the aromatic core molecules. Typical core-core distance in the column is about 0.35 nm while the inter-columnar distance is about 2-4 nm depending on the aromatic core and the chain length of the flexible alkyl groups. Due to the very small core-core distance and large column-column distance, the electron transport through the columns is very facile compared to transport across the columns and hence they are well-known for their quasi-one-dimensional electrical conductivity behaviour. The anisotropy in the conductivity has been reported to be about 10^3 to 10^6 [15], which means that the conductivity along the column axis is 10^3 to 10^6 times more than that in the direction perpendicular to the column. A schematic representation of the columnar hexagonal phase is represented in the Figure 1.3. In this thesis, we have extensively used the columnar hexagonal phase for the studies, utilising their one-dimensional conductivity properties.

1.1.1.4 Properties of Columnar Hexagonal Phase

As mentioned before, the columnar hexagonal phase (Col_h phase) is formed by the disc like molecules having an aromatic core and flexible aliphatic chains. The aromatic core may be either electron rich like benzene, anthracene, triphenylene etc or may be electron deficient cores like anthraquinone. Due to the strong core-core interactions in these phases, they show quasi-one-dimensionality in their electrical conductivity, that have been explored in many

fields like molecular electronics [16], photovoltaic cells [17], solar cells [18], organic light emitting diodes [19] and sensors [20]. The electrical conductivity of the pure columnar phase is very less as the band gap of these molecules is quite large, about 4 eV. They may be converted to semiconductors by the addition of dopants like $AlCl_3$ [21, 22], $NOBF_4$[15, 23, 24], TNF[25], iodine [26] or gold nanoparticles [27, 28]. These studies show that dopants at low concentrations can enhance the electrical conductivity of the phase by several orders of magnitude without altering the liquid crystalline order.

1.1.2 Nanomaterials

Nanomaterials may be defined as materials where at least one of their dimension is below 100 nm. Due to their special properties, these materials have captured wide interest in fundamental research as well as technological applications for the last few years. These materials have some unique properties due to their nanometer size and as a result of which, they deviate from the classical behaviour to the quantum behaviour. Gold nanoparticles are an important component of nanoscience research that finds several advantages over other nanoparticles and quantum dots as far as functionality and stability is concerned. The synthesis, stability and processability of the gold nanoparticles have become very easy after the two-phase chemical synthetic route proposed by Brust *et al.* in 1994 [29]. The facile synthesis of thiol functionalised nanoparticles by the Brust method revived interest in the gold nanoparticle research all over the world [30]. This enabled the attachment of several terminally functionalised thiols on the nanoparticles and therefore further surface functionalisation of the thiol protected nanoparticles with biomaterials including enzymes and proteins. This finds applications in the areas like biosensors [31]. In the present thesis, we have used gold nanoparticles for the preparation of nanocomposites and their characterisation studies. The following sections describe the common methods of synthesis, properties and applications of these nanomaterials.

1.1.2.1 Gold Nanoparticles

Gold nanoparticles (GNPs) may be considered as the oldest of all the colloids in the ancient history, as the gold colloids are reported to exist in 4^{th} century B. C. [30] and were used for several medical applications in the past. The present day nanoparticle research concentrate on particles having sizes up to 20 nm. These nanoparticles find wide applications in different areas. We discuss below the synthesis, properties and applications of the gold nanoparticles.

1.1.2.2 Synthesis of Nanoparticles

Citrate Reduction: The citrate reduction method was reported first in 1951 by Turkevitch [32] and still in use for the synthesis of gold nanoparticles. Citrate is added to the chloroauric acid where the former reduces the Au(III) and act as a stabilising agent too. The ratio of citrate to chloroaurate can be used for the regulation of size of the nanoparticles.

Brust method: The Brust method is based on the chemical reduction of $AuCl_4^-$ ions to Au atoms using $NaBH_4$. $AuCl_4^-$ is transferred from aqueous phase to the toluene phase using tetraoctylammonium bromide as a phase transfer catalyst and reduced by $NaBH_4$ in the presence of dodecanethiol [29]. The thiol molecules readily binds with the surface gold atoms forming Au-S bonds, that are highly stable against temperature and time. The advantages of this method over other synthetic routes is that the synthesis, purification and processing is easy. Moreover the nanoparticles can be functionalised with any thiol molecules and therefore by using a terminally functionalised thiol, the nanoparticles can be attached to other molecules, including biomolecules, and the reactions can be carried out easily in the solution phase. Nanoparticles of specific sizes in the range of 1.2 to 5 nm can be prepared easily by this method. The nanoparticles can be re-dissolved in organic media and further extracted any number of times without aggregation, similar to other organic molecules. Due to these reasons, Brust method has become the most popular method for the gold nanoparticle synthesis.

Gold nanoparticles have also been stabilised by disulphides, thioether, dithiol and other sulphur containing organic molecules. Among all the sulphur containing stabilisers, organic

thiols are the commonly used groups due to the stability of the nanoparticles and the facile handling. Nanoparticles can also be stabilised with phosphine, amine and carboxylate ions. Polymers and many surfactants are also shown to be able to stabilise the nanoparticles even-though such GNPs are not as stable as the thiol protected GNPs.

GNPs stabilised by surfactants and polymers are also reported in the literature. The synthesis of nanoparticles in surfactant based media have been carried out where the surfactant molecules act as stabilisers and in some cases, they have been used as the reducing agent also. The synthesis is reported in a variety of surfactant media like Triton X-100, AOT, CTAB etc. [33, 34, 35, 36, 37].

1.1.2.3 Properties of GNPs

The structure of the nanoparticles have been studied in the literature extensively and it has been shown that the smallest particles have 12 gold atoms surrounding another gold atom in a close packed arrangement that totally contains 13 atoms. In bigger nanoparticles, the subsequent layers of gold atoms are shown to contain $10n^2 + 2$ atoms where n is the layer number. Hence the second layer contains 42 atoms forming Au_{55} cluster, third layer contains 92 atoms forming Au_{147} cluster and so on.

Surface Plasmon Resonance of GNPs: The nanoparticles are important as the properties of these clusters are different from the individual atoms and the bulk metals. This results from the quantum confinement of the electrons in the clusters, which arises when the de Broglie wavelength of the valence electrons are comparable to the size of the particles itself. Under such conditions the particles behave as electronically zero dimensional quantum dots. The electrons trapped in the clusters exhibit a characteristic collective oscillation. This oscillation gives rise to the so-called plasmon resonance band (PRB) or surface plasmon resonance (SPR) observed near 520 nm for the 3-20 nm diameter nanoparticles for which range the size-dependent quantisation occurs. Some of the major features of surface plasmon band of GNPs are [30]:

(i) its position at around 520 nm

(ii) its sharp decrease in intensity with decreasing core size, for GNPs with 1.4-3.2 nm core diameter due to the onset of quantum size effects. It has been shown that the damping of the surface plasmon band varies inversely with radius due to surface scattering of the conduction electrons which is accompanied by broadening of the plasmon bandwidth.
(iii) step-like spectral structures indicating transition to the discrete unoccupied levels of the conduction band with monodispersed GNPs with core diameters between 1.1 and 1.9 nm.
(iv) the surface plasmon band is absent for GNPs with core diameter less than 2 nm, as well as for bulk gold. With elliptical particles, the band is shifted to higher wavelength as the spacing between particles is reduced, and this shift is well described as an exponential function of the distance between the two particles.

The size-dependent confinement of the electrons results in the formation of selective energy levels by these standing electron waves. Such energy levels can be obtained from the scanning tunneling microscopy studies during the tunneling of electrons between tip and the nanoparticles which is known as the Coulomb blockade. This can be observed when the electrostatic energy $E_{el} = e^2/2C$ is more than the thermal energy (k_bT) where C is the capacitance of the nanoparticle. This shows that the Coulomb blockade can be observed only when the capacitance is very low or the size of the particle is very low. For nanoparticles with size about 5 nm, the capacitance is of the order of 10^{-18} F/cm^2 and hence the Coulomb blockade exhibits.

1.1.2.4 Applications of Nanoparticles

Biological Applications: Due to the unique properties of the nanoparticles and the easy functionalisation with a variety of molecules using different functional terminal groups, they find diverse applications in the field of biosensors, catalysis etc. [31]. The review by Katz *et al.* has discussed in detail about the different routes for the enzyme or protein functionalisation of the nanoparticles. The nanoparticles can be either functionalised through electrostatic interactions between the stabiliser and the biomaterials. This is possible when the nanoparticles are stabilised by ionic groups like citrate or thiols with terminal ionic groups.

With terminally functionalised thiols as stabilisers, like amino or carboxyl terminated thiols, nanoparticles can be covalently attached to the biomaterials. Specific interactions can also be used for the functionalisation if the GNPs are stabilised using biomolecules like lysine [31].

Electrochemical Studies: Viologen thiols have been used as redox-active linkers in order to study the electron transfer between the linked GNPs [38]. GNPs are also reported to be capable of tuning the electrochemical properties of the electrode/solution interface using the $[Fe(CN)_6]^{4-|3-}$ redox system [39].

Catalysis: Gold nanoparticles are very good catalysts for a variety of reactions. For example, they are excellent catalysts for the CO oxidation and a large number of studies have been reported in this field [31]. The GNPs are also shown to catalyse methanol oxidation and oxygen reduction and have several potential applications in the field of fuel cells [40, 41].

1.1.3 Self-Assembled Monolayers

Surface modification of metals is of intense research interest for both fundamental studies as well as for their potential applications. Among several type of surface modifications, functionalisation of the metal surface with organic molecules possess a wide range of applications, as they facilitate link-up with a variety of other molecules. Two methods that have been widely used for the surface functionalisation of noble metal surfaces are Langmuir Blodgett (LB) films and the self-assembled monolayers (SAMs) [42, 43, 44].

In Langmuir adsorption, the organic molecules get adsorbed on the metal surface, due to the weak van der Waals forces acting between the metal surface and the adsorbates. Since the force of attraction is weak, the process lack specificity and high stability. The method has the potential to form multilayers of organic films on the surface. The LB films are formed by the following method: amphiphilic molecules are spread over the water surface, that form a monolayer at the air-water interface at low concentrations, which is known as the Langmuir monolayer. Dipping a suitable substrate like metals into the interface makes the amphiphilic molecules to transfer onto the substrate forming a layer on the substrate, which is known

as LB film. Depending on the nature of the substrate, hydrophilic or hydrophobic, either a single layer or a bilayer may be formed on the substrate. Repeated dipping may result in the formation of multilayers of the organic molecules on the substrate surface [45, 46].

Self-Assembled Monolayers (SAMs) are formed by spontaneous adsorption of certain molecules on the surface. They are ultrathin films of organic molecules with thickness corresponding to a single molecular layer due to the formation of chemical bond between the substrate and the organic molecules. The preparation of SAMs is a simple procedure, in which a cleaned metal surface is dipped into a dilute solution of certain organic molecules. The SAMs possess a well ordered crystalline arrangement of the molecules on the surface. Among several self-assembled monolayers, the most extensively studied system is that of organic thiols on the gold surface. SAMs of different thiols on silver [47, 48, 49], copper [50, 51, 52], platinum [53, 54] and palladium [55] surfaces are also reported. Apart from SAMs of thiols, monolayer formation of sulphides, disulphides and dithiols have also been studied in the literature [56].

Three steps are involved in the process of self-assembled monolayer formation and are depicted in Figure 1.4. The first step is the chemisorption of the head group onto the substrate, which is an exothermic process. The very strong molecule-substrate interactions result in the pinning of the head group to a specific site on the surface of a substrate through a chemical bond. The gold-sulphur bond is covalent in nature with slight polarity as there is a large difference in the electronegativity of these two elements. The energy associated with such chemisorption is of the order of tens of kcal.mol^{-1} and for thiolate adsorption on gold the enthalpy of adsorption is $\sim$40-50 kcal.mol^{-1}. Due to the exothermic process in the first step, thiol molecules try to occupy all the available bonding sites on the gold surface leading to a high coverage of the monolayer. The second step is the inter chain van der Waals interactions among the alkyl group. The energy associated with this process is only a few kcal.mol^{-1} and leads to the crystalline arrangement of alkyl chains. The third and final step is the re-orientation of the terminal groups. For simple alkanethiols, methyl group is the terminal group. FTIR [57] and helium diffraction [58] studies indicate that these terminal

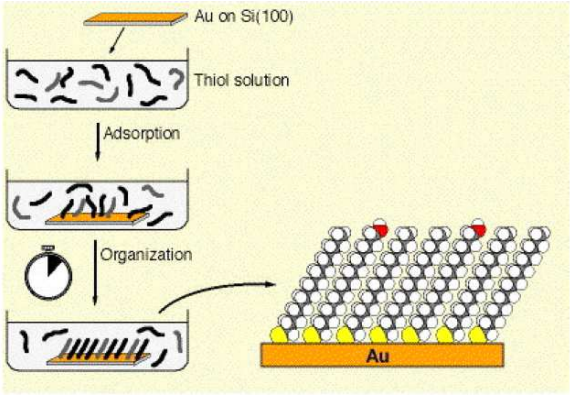

Figure 1.4: Schematic representation of the steps involved in the formation of self-assembled monolayer

groups are disordered under ambient conditions as the energy cost for this is in the order of few k_BT.

1.1.3.1 Nature of Bonding

Both the alkanethiols and disulphides adsorb onto gold substrate to form the same thiolate (RS^-) species. The reaction of dialkyldisulphides with gold is an oxidative addition reaction as follows.

$RS–SR + Au_n^0 \rightarrow 2\ R–S^-–Au^+ + Au_{n-1}^0$

In the case of alkanethiol, the reaction may be considered as an oxidative addition of the thiol (S-H) bond to the gold surface, followed by a reductive elimination of hydrogen. When a clean gold surface is used for the monolayer preparation, the proton may probably end as H_2 molecule. The chemical reaction occurs in this case can be expressed as follows:

$R–S–H + Au_n^0 \rightarrow R–S^-–Au^+ + Au_{n-1}^0 + \frac{1}{2}H_2$

The combination of hydrogen atoms at the gold surface to give H_2 molecule is an important exothermic step in the overall chemisorption energy involved in the process of self-assembly. During the chemisorption process, the thiolate species has been formed, as can be seen from the equation represented above, which is verified by XPS [59, 60, 61], FTIR spectroscopy [62], FT-mass spectrometry [63], electrochemistry [64] and Raman spectroscopy [65].

The characterisation of the monolayers may be carried out using a variety of experi-

mental techniques including electrochemical, FTIR, Raman spectroscopy, surface plasmon resonance spectra, ellipsometry, contact angle, quartz crystal microbalance, scanning probe techniques and high vacuum techniques like X-ray photoelectron spectroscopy, Auger electron spectroscopy, high resolution electron energy loss spectroscopy, low energy electron diffraction and temperature programmed desorption. NMR, small-angle X-ray scattering, differential scanning calorimetry (DSC) and thermogravimetric analysis have also been employed for the characterisation of the monolayers [66]. The basic principles of some of the techniques that have been used in this thesis is described in the second section of this chapter.

1.1.3.2 Applications of SAMs

SAMs find a variety of potential applications in the field of molecular electronics, memory storage, molecular capacitors, biosensors, photolithography, wetting and corrosion protection. In addition, it is well known that monolayer acts as an electron transfer barrier for several redox species between the metal surface and the solution. In other words, the monolayer acts as an insulating layer between the metal and the environment and retards the further reaction of surface atoms, which is used for the corrosion inhibition. SAMs have also been used for the studies of single molecular electronic properties using either scanning tunneling microscopy or scanning tunneling spectroscopy. By these two methods, a single molecule can be addressed on the surface and the electronic properties of these molecules can be studied. Using dithiols, two metal surfaces can be interconnected resulting in a molecular wire between two electrodes. It has been shown that the wetting properties of the surface can be tuned by using thiols that have different terminal functional groups. For example, carboxyl terminal group provides a hydrophilic monolayer surface while methyl group in the terminal position results in highly hydrophobic surface. This also influences the orientation of the water molecules at the monolayer/water interface and it has been shown that the long chain alkanethiol monolayers results in the formation of a hydrophobic gap at the interface [67, 68]. This hydrophobic gap reduces the interfacial capacitance in alkanethiol monolayers to a large extent, while for monolayers with polar functional groups the capacitance decreases

only to a small extent. As mentioned before, the principle of SAMs has been widely used for the synthesis of monolayer protected nanoparticles especially gold nanoparticles [29]. The thiol functionalisation of the nanoparticles is to be highly stable and such nanoparticles are solution processable for further studies.

One of the main advantage of the SAMs is the possibility for further functionalisation of the surface through terminal functional groups like carboxyl, amino or other derivatisable groups at the terminal positions. Such groups can be easily attached with different organic molecules, redox probes, enzymes, proteins or other biomaterials [69, 70, 71]. Such biofunctionalised monolayers have been widely used for the sensor applications [72, 73, 74]. One of the recent advancement in the monolayer study is the lithography, where different patterns can be formed on the metal surface using the organic thiol molecules [75, 76]. In this thesis, we have focused our research on the electron barrier properties of monolayers which exhibit bulk liquid crystalline properties and also mixed monolayer modified gold surfaces. We have used electrochemical, FTIR and scanning probe techniques for the characterisation of these monolayers.

1.2 Experimental Techniques

This section deals with the basic principles of the several experimental techniques that have been used during the thesis work. They are broadly classified into three types as electrochemical, surface probe and bulk physical characterisations. Among the electrochemical techniques, we have extensively used DC technique like cyclic voltammetry and ac technique like electrochemical impedance spectroscopy. For the topographical information of the surfaces, scanning tunneling microscopy (STM) was used. Grazing angle Fourier transform infrared spectroscopy, UV-visible spectroscopy and photoluminescence spectroscopy were used to characterise some of the materials. Polarising optical microscopy (POM), differential scanning calorimetry (DSC) and small angle X-ray scattering (SAXS) were employed for the characterisation of the liquid crystalline samples that are used in our studies. Electri-

cal conductivity studies, both DC as well as ac conductivity, were used for investigating the electron and ion transport characteristics of the liquid crystalline samples.

1.2.1 Electrochemical Techniques

1.2.1.1 Cyclic Voltammetry

Cyclic voltammetry, commonly known as CV, is one of the most extensively used electrochemical potential sweep techniques. The simplest of potential sweep techniques is linear sweep voltammetry (LSV), which involves sweeping the electrode potential between the limits V_1 and V_2 at a known sweep rate, ν and measuring the current flow through the electrochemical system. In the case of cyclic voltammetry (CV) the initial potential sweep is similar to that in LSV, but after reaching the potential V_2 instead of terminating the scan, the sweep is reversed at the same scan rate as the forward sweep. A typical potential-time profile used in CV is shown in the Figure 1.5. In CV, the potential of the working electrode sweeps between the initial, V_1 and final V_2 values in the forward and reverse direction, and the corresponding current at the working electrode is measured. Hence CV represents the current vs. potential in the electrochemical cell. The current arises due to two reasons

i) Faradaic current resulting from various electrochemical processes like redox reactions, absorption etc and

ii) due to the double layer charging of the electrode|electrolyte interface leading to the capacitance current [77, 78].

A plot of measured current as a function of applied potential is known as cyclic voltammogram from which the potential corresponding to different processes can be obtained. From the dependence of peak current on the sweep rate, information regarding coupled homogeneous reactions, adsorption as well as the kinetic parameters and the mechanism of different heterogeneous reactions occurring on the electrode surface can be obtained. The shape of the cyclic voltammogram depends on the type of redox reactions. Figure 1.6 shows a typical cyclic voltammogram for a reversible one-electron transfer process.

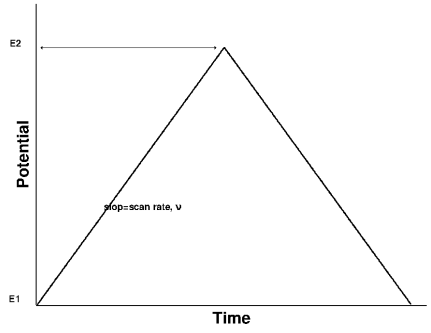

Figure 1.5: Typical potential-time profile applied in a cyclic voltammetric experiment

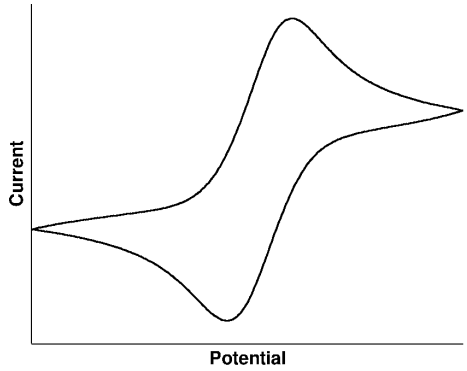

Figure 1.6: Typical current-potential profile in a cyclic voltammetric experiment

For a typical reversible one-electron redox reaction of the type,

$$O + ne^- \rightleftharpoons R$$

where O is the oxidised species and R is the reduced species. The rate of charge transfer is always greater than the rate of mass transfer at all potentials which means that the redox reaction is under diffusion control. The ratio of concentrations of oxidant and reductant species of a reversible reaction is given by Nernst equation and a concentration gradient exists within the region near the electrode surface known as Nernst diffusion layer, where the concentration gradient of the electroactive species is linear. The Nernstian equilibrium is always maintained at the electrode surface and at all the potentials. Based on this, the shape of current-potential profile for a one-electron reversible redox reaction, as shown in Figure 1.6, can be explained as follows. When the potential of the electrode is made more negative, at a characteristic potential for the redox species, the surface concentration of the reactant O decreases progressively due to reduction, thereby increasing the concentration gradient which leads to an increase in the current. Therefore the surface concentration of O decreases from its bulk value in order to satisfy the Nernst equation and a concentration gradient is setup. As a result, there is a flow of current proportional to this concentration gradient at the electrode. Due to diffusion of ions, the concentration gradient does not remain constant and it starts to decrease. At the same time, the electrode potential is also continuously changing leading to a further decrease of surface concentration of O until it effectively reaches zero.

Once the concentration of O reaches zero, the gradient decreases due to the accumulation of reduced species R, in the vicinity of the electrode surface (relaxation effect) and hence the current flow also decreases. Overall, this behaviour gives rise to a peak shaped current-potential profile as shown in Figure 1.6. Using similar arguments used for the forward sweep, it can be shown that the current change on reverse sweep also exhibit a peak shaped response but with an opposite sign. On increasing the sweep rate, the concentration gradient as well as the current resulting from it also increases due to the shorter time scale of the experiment leading to less relaxation effect.

The peak current density I_p of the cyclic voltammogram is related to various parameters by the following relationship:

$$I_p = -0.4463nF[nF/RT]^{\frac{1}{2}}C_o^{\infty}D^{\frac{1}{2}}\nu^{\frac{1}{2}}$$

where, I_p is the peak current density in A/cm^2, n is the number of electrons involved in the redox reaction, F is Faraday constant, R is the ideal gas constant, T is the absolute temperature, C_o^{∞} is the concentration of reactant O in mol/cm^3, D is the diffusion coefficient in cm^2/s and ν is the scan rate in V/s. This equation is known as the Randles-Sevcik equation and at room temperature (25 °C), this equation reduces to the form,

$$I_p = (-2.69 \times 10^5)n^{\frac{3}{2}}C_o^{\infty}D^{\frac{1}{2}}\nu^{\frac{1}{2}}$$

From the above equation, it can be noted that the peak current density of the reversible reaction is directly proportional to the concentration of the electroactive species, square root of the diffusion coefficient and also to the square root of the scan rate. The sign of the current is negative because it is the current for cathodic reaction (as denoted by the convention followed).

For a reversible system the conditions are as follows [78]:

1. $\Delta E_p = |E_p^a - E_p^c|$ = 59/n mV
2. $|E_p - E_{p/2}|$ = 59/n mV
3. $|I_p^A/I_p^C|$ = 1
4. $I_p \propto \nu^{1/2}$ and passes through the origin

5. E_p is independent of ν

6. At potentials beyond E_p, I$\propto t^{-1/2}$

Apart from the reversible reactions cyclic voltammetry can be used to find out the quasi-reversible and irreversible nature of the electrochemical redox reactions. There are separate conditions to verify the quasi-reversibility and irreversibility of a given system.

1.2.1.2 Electrochemical Impedance Spectroscopy

Electrochemical impedance spectroscopy (EIS) is an ac technique for the electrochemical studies. In contrast to cyclic voltammetry, which is a DC technique, where the electrochemical system is perturbed far from equilibrium, EIS involves the application of a very small perturbation where the system is close to the steady state equilibrium. The EIS measurements involve essentially a small perturbation of the electrode potential from the equilibrium potential by the application of a sinusoidal signal of 5-10 mV peak-to-peak amplitude in a range of frequencies and measuring the response of the electrochemical system. Usually, the response in terms of current to the perturbation, differs in phase and amplitude from the applied voltage signal. Figure 1.7 shows the sinusoidal signal of perturbation and response of the electrochemical system.

The measurement of phase difference and amplitude of the responce signal compared to the applied signal over a wide frequency range can be used for the analysis of different electrode processes like double layer charging, kinetics of redox reactions, diffusion of the redox probes, homogeneous and heterogeneous electron transfer reactions and coupled chemical and redox reactions. The impedance spectroscopy has been extensively used in the study of corrosion, battery, membranes, ionic solids, solid electrolytes, chemically modified electrodes and template deposited porous electrodes.

In many of the measurements involving the fast electron transfer reactions, the information has to be obtained at very short times, otherwise diffusion rather than the kinetics becomes the rate determining process. In such a case, the ac techniques are widely used to

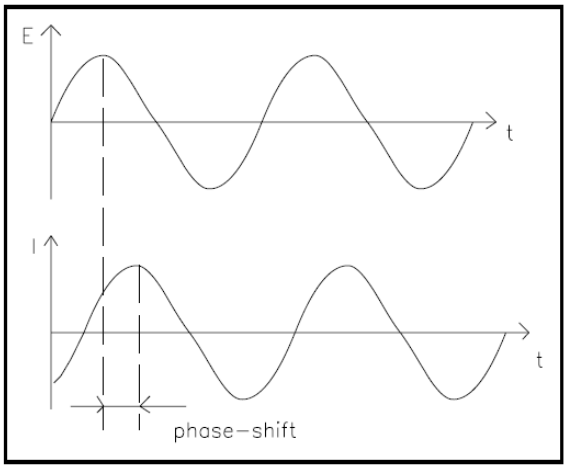

Figure 1.7: Schematic representation of a small sinusoidal applied perturbation (E) and the current responce (I)

determine the rate constant for the fast redox reactions. Due to the small perturbation, the system is in the linear regime and the advantage lies in the ability to treat the response theoretically using the linearised current-potential characteristics. Since, the working region in this method is very close to the equilibrium, the detailed knowledge about the behaviour of the current-voltage response over a large range of overpotential is not required. This simplifies the treatment of kinetics and diffusion equations. Using this method, the high precision measurements can be made because the response is indefinitely steady and therefore can be averaged over a long period. Usually, a comparison is made between the electrochemical cell and an equivalent circuit, which contains a combination of resistors and capacitors that are assumed to behave like an electrochemical cell under consideration. The aim of the impedance measurements is to interpret these equivalent circuits and the values determined using these circuits, in terms of the interfacial phenomena occurring at the electrode-solution interface. The impedance spectroscopy is frequently used for the evaluation of heterogeneous charge transfer parameters and to study the double layer structure.

Principles of ac Circuits

The electrochemical response of a cell to an ac perturbation can be analysed by the knowledge of fundamental principles of ac circuits. If a sinusoidal signal of voltage

$V = V_0 sin(\omega t)$ is applied to an electrical circuit that contains a combination of resistors and capacitors, the response is a current, which is given by, $I = I_0 sin(\omega t + \phi)$, where V_o is the maximum amplitude, I_o is the maximum current, ω is the angular frequency and ϕ is the phase angle between the perturbation and response. The proportionality factor between V and I is known as the impedance Z. In phasor terms the rotating vectors are separated in the polar diagram by the angle.

In the case of a pure resistor, R, the phase angle ϕ is zero. According to Ohms law, V = IR, which leads to $I = V_0 sin\omega t$ / R. There is no phase difference between the applied potential and the response current. For a pure capacitor, C, the current I is given by, $I = C\frac{dV}{dt}$. On substituting the value of V as $V_0 sin(\omega t)$ and differentiating, the equations becomes,

$$I = \omega C V_0 sin(\omega t + \pi/2)$$

$$I = V_0 sin(\omega t + \pi/2)/X_C$$

where $X_C = (\omega C)^{-1}$ is known as the capacitive reactance. Here we find that the phase angle is $\pi/2$, implying that the current leads the potential by 90°or $\pi/2$ in the case of a pure capacitor. Similarly, for a circuit element containing a pure inductance, the potential leads the current by 90°or $\pi/2$.

Equivalent Circuit of an Electrochemical Cell

In general, an electrode|solution interface can be considered as an impedance to a small sinusoidal excitation. The impedance of such kind of electrochemical interface is a complex function, Z(ω) that can be expressed either in polar coordinates or in Cartesian coordinates, as shown below:

$Z(\omega) = |Z|e^j$

$Z(\omega) = Z'(\omega) + j\ Z''(\omega)$

$|Z|^2 = |Z'_{re}|^2 + |Z''_{im}|^2$

where Z'_{re} and Z''_{im} are the real and imaginary components of the impedance.

The phase angle ϕ can be expressed as,

ϕ = Arctan $\frac{Z_{im}}{Z_{re}}$ = Arctan$\frac{(Z''(\omega)}{Z'(\omega)}$ and

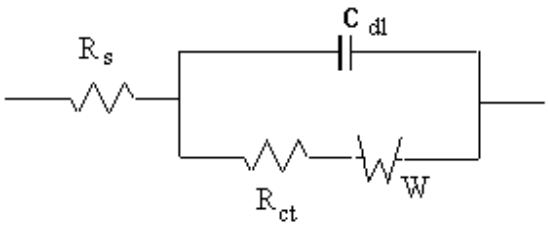

Figure 1.8: A simple Randle's equivalent circuit for a diffusion controlled reaction

Z_{re} or $Z'(\omega) = |Z|\cos\phi$

Z_{im} or $Z''(\omega) = |Z|\sin\phi$

Hence the electrode|electrolyte interface of the electrochemical cell can be represented by a suitable equivalent circuit consists of resistors and capacitors that pass current with the same amplitude and the same phase angle under a given excitation. In Figure 1.8 an equivalent circuit popularly known as Randles equivalent circuit for a diffusion controlled electron transfer reaction is shown which contains the solution resistance, R_s, the double layer capacitance C_{dl}, the charge transfer resistance, R_{ct} and the Warburg impedance Z_W, which is related to the diffusion of the redox probe.

The total current on the working electrode is obtained by the sum of distinct contributions from the Faradaic current I_f and the double layer charging current I_c. The double layer capacitance arises from the charges stored at the electrode|electrolyte interface. This double layer structure closely resembles a pure capacitor and hence it is represented by the element C_{dl} in the equivalent circuit. The Faradaic impedance Z_f can be separated into two components namely, the charge transfer resistance, R_{ct} and the Warburg impedance, Z_W. The charge transfer resistance, R_{ct} denotes a resistance offered to the electron transfer process and Z_W represents resistance to the mass transfer process or diffusion. Z_W depends on the frequency of the perturbation. At high frequencies, the Warburg impedance is small because the reactants do not have to diffuse very far. In contrast, at low frequencies, the diffusing reactants have to move very far, thereby increasing the Warburg impedance. The uncompensated solution resistance denoted by R_s exists between the working electrode and the reference electrode. In the equivalent circuit representation, the uncompensated solution

resistance, R_s is inserted as a series element since all the current has to pass through this element. For a planar diffusion, the value of R_{ct} can be expressed as,

$$R_{ct} = \frac{RT}{nFI_0}$$

where I_0 is the exchange current density. The solution resistance R_s is given by the following expression,

$$R_s = \frac{x}{\kappa A}$$

where x is the distance of the capillary tip from the electrode, κ is the conductivity of the solution and A is the area of the electrode.

The values of R_{ct} and Z_W indicates whether a redox reaction is charge-transfer controlled or diffusion controlled reaction. For reactions with large I_o value, R_{ct} will be proportionately less and dominated by z_W leading to a diffusion controlled reaction. On the other hand, for very small I_o value, where the kinetics of the reaction is very less, R_{ct} will be very high, that results in a kinetically controlled reaction. The total analysis of the impedance is known as complex plane impedance analysis. Randles equivalent circuits are used for the representation of the elements involved in the circuits which are series and parallel combination of the different elements like capacitors and resistors. This has two limiting cases. At low frequencies, as $\omega \to 0$, the real and imaginary parts of impedance are given by,

$Z' = R_s + R_{ct} + \sigma\omega^{-1/2}$

$Z'' = \sigma\omega^{-1/2} + 2\sigma^2 C_{dl}$

where

$$\sigma = \frac{RT}{2^{\frac{1}{2}} n^2 F^2 D^{\frac{1}{2}} A}\left(\frac{1}{C_O} + \frac{1}{C_R}\right)$$

in which, D is the diffusion coefficient of the species in solution, A is the area of the electrode, C_0 and C_R are the bulk concentrations of the oxidised and reduced species. On rearranging these equations, we get,

$Z'' = Z' - R_s - R_{ct} + 2\sigma^2 C_{dl}$

This is the equation of a straight line of unit slope and with an intercept on the real Z' axis given by $R_s + R_{ct} - 2\sigma^2 C_{dl}$. At high frequencies where the Warburg impedance is negligible

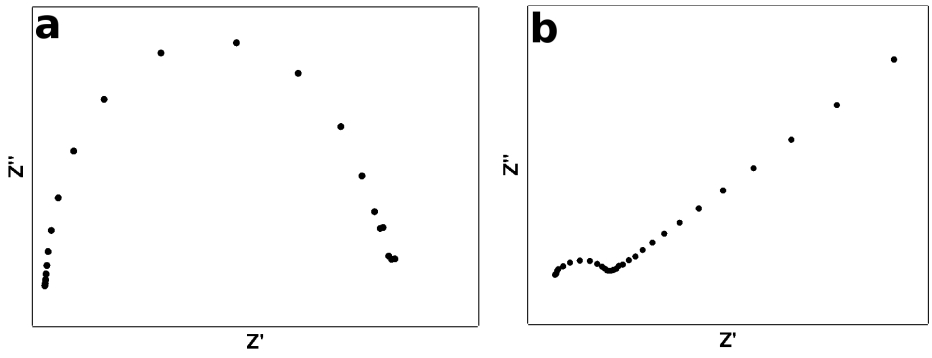

Figure 1.9: Nyquist plot for a) kinetically controlled reaction and b) diffusion controlled reaction

in comparison to R_{ct}, the two components are represented by,

$Z' = R_s + R_{ct}/(1+\omega^2 R_{ct}^2 C_{dl}^2)$ and

$Z'' = C_{dl} R_{ct}^2 \omega/(1+\omega^2 R_{ct}^2 C_{dl}^2)$

Eliminating ω from these two equations gives,

$(Z' - R_s - R_{ct}/2)^2 + (Z'')^2 = (R_{ct}/2)^2$

which is the equation of a circle with centre at $Z' = R_s + R_{ct}/2$ and a radius of $R_{ct}/2$. A plot of the whole expression for Z' verses Z'', which is known as Cole-Cole plot, for a kinetically controlled and a diffusion controlled reactions are shown in the Figure 1.9.

The Cole-Cole plot of a charge transfer controlled reaction shows a semicircle and it is obtained by plotting the values of Z' and Z'' at different frequencies. It is also known as the Nyquist plot. At infinite frequency, Z'' approaches zero as the capacitance in the equivalent circuit offers a very little impedance. At low frequencies, the impedance is purely resistive, because the reactance of C is very large. The solution resistance has the effect of translating the semicircle on the Z' axis. R_s can be determined by reading out the real axis value at the high frequency intercept. C_{dl} can be obtained from the maximum value of Z'' in the semicircular region where $\omega = 1/R_{ct}C_{dl}$. The diameter of the semicircle provides the value of R_{ct}. For a diffusion-controlled reaction, Warburg impedance is an additional term. At low frequencies, it varies inversely with frequency and at very low frequencies, it increases and dominates, leading to a straight line with a phase angle of 45°. Another

way of representing the impedance data is by the Bode plot, where both the logarithm of the modulus of impedance (log|Z|) and the phase angle are plotted in the y-axis against a common abscissa of frequency (in logarithmic scale). On such a plot a pure resistance is denoted by a horizontal line and a constant phase angle ϕ of 0°, while a capacitor is a straight line of unit slope and a constant phase angle ϕ of 90°.

The impedance measurements must be made over a wide range of frequencies in order to attain the high frequency limit of the impedance, which is equal to the electrolyte resistance. At high frequencies, the capacitive effect is attributed to a pure double layer capacitance. The frequency range for the measurement may be from 100 mHz to 10 MHz, depending on the electrochemical system employed for the analysis. There are different types of methods used to measure the impedance of an electrochemical system namely, Wheatstone bridge, analogue ac analyser, phase sensitive detection, sine wave correlation, frequency response analyser and Fourier transform methods [77, 78]. In our work, we have carried out the impedance measurements using a Perkin Elmer Model 5210 lock-in amplifier controlled by PowerSine software. Phase sensitive detection method was employed for the measurement of the impedance of the electrochemical cell above 5 Hz using a single-sine technique that provides the highest accuracy. Below 5 Hz, the measurement of impedance was performed using a fast Fourier transform technique based on multi sine experiments that avoids any drift or change in the impedance value of the electrochemical system. The potential of the working electrode is held at a desired DC potential of interest using a potentiostat. A small amplitude of sinusoidal ac voltage with 5-10 mV peak-to-peak is applied to the cell from a lock-in amplifier. The current output from the cell has a phase difference with respect to the input voltage. The lock-in amplifier measures this phase difference and amplitude of the current response, which can be converted to the real and imaginary part of the impedance.

1.2.2 Scanning Probe Techniques

Scanning probe microscopy contains mainly two techniques, scanning tunneling microscopy (STM) and atomic force microscopy (AFM). STM works on the principle of quantum me-

chanical tunneling of electrons between two conducting samples separated by a very small distance of the order of a few nanometers and by applying a bias voltage of the order of hundreds of mV. The current flow due to the tunneling is directly related to the distance between the samples and exponentially decays with distance. The measurement of current over scanning the surface using a tip allows us to get the information about the topography of the sample surface. While STM can be used for only electrically conducting surfaces, atomic force microscopy can be used for even non-conducting surfaces too. AFM is similar to STM in the functioning except the probe, where the force acting between tip and the sample is measured. In STM and AFM, the tip feels the sample surface rather than seeing the surface. The basic principle of STM is described in the following paragraphs.

1.2.2.1 Scanning Tunneling Microscopy

The Scanning tunneling microscopy, abbreviated as STM, is a versatile tool to obtain the topographic images of smooth conductive surfaces in the area of surface science [79]. Scanning tunneling microscope was invented by Gerd Binnig and Heinrich Rohrer [80] at the IBM Zurich Research Laboratory, Switzerland in the year 1982 for which they got the Nobel prize in the year of 1986. It can be used in the investigation of very small areas of surfaces in the order of subnanometers to micrometers with high precision. It also has the advantage of studying atomically smooth conducting surfaces in a variety of environments like ultra high vacuum (UHV), air and electrolytic media. In a typical STM experiment an atomically sharp metallic tip made up of either Pt, Pt/Ir, Pt/Rh or W is brought very close to the surface with the separation of the order of few angstroms between them. The movement of the tip in all the three direction is carried out with the help of piezoelectric crystals. Application of a small potential difference ($\sim$0.1 V) between the sample surface and the tip leads to the flow of tunneling current in the order of pA to nA [81]. This tunneling is due to the fact that the electron wave functions of the tip and the sample overlap. The tunneling current is of the form

$$I_t = Ve^{-kd}$$

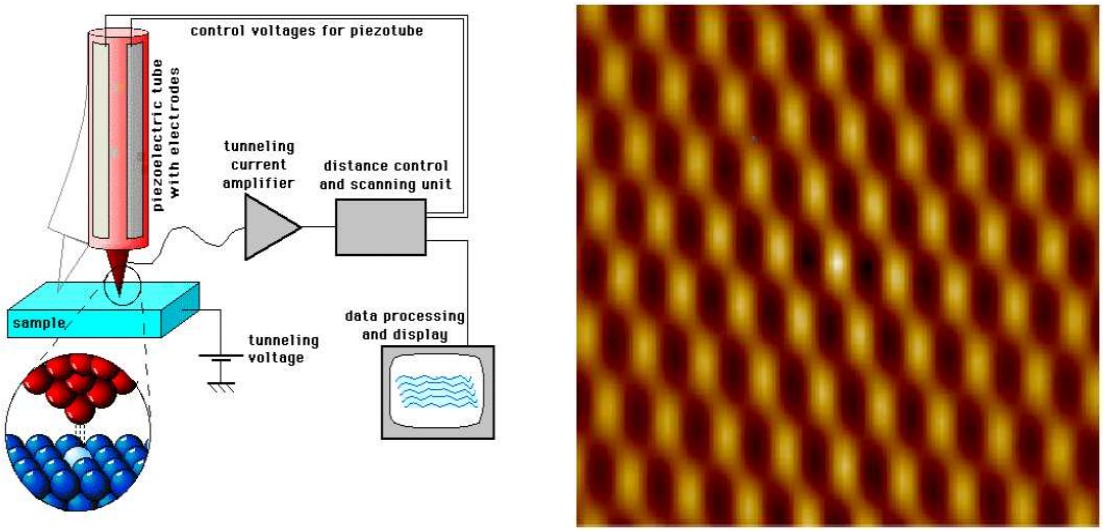

(a) Schematic diagram of the working principle of a scanning tunneling microscopy

(b) A 2 nm × 2 nm scanning tunneling microscopic image of HOPG sample

Figure 1.10: Schematic representation of scanning tunneling microscope

where I_t is the tunneling current, V is the bias voltage, k is a constant that includes the work function of the material and d is the minimum distance between the tip and the sample. The exponential dependence of the tunneling current on the tip-sample distance makes it possible to use the current in a feedback loop to control the tunneling current or the tip-sample distance precisely using a piezoelectric scanner unit. By applying a voltage for the X-Y scanner the tip scans a precise area and at each position, it measures the current. Since the current varies exponentially with the distance between tip and sample, the topography of the sample can be obtained. STM basically gives the local density of states (LDOS) of the sample rather than the surface topography. The high resolution of STM originates from the exponential dependence of the current on the distance. A pictorial representation of the principle of STM is shown in the Figure 1.10(a).

There are two modes of operation in STM, constant current (CC) and constant height (CH) modes. In the CC mode, the tip scans the surface in the XY plane (sample plane) and the feedback is adjusted in the Z-direction in such a way that the tunneling current remains the same. Hence the feedback voltage is a direct function of the topography of the sample

surface. This means that the image in the CC mode is a function of the feedback voltage vs. X and Y coordinates. In the CH mode the tip scans the sample at a constant plane without any feedback. Since the tunneling current depends on the distance, the variation of the current gives information about the topography of the sample surface. The main disadvantage of this mode is that it can be used only for atomically smooth surfaces, as otherwise the tip may crash on a rough sample surface during scanning.

We have carried out the STM studies using a scanning tunneling microscope that was designed and fabricated in our laboratory [82, 83]. Very sharp tips having typically one atom at the edge can be prepared by electrochemical etching of inert metal wires such as W, Pt-Rh or Pt-Ir. The Pt-Rh wire of 0.25 mm diameter is etched using an ac voltage in an electrolytic solution containing 5% NaCl and 5% $NaNO_3$, whereas the W tips are prepared by etching in 5% KOH solution. The tip obtained by this method is dipped in HF solution to remove any surface oxides, rinsed in distilled water and dried before using as a probe for the STM measurement. Before each experiment the STM is calibrated using atomic resolution images of ZYA grade highly oriented pyrolytic graphite (HOPG) (Advanced Ceramic Co, USA). The images were analysed using scanning probe image processor software (SPIP, Image Metrology, Denmark). Figure 1.10(b) shows the 2 nm x 2 nm constant current STM image of the HOPG obtained using the home built STM in our laboratory. The hexagonal symmetry pattern of the graphite lattice can be clearly seen from the image.

1.2.3 Spectroscopic and Other Techniques

1.2.3.1 Fourier Transform Infrared Spectroscopy

Fourier transform infrared (FTIR) spectroscopy, is based on the interaction of the infrared (IR) radiation with a sample (liquid or solid) and measuring the frequencies at which the sample absorbs the radiation. The FTIR spectrometer records the intensities of absorption or transmittance over a range of frequency, which is expressed in terms of wave numbers. The key components of the FTIR spectrometer are the source, the interferometer and the

detector. The interferometer provides a method to measure all the frequencies simultaneously by modulating the intensity of individual frequencies of radiation before the detector picks up the signal. The output of an interferometer after scanning over the frequency range is known as an interferogram, which is a plot of intensity versus the mirror position. Using the mathematical process of Fourier transform (FT), a computer converts this interferogram into a spectrum, which is the final output from the FTIR spectrometer. The chemical structure and the presence of various functional groups in the given sample can be identified from this spectrum, as the chemical functional groups absorb IR radiation only at their characteristic frequencies.

In addition to bulk samples, FTIR can be used in surface science mainly to study ultra thin organic films on various metallic and non-metallic surfaces essentially to characterise the molecular packing and orientation on the surface [59, 84]. The spectrum is obtained using either internal or external reflection modes of operation. The internal reflection mode is known as the attenuated total reflection (ATR) spectroscopy, whereas the external reflection mode is known as Reflection-Absorption or Grazing Angle spectroscopy. ATR is a multiple internal reflectance technique, where the beam is directed into an angled crystal and reflected within the crystal until it emerges out from the other end where it has been collected. The number of reflections depends on the angle of incidence upon the crystal. The crystal is usually made of KRS-5, zinc selenide or germanium [85]. In grazing angle reflection or external reflection, which is a mirror like reflection from the surface of a sample, the infrared radiation is directed onto the surface of a sample at an angle of incidence θ_I. For an external reflectance, the angle of reflection, θ_R, is equal to the angle of incidence, θ_I. The amount of radiation reflected from the sample depends on the angle of incidence, refractive index, surface roughness and the absorption properties of the sample. The angle of incidence is selected on basis of the thickness of coating of the sample. For very thin film coatings in the range of nanometer thickness like ultra thin organic films, an angle of incidence of 85°-88°is used. Reflectance measurements at this angle of incidence are often called as grazing angle measurements. The reflection-absorption spectrum for a monolayer of organic molecules

adsorbed onto a metal surface is measured mostly at a higher angle of incidence. In these cases, the measurements are mainly based on the p-polarisation component of the incident light, which alone is allowed to pass through the sample surface [86]. The p-polarisation component of the incident light has its orientation parallel to the plane of incidence. On the other hand, the s- polarisation component of the incident light has its orientation perpendicular to the plane of incidence. Hence the s-polarisation component of the incident light does not interact with ultra thin film samples on metal surface and therefore does not contribute to any spectral signal. It is clear that the grazing angle FTIR spectra obtained in the case of monolayer modified surfaces are due to the interaction of only p-polarised light, which results in clear spectra. The spectrum of an ultra thin organic film modified metal substrate is obtained by the ratio of the absorbance spectrum of the monolayer-coated surface with a suitable blank spectrum (taken on a bare substrate). The relative intensities of the absorption peaks in the spectrum are affected mainly by the average orientation of transition dipoles relative to the surface. A transition dipole parallel to the metal surface will exhibit a greatly attenuated peak in intensity relative to the transition dipole perpendicular to the metal surface. From this analysis, the average orientation of the monolayer chains and the terminal groups can be obtained. The peak positions in the spectra also provide information about the dynamic behaviour and the state (for example the crystalline like, liquid like structure) of the monolayer.

In our work, we have carried out the FTIR spectroscopy studies for the SAM modified surfaces using a FTIR 8400 model (SHIMADZU) with a fixed 85° grazing angle attachment (FT-85; Thermo Spectra-Tech). The FT-85 grazing angle attachment does not use the mirror like conventional reflectance accessories. Instead, it uses silicon refracting optical elements with the existing beam diverge in the sample compartment to obtain a high, 85° angle of incidence. The unique design of the FT-85 also features the built-in polarising elements. The silicon refracting elements are positioned at an angle, which allow only the p-polarisation light to pass through the sample. The samples are placed on the horizontal sampling surface of the accessory. The sample area is approximately 10 mm wide and 40-50 mm long.

1.2.3.2 Polarising Optical Microscopy (POM)

Polarised optical microscopes can be used for both the qualitative and quantitative analysis of materials that have optical anisotropy. They are designed mainly to observe the birefringent changes occurring in the anisotropic materials. The working principle of POM depends on the interaction of plane-polarised light with the anisotropic material and the light reflected from the specimen. For this purpose, the polariser and analyser are used. When the electric field vectors of a light wave are restricted to a single plane using the filter known as the polariser, then the light is said to be polarised with respect to the direction of propagation and all waves vibrate in the same plane. The analyser is oriented perpendicular to the polariser, which means that the polariser only transmits light that vibrates in one plane and the analyser transmit light that vibrates in the perpendicular direction. If the light from the polariser is not affected by the anisotropic material, then no light will pass through the analyser. When light passes through the anisotropic materials it splits into two beams that vibrate perpendicular to each other. Because each of these beams travels in different directions in the specimen, they will encounter different resistance to their motion and so will travel at different speeds. The term birefringence means difference between the maximum and minimum indices of refraction in an anisotropic material.

When the plane-polarised light is allowed to interact with a birefringent (or doubly-refracting) specimen, two individual wave components that are polarised in mutually perpendicular planes are produced. The velocities of these components are different and vary with the propagation direction through the specimen. After exciting the specimen, the light components become out of phase, but are recombined with constructive and destructive interference when they pass through the analyser. POM is a contrast-enhancing technique that improves the quality of the image obtained with birefringent materials. In our studies, we have used POM for identifying the liquid crystalline phases. As mentioned under the topic of liquid crystals, they are highly anisotropic materials and thereby interact differently with a plane-polarised light. Since the molecular arrangement and the associated defects are different in each phase, they show characteristic textures under cross-polarised light. In our

studies, we have used POM to characterise the different liquid crystalline phases formed by the self-assembly of surfactant molecules and the thermotropic liquid crystalline phases using textural analysis. Figure 1.11 shows a typical texture of columnar hexagonal liquid crystalline phase using a POM.

Figure 1.11: Polarising optical micrographic image of the columnar hexagonal phase of Triton X-100/water system

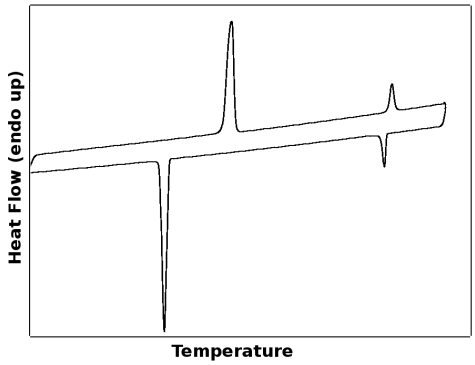

Figure 1.12: Differential scanning calorimetric trace for a thermotropic columnar hexagonal liquid crystalline phase

1.2.3.3 Differential Scanning Calorimetry

Differential scanning calorimetry (DSC) is a thermoanalytical method. This is mainly used for the analysis of phase transitions during heating or cooling. The enthalpy of the system is measured as a function of temperature. During the phase transitions, which can be either endothermic or exothermic, the temperature vs. enthalpy graph shows a peak. DSC provides very useful information in the research of liquid crystal phase transitions, especially in the thermotropic liquid crystals. A typical DSC curve is shown in the Figure 1.12. The peak position gives information about the temperature of phase transition while the area under the peak gives the enthalpy of phase transition which is related to the ordering of the two phases before and after the phase transitions.

1.2.3.4 Small Angle X-ray Scattering

X-ray diffraction is a powerfull technique for the analysis of the crystalline and liquid crystalline samples and is obtained as the reflection of an X-ray beam from a group of parallel and equally spaced atomic planes, on the basis of Bragg's law [87]. Diffraction occurs as the waves interact with a regular structure whose repeat distance is about the same as the wavelength of X-rays. X-rays have wavelengths of the order of a few angstroms, the same as typical inter-atomic distances in crystalline solids and in the liquid crystalline samples. W.L. Bragg observed that on a periodic arrangement, X-rays scattered from a crystalline solid could constructively interfere to produce a diffracted beam and has given a relationship based on the several factors known as the Braggs law. The schematic representation of this law is shown in the Figure 1.13(a).

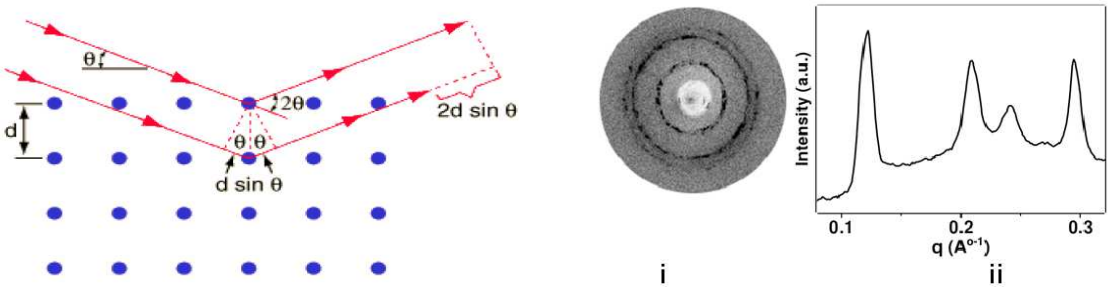

(a) Schematic representation of the scattering of X-ray leading to the Bragg's law

(b) i) Small angle X-ray scattering image and ii) scattering vector vs. intensity plot for the columnar hexagonal phase of Triton X-100/water system

Figure 1.13: The principle of Small-angle X-ray scattering and a typical experimental X-ray scattering data

Small angle X-ray scattering can be used for the qualitative as well as quantitative technique for the analysis of different liquid crystalline phases. This is based on the principle that the X-rays that have very small wavelength of the order of few Å get scattered by the different planes in the crystals. Diffraction of the X-rays occur when the rays interact with periodic structures of similar distances. When a monochromatic X-ray beam of wavelength λ is incident on lattice planes with an angle θ, the diffraction occurs if the path of rays reflected

by successive planes (with a distance d) is a multiple of the wavelength. The scattering is then governed by the equation $n\lambda = 2dsin\theta$ where n is the order of scattering (for first order scattering n=1 etc), λ is the wavelength of the X-ray used, d is the distance between two crystal planes and θ is the scattering angle [87]. The equation implies that for a given wavelength of X-rays, as the distance between different planes increases, the scattering angle θ decreases. For the liquid crystalline samples, the typical d-spacings are in few tens of angstroms, the scattering angle will be very less and hence normally small angle has to be employed for the analysis of liquid crystals. The peaks in the scattering vector vs. intensity plot is due to the scattering by different planes in the liquid crystals. Each type of phase gives its own characteristic ratio in the scattering vector which can be used for the identification of the particular type of mesophase. A typical SAXS pattern for a columnar hexagonal liquid crystalline sample is shown in the Figure 1.13(b).

1.3 Aim of the Thesis

As mentioned in the first part, liquid crystals are the intermediate phases between crystalline and liquid phases that are formed by the aggregation of organic molecules in the case of thermotropic liquid crystals or by the aggregation of micelles in the case of lyotropic liquid crystals. The thermotropic columnar hexagonal phase, one of our focus, has several technological applications in the field of solar cells, photovoltaic cells, molecular electronics, and sensors owing to its quasi-one-dimensional electrical conductivity. The lyotropic liquid crystals are of fundamental interest due to their resemblance with biological media and as confined reactors inside the micelles while they are of significant technological importance due to the surface active agents involved in the formation of these phases. Self-assembled monolayers can be considered as a surface analogue of the aggregates where the organic molecules self-assemble in a close-packed arrangement, and has several applications as described before. On the other hand, nanomaterials have several interesting properties that leads to many potential applications. For example, the unique properties of gold nanoparticles have been

utilised for many applications including in the biological field. These nanomaterials have also been demonstrated for applications like targeted drug delivery, sensors etc. This thesis describes the electrochemical and electrical conductivity studies using these self-organised systems.

The experimental results in the present thesis has been divided into 4 chapters.

Chapter 2 describes the electrochemical reactions of several redox probes that are studied in the lyotropic columnar hexagonal liquid crystalline phase (H1 phase) of Triton X-100/water system. It is observed that the half-peak potential of the redox reactions shifts in the liquid crystalline phase compared to the conventional solvent systems, and the shift depends on the nature of the redox probe. The diffusion of the redox probes are found to decrease in the H1 phase compared to the solvent phase. The extent of decrease depends on the nature of the redox probe. A comparative analysis of the cyclic voltammetric and the electrochemical impedance studies show that the diffusion of the probes follow the linear diffusion characteristics irrespective of the columnar hexagonal order of the surfactant-based micelles which is present in the liquid crystalline medium.

Chapter 3 presents the experimental results in the dispersion of gold nanoparticles in the columnar hexagonal phase of Triton X-100/water system and in the reverse columnar hexagonal phase of AOT. The dispersions were characterised using POM and SAXS studies. The studies show that the dispersion of nanoparticles at low concentration retains the liquid crystalline order of the two systems. This chapter also describes our experimental results on the ionic conductivity studies on lyotropic liquid crystalline phases that are formed by the non-ionic surfactant Triton X-100/water system. The unexpected very high ionic conductivity in the phase has been explained on the basis of Grotthus mechanism that depends on the hydrogen bonding network present in the medium. This is further explored by the addition of urea which is a well-known chaotropic agent which can disturb the hydrogen-bond network and results in the decrease in ionic conductivity of the systems. On the other hand, the addition of gold nanoparticles at low concentrations enhance the ionic conductivity.

Chapter 4 describes the electrical conductivity studies of thermotropic columnar hexago-

nal phase that are formed by the triphenylene based discotic molecules. This phase has quasi-one-dimensional electrical conductivity behaviour due to the stacking of disc-like molecules. We have studied the addition of two new dopants namely, ferrocenium tetrafluoroborate and chloroauric acid in the discotic matrix. The formation of charge-transfer complexes in the composites and the resultant enhancement in the electrical conductivity of the columnar phase is presented in the chapter. The ionic conductivity studies of some ionic liquid crystals that possess columnar hexagonal phase is also presented in this chapter.

Chapter 5 of the thesis deals with the electrochemical studies of self-assembled monolayers of organic thiols on the gold surface. First part of this chapter describes the monolayers of rod-like liquid crystalline cyanobiphenyl based disulphides, that show nematic phase in the bulk. The second part describes the monolayers formed by triphenylene based thiols, that show columnar hexagonal mesophase in the bulk. The electron barrier properties of these monolayers are studied using cyclic voltammetry and electrochemical impedance spectroscopy.

Chapter 6 summarises the results we have obtained from our studies. In this chapter, we also propose some of the experiments that has to be carried out for a better understanding of some of the topics covered in the thesis.

In general, the thesis describes the experimental results on the electrochemical and electrical conductivity studies in different self-organised systems, where the self-organisation is either lyotropic and thermotropic liquid crystalline phases or the self-assembled monolayers of organic thiols on gold surface. We present some of the significant results of our investigation on these topics in the following chapters.

Bibliography

[1] Goodby, *Handbook of Liquid Crystals*, John Wiley & Sons, London, 2nd edn., 2004.

[2] S. Kumar, *Chem. Soc. Rev.*, 2006, **35**, 83.

[3] J. N. Israelachivli, *Intermolecular and Surface forces*, Academic Press, San Diego, CA, 2nd edn., 1991.

[4] D. F. Evans, *J. Phys. Chem.*, 1986, **90**, 2817.

[5] S. T. Hyde, *Handbook of Applied Surface and Colloid Chemistry*, John Wiley & Sons Ltd., 2001.

[6] V. Luzzati and F. R. Husson, *Nature*, 1966, **210**, 1351.

[7] V. Luzzati, A. Tardieu, T. G. Krzywicki, E. Rivas and F. R. Husson, *Nature*, 1968, **220**, 485.

[8] K. Reizlein and H. Hoffmann, *Surfactants, Micelles, Microemulsions and Liquid Crystals*, Springer, Berlin, 1984.

[9] R. Bartolino, T. Chiaranza, M. Meuti and R. Compagnoni, *Phys. Rev. A*, 1982, **26**, 1116.

[10] K. Bayer, *J. Colloids and Surface A*, 1982, **1**, 1932.

[11] L. Coppola, R. Muzzalupo, G. A. Ranieri and M. Terenzi, *Langmuir*, 1995, **11**, 1116.

[12] A. Caria and A. Khan, *Langmuir*, 1996, **12**, 6282.

[13] F. Reinitzer, *Monatsh. Chem.*, 1888, **9**, 421.

[14] S. Chandrasekhar, B. K. Sadashiva and K. A. Suresh, *Pramana J. Phys.*, 1977, **9**, 471.

[15] S. Chandrasekhar and V. S. K. Balagurusamy, *Proc. R. Soc. Lond. A,* 2002, **458**, 1783.

[16] S. Laschat, A. Baro, N. Steinke, F. Giesselman, C. Hagele, G. Scalia, R. Judele, E. Kapatsina, S. Sauer, A. Schreivogel and M. Tosoni, *Angew. Chem. Int. Ed.*, 2007, **46**, 4832.

[17] L. S. Mende, A. Fechtenkotter, K. Mullen, E. Moons, R. H. Friend and J. D. Macknzie, *Science*, 2001, **293**, 1119.

[18] S. Segeyev, W. Pisula and Y. H. Greets, *Chem. Soc. rev.*, 2007, **36**, 1902.

[19] I. Seguy, P. Destruel and H. Bock, *Synth. Met.*, 2000, **111-112**, 15.

[20] N. Boden, R. J. Bushby, J. Clements and B. Movaghar, *J. Mater. Chem.*, 1999, **9**, 2081.

[21] N. Boden, R. J. Bushby, J. Clements, M. V. Jesudason, P. F. Knowles and G. Williams, *Chem. Phys. Lett.*, 1988, **152**, 94.

[22] N. Boden, R. J. Bushby and J. Clements, *J. Chem. Phys.*, 1993, **98**, 5920.

[23] E. O. Arikainen, N. Boden, R. J. Bushby, J. Clements, B. Movaghar and A. Wood, *J. Mater. Chem.*, 1995, **5**, 2161.

[24] N. Boden, R. J. Bushby, A. N. Cammidge, J. Clements and R. Luo, *Mol. Cryst. Liq. Cryst.*, 1995, **261**, 251.

[25] V. S. K. Balagurusamy, S. krishnaprasad, S. Chandrasekhar, S. Kumar, M. Manickam and C. V. Yelamaggad, *Pramana J. Phys.*, 1999, **53**, 3.

[26] G. B. M. Vaughan, P. A. Heiney, J. P. M. Jr. and A. B. S. III, *Phys. Rev. B*, 1992, **46**, 2787.

[27] S. Kumar, S. K. Pal, P. S. Kumar and V. Lakshminarayanan, *Soft Matter*, 2007, **3**, 896.

[28] L. A. Holt, R. J. Bushby, S. D. Evans, A. Burgess and G. Seeley, *J. Appl. Phys.*, 2008, **103**, 063712.

[29] M. Brust, M. Walker, D. Bethell, D. J. Schriffin and R. Whyman, *J. Chem. Soc. Chem. Commun.*, 1994, 801.

[30] M.-C. Daniel and D. Astruc, *Chem. Rev.*, 2004, **104**, 293.

[31] E. Katz and I. Willner, *Angew. Chem. Int. Ed.*, 2004, **43**, 6042.

[32] J. Turkevitch, P. C. Stevenson and J. Hillier, *Discuss. Faraday Soc.*, 1951, **11**, 55.

[33] S. K. Ghosh, N. Sarma, M. Mandal, S. Kundu, K. Esumi and T. Pal, *Current Science*, 2003, **84**, 791.

[34] A. P. Herrera, O. Resto, J. B. Briano and C. Rinaldi, *Nanotechnology*, 2005, **16**, S618.

[35] L. Y. Wang, X. Chen, Y. C. Chai and J. C. Hao, *Colloid Surf. A*, 2007, **293**, 95.

[36] P. Calandra, G. Giordano, A. Longo and V. T. Liveri, *Mater. Chem. Phys.*, 2006, **98**, 494.

[37] L. Wang, X. Chen, J. Zhan, Y. Chai, C. Yang, L. Xu, W. Zhuang and B. Jing, *J. Phys. Chem. B*, 2005, **109**, 3189.

[38] D. I. Gittins, D. Bethell, R. J. Nichols and D. J. Schriffin, *Adv. Mater.*, 1999, **11**, 737.

[39] W. Cheng, S. Dong and E. Wang, *Langmuir*, 2002, **18**, 9947.

[40] S. Guo and E. Wang, *Anal. Chim. Acta*, 2007, **598**, 181.

[41] B. K. Jana and C. R. Raj, *Langmuir*, 2007, **23**, 4064.

[42] A. Ulmann, *An introduction to ultrathin organic films from Langmuir-Blodgett to self-assembly*, Academic Press, San Diago, CA, 1991.

[43] H. O. Finklea, *Encyclopedia of analytical Chemistry*, Academic Press, Wiley, Chichester.

[44] H. O. Finklea, *Electroanalytical Chemistry*, Marcel Decker, New York, 1996.

[45] G. G. Roberts, *Langmuir-Blodgett Films*, Plenum Press, New York, 1990.

[46] D. K. Schwartz, *Surf. Sci. Rep.*, 1997, **27**, 245.

[47] S.-C. Chang, I. Chao and Y.-T. Tao, *J. Am. Chem. Soc.*, 1994, **116**, 6792.

[48] S. W. Han, S. J. Lee and K. Kim, *Langmuir*, 2001, **17**, 6981.

[49] T. S. Phanindra and A. K. Raychaudhuri, *J. de Phys. D: Appl. Phys.*, 2007, **10**, 3182.

[50] P. E. Laibinis and G. M. Whitesides, *J. Am. Chem. Soc.*, 1992, **114**, 9022.

[51] M. M. Sung and Y. Kim, *Bull. Korean Chem. Soc.*, 2001, **22**, 748.

[52] H. Ron, H. Cohen, S. Matlis, M. Rappaport and I. Rubinstein, *J. Phys. Chem. B*, 1998, **102**, 9861.

[53] R. Brito, R. Tremont and C. R. Cabrera, *J. Electroanal. Chem.*, 2004, **574**, 15.

[54] K. Shomazu, Y. Sato, I. Yagi and K. Uosaki, *Bull. Chem. Soc. Jpn.*, 1994, **67**, 863.

[55] J. C. Love, D. B. Wolfe, R. Haasch, M. L. Chabinyc, K. E. Paul, G. M. Whitesides and R. G. Nuzzo, *J. Am. Chem. Soc.*, 2003, **125**, 2597.

[56] H. Schonherr, F. J. B. Kremer, S. Kumar, J. A. Rego, H. Wolf, H. Ringsdorf, M. Jaschke, H.-J. Butt and E. Bamberg, *J. Am. Chem. Soc.*, 1996, **118**, 13051.

[57] R. G. Nuzzo, E. M. Korenic and L. H. Dubois, *J. Chem. Phys.*, 1990, **93**, 767.

[58] N. Camillone, C. E. D. . Chidsey, G.-Y. Liu and G. Scoles, *J. Chem. Phys.*, 1993, **98**, 4234.

[59] M. D. Porter, T. B. Bright, D. L. allara and C. E. D. Chidsey, *J. Am. Chem. Soc.*, 1987, **109**, 3559.

[60] M. M. Walczak, C. Chung, S. M. Stole, C. A. Widrig and M. D. Porter, *J. Am. Chem. Soc.*, 1991, **113**, 2370.

[61] R. G. Nuzzo, F. A. Fusco and D. L. Allara, *J. Am. Chem. Soc.*, 1987, **109**, 2358.

[62] R. G. Nuzzo, B. R. Zegarski and L. H. Dubois, *J. Am. Chem. Soc.*, 1987, **109**, 733.

[63] R. G. Nuzzo, L. H. Dobois and D. L. Allara, *J. Am. Chem. Soc.*, 1990, **112**, 558.

[64] Y. Li, J. Huang, R. T. McIver and J. C. Hemminger, *J. Am. Chem. Soc.*, 1992, **114**, 2428.

[65] C. A. Widrig, C. Chung and M. D. Porter, *J. Electroanal. Chem.*, 1991, **310**, 335.

[66] R. H. Terrill, T. A. Postrthwaite, C. Chen, C. D. poon, A. Terzis, A. Chen, J. E. Hutchison, M. R. Clark, G. Wignall, J. D. Londono, R. Superfine, M. Falvo, C. S. J. Jr., E. T. Samulski and R. W. Murray, *J. Am. Chem. Soc.*, 1995, **117**, 12537.

[67] U. K. Sur and V. Lakshminarayanan, *J. Colloid Interface Sci.*, 2002, **254**, 410.

[68] V. Lakshminarayanan and U. K. Sur, *Pramana J. Phys.*, 2003, **61**, 361.

[69] W. H. Scouten, J. H. T. Luong and R. S. Brown, *Tr. Biotech.*, 1995, **13**, 178.

[70] M. Mrksich and G. M. Whitesides, *Annu. Rev. Biophys. Biomol. Struct.*, 1996, **25**, 55.

[71] J. J. Gooding, F. Mearns, W. Yang and J. Liu, *Electrocatalysis*, 2003, **15**, 81.

[72] T. Wink, S. J. van zuilen, A. Bult and W. P. Bennekom, *Analyst*, 1997, **122**, 43R.

[73] J. J. Gooding and D. B. Hibbert, *Tr. Anal. Chem.*, 1999, **18**, 525.

[74] N. K. Chaki and K. Vijayamohanan, *Biosensors and Bioelectronics*, 2002, **17**, 1.

[75] G.-Y. Liu, S. Xu and Y. Qian, *Acc. Chem. Res.*, 2000, **33**, 457.

[76] S. Kramer, R. R. Fuierer and C. B. Gorman, *Chem. Rev.*, 2003, **103**, 4367.

[77] A. J. Bard and L. R. Faulkner, *Electrochemical Methods Fundamentals and Applications*, John Wiley and Sons, Noida, 2nd edn., 2004.

[78] R. Greef, R. Peat, L. M. Peter, D. Pletcher and J. Robinson, *Instrumental Methods in Electrochemistry*, Ellis Horwood Ltd., Chichester, Great Britain, 1990.

[79] C. J. Chen, *Introduction to Scanning Tunneling Microscopy*, Oxford University Press, New York, 1993.

[80] G. Binning and H. Rohrer, *Appl. Phys. Lett.*, 1982, **40**, 178.

[81] C. Bai, *Scanning Tunneling Microscopy and its applications*, Springer, Berlin, 1992.

[82] V. Lakshminarayanan, *Current Science*, 1998, **74**, 413.

[83] M. Jayadevaiah and V. Lakshminarayanan, *Meas. Sci. Technol.*, 2004, **15**, N35.

[84] C. E. D. Chidsey and D. N. Loiacono, *Langmuir*, 1990, **6**, 682.

[85] P. R. Griffiths and J. de Haseth, *Fourier Transform Infrared Spectroscopy*, Wiley Inter Science, New York, 1986.

[86] J. F. Blanke, S. E. Vincent and Overend, *Spectrochim. Acta A*, 1976, **32**, 163.

[87] C. W. Bunn, *Chemical Crystallography An Introduction to Optical and X-ray Methods*, Clarendon Press, Oxford, 2nd edn., 1961.

Chapter 2

Electron transfer Studies of Redox Probes in the Columnar Hexagonal Phase of Triton X-100/Water System

Lyotropic liquid crystalline phases are of fundamental interest in biological studies since some of these phases have been shown to mimic biological environment. A fine example for this is the lamellar phase in aqueous medium formed by surfactants which is similar to the bilayer or lamellar phases formed by the lipids in the living systems. Due to this unique property of the lyotropic liquid crystalline phases, it is interesting to explore them for the study of many of the complex processes occurring in the biological media. Among them, electron transfer reactions play a major role as they hold a key to many of the biological processes. There are several reports on the electrochemical studies in the micellar as well as cubic and lamellar liquid crystalline phases. The present chapter describes our experimental results on electron transfer reactions in the columnar hexagonal phase, which is also referred to as H1 phase, of Triton X-100/water system. We have studied a variety of redox probes in this liquid crystalline phase. Cyclic voltammetry (CV) and electrochemical impedance spectroscopy (EIS) techniques have been used to understand the half-peak potentials of redox reactions as well as kinetics of the reaction and the diffusion characteristics of the redox probes.

2.1 Introduction

Surface active agents or surfactants are molecules that have both hydrophilic and hydrophobic parts. The hydrophilic groups are called the head group of the surfactant, while the hydrophobic part corresponds to the tail of the molecules. The head group may be either cationic, anionic or neutral in charge. The tail group normally consists of hydrocarbon chains. The aggregation of these surface active agents or surfactants in the solvent results in the formation of micelles above a particular concentration, known as the critical micellar concentration (CMC). The CMC may vary depending upon the nature of the surfactant, solvent as well as temperature. For concentrations below the CMC, the solution behave like a simple salt solution, but for concentrations above CMC the solution properties deviate from the normal behaviour due to the aggregation of these molecules to form the micelles of different geometries. These micelles may aggregate further at higher concentration of the surfactants, leading to a 2-dimensional network to form the liquid crystalline phases. Nematic, smectic, lamellar, cubic and columnar hexagonal phases are some of the examples of liquid crystalline phases formed by the surfactant molecules in the aqueous medium.

Electrochemical studies provide a powerful method to characterise electron transfer and transport properties of redox species in electrolytic media. Techniques like cyclic voltammetry (CV) and electrochemical impedance spectroscopy (EIS) can be considered as primary tools for this purpose. Preliminary information about the media can be obtained by cyclic voltammetry. For example, Mandal has shown that the self-diffusion coefficient of micelles in aqueous media can be measured using CV in the presence of a redox probe like ferrocene, which are hydrophobic and therefore occupy the hydrophobic inner core of the micelle [1]. The approximation used in their study was that since each micelle contains one molecule of the redox probe, the measurement of the diffusion coefficient of ferrocene provides the self-diffusion coefficient of the micelle. Similar studies can provide information about the micellar structure as well as the interaction between redox probes and the surfactants in the medium.

Electron transfer studies in the micellar systems have been studied extensively by several groups. Lee *et al.* have studied the effect of surfactants on the reduction potential of viologen molecules in micelles and showed that the formal potential of viologen redox reaction varies with the nature of the surfactant used [2]. They have observed that viologen has the highest redox potential in the Triton X-100 micelle, followed by the micelles formed by cationic and anionic surfactants. This behaviour has been explained in terms of the stability of the ions in the micelles. Electrochemical studies on the diffusion of ferrocene in different micelles showed that the diffusion coefficient values are significantly lower in the micellar media compared to the values in the solvent media [1]. Chen *et al.* have studied the redox reaction of ferrocene in a nitrobenzene-water emulsion and reported that the peak potentials shift in the emulsion phase [3]. Kostela *et al.* have reported the redox reactions of a viologen derivative, N-tetradecyl-N'-methylviologen (TMV) in a variety of surfactants. They have shown that the half-peak potential variation depends upon the charge of the surfactant. The $E_{1/2}$ value was the lowest in a negatively charged micelle while it was highest in the nonionic micellar medium [4]. Molina *et al.* have demonstrated that electrochemical studies provide a method of revealing the behaviour of redox probes in the reverse micelles of AOT/water system [5]. Rusling *et al.* have carried out a series of electrochemical experiments in the micellar media and studied different redox species like bromophenyls [6], allyl halides [7], bipiridyl derivatives [8] and biphenyls [9]. They have also demonstrated that the electrocatalytic effects of molecules change with the nature of the micellar media formed by different surfactants [10, 11, 12, 13, 14].

There are several reports in the literature on the study of redox reactions and catalytic effects in the liquid crystalline phases. Bilewicz *et al.* have utilised lyotropic liquid crystalline cubic phase modified catalytically active electrodes for sensor applications [15]. In this study, the cubic phase was prepared from monoolein-water systems. Ropers *et al.* have used a cubic phase for the immobilisation of cholesterol oxidase on electrodes, where the cubic phase was prepared from either monoolein or fluorinated ethoxylated alcohol. They have demonstrated that the cubic phase offers a good medium for the immobilisation of enzymes

[16]. Rowinski *et al.* have studied the diffusion properties of hydrophilic redox probes, *viz.*, ferrocenecarboxylic acid and $[Ru(NH_3)_6]^{3+}$ in a bicontinuous lipidic cubic phase, and found that the diffusion of these species in the hydrophilic channels is more efficient than in the widely used Nafion membrane, a proton-conducting perfluorosulfonate gel [17, 18]. Biosensors based on the cubic phases dispersed with membrane lipids have also been reported [19]. Razumas *et al.* have studied the electrochemical behaviour of cytochrome-c in cubic phases [20]. They have also demonstrated that these cubic phases can be used for the redox behaviour of biologically important compounds like ubiquinone [21], ferrocene derivatives [22], vitamine K_1 [23] and enzymes [24, 25]. They have observed that the diffusion coefficient values of the redox probes have decreased in the liquid crystalline phase compared to the solvent phase [22]. Kostela *et al.* have studied the diffusion and electron-transfer properties of several redox systems in a bicontinuous cubic phase and in a lamellar phase of monoolein and amphiphilic viologen derivatives using cyclic voltammetry and chronocoulometry [4, 26, 27]. They have reported a significant decrease in the diffusion coefficient of the redox probes in the cubic phase compared to the typical solvent phases.

In the present chapter, we describe the results of the CV and EIS studies of different redox probes in the columnar hexagonal liquid crystalline phase of Triton X-100/water system. Polarising optical microscopy and small-angle X-ray scattering studies confirm that the liquid crystalline phase is retained even after the addition of redox probes as well as supporting electrolytes. We have carried out cyclic voltammetric studies for determining the redox potentials and found that the shifts in the half-peak potentials depend upon the nature of the redox probes and their interaction with the liquid crystalline phase. The diffusion coefficient of the redox probes are lower in the liquid crystalline phase compared to the solvent phase. The extent of decrease is found to depend on the nature of the redox probe used. The reasons for the half-peak potential shifts and the decrease in the diffusion coefficient values are discussed later in the chapter.

2.2 Experimental Section

2.2.1 Chemicals

Potassium ferrocyanide (Loba), Potassium ferricyanide (Qualigens), hexaammineruthenium (II) chloride (Aldrich), hexaammineruthenium (III) chloride (Alfa Aeser), 4-benzoquinone (Lancaster), 4-hydroquinone (Loba Chemie), methylviologen (Aldrich), ferrocene (Acros Organics), ferrocenium tetrafluoroborate (Aldrich), ferrocenemethanol (Aldrich), sodium fluoride (SD), lithium perchlorate (Acros Organics), potassium chloride (Ranbaxy) and Propylene carbonate (Merck) were of analytical grade and were used as received. The non-ionic surfactant Triton X-100 was obtained from Aldrich. Millipore water of resistivity 18 MΩcm was used for the preparation of all the samples.

2.2.2 Preparation of the Electrolytes

For the electrochemical studies in the aqueous medium, 1 mM solution of the redox probe was prepared in water and mixed with 0.1 M of the supporting electrolyte. Ferrocene and ferrocenemethanol reactions were carried out in propylene carbonate medium as these two redox probes are insoluble in the aqueous medium.

The columnar hexagonal phase (H1 phase) was prepared using 42 wt% Triton X-100 and 58 wt% water as reported earlier [28]. According to the phase diagram of Triton X-100/water system, this composition forms the columnar hexagonal phase [29]. A 6 ml of the mixture of the above composition was stirred well and heated to about 35 °C, which is above the columnar to isotropic phase transition for the H1 phase of this system. The mixture was then sonicated for about 10 minutes. The sample was allowed to cool down to room temperature, which resulted in the formation of the H1 phase.

The electrochemical studies in the H1 phase were carried out with 1 mM concentration of the redox probe and 0.1 M concentration of the supporting electrolyte prepared as aqueous solution and mixed with Triton X-100. The electrolyte was prepared by first heating and later ultrasonicating in the isotropic phase (∼35 °C). The solution was then cooled down to room

temperature and used as electrolyte for the electrochemical studies.

2.2.3 POM and SAXS

Polarising optical microscopic (POM) studies of the samples were carried out using an Olympus POM instrument coupled with a Mettler heater. The textures were taken by sandwitching the samples between a glass slide and a cover slip. The samples were heated to the isotropic phase and the images were taken while cooling from the isotropic phase. The small angle X-ray scattering (SAXS) studies have been carried out using an X-ray diffractometer (Rigaku UltraX 18) operating at 50 kV and 80 mA using Cu Kα radiation having a wavelength of 1.54 Å. Samples were prepared by filling a capillary with the liquid crystalline sample and sealed. All scattering studies were carried out at room temperature.

2.2.4 Electrode Pretreatment

The gold disk electrode fabricated in our laboratory was used as the working electrode, which has a diameter of 0.5 mm and a geometric area of about 0.002 cm^2. The electrode was polished with 1 μm, 0.3 μm, and finally with 0.05 μm alumina slurries and ultrasonicated in water for 1 min. It was then cleaned with diluted aquaregia (3 : 1 : 4 mixture of con. HCl, con. HNO_3 and water) and rinsed with millipore water. The same procedure was followed before each experiment.

2.2.5 Electrochemical Studies

All the electrochemical experiments were carried out at room temperature. A model 263A potentiostat (EG&G) was used for the cyclic voltammetric studies. A single cell with a three-electrode system was used for the electrochemical studies with a saturated calomel electrode (SCE) as the reference electrode and platinum foil as the auxiliary electrode. In propylene carbonate, a silver electrode was used as a quasi-reference electrode, the potential of which was converted to that of SCE. All the plots shown in this chapter are for the third cycle of the

cyclic voltammogram. Electrochemical impedance spectroscopic studies were performed using a model 5210 lock-in amplifier (Perkin-Elmer Instruments) with Power Suite software (EG&G) interfaced with a PC. The impedance measurements were carried out over a wide frequency range from 100 mHz to 100 kHz with an ac amplitude of 10 mV. This ac signal was applied at a DC potential that corresponds to the formal potential or the half-peak potential, as the case may be, of the redox system. The impedance data were analysed using ZSimpWin software (EG&G).

2.3 Results and Discussion

2.3.1 Polarising Optical Microscopy

Polarising optical microscopy (POM) studies provide a preliminary assessment of the different liquid crystalline phases. We have used POM to characterise the liquid crystalline phases before and after the addition of electrolytes. This is essential to ensure that the electrolyte is in the liquid crystalline phase during the electrochemical studies. Figure 2.1 shows the POM images of the different systems used in the studies. The texture obtained for the pure Triton X-100/water system is also provided for comparison. As can be seen from the Figure 2.1(a), the pure Triton X-100/water system shows the typical texture of columnar hexagonal phase (H1 phase). Figure 2.1(b) to 2.1(f) show the textures obtained for the H1 phase that contains ferrocyanide|ferricyanide, hexaammineruthenium(II |III), benzoquinone|hydroquinone, methyl viologen and ferrocene|ferrocenium redox probes respectively in the presence of supporting electrolytes. All these textures are typical of the lyotropic liquid crystalline phase, indicating that the H1 phase is retained even after the addition of redox probes as well as the supporting electrolyte.

2.3.2 Small Angle X-ray Scattering

Small angle X-ray scattering studies were carried out to confirm the liquid crystalline phases formed by the systems. Figure 2.2(a) shows the plot of wavevector vs. intensity graph for

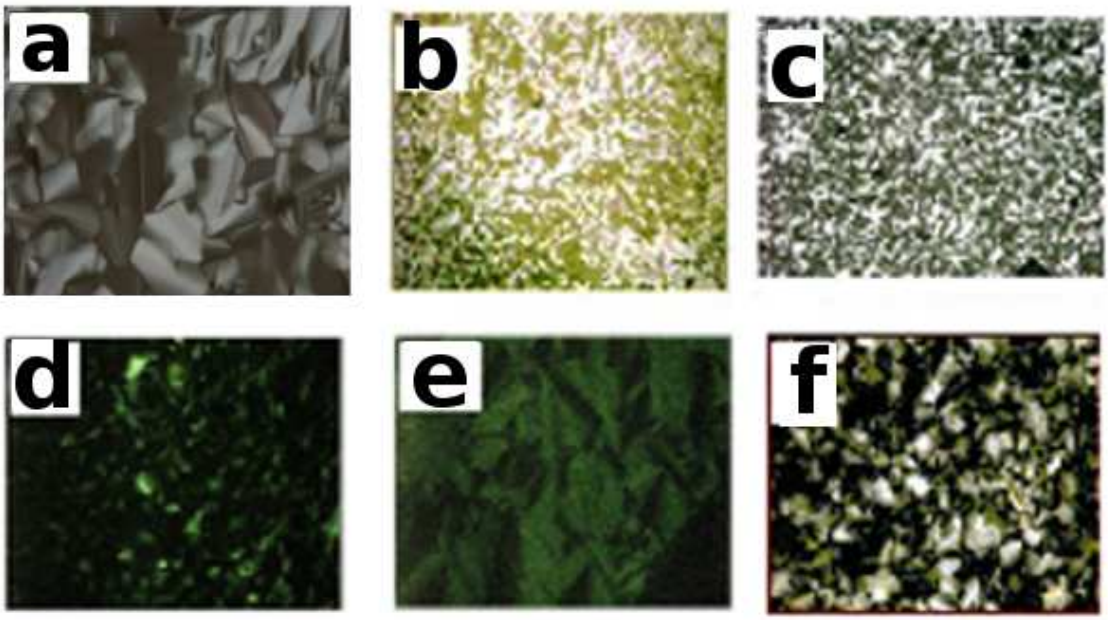

Figure 2.1: Polarising optical micrographic textures of a) the pure H1 phase and with b) ferrocyanide/ferricyanide, c) hexaammineruthenium(II/III) chloride, d) hydroquinone/benzoquinone, e) methyl viologen and f) ferrocene/ferrocenium redox probes in the presence of supporting electrolyte

the Triton X-100/water system obtained at room temperature. The peaks follow the order of $1:\sqrt{3}:2$ which is the typical ratio for the columnar hexagonal phase. Figure 2.2(b) shows the wavevector-intensity graph for the system containing 1 mM hydroquinone |1 mM benzoquinone in the presence of 0.1 M NaF as supporting electrolyte, which also follows the same ratio indicating that the columnar phase is not altered by the addition of redox probes. Similar plots were obtained for the H1 phase with other redox systems also. We have calculated the *d* spacing for all the systems using the equation

$$d = \frac{2\pi}{q}$$

The *d* value for the pure H1 phase was 52.54 Å while for the H1 phase with the quinone system, the value was 52.33 Å. The SAXS studies support the POM studies that all the systems chosen for the electrochemical studies retain the liquid crystalline phase even after the addition of redox probes and the supporting electrolyte. However, we have observed that

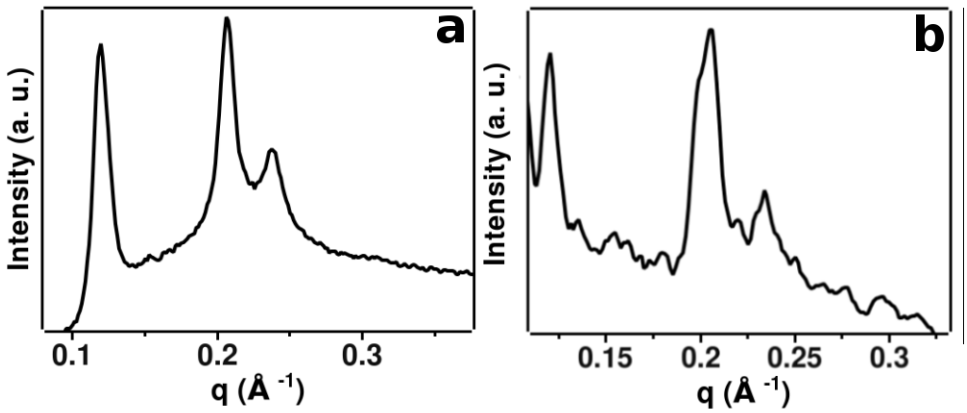

Figure 2.2: Intensity vs. scattering vector in small-angle X-ray scattering studies of a) pure H1 phase and b) 1mM hydroquinone|benzoquinone/0.1M TBATFB/H1 phase. The peaks follows the $1:\sqrt{3}:\sqrt{4}$ ratio indicating the retention of the H1 phase

higher concentration of redox probes and supporting electrolyte disturb the H1 phase and hence their concentrations have been optimised to 1 mM and 0.1 M respectively.

2.3.3 Electrochemical Studies

2.3.3.1 Cyclic Voltammetry

We have carried out cyclic voltammetric studies of a variety of redox probes in the H1 phase of Triton X-100/water system. For comparison, these studies were also carried out in their respective solvent media (either aqueous phase or propylene carbonate medium) normally used for electrochemical reaction. Before the redox reactions in the H1 phase, CV was performed in the bare H1 medium containing only the supporting electrolyte. The CV in the bare H1 phase is shown in Figure 2.3(a). It is clear that there is no redox process occurring in the medium except the normal capacitive behaviour. This indicate that the H1 phase can be used as a medium for the studies of electrochemical redox reactions. In the following sections, we will present the CV results for the different redox systems in the aqueous and H1 phases.

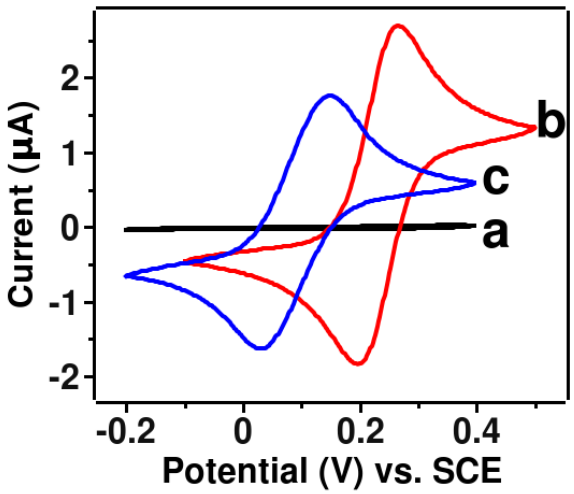

Figure 2.3: Cyclic voltammogram in a) the presence of only supporting electrolyte, 0.1 M TBATFB in the H1 phase, b) 1 mM $Fe[(CN)_6]^{4-|3-}$/0.1 M NaF in the aqueous phase and c) 1 mM $Fe[(CN)_6]^{4-|3-}$ 0.1 M TBATFB in the H1 phase at a scan rate of 20 mV/s

Table 2.1: Anodic and cathodic peak potentials (E_p^a and E_p^c), peak separation (ΔE_p), and half-peak potentials ($E_{1/2}$) for the 1 mM $[Fe(CN)_6]^{4-|3-}$ redox reaction

Medium	Scan Rate (mV/s)	E_p^a (mV)	E_p^c (mV)	ΔE_p (mV)	$E_{1/2}$ (mV)
0.1 M NaF/H_2O	10	198	130	68	164
	20	194	130	64	162
	50	196	130	66	163
	100	206	128	78	167
0.1 M NaF/H1 phase	10	146	68	78	107
	20	144	64	80	104
	50	146	66	80	106
	100	150	74	76	112
0.1 M TBATFB/H1 phase	10	94	32	62	63
	20	88	24	64	56
	50	94	22	72	58
	100	100	20	80	60

2.3.3.2 Ferrocyanide/Ferricyanide System

Figure 2.3 shows the cyclic voltammogram obtained at a scan rate of 20 mV/s in a mixture of 1 mM potassium ferrocyanide and 1 mM potassium ferricyanide in the aqueous phase and in the columnar phase using 0.1 M NaF as the supporting electrolyte. It can be seen from the CV that peak current decreases and the redox potentials have shifted to more negative values in the H1 phase compared to the aqueous phase. Table 2.1 shows the peak potentials measured at different sweep rates for the redox systems in the aqueous and H1 phases using different supporting electrolytes, *viz.*, NaF and TBATFB. The peak potentials have shifted from $E_p^a = 194$ mV to $E_p^a = 144$ mV and from $E_p^c = 130$ mV to $E_p^c = 64$ mV in the H1 phase. In other words, there is a large negative shift of the half-peak potential by about 58 mV from the aqueous phase to the H1 phase with NaF as the supporting electrolyte. From the table we find that the shift in the half-peak potentials is still more negative by about 106 mV when TBATFB is used as the supporting electrolyte in the H1 phase at a sweep rate of 20 mV/s. This clearly shows that shift in the half-peak potential depends on the nature of the supporting electrolyte used. Though the peak separation (Δ E_p) and its variation with the sweep rate in the cyclic voltammogram show a quasi-reversible nature, a more detailed study of the mass-transfer behaviour has been carried out using electrochemical impedance spectroscopic studies and will be presented later in this chapter.

2.3.3.3 Hexaammineruthenium (II/III) System

Figure 2.4 shows the cyclic voltammogram obtained for 1 mM $[Ru(NH_3)_6]^{2+|3+}$/0.1 M $LiClO_4$ in the aqueous phase and 1 mM $[Ru(NH_3)_6]^{2+|3+}$ /0.1 M TBATFB in the columnar phase. Table 2.2 presents the peak potentials measured at different sweep rates for the redox system in different media. There is a small negative shift in peak potentials in the H1 phase compared to the aqueous phase. We have also studied the same redox reaction in 0.1 M KCl as the supporting electrolyte both in the aqueous and in the H1 phase, for which the peak potentials and peak separations are shown in Table 2.2. The shifts in peak potentials in this case are small at the different scan rates studied. The relatively smaller changes in the half-peak

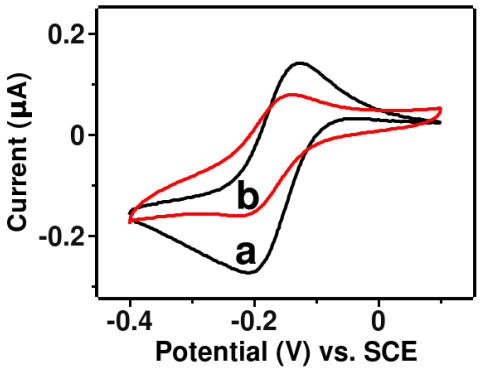

Figure 2.4: Cyclic voltammogram in 1 mM $[Ru(NH_3)_6]^{2+|3+}$ / 0.1 M NaF in a) aqueous medium and b) 1 mM $[Ru(NH_3)_6]^{2+|3+}$ / 0.1 M TBATFB in the H1 phase at a scan rate of 20 mV/s

Table 2.2: Anodic and cathodic peak potentials (E_p^a and E_p^c), peak separation (ΔE_p), and half-peak potentials ($E_{1/2}$) for the 1 mM $[Ru(NH_3)_6]^{2+|3+}$ redox reaction

Medium	Scan Rate (mV/s)	E_p^a (mV)	E_p^c (mV)	ΔE_p (mV)	$E_{1/2}$ (mV)
0.1 M $LiClO_4/H_2O$	10	-130	-206	76	-168
	20	-130	-202	72	-166
	50	-134	-204	70	-169
	100	-130	-206	76	-168
0.1 M TBATFB/H1 Phase	10	-140	-220	80	-180
	20	-140	-214	74	-177
	50	-140	-210	70	-175
	100	-140	-216	76	-178
0.1 M KCl/H_2O	10	-146	-207	61	-180
	20	-150	-212	62	-181
	50	-158	-220	62	-189
	100	-168	-230	62	-189
0.1 M KCl/H1 Phase	10	-160	-230	70	-195
	20	-158	-220	62	-189
	50	-151	-218	67	-189
	100	-166	-232	66	-199

potentials shown in the table can also be attributed to the different supporting electrolytes used in the aqueous and H1 phases. In other words, unlike the case of $[Fe(CN)_6]^{4-|3-}$, the redox potential of hexaammineruthenium(II/III) system is not significantly affected by the solution matrix. The CV in the H1 phase also shows that there is a significant decrease in the peak current in the H1 phase compared to aqueous phase.

2.3.3.4 Hydroquinone/Benzoquinone System

Figure 2.5 shows the cyclic voltammograms of 1 mM benzoquinone|1 mM hydroquinone in the aqueous phase and H1 phase with 0.1 M NaF as the supporting electrolyte. The curve shows that the redox reaction is under diffusion controlled regime both in the aqueous phase as well as in the H1 phase. It is clear from the comparison of the CVs that the peak currents are lower in the H1 phase when compared to the aqueous phase. The system shows two redox peaks in accordance with the reported mechanism of a two electron transfer reaction as given below [30]

$Bq + e^- \rightleftharpoons Bq^-$ ——— (1)

$Bq^- + e^- \rightleftharpoons Bq^{2-}$ —— (2)

The peaks corresponding to the reaction (2) is rather broad and could not be measured accurately. The potentials corresponding to the reaction (1) in both the phases are presented in Table 2.3. As is clear from the table, the system undergoes a quasi-reversible redox reaction in both aqueous and H1 phase with a peak separation of 80 mV. The important point to be noted from the table is the shift in the half-peak potentials in the H1 phase as compared to the aqueous phase. For example, at the scan rate of 20 mV/s, the $E_{1/2}$ in the aqueous phase is 152 mV while in the H1 phase, it has shifted to 87 mV. In other words, the $E_{1/2}$ has shifted to more negative potential in the H1 phase.

2.3.3.5 Methylviologen System

Figure 2.6 shows the CV of 1 mM methylviologen/0.1 M NaF system in the aqueous phase and in the H1 phase. The peak potentials for the system at different scan rates are shown in

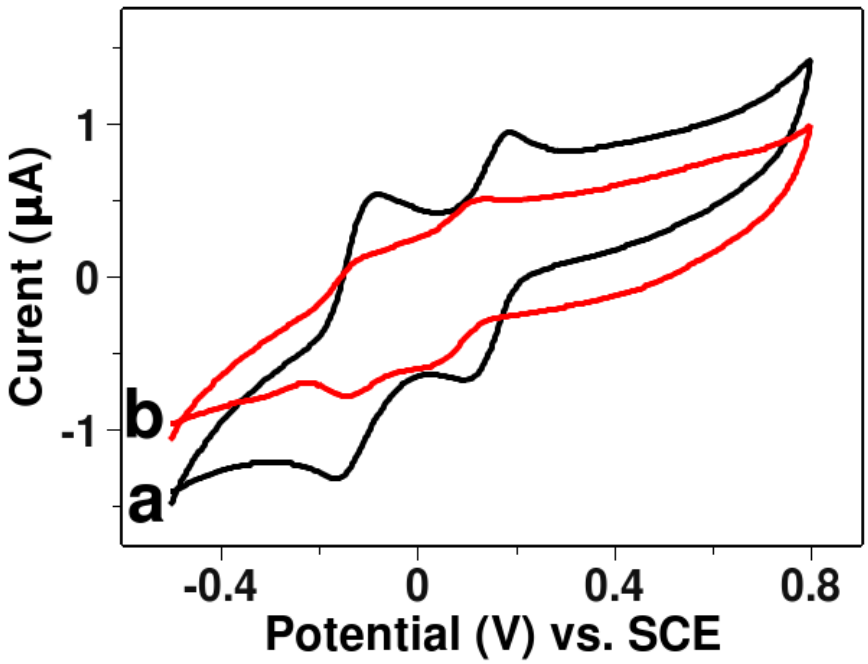

Figure 2.5: Cyclic voltammogram in 1 mM hydroquinone|benzoquinone / 0.1 M NaF system in a) aqueous medium and b) H1 phase at a scan rate of 20 mV/s

Table 2.3: Anodic and cathodic peak potentials (E_p^a and E_p^c), peak separation (ΔE_p), and half-peak potentials ($E_{1/2}$) for the 1 mM benzoquinone |hydroquinone redox reaction in the presence of 0.1 M NaF as supporting electrolyte

Medium	Scan Rate (mV/s)	E_p^a (mV)	E_p^c (mV)	ΔE_p (mV)	$E_{1/2}$ (mV)
Aqueous phase	10	180	95	85	138
	20	184	120	64	152
	50	184	101	83	143
	100	190	96	94	143
H1 Phase	10	112	41	81	75
	20	124	50	74	87
	50	135	33	102	84
	100	131	34	97	83

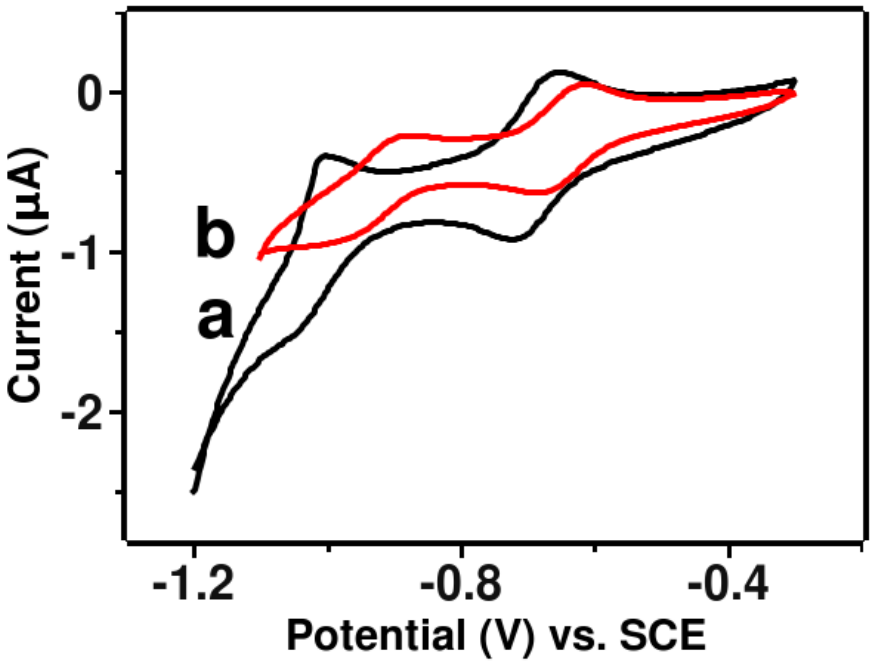

Figure 2.6: Cyclic voltammogram in 1 mM methylviologen / 0.1 M NaF in a) aqueous phase and b) H1 phase at a scan rate of 20 mV/s

Table 2.4: Anodic and cathodic peak potentials (E_p^a and E_p^c), peak separation (ΔE_p), and half-peak potentials ($E_{1/2}$) for the 1 mM methylviologen redox reaction

Medium	Scan Rate (mV/s)	E_p^a (mV)	E_p^c (mV)	ΔE_p (mV)	$E_{1/2}$ (mV)
0.1 M NaF/H_2O	10	-653	-715	62	-684
	20	-654	-718	64	-686
	50	-654	-714	60	-684
	100	-651	-719	68	-685
0.1 M NaF/H1 phase	10	-616	-676	60	-646
	20	-608	-670	62	-639
	50	-612	-678	66	-645
	100	-614	-676	62	-645

the Table 2.4. Two redox peaks have been observed for the methylviologen corresponding to the two electron transfer processes which is in accordance with the previous reports. This corresponds to the folowing two one-electron transfer reactions:

$mv \rightleftharpoons mv^{+} + e^{-}$ ——— (3)

$mv^{+} \rightleftharpoons mv^{2+} + e^{-}$ ——- (4)

Since the first redox peak could not be defined accurately in the CV at all the scan rates, the peak potential values were analysed for the second redox peak and they are presented in Table 2.4. The peak separation for the second redox peak in both the media is about 65 mV. A further examination of Table 2.4 reveals that the half-peak potentials have shifted to a more positive value in the H1 phase compared to the aqueous phase. At the scan rate of 20 mV/s, the $E_{1/2}$ for the methylviologen system in the H1 phase is -639 mV compared to -686 mV in the aqueous phase. This is contrary to the observation in the case of benzoquinone|hydroquinone where the $E_{1/2}$ has been shifted to a more negative potential. However, the positive shift in this case is comparatively less as compared to the negative shift for the benzoquinone|hydroquinone system.

2.3.3.6 Ferrocene/Ferrocenium System

We have studied the cyclic voltammetric characteristics of ferrocene|ferrocenium redox reaction in an organic solvent (propylene carbonate) medium as well as in the H1 phase using 0.1 M TBATFB as the supporting electrolyte in both the media. Figure 2.7 shows the cyclic voltammograms of the mixture in the propylene carbonate medium and in the H1 phase at a scan rate of 20 mV/s. Table 2.5 shows the peak potentials and the peak separations for the redox reaction in propylene carbonate and in the H1 phase. Clear and well-defined redox peaks were obtained in the H1 phase with a peak separation which is almost the same as that in the propylene carbonate medium. However, the peak potentials in the H1 phase have shifted from $E_p^a = 178$ mV to $E_p^c = 310$ mV and from $E_p^c = 108$ mV to $E_p^c = 242$ mV. In other words, there is a large positive shift in the peak potentials from the propylene carbonate medium to the H1 phase by about +133 mV at a scan rate of 20 mV/s. The peak current in

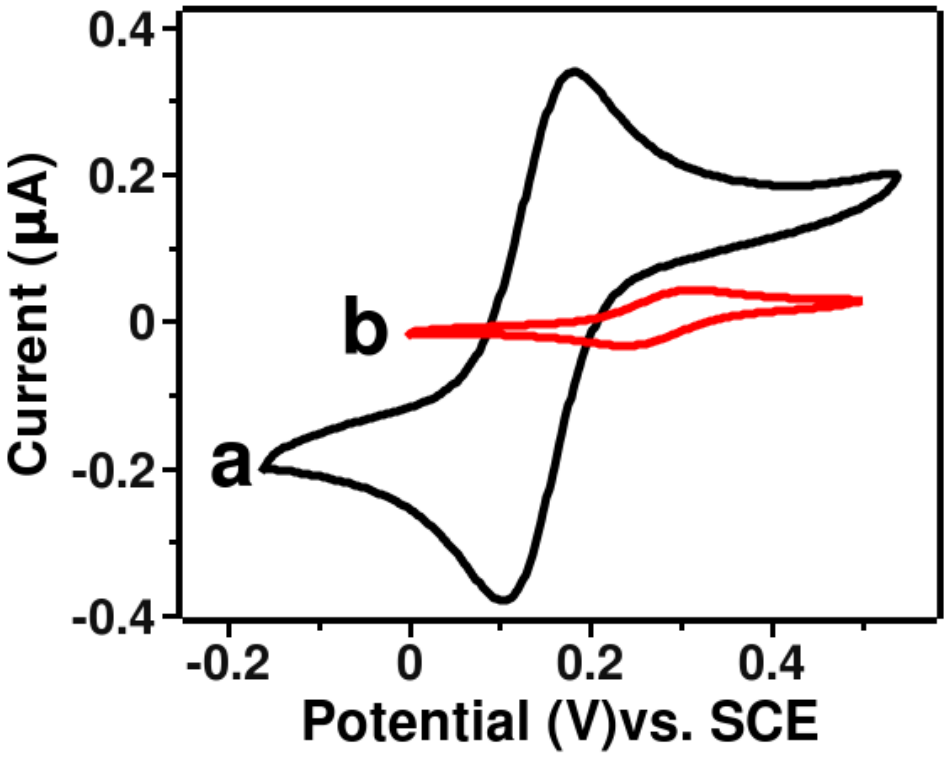

Figure 2.7: Cyclic voltammogram for 1 mM ferrocene|ferrocenium / 0.1 M TBATFB system in a) propylene carbonate medium and b) H1 phase at a scan rate of 20 mV/s

Table 2.5: Anodic and cathodic peak potentials (E_p^a and E_p^c), peak separation (ΔE_p), and half-peak potentials ($E_{1/2}$) for the 1 mM ferrocene|ferrocenium redox reaction in the presence of 0.1 M TBATFB as supporting electrolyte

Medium	Scan Rate (mV/s)	E_p^a (mV)	E_p^c (mV)	ΔE_p (mV)	$E_{1/2}$ (mV)
Propylene carbonate	10	176	108	68	142
	20	178	108	70	143
	50	178	108	70	143
	100	172	102	70	137
H1 phase	10	310	240	70	275
	20	310	242	68	276
	50	313	242	70	278
	100	314	236	78	275

the H1 phase has also decreased significantly compared to the propylene carbonate medium.

2.3.3.7 Ferrocenemethanol System

Figure 2.8 shows the cyclic voltammogram of the ferrocenemethanol system in propylene carbonate and in the H1 phase using 0.1 M TBATFB as the supporting electrolyte. Table 2.6 presents the redox potentials of the system in both the media. It can also be seen from the table that the half-peak potentials have shifted to a more negative value by 270 mV in the H1 phase compared to the propylene carbonate medium. This is in contrary to the ferrocene redox reaction as mentioned above, where the $E_{1/2}$ had shifted to more positive potential. This shows that the hydroxyl group substitution on the ferrocene molecule has a large effect on the redox behaviour of ferrocenemethanol. From the CV, it is also observed that the peak current has reduced significantly in the H1 phase compared to the solvent phase.

2.3.4 Behaviour of Peak Current vs. Scan Rate

We have calculated the average of anodic and cathodic peak currents for all the redox probes in the solvent phase as well as in the H1 phase for different scan rates. Figures 2.9 and 2.10 show the plot of the average peak current as a function of the square root of scan rate ($\sqrt{\nu}$). It may be noted that the peak currents are very less in the H1 phase as compared to the solvent phase. It is clear that the peak current varies linearly with $\sqrt{\nu}$ in all the systems following the Randles-Sevcik equation,

$$i_p = (2.69 \times 10^5) n^{3/2} A D_o^{1/2} C^{\infty} \nu^{1/2}$$

where i_p is the peak current, n is the number of electrons involved in the redox reaction, A is the area of the electrode, D_o is the diffusion coefficient of the probe, C^{∞} is the bulk concentration of the redox probe and ν is the scan rate. For a redox reaction undergoing linear diffusion characteristics, the peak current should vary with $\nu^{1/2}$ irrespective of the scan rate. The reasonably good linear fit in all the systems points to the fact that the redox reactions presented here follow the semi-infinite linear diffusion even in the H1 phase.

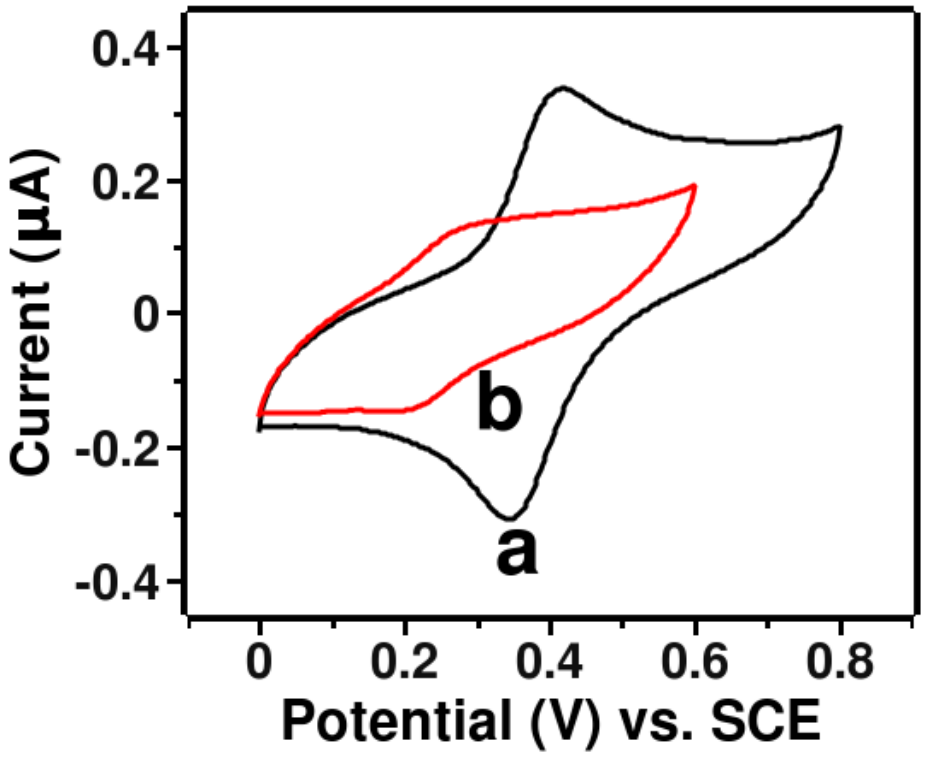

Figure 2.8: Cyclic voltammogram in 1 mM ferrocenemethanol/0.1 M TBATFB system in a) propylene carbonate and b) H1 phase at a scan rate of 20 mV/s

Table 2.6: Anodic and cathodic peak potentials (E_p^a and E_p^c), peak separation (ΔE_p), and half-peak potentials ($E_{1/2}$) for the 1 mM ferrocenemethanol redox reaction in presence of 0.1 M TBATFB as supporting electrolyte

Medium	Scan Rate (mV/s)	E_p^a (mV)	E_p^c (mV)	ΔE_p (mV)	$E_{1/2}$ (mV)
Propylene carbonate	10	552	488	64	520
	20	554	494	60	524
	50	578	500	78	539
	100	580	490	90	535
H1 Phase	10	286	218	68	272
	20	292	210	82	251
	50	296	198	98	247
	100	296	196	100	246

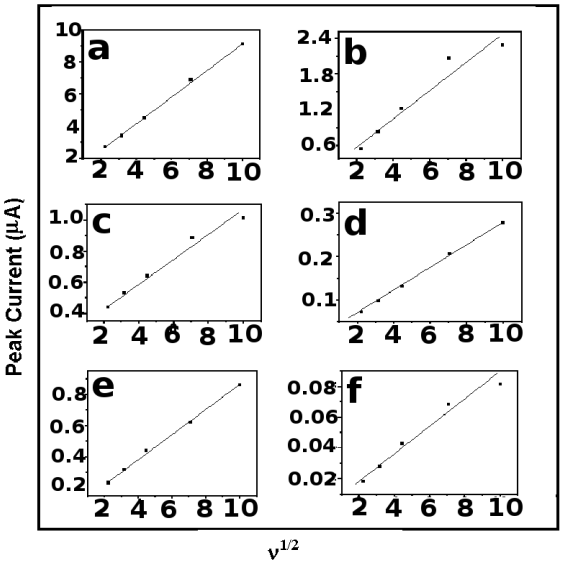

Figure 2.9: Plot of average peak current vs. square root of scan rate in the solvent phase and H1 phase, a) $[Fe(CN)_6]^{4-|3-}/H_2O$, b) $[Fe(CN)_6]^{4-|3-}$/H1 phase, c) $[Ru(NH_3)_6]^{2+|3+}/H_2O$, d) $[Ru(NH_3)_6]^{2+|3+}$/H1 phase, e) ferrocene|ferrocenium/propylene carbonate and f) ferrocene|ferrocenium/H1 phase

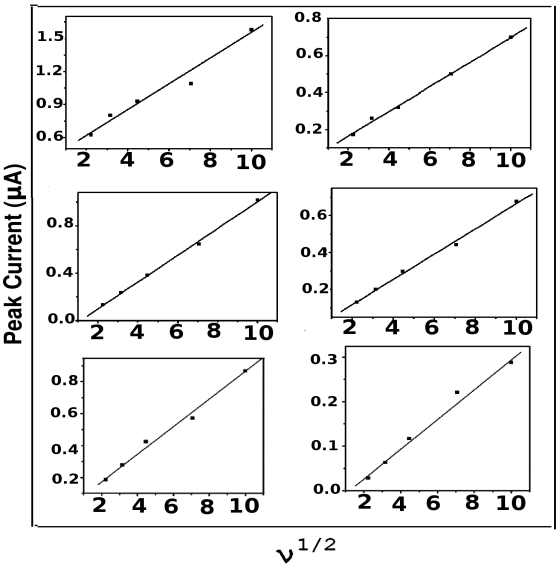

Figure 2.10: Plot of average peak current vs. square root of scan rate in the solvent phase and H1 phase, a) hydroquinone|benzoquinone/H_2O, b) hydroquinone|benzoquinone/H1 phase, c) methylviologen/H_2O, d) methylviologen/H1 phase, e) ferrocenemethanol/propylene carbonate and f) ferrocenemethanol/H1 phase

2.3.5 Discussions on the Half-peak Potential Shifts in the CV

From the cyclic voltammograms, we find that there is significant shift in the half-peak potentials for several redox systems in the liquid crystalline phases (Tables 2.1- 2.6). In what follows, we therefore attempt to rationalise these potential shifts in terms of the nature of the redox species and the liquid crystalline environment in which the electron transfer process take place.

Lee *et al.* have reported the formal potential shifts of viologen compounds in the micellar media formed by SDS, CTAB, and Triton X-100 surfactants, where the redox potential was found to be the maximum in the case of Triton X-100, a nonionic surfactant micelle [2]. This means that the oxidation of viologen is less favoured in the Triton X-100 micelles compared to the aqueous phase. They explained this phenomenon as arising due to better stability and the binding of the redox couple in the micelle. Ryabov *et al.* have reported the potential shift of the ferrocene redox reaction in different micelles formed by anionic, cationic and nonionic surfactants [31]. In their study, the equilibrium potential shifted to a more negative potential in the case of SDS, an anionic surfactant. In the case of cationic (CTAB) and nonionic (Triton X-100) surfactant micelles, the formal potentials had shifted to a more positive potential. They attributed this behaviour to the stability of the redox species in the micelles, where the ferrocene molecule is present inside the hydrophobic core while the hydrophilic ferrocenium ion prefers the outside hydrophilic part of the micelle.

2.3.5.1 Ferrocyanide/Ferricyanide Reaction

We have observed, as shown in Table 2.1 that in the case of the ferrocyanide|ferricyanide couple, the half-peak potential shifts to a more negative value and the extent of this shift is dependent on the supporting electrolyte used. In the micellar state of CTAB/hexadecane/1-butanol/water, for example, the negative potential shift was attributed to the hydrogen-bonding effects between the cyano groups of the probe and the water molecules associated with the micelle [32]. Since in the micellar state, most of the water molecules are bounded with the surfactant to form the micelle, it is expected that the total solvation sphere of the

redox probe to be correspondingly reduced in the micelle, compared to the aqueous medium. Moreover the stability of the ions in the micellar media also contributes to the redox potentials of the probes. In the present case, during the oxidation process of $[Fe(CN)_6]^{4-}$ to $[Fe(CN)_6]^{3-}$, as shown in Figure 2.11, the transformation involves a decrease in the charge of the redox species. In a micelle formed by a nonionic surfactant such as Triton X-100, a less charged species will be more stable, which means ferricyanide is more stable than ferrocyanide. As a result, the oxidation is more favoured and the half-peak potential shifts to a more negative potential. Moreover, since both the redox species involved in the reaction are water soluble and charged, they will prefer the hydrophilic outer boundary of the cylindrical micelles as depicted in Figure 2.12. It is well-known that, due to the extensive hydrogen bonding of the water molecules with the hydrophilic ethoxy groups of Triton X-100, there is a layer of bound water attached to these cylindrical micelles. Consequently, the electroactive ions are considerably less hydrated in the free water depleted H1 phase compared to the aqueous electrolytes. This means that the solvent reorganisation energy in this case is lower, which causes the peak potentials to shift to a more negative value in the H1 phase. In the case of the $[Fe(CN)_6]^{4-|3-}$ couple, the negative shift in the half-peak potential is significantly greater in the TBATFB supporting electrolyte than in NaF. The reason for this can be the hydrophobic nature of the counterion in TBATFB, which makes the water molecules more tightly bound to the cylindrical micelles, leaving the redox species relatively less hydrated than in NaF. On the contrary, it was observed by Molina *et al.* that the half-peak potential was shifted to higher value, in the AOT reverse micellar state. This shift was a function of the AOT concentration for the redox reaction of ferrocyanide|ferricyanide reaction. This positive shift was explained due to the association of the counter ions (K^+ ions) with the redox probe. They have shown that as the association increases, the $E_{1/2}$ shifts to more positive value [5].

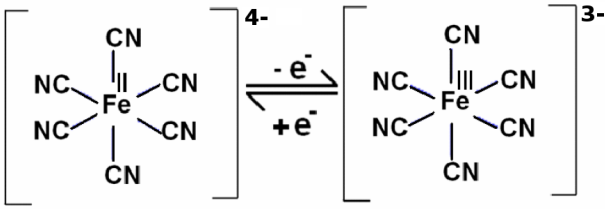

Figure 2.11: A representation of the redox reaction of ferrocyanide/ferricyanide reaction

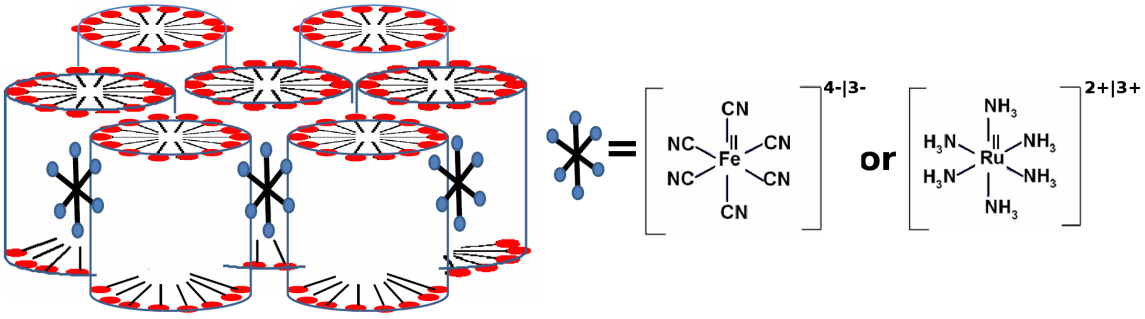

Figure 2.12: A pictorial representation of the occupation of hydrophilic redox probes in the intercolumn spacing of the micelles in the liquid crystalline phase (model not to scale)

2.3.5.2 Hexaammineruthenium(II/III) Reaction

For the $[Ru(NH_3)_6]^{2+|3+}$ reaction as shown in Figure 2.13, however, the shift in the half-peak potential is negligible when the same supporting electrolyte (0.1 M KCl) is used both in the aqueous phase and in the H1 phase, as shown in Table 2.2. The observed negative shift in the half-peak potential is also small in the case of different supporting electrolytes (0.1 M $LiClO_4$ in the aqueous phase and 0.1 M TBATFB in the H1 phase). These observations point to the fact that the outer sphere electron-transfer process of the $[Ru(NH_3)_6]^{2+|3+}$ reaction is extremely facile, and therefore, the change in the electrolytic medium does not significantly change the energetic cost involved in the reaction and hence the half-peak potentials.

In general, the electron transfer reactions between the electrode and the redox probes in the solution, which is generally referred to as heterogeneous electron transfer, can occur by two mechanisms, *viz* outer-sphere and inner-sphere electron transfer mechanisms [33]. In the inner sphere electron transfer mechanism, the redox probe comes in direct contact with the electrode surface and the reaction proceed through a bond-breaking accompanied

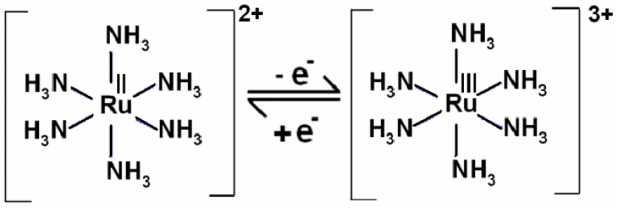

Figure 2.13: A representation of the redox reaction of hexaammineruthenium(II/III) system

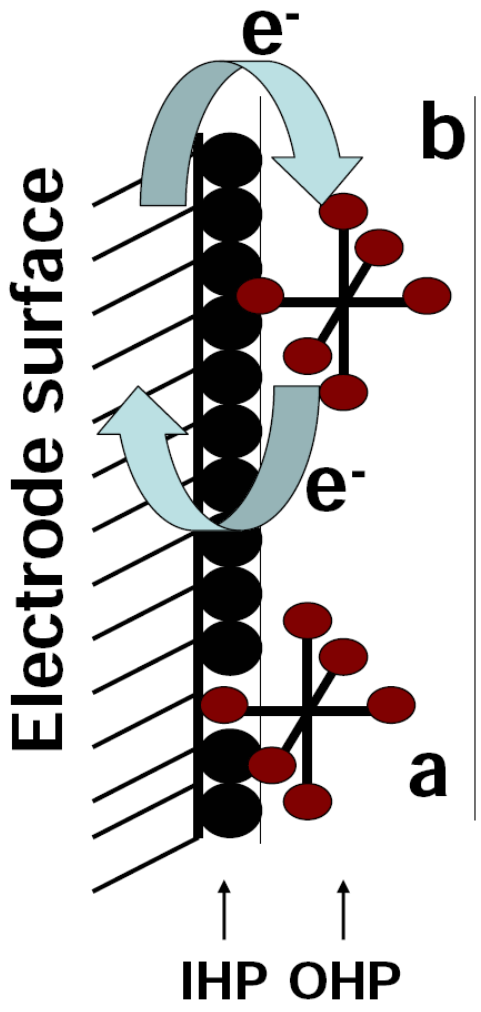

Figure 2.14: A schematic model of the electrode-electrolyte interface for a) inner-sphere and b) outer-sphere heterogeneous electron transfer reactions

by new bond formation. Under this mechanism, the redox probe has to present in the inner-Helmholtz plane of the electrode-solution interface. For this, the probe should penetrate through the solvation layer of the electrode surface and the hydration layer of the probe itself. On the other hand, in the outer sphere mechanism, the redox probe is not necessarily in direct contact with the electrode surface, and may even present in the outer-Helmholtz plane of the electrode-solution interface. A schematic diagram of these two mechanisms are shown in Figure 2.14. In the figure, IHP represents the inner-Helmholtz plane of the adsorbed species on the electrode surface and OHP represents the outer-Helmholtz plane, where the molecules are close to the electrode but are not in direct contact with the electrode surface [34].

2.3.5.3 Hydroquinone/Benzoquinone Reaction

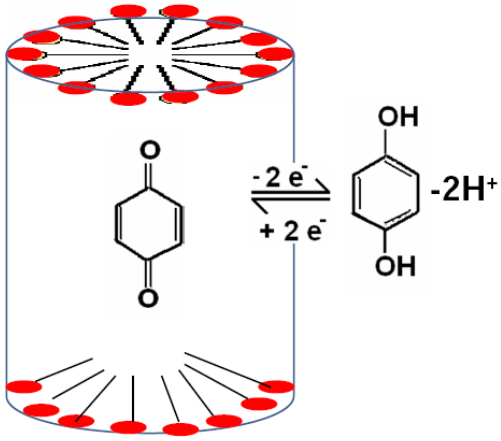

Figure 2.15: A schematic representation of the redox reaction of hydro-quinone|benzoquinone reaction in the liquid crystalline phase

The redox reactions of quinone systems, summarised in Table 2.3, are more complex when compared to other common redox probes, due to the involvement of protons. The mechanism of the redox probes like quinones in non-aqueous solutions in the presence of proton donors have been studied previously [35]. The solvent effect on the redox reaction have been reported in the literature in different organic solvents [36, 37]. It has been shown that in an organic medium, the potential of the redox reaction of benzoquinone may be tuned

by the addition of benzoic acid, which can act as a proton donor [38]. On the other hand, the effect of substitution on the aromatic ring in the redox reaction in organic media has been studied by Bauscher *et al.* [39]. Recently, in the cubic system, it has been observed that the redox process of quinone system is quasi-reversible [18]. The reduction of benzoquinone in a non-buffered solution results in the formation of different reduced species like Bq^{2-}, BqH^{-} as well as BqH_2 as reported by Quan and coworkers [30]. It is known that the hydroquinone is more hydrophilic compared to the benzoquinone. Hence the redox reaction of the quinone system results in a transition between hydrophobic benzoquinone and hydrophilic hydroquinone, as shown in Figure 2.15. In the H1 phase, benzoquinone is stabilised inside the core of the cylindrical micelle by the hydrophobic interactions, which is absent in the aqueous phase. Moreover hydroquinone can form hydrogen bonds with the water molecules outside the micelle. In the H1 phase, most of the water molecules are bound to the micelles, leaving fewer molecules that are capable of hydrating the reduced species. As a result, the energy cost of breaking the hydrogen bond of hydroquinone during oxidation is lesser in the H1 phase compared to the aqueous phase. In other words, the oxidation is more favoured in the H1 phase compared to the aqueous phase and the half peak potential shifts to a more negative value in the H1 phase.

2.3.5.4 Methylviologen Reaction

We have observed that the half-peak potentials of the viologen system shift to more positive values in the H1 phase compared to the aqueous medium as shown in Table 2.4. This positive half-peak potential shift of viologen system may be explained as follows. The oxidation of the methylviologen results in the mono and dicationic species as mv^{+} and mv^{2+}. The oxidation increases the net charge on the redox probe. In the H1 phase, most of the water molecules are bound to the surfactant molecules to form the cylindrical micelles of the columnar phase and therefore the hydration for the oxidised species is less in the H1 phase compared to the aqueous phase. For the hydration to occur, the hydrogen bonding between the water molecules and the surfactants has to be broken. This is energetically less

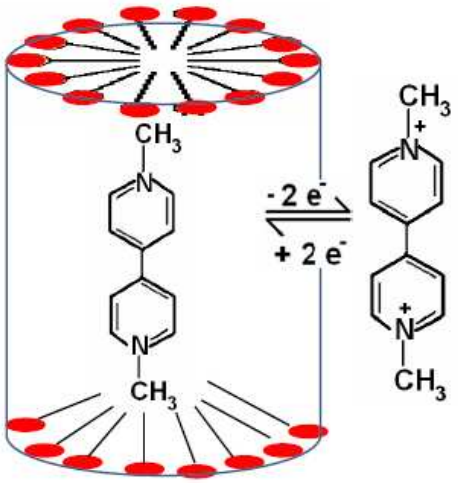

Figure 2.16: A schematic representation of methylviologen redox reaction in the liquid crystalline phase

favoured. As a result, the oxidised species is less stable in the H1 phase and hence the oxidation reaction is not favoured. Further, since methylviologen is hydrophobic, it prefers to stay inside the cylindrical micelles of Triton X-100/water system as shown in Figure 2.16. In other words, the reduced species is surrounded by the surfactant molecules. As a result of this, the oxidation needs more energy to leave the inside of the cylindrical micelle without a corresponding gain in the hydration energy at the intercolumn spacing.

2.3.5.5 Ferrocene/Ferrocenium Reaction

In the present study, for the ferrocene|ferrocenium couple, as presented in Table 2.5, we have observed a large positive shift in the half-peak potential by about 135 mV in the H1 phase. This can be attributed to the stability of the ferrocene and ferrocenium species in the system in a similar manner as reported earlier [3, 31]. It is known that hydrophobic molecules occupy the hydrophobic core of the hexagonal columns of the liquid crystalline phase [40]. Ferrocene is neutral and hydrophobic in nature, and therefore occupy the hydrophobic core of the micelle while the ferrocenium, the oxidised species, is a charged ion and hydrophilic in nature and therefore prefers the inter-columnar space containing water molecules as shown

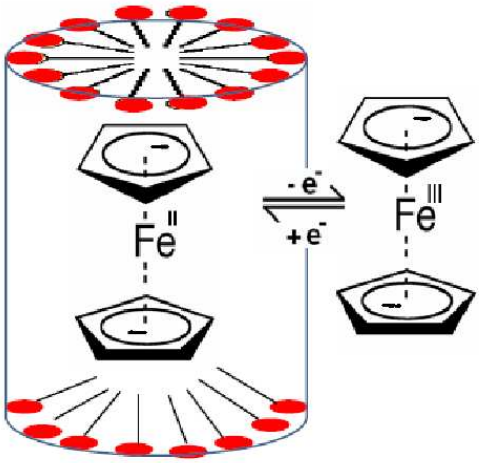

Figure 2.17: A schematic diagram of ferrocene|ferrocenium redox reaction in the liquid crystalline phase

in Figure 2.17. This means that for the ferrocene|ferrocenium redox reaction, there is a change from a hydrophobic, neutral species to a hydrophilic charged species and *vice versa*. Obviously, this process leads to a large reorientation of water molecules constituting the liquid crystalline medium, and as a result of the energetic cost involved, the half-peak potentials shift to more positive values.

2.3.5.6 Ferrocenemethanol Reaction

From the Table 2.6, we have observed a negative shift in the half-peak potentials for the ferrocenemethanol system in the H1 phase compared to the aqueous phase. Ferrocenemethanol has the hydroxyl functionalisation in the side chain and therefore hydrophilic in nature which makes it to occupy the partially water rich space at the outer boundary layer of the micelle in the H1 phase. But the oxidised species is much more hydrophilic and therefore will prefer to leave the inside of the micelle altogether and stay at the inter-columnar space of the micelle, which is depicted in Figure 2.18. As a result, the energy cost in the reorganisation of the ferrocenemethanol from the outer boundary layer of the micelle to outside the micelle during the oxidation is relatively small. Here, the oxidised species can form hydrogen bond with the

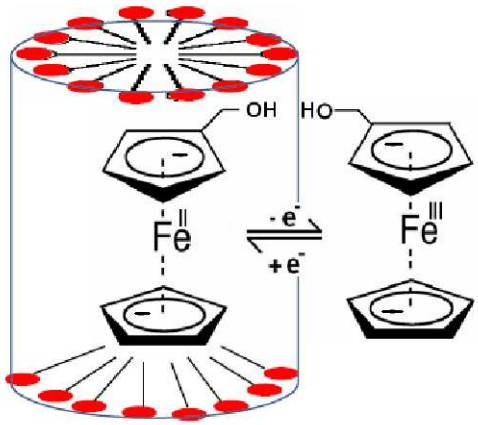

Figure 2.18: A schematic diagram of ferrocenemethanol redox reaction in the liquid crystalline phase

water molecules, which can stabilise the ions. The oxidised species can also interact with the electron rich polyethoxy chain of the surfactant molecules. These two interactions along with the lesser reorganisation energy result in a negative potential shift for the ferrocenemethanol system. This negative shift is in contrast to the positive half-peak potential shift observed for ferrocene system as discussed in section 2.3.5.5. For the ferrocene system, the reduced species occupy the space inside the micelle due to the hydrophobic nature and as a result the reorganisation energy is more during the oxidation. Also the ferrocenium ions can not form hydrogen bonds with the water molecules. Due to these two reasons, the half-peak potential of the ferrocene system shifts to a more positive potential.

2.3.6 Electrochemical Impedance Spectroscopy

We conducted electrochemical impedance spectroscopic (EIS) studies for all the above mentioned redox probes in their respective solvent medium as well as in H1 phase. The EIS studies were carried out at the half-peak potentials of the redox probes in the respective media, which are measured from the cyclic voltammetric studies. Figure 2.19 show the impedance plots for the $[Fe(CN)_6]^{4-|3-}$, $[Ru(NH_3)_6]^{2+|3+}$, hydroquinone|benzoquinone, methylviologen, $Fc|Fc^+$ and ferrocenemethanol redox reactions in solvent and in the liquid crystalline

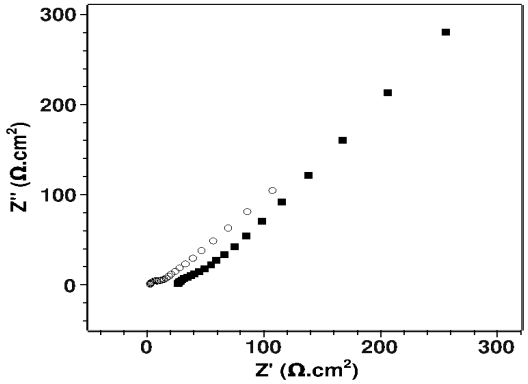

(a) Ferrocyanide/ferricyanide at 0.162 V (0.1 M NaF) (○) and 0.104 V (0.1M TBATFB) (■)

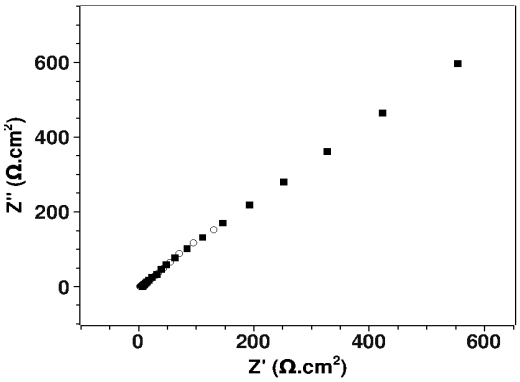

(b) Hexaammineruthenium(II/III) chloride at -0.166 V (0.1 M $LiClO_4$)(○) and -0.177 V (0.1 M TBATFB) (■)

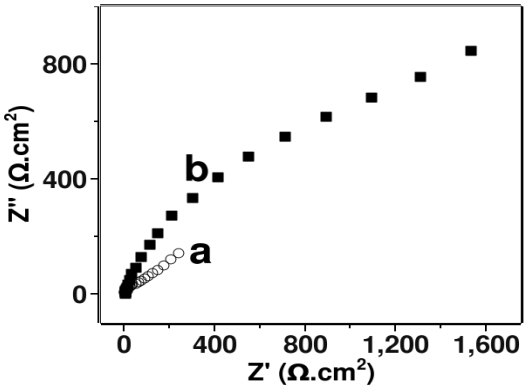

(c) hydroquinone|Benzoquinone (0.1 M NaF) at 0.152 V (○) and 0.087 V (■)

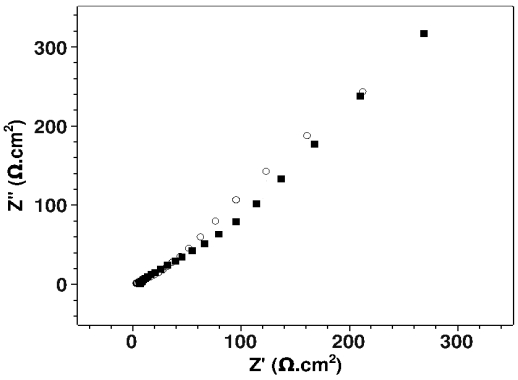

(d) Methyl viologen system (0.1 M NaF) at -0.686 V (○) and -0.639 V (■)

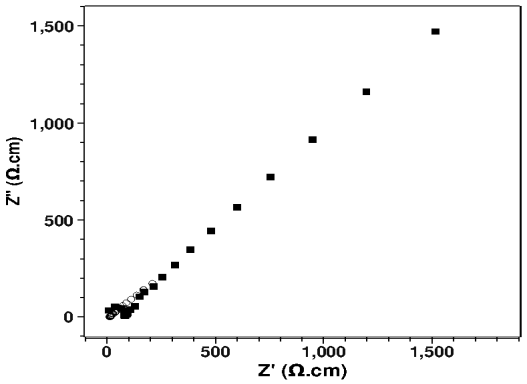

(e) Ferrocene|ferrocenium system (0.1 M TBATFB) at 0.143 V (○) and 0.276 V (■)

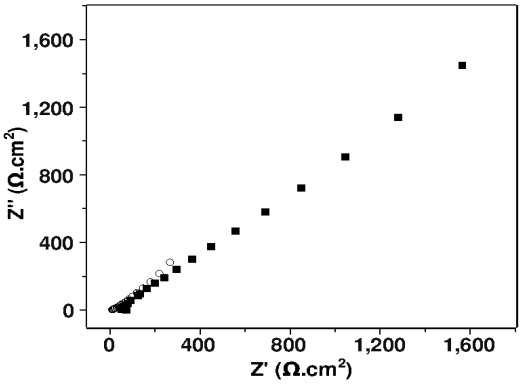

(f) Ferrocenemethanol system (0.1 M TBATFB) at 0.524 V (○) and 0.251 V (■)

Figure 2.19: Nyquist plots of the electrochemical impedance spectrum for the redox systems in the solvent medium (○) and in the H1 phase (■) at the formal potential (vs. SCE) of the corresponding redox reaction

phases. The impedance data for all the redox systems shown in the figure were studied using equivalent circuit analysis. We have used the standard Randles equivalent circuit with R_u in series with the parallel combination of double-layer capacitance (C_{dl}) and charge transfer resistance (R_{ct}) with Warburg impedance (Z_W) in series, *i.e.,* R(C(RW)). A general description on the equivalent circuit fitting of EIS data has been provided in chapter 1. The values obtained using the above Randle's circuit by the best fitting of the impedance data are shown in Table 2.7. From the table, we find that the solution resistance or the uncompensated resistance, R_u is increased in the liquid crystalline phase for all the redox systems. The higher solution resistance arises from the nature of the liquid crystalline medium with its confined geometry and lower ionic conduction channels. On the other hand, the analysis yielded no significant R_{ct} for the $[Ru(NH_3)_6]^{2+|3+}$ and Fc $|Fc^+$ reactions in the solvent medium as well as in the liquid crystalline phase. However, there is a small charge-transfer resistance (R_{ct}) associated with the ferrocyanide redox reaction as shown in Table 2.7. Warburg impedance, Z_W is also higher, indicating that the diffusion of the redox species is slower in the columnar phase. A similar behaviour is also exhibited by the redox systems of hexaammineruthenium(II/III) and also ferrocene|ferrocenium. For the benzoquinone|hydroquinone and ferrocenemethanol reactions, the R_{ct} values have increased from 40 Ωcm^{-2} to 742 Ωcm^{-2} and 9 Ωcm^{-2} to 66 Ωcm^{-2} respectively, indicating that the kinetics of the reaction in the H1 phase is slower than in the solvent medium. In contrast, for the methylviologen system, the R_{ct} value has decreased from 926 Ωcm^{-2} to 8 Ωcm^{-2} indicating that the reaction in the H1 phase is faster compared to the aqueous medium.

We have calculated the diffusion coefficient of the redox species using the following equations: [34, 41]

$$Z_W = \sqrt{\frac{2}{\omega}}.\sigma$$

$$\sigma = \frac{RT}{2^{\frac{1}{2}} n^2 F^2 D^{\frac{1}{2}} A}\left(\frac{1}{C_O} + \frac{1}{C_R}\right)$$

where Z_W is the Warburg impedance, ω is the angular frequency applied, n is the number of electrons involved in the redox reaction, F is the Faraday constant, R is the universal gas constant, T is the temperature (in K), D is the diffusion coefficient of the redox species, A

Table 2.7: Values of the solution resistance (R_u), double-layer capacitance (C_{dl}), charge-transfer resistance (R_{ct}) and Warburg impedance (Z_W) calculated by fitting the impedance data

System	solvent Phase				H1 phase			
	R_u	C_{dl}	R_{ct}	Z_W	R_u	C_{dl}	R_{ct}	Z_W
	Ω	F/cm^2)	Ω.cm^2)	S.s$^{1/2}$.cm^2)	Ω	F/cm^2)	Ω.cm^2)	S.s$^{1/2}$.cm^2)
$[Fe(CN)_6]^{4-\|3-}$/NaF	1320	$3.99x10^{-5}$	7.03	$9.00x10^{-3}$	4460	$2.73x10^{-5}$	10.45	$3.83x10^{-3}$
$[Fe(CN)_6]^{4-\|3-}$/TBATFB					13590	$4.47x10^{-5}$	7.63	$3.75x10^{-3}$
$[Ru(NH_3)]_6^{2+\|3+}$/$LiClO_4$	1607			$3.29x10^{-3}$				
$[Ru(NH_3)]_6^{2+\|3+}$/TBATFB					$1.53x10^4$	$5.06x10^{-5}$		$1.63x10^{-3}$
Fc |FcTFB/TBATFB	5173			$4.63x10^{-3}$	$2.02x10^4$	$1.05x10^{-5}$		$5.44x10^{-4}$
Bq|Qh/NaF	1123	$1.88x10^{-4}$	40	$5.1x10^{-3}$	3191	$1.1x10^{-4}$	742.8	$1.6x10^{-2}$
mv/TBATFB	823	$1.19x10^{-4}$	926	$2.2x10^{-3}$	2591	$5.9x10^{-4}$	8.15	$3.3x10^{-3}$
Fm/TBATFB	5270	$1.52x10^{-5}$	9	$3.3x10^{-3}$	$2.5x10^4$	$1.8x10^{-5}$	66.26	$5.8x10^{-4}$

is the area of the electrode, and C_O and C_R are the bulk concentrations of the oxidised and reduced species in the solution, respectively. The above calculation assumes that the active area (A) of contact of the electrode with the redox molecules is the same in the H1 phase as well as in the solvent medium. Since this assumption is not strictly valid, the calculated diffusion coefficient is called the apparent diffusion coefficient [4, 26, 27]. The D_{app} values calculated from the Warburg impedance for all the redox systems are shown in Table 2.8.

From the Table 2.8, we find that the values of the diffusion coefficients are lower in the H1 phase compared to the solvent phase for all the redox systems studied in this work. It is clear that the diffusion coefficient values for the ferrocyanide|ferricyanide system has decreased by almost an order of magnitude in the H1 phase. For the hexaammineruthenium(II/III) system the extent of decrease is significantly less. A similar behaviour was observed for the methylviologen system also. On the other hand, there was a large decrease in the diffusion coefficient of benzoquinone|hydroquinone, ferrocene|ferrocenium and ferrocenemethanol systems.

Both the oxidised and reduced species of ferrocyanide|ferricyanide and hexaammineruthenium(II/III) systems are hydrophilic and therefore present in the intercolumnar spacings containing water molecules, as presented in Figure 2.12. The diffusion of these two redox species therefore proceeds relatively uninhibited that results in a smaller decrease in the diffusion coefficient in the H1 phase. These observations are also in agreement with our earlier conclusions from the peak potential measurements. Similar observations were

Table 2.8: Diffusion coefficient values of the redox probes in the solvent medium (D) and in the columnar hexagonal phase (D_{app})

Redox system	Medium	Diffusion coefficient (cm^2/s)
$[Fe(CN)_6]^{4-\|3-}$	NaF/H_20	$2.00x10^{-5}$
	NaF/H1 phase	$4.3x10^{-6}$
	TBATFB/H1 phase	$3.13x10^{-6}$
$[Ru(NH_3)_6]^{2+\|3+}$	0.1M NaF/H1	$3.7x10^{-6}$
	0.1M TBATFB/H1 phase	$7.7x10^{-7}$
	0.1M KCl/H_2O	$1.24x10^{-5}$
	0.1M KCl/H1 phase	$6.81x10^{-7}$
Quinone	0.1M NaF/H_2O	$3.26x10^{-6}$
	0.1M NaF /H1 phase	$8.6x10^{-8}$
Viologen	0.1M NaF/H_2O	$5.1x10^{-6}$
	0.1M NaF/H1 phase	$2.9x10^{-6}$
$Fc\|Fc^+$	0.1M TBATFB/PC	$6x10^{-6}$
	0.1mM TBATFB/H1 phase	$8.1x10^{-8}$
ferrocenemethanol	0.1M TBATFB/PC	$3.1x10^{-6}$
	0.1M TBATFB/H1 phase	$9.8x10^{-8}$

made by Rowinski *et al.* in the bicontinuous cubic phase where they found that the diffusion coefficient of $[Ru(NH_3)_6]^{2+|3+}$ in the cubic phase was 25% of its value in the solution phase [18]. Similarly, Kostela *et al.* found that the D value has decreased to 21% of the value in the aqueous phase for $[Ru(NH_3)_6]^{2+|3+}$ redox system in a bicontinuous cubic phase [27]. These results support our conclusion, where we have observed that for the same redox probe, the diffusion coefficient is 21% of its value in the aqueous solution. It is therefore clear that the diffusion rate is not significantly affected for a hydrophilic redox species such as hexaamminеruthenium(II/III) in lyotropic liquid crystalline phases as long as abundant hydrophilic channels are available in the liquid crystalline matrix. The very small decrease in the D_{app} for the methylviologen system may arise because of the shape of the molecules. Unlike all other redox probes we have studied, methylviologen is a rod like molecule (Figure 2.16),

which can move relatively easily through the aqueous channels outside the micelles.

Table 2.8 also demonstrate that the D_{app} value for the benzoquinone|hydroquinone system has decreased by more than an order of magnitude in the H1 phase. This large decrease in the D_{app} of the system can be explained in terms of the restricted mobility of the benzoquinone in the hydrophobic core of the H1 phase. Moreover hydroquinone can form hydrogen bonds with the surfactant-bounded water clusters, thereby inhibiting the diffusion of the species. For ferrocene|ferrocenium couple, the reduction in the diffusion coefficient values can be explained due to the nature of the ferrocene molecule, which is neutral and hydrophobic and therefore prefers to occupy the hydrophobic core of the hexagonal columns. Within these columns, the diffusion of the ferrocene molecules is significantly inhibited. Similarly for the ferrocenemethanol system, the diffusion coefficient has decreased by almost 30 times in the H1 phase compared to the propylene carbonate medium. This can be rationalised as due to the interaction of reduced species inside the micelle and the oxidised species with the polyethoxy chain and water molecules outside the micelle similar to the $Fc|Fc^{+}$ system. We have observed that the oxidised ferrocenium ions act as a strong electron acceptor, which can interact with the polyethoxy chains of the surfactant molecules. This also contributes to the decrease in the D_{app} values. Similar trend in the diffusion coefficient values for the ferrocene systems was also reported in the literature in the micellar as well as in the cubic phases [1, 17, 18, 27].

Interestingly ferrocene and ferrocenemethanol systems offer contrasting behaviours. For the ferrocene system, the half-peak potential has shifted to a more positive potential, while for the ferrocenemethanol, the shift is towards lower potential when compared to propylene carbonate medium. This shows that the nature of the functional group attached to the redox probe affects its charge-transfer on the electrode. It is also observed that the reversibility of the system decreases after hydroxyl group functionalisation. This is clear from the Table 2.7 and Table 2.8 when comparing the peak potentials for ferrocene and ferrocenemethanol. On the other hand, the diffusion coefficient values for both the systems were found to be quite similar.

We can rationalise the CV and EIS results and the close agreement between these two techniques from the Randles-Sevcik equation, according to which, $i_p \propto D^{1/2}$ relation, where i_p is the peak current and D is the diffusion coefficient of the probe. Table 2.9 shows the

Table 2.9: Ratios of peak currents measured from cyclic voltammetry and $D^{\frac{1}{2}}$ calculated from the electrochemical impedance spectroscopy in the H1 phase and solvent phase

Redox species	$I_p(H1)/I_p(solvent)$	$D_{app}^{\frac{1}{2}}(H1)/D_{app}^{\frac{1}{2}}(solvent)$
$[Fe(CN)_6]^{4-\|3-}$	0.400	0.465
$[Ru(NH_3)_6]^{2+\|3+}$	0.502	0.456
Benzoquinone |Hydroquinone	0.275	0.162
Methylviologen	0.683	0.754
Fc $\|Fc^+$	0.102	0.116
Ferrocenemethanol	0.227	0.178

comparison of the ratio of peak currents measured using the CV and the ratio of square root of the diffusion coefficients, which are measured using electrochemical impedance method in aqueous and H1 phase. The reasonable agreement of these two ratios obtained by two different methods supports our proposition that planar diffusion controlled model for the redox reaction is valid in both aqueous as well as in the H1 phase.

2.4 Conclusion

We have presented the electron-transfer studies of six different redox species on a gold electrode in a lyotropic columnar hexagonal liquid crystalline phase (H1 phase) formed by a non-ionic surfactant, Triton X-100, and water. We find that the half-peak potentials are shifted significantly in the H1 phase in the ferrocyanide|ferricyanide, hydroquinone|benzoquinone, methyl viologen, ferrocene|ferrocenium and ferrocenemethanol systems. The extent of shift and the direction are dependent on the nature of the redox probe. This shift has been attributed due to the nature of interactions between the redox probes and the surrounding environment in the liquid crystalline medium. However in the hexaammineruthenium system, there is very little shift in the $E_{1/2}$ values. In addition, the diffusion coefficients of all the redox species are significantly reduced in the columnar phase as compared to the respective solvent media. We have rationalised the shift in $E_{1/2}$ and D values in terms of the nature of the redox species and their interactions with the liquid crystalline environment in which the

electron transfer process takes place.

As described before, the lyotropic liquid crystalline phases are formed by the aggregation of micelles at higher concentration of the surfactants. Since the constituent components in the lyotropic liquid crystalline phases are the same as that of the micelles, a close similarity can be found in the qualitative properties of the redox probes in the micellar phase as reported earlier in literature and in the liquid crystalline phases presented here. This is due to the fact that the nature of interactions are similar between the surfactant molecules and the redox probes in both the media. This is also reflected in the behaviour of the shift in the half-peak potentials of the redox probes in the micellar and liquid crystalline phases when both the phases are formed by same surfactant. On the other hand, the orientation of the redox probes may vary depending upon the nature of the liquid crystalline phase formed. For example, the occupation of redox probes in the hydrophilic or hydrophobic part of the liquid crystal have large implications in the diffusion coefficient of the redox probes. As a result, the values of the measured diffusion coefficients of the redox probes depend upon the structure of the liquid crystalline phase, more than the nature of the surfactant that forms the phase.

From these studies we conclude that despite the surfactant organisation in the liquid crystalline phase with columnar arrangement, the diffusion field due to the redox species on the macro electrode remains linear just as in the aqueous medium. This conclusion provides a useful basis for further investigations regarding electron transfer processes in biological species or the transport properties of drugs that are dissolved or delivered in organised systems. We therefore believe that this simple system provides a controlled environment for studying and understanding electron transfer processes in biological and physiological media.

Bibliography

[1] A. B. Mandal, *Langmuir*, 1993, **9**, 1932.

[2] C. W. Lee, M. Kyung and J. M. Jang, *Langmuir*, 1993, **9**, 1934.

[3] J. Chen, O. Ikeda and K. J. Aoki, *Electroanal. Chem*, 2001, **496**, 88.

[4] J. Kostela, M. Elmgren, P. Hansoon and M. Almgren, *J. Electroanal. Chem.*, 2002, **536(1-2)**, 97.

[5] P. G. Molina, J. J. Silber, N. M. Correa and L. Sereno, *J. Phys. Chem. C*, 2007, **111**, 4269.

[6] J. F. Rusling, C.-N. Shi, D. K. Gosser and S. S. Shukla, *J. Electroanal. Chem.*, 1988, **240**, 201.

[7] G. N. Kamau and J. F. Rusling, *J. electroanal. Chem.*, 1988, **240**, 217.

[8] G. N. Kamau, T. Leipert, S. S. Shukla and J. F. Rusling, *J. Electroanal. Chem.*, 1987, **233**, 173.

[9] J. F. Rusling and D. J. Howe, *Inorg. Chim..Acta*, 1994, **226**, 159.

[10] J. F. Rusling, *Trends in Anal. Chem.*, 1988, **7**, 266.

[11] M. O. Iwunze and J. F. Rusling, *J. Electroanal. Chem.*, 1989, **266**, 197.

[12] H. Zhano and J. F. Rusling, *Talanta*, 1993, **40**, 741.

[13] J. F. Rusling, *Microporous Mater.*, 1994, **3**, 1.

[14] J. Gao and J. F. Rusling, *J. Electroanal. Chem.*, 1998, **449**, 1.

[15] R. Bilewicz, P. Rowinski and E. Rogalska, *Bioelectrochemistry*, 2005, **66**, 3.

[16] M. H. Ropers, R. Bilewicz, M. J. Stebe, A. Hamidi, A. Miclo and E. Rogalska, *Phys. Chem. Chem. Phys.*, 2001, **3**, 240.

[17] P. Rowinski, R. Bilewicz, M. J. Stebe and E. Rogalska, *Anal. Chem.*, 2002, **74**, 1554.

[18] P. Rowinski, A. Korytkowska and R. Bilewicz, *Chem. Phys. Lipids*, 2003, **124**, 147.

[19] E. Nazaruk, R. Bilewicz, G. Lindblom and B. L. Sethson, *Anal. Bioanal. Chem.*, 2008, **391**, 1569.

[20] V. Razumas, K. Larsson, Y. Miezis and T. Nylander, *J. Phys. Chem.*, 1996, **100**, 11766.

[21] V. Razumas, Z. Talaikyt, J. Barauskas, T. Nylander and Y.Miezis, *Prog. Colloid Polym. Sci.*, 1998, **108**, 76.

[22] J. Barauskas, V. Razumas, Z. Talaikyt, A. Bulovas, T. Nylander, D. Taurait and E. Butkus, *Chem. Phys. Lipids*, 2003, **123**, 87.

[23] F. Caboi, T. Nylander, V. Razumas, Z. Talaikyt, M. Monduzzi and K. Larsson, *Langmuir*, 1997, **13**, 5476.

[24] V. Razumas, J. Kanapieniene, T. Nylander, S. Engstrom and K. Larsson, *Anal. Chim. Acta*, 1994, **289**, 155.

[25] T. Nylander, C. Mattisson, V. Razumas, Y. Miezis and B. Hkansson, *Colloid Surf. A*, 1996, **114**, 311.

[26] J. Kostela, M. Elmgren and M. Almgren, *Electrochim. Acta*, 2005, **50(16-17)**, 3333.

[27] J. Kostela, M. Elmgren, M. Kadi and M. Almgren, *J. Phys. Chem. B*, 2005, **109**, 5073.

[28] V. Ganesh and V. Lakshminarayanan, *J. Colloid Interface Sci.*, 2005, **2**, 22.

[29] K. Bayer, *J. Colloid Interface Sci.*, 1982, **86**, 73.

[30] M. Quan, D. Sanchez, M. F. Wasylkiw and D. K. Smith, *J. Am. Chem. Soc.*, 2007, **129**, 12847.

[31] A. D. Ryabov, A. Amon, R. K. Gorbatova, E. S. Ryabova and B. B. Gnedenko, *J. Phys. Chem.*, 1995, **99**, 14072.

[32] R. A. Mackay, S. A. Myers, L. Bodalbhai and A. B. Toth, *Anal. Chem.*, 1990, **62**, 1084.

[33] M. J. Weaver and F. C. Anson, *Inorg. Chem.*, 1976, **15**, 1871.

[34] A. J. Bard and L. R. Faulkner, *Electrochemical Methods Fundamentals and Applications*, John Wiley and Sons, Noida, 2nd edn., 2004.

[35] B. R. Eggins and J. Q. Chambers, *J. Electrochem. Soc. Electrochem. Sci.*, 1970, **117**, 186.

[36] K. Sasaki, T. Kashimura, M. Ohura, Y. Ohsaki and N. Ohta, *J. Electrochem. Soc.*, 1990, **137**, 2437.

[37] N. Gupta and H. Linschitz, *J. Am. Chem. Soc.*, 1997, **119**, 6384.

[38] M. Gomez, I. Gonzalez, F. J. Gonzalez, R. Vargas and J. Garza, *Electrochem. Commun.*, 2003, **5**, 12.

[39] M. Bauscher and W. Maentele, *J. Phys. Chem.*, 1992, **96**, 11101.

[40] V. Ganesh and V. Lakshminarayanan, *Langmuir*, 2006, **22**, 1561.

[41] R. Greef, R. Peat, L. M. Peter, D. Pletcher and J. Robinson, *Instrumental Methods in Electrochemistry*, Ellis Horwood Ltd., Chichester, Great Britain, 1990.

Chapter 3

Dispersion of Thiol Protected Gold Nanoparticles in Lyotropic Liquid Crystalline Phases

This chapter describes a novel method of dispersion of thiol-protected gold nanoparticles in two different lyotropic liquid crystalline phases *viz*, the columnar hexagonal phase (H1 phase) of Triton X-100/water system and the reverse columnar hexagonal phase (H2 phase) of AOT system. We find that the dispersion of the nanoparticles retains the mesophase structure with an increase in the liquid crystalline order in both the H1 and H2 phases. These types of dispersions of the nanoparticles in the liquid crystalline matrix are interesting as they possess an ordered structure of the liquid crystalline phase while retaining the unique properties of the nanomaterials. This chapter also discusses the results of the ionic conductivity studies of the H1 phase formed by Triton X-100/water system. Surprisingly the ionic conductivity values of these systems are very high even though the phase is formed by the nonionic surfactant, Triton X-100. We find that the addition of gold nanoparticles increases the liquid crystalline order and also the ionic conductivity of the medium. On the other hand, the addition of chaotropic agents like urea results in a decrease in the ionic conductivity values. Based on these observations, the very high ionic conductivity of these systems could be explained on the basis of Grotthus mechanism, which rely on the proton transfer pathways by the water clusters. Hence the conductivity of these systems resembles the proton

conductivity in proteins as the same mechanism takes place in both the systems.

3.1 Introduction

The lyotropic liquid crystalline phases possess potential applications in both fundamental research and in the technology [1]. These lyotropic phases are also important due to their resemblance to biological systems as many of the proteins have been shown to form such ordered phases in the aqueous medium. For example, the lipids are known to form lamellar phase by forming the bilayer structure in the biological environment as well as in aqueous solutions. The lyotropic liquid crystalline phases formed by nonionic surfactants are of special interest as they do not contain any ionic species in the phase. Due to this, the interference of ions including the counter ions of the surfactants can be avoided. The nonionic surfactant Triton X-100 in the aqueous medium has been shown to form a hexagonal columnar phase and a lamellar phase [2]. A detailed investigation of the columnar phase (H1 phase) of the system was studied by Ahir *et al.* using a variety of experimental techniques [3]. Galatanu *et al.* have studied the phase diagram of the ternary system containing polyacrylic acid (PAA), Triton X-100 and water. They have shown that the PAA changes the melting point of the liquid crystalline phases of the Triton X-100/water system without changing the columnar hexagonal order where the polyacrylic acid interacts with the polyethoxy chain of Triton X-100 molecules [4].

The columnar hexagonal phase (H1 phase) of this system has been used as a medium for different applications. Nickel deposits formed in this medium with the addition of nickel salts were found to be highly porous and explored for the supercapacitor applications [5]. This H1 phase has also been explored for the formation of self-assembled monolayers of organic thiols on the gold surface and the results have shown that such monolayers are more compact compared to the monolayers formed through typical solutions [6]. The dispersion of carbon nanotube in the H1 phase has been reported by Regev *et al.* where they have shown that single walled carbon nanotubes can be well dispersed in the medium without altering the liquid crystalline order [7]. In the present chapter, we describe our experimental results on the dispersion of thiol-protected gold nanoparticles in the H1 phase. The chapter also describes the ionic conductivity studies in this medium. The effect of addition of gold

nanoparticles and urea on the ionic conductivity is also described in this chapter.

3.2 Dispersion of GNPs in the liquid crystalline phase

Integration of nanoparticles with liquid crystals is of interest for the past several years. Lee *et al.* have reported the synthesis of silver nanoparticles in the H1 phase of Triton X-100/water system [8]. In their studies, the Triton X-100 acts as a reducing agent while the columnar phase has controlled the growth and aggregation of the silver nanoparticles. They have shown that the growth of these nanoparticles has not altered the columnar structure of the Triton X-100/water system. Triton X-100 molecules are also shown to be capable of reducing palladium ions to Pd nanoparticles [9]. Wang *et al.* have reported the synthesis of nano and micro plates of gold with triangular or hexagonal shape by the reduction of chloroauric acid in the liquid crystalline phase formed by polyethoxy-polypropyloxy-polyethoxy block copolymers where the oxyethylene groups act as the reducing agents for Au(III) ions [10]. Gascon *et al.* have reported the synthesis of narrow-dispersed gold nanoparticles in the smectic phase than in the isotropic phase [11]. The preparation of gold fractal structures in the lamellar phase has also been reported in the literature [12]. It was shown that the gold nanoparticles form inside the multilamellar vesicles and the relationship between the lamellar arrangement and the nanoparticle size has been studied [13]. The synthesis of micron size gold nanoplates and nanobelts in a lyotropic liquid crystalline phase made up of block copolymers has also been demonstrated previously [14].

Dispersion of nanomaterials in liquid crystalline systems provides several advantages due to the unique properties of these nanomaterials and the self-organised structure of the liquid crystalline phases. There are several reports on the synthesis of nanoparticles in the presence of surfactants and micelles. Herrera *et al.* have prepared the nanoparticles using surfactants in a reverse micelle [15], while Jana *et al.* have studied the gold nanoparticles that are covered with CTAB molecules [16]. Ghosh *et al.* have reported Triton X-100 as stabiliser for gold nanoparticles [17]. The synthesis and stabilisation of nanoparticles by AOT and its incorporation into the reverse micelles of AOT have also been reported [18, 19].

The gold nanoparticles in an aqueous micellar medium provide potential applications for both drug delivery as well as immunoassay studies. Here, we describe our studies on the in-

tegration of hexanethiol and cyanobiphenylthiol (10CB-thiol)- protected gold nanoparticles in highly ordered lyotropic hexagonal columnar liquid crystalline systems. The hexagonal columnar phase was made either by a Triton X-100/water system or by a pure AOT system. While Triton X-100/water system has a normal hexagonal columnar structure (H1 phase), AOT exhibits a reverse hexagonal columnar liquid crystalline phase (H2 phase) [20, 21, 22, 23, 24]. The dispersions were characterised using polarising optical microscopy (POM) and small-angle X-ray scattering (SAXS) studies.

3.2.1 Experimental Procedures

Chemicals: Triton X-100 (Spectrochem), $HAuCl_4.3H_2O$ (Aldrich), $NaBH_4$ (Aldrich), hexanethiol (Aldrich), tetraoctylammonium bromide (Aldrich), AOT (sodium (2-ethylhexyl) sulfosuccinate) (SD fine Chem. Ltd), and toluene (Aldrich) were used as received. 10CB Thiol (4′-[10-sulfanyldecyl)oxy][1,1′-biphenyl]-4-carbonitrile) was synthesised by S. Kumar *et al.* as reported earlier [25]. Millipore water of resistivity 18 MΩ.cm was used for the preparation of all the samples.

Gold nanoparticle Preparation: Gold nanoparticles (GNPs) covered with hexanethiolate monolayer were synthesised by S. Kumar *et al.* [26, 27] by following the literature method [28, 29]. In brief, a solution of tetraoctylammonium bromide (1.1 g) in toluene (65 mL) was added with stirring to a solution of 158 mg of $HAuCl_4.3H_2O$. This solution was stirred for 20 min and mixed with n-hexanethiol (142 mg) with further stirring for 10 min. A solution of 450 mg of $NaBH_4$ dissolved in 5 mL of water was added to the above mixture. The reaction mixture was stirred at room temperature for 24 h. The organic phase was separated, evaporated to about 2-3 mL in a rotary evaporator under vacuum at room temperature, mixed with 50 mL of ethanol and centrifuged at 5000 rpm for 1 h. The supernatant liquid was removed and the resulting hexanethiol-protected gold nanoparticles were dissolved in about 1 mL of dichloromethane and precipitated with ethanol. The centrifugation and re-dispersal process was repeated several times to ensure the complete removal of noncovalently bound organic material. Removal of the solvent afforded 60 mg of hexanethiol-capped gold nanoparticles (C_6GNP). It has been shown that this procedure results in the formation of GNPs with an average composition of $Au_{140}[S(CH_2)_5\text{-}CH_3]_{53}$ [29]. The 10CB-thiol stabilised gold nanopar-

ticles (10CB-GNP) were prepared by following a similar procedure.

Preparation of GNP Dispersions: The lyotropic hexagonal columnar liquid crystalline phase (H1 phase) was prepared with a composition of 42 wt% Triton X-100 and 58 wt% water as described in chapter 2, by following the procedure reported earlier [6, 30]. A total of 2 mL of this mixture was heated to about 35 °C to the isotropic phase, and 12 mg of the hexanethiol functionalised GNPs were dispersed in this medium. This was followed by ultrasonication for 10 min and was allowed to cool down to 25 °C. Two more samples with compositions of 2.4 mg of GNP/2 mL of H1 phase and 1 mg of GNP/2 mL of H1 phase were prepared following the same process. For 10CB-thiolated GNP, two samples of compositions of 1 mg of GNP/2 mL of H1 phase and 0.5 mg of GNP/2 mL of H1 phase were prepared by the same procedure. The samples were homogeneous in nature, indicating that the GNPs are well-dispersed in the H1 phase and found to be stable for several days. For the preparation of GNP dispersions in AOT, 1 mg of the nanoparticles was mixed with 2 g of pure AOT, that was dissolved in diethyl ether. This solution was mixed well, and the solvent was evaporated to obtain the GNP dispersion in AOT. A picture of these dispersion are shown in Figure 3.1.

Characterisation: Scanning tunneling microscopic images were taken using an STM that has been fabricated in our laboratory. The nanoparticles were dispersed over an ITO coated glass plate. The scanning was carried out under constant current mode with a bias voltage of +100 mV and a reference current of 1 nA. Electrochemically etched tungsten wire was used as the tip for scanning. The images were analysed using Scanning Probe Image Processor software (SPIP, Image Metrology, Denmark). The polarising optical microscopic studies of the samples were carried out using an Olympus POM instrument. The textures were taken by sandwiching the samples between glass slides and cover slips. In the Triton X-100/water system, the samples were heated to the isotropic temperature and the images were obtained while cooling. For the AOT samples, the textures were taken at room temperature. The small-angle X-ray scattering studies were carried out using an X-ray diffractometer (Rigaku, UltraX 18) operating at 50 kV and 80 mA using Cu Kα radiation having a wavelength of 1.54 Å. Samples were prepared by filling the capillary with the liquid crystal or the GNP dispersion and sealed. All the scattering studies were carried out at room temperature.

Figure 3.1: A photograph of the dispersions of hexanethiol protected GNPs in a) H1 phase of Triton X-100/water system and b) H2 phase of AOT

3.2.2 Results and Discussion

3.2.2.1 Dispersion of GNPs in Triton X-100/Water System

From the STM studies, as shown in Figure 3.2, the size of hexanethiol capped gold nanoparticles was measured to be about 3.6 nm. This measured size includes the nanoparticle core and the hexanethiol molecules around the core that are used to stabilise the nanoparticles.

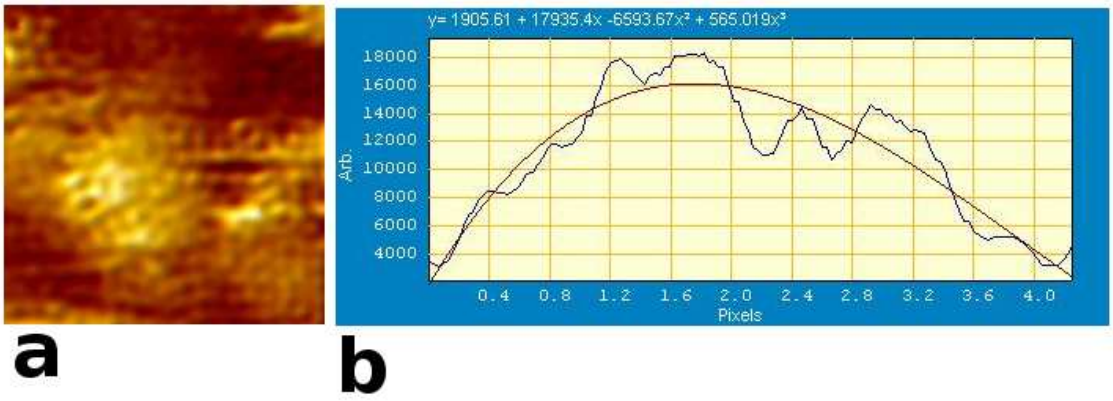

Figure 3.2: a) Scanning tunneling microscopic image of the hexanethiol capped gold nanoparticle and b) line profile for the image

Figure 3.3(a) shows the texture of pure H1 phase formed by the Triton X-100/water

system. Figure 3.3(b) and 3.3(c) show the textures obtained for the dispersions containing 1 mg of GNP/2 mL of Triton X-100/water system for the hexanethiolated and 10CB-thiolated GNPs, respectively. All these dispersions show the typical texture of H1 phase, which were stable down to room temperature. These images indicate that the H1 phase is retained in all these samples. We have observed that the temperature corresponding to the isotropic to columnar phase transition varies with the GNP concentration in these dispersions. The transition temperature of pure H1 system is 29 °C, while for the sample containing 1 mg of C6-GNP/2 mL of H1 phase, the transition temperature has shifted to 33.1 °C. This increase in the transition temperature clearly shows that the nanoparticles stabilise the H1 phase of the Triton X-100/water system. But at higher concentrations of GNPs, the transition temperature again decreases (32.9 °C for 2.4 mg of GNP/2 mL of H1 phase and 31.9 °C for 12 mg of GNP/2 mL of H1 phase), which may be attributed to the beginning of the phase separation. For the 10CB-thiolated GNPs, the transition temperature is 33.1 °C for the concentration of 0.5 mg of GNP/2 mL of H1 phase and 33.6 °C at the concentration of 1 mg of GNP/2 mL of H1 phase.

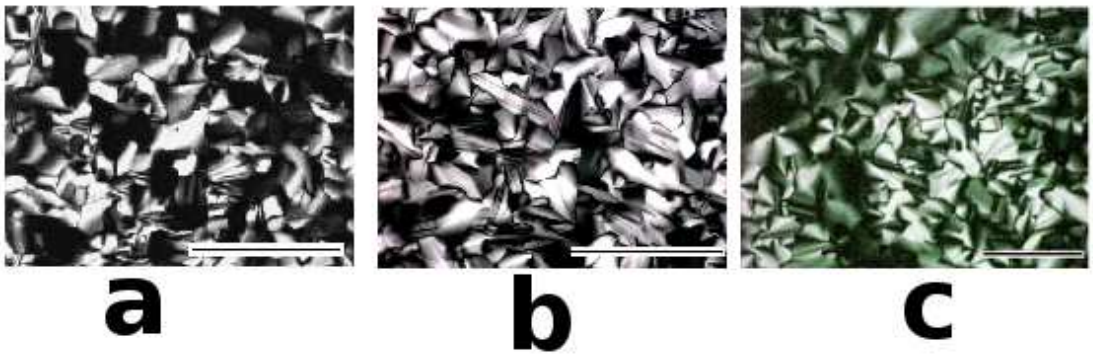

Figure 3.3: Polarising optical micrographic textures obtained for a) pure H1 phase of Triton X-100/water system, b) C_6GNP/H1 phase and c) 10CB-GNP/H1 phase. Scale bar=100 μm

For a better understanding of the liquid crystalline phase of the dispersions, we have carried out the small angle X-ray scattering (SAXS) studies of the pure and the GNP dispersed Triton X-100/water systems. Figure 3.4 shows the intensity vs. scattering vector q for the different samples. It is observed that the peaks in Figure 3.4 follow the ratio $1:\sqrt{3}:\sqrt{4}:\sqrt{7}$. This indicates that the columnar hexagonal order with P6mm space group exists in the pure Triton X-100/water system as well as in the dispersions [31]. This is in agreement with the

POM results described above. From the scattering vector, we have calculated the *d* spacing for all the samples and are presented in Table 3.1, where the different peaks corresponds to (1,0), (1,1), (2,0), and (2,1) scattering planes in the phase. We have calculated the lattice parameters from the peak corresponding to the (1,0) plane using the equation [32]

$$a = \frac{2d}{\sqrt{3}}$$

The main scattering peak in the SAXS corresponds to a lattice parameter value of 60.66 Å, 60.01 Å and 61.60 Å for the pure H1 phase, C6-GNP-dispersed H1 phase, and 10CB-GNP-dispersed H1 phase, respectively.

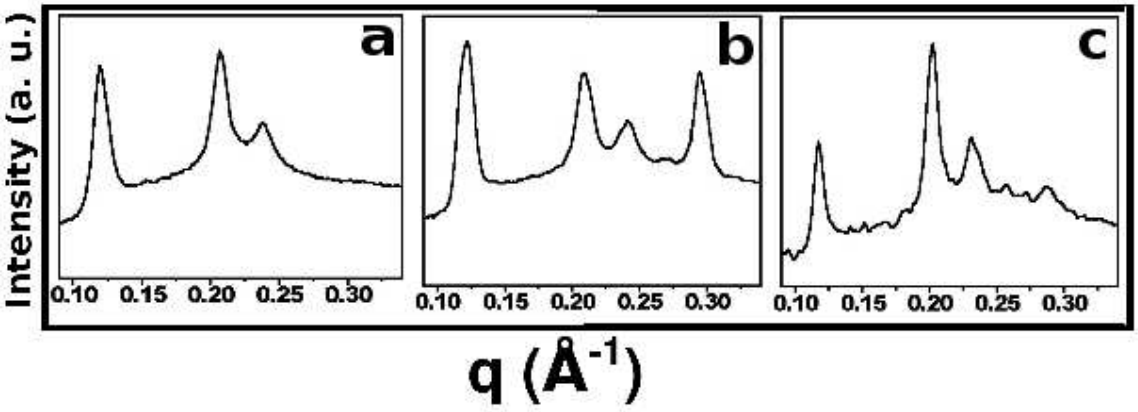

Figure 3.4: Scattering vector vs. intensity plots obtained from the SAXS for a) pure H1 phase of Triton X-100/water system, b) C6GNP/H1 phase and c) 10CB-GNP/H1 phase

Table 3.1: The *d* values in Å of the Triton X-100/Water system and 1 mg of GNP/2 mL of Triton X-100/Water system measured by SAXS studies at room temperature

	d_1	d_2	d_3	d_4
Pure H1 phase	52.54	30.42	26.29	-
C6-GNP/H1 phase	51.97	29.85	26.15	20.80
10CB-GNP/H1 phase	53.35	31.04	27.20	21.88

Since the change in the *d* values is small for the GNP-dispersed system compared to the pure H1 phase, it indicates that the dispersions do not significantly alter the columnar arrangement of the Triton X-100/water system in both the dispersions. Due to the large size

of the nanoparticles of about 3.6 nm, they can not be accommodated within the core of the micelles, but are present outside the boundaries of the columns and interdomain spacings. This observation is in agreement with the SAXS studies. If the gold nanoparticles have to reside inside the hydrophobic core of Triton X-100/water micelles, then the large size of the thiol stabilised GNPs would have severely distorted the hexagonal columns (about 5 nm). Such a distortion should have resulted in a large increase in the *d* spacing as measured by the SAXS studies. On the other hand, the GNPs will prefer the inter-domain spaces due to higher entropic gain instead of being confined inside the hydrophobic columns. The nanoparticles have sufficient space between the domain planes.

It is clear from the Figure 3.4 and the Table 3.1 that all the GNP-dispersed systems show the columnar hexagonal phase. The additional Bragg peak at the $\sqrt{7}$ position due to the (2,1) reflections shows that the H1 phase is more ordered within the core after the addition of GNPs. For the hexanethiol-GNP dispersed systems, the *d* values have decreased compared to the pure H1 phase. This can be explained on the basis of our proposed model of the dispersions. For the hexanethiol capped GNPs, the terminal groups are hydrophobic in nature, while for the micelles, the outer boundary is hydrophilic. As a result, for minimising the hydrophobic-hydrophilic interactions between the GNPs and the polar boundaries of the cylindrical micelles, the individual columns will tend to shrink, which results in the reduction of *d* values. On the other hand, we have observed a small increase in the *d* spacing for the 10CB-thiolated GNP dispersion. Here the interaction between the terminal polar cyano group of the nanoparticles and the water molecules on the micelle leads to a small expansion of the micellar core that leads to an increase in the *d* values.

Assuming a spherical shape, and the average size of these nanoparticles to be 4 nm with the molecular formula for the hexanethiol stabilised GNPs to be $Au_{140}[S(CH_2)_5CH_3]_{53}$ [28, 29], we have calculated the molar ratio and the volume fraction of these dispersions. We obtain a volume fraction of about 1:3300 for the GNP:H1 phase for the dispersion of 1 mg C6-GNP/H1 phase. This indicates that the number of GNPs in the dispersions is not significantly high to perturb the *d* spacing of the columns, which is in agreement with our POM and small-angle X-ray scattering studies.

3.2.2.2 Dispersion of GNPs in AOT

The dispersions of both hexanethiolated and 10CB-thiolated GNPs in the reverse hexagonal phase of AOT (H2 phase) have been prepared as described before in the experimental section. A picture of the dispersion is shown in Figure 3.1(b). Since the nanoparticles may not be stable up to the transition temperature of AOT (of about 180 °C), the polarising optical micrographic images were taken at room temperature without heating and subsequent cooling as is done in the case of H1 phase of Triton X-100/water system discussed earlier. Figure 3.5 presents the POM images obtained for the pure AOT and the dispersions. It is clear from the figure that the pure AOT forms a reverse hexagonal phase (H2 phase) and the dispersions have retained the H2 phase.

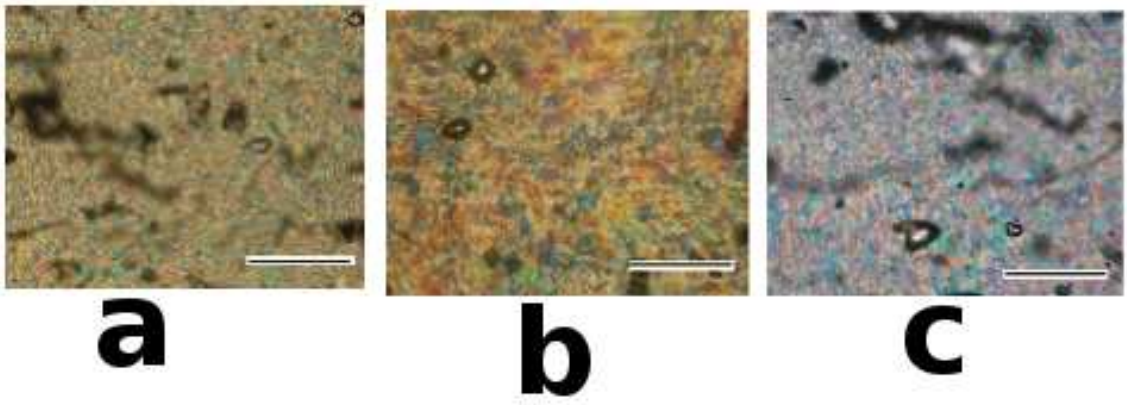

Figure 3.5: Polarising optical micrographic textures obtained for a) pure H1 phase of AOT, b) C6-GNP/AOT and c) 10CB-GNP/AOT. Scale bar=50 μm

We have carried out SAXS studies of the pure AOT as well as the GNP-dispersed AOT systems at room temperature. Figure 3.6 represents the diffraction patterns obtained for these samples, where the intensity is plotted against the scattering vector q. In the case of C6-GNP and 10CB-GNP-dispersed in AOT, the magnitude of the scattering vectors, q follows the ratio $1:\sqrt{3}:\sqrt{4}$ corresponding to the (1,0), (1,1), and (2,0) reflections from a 2-D hexagonal lattice indicating the retention of the H2 phase. The *d* spacings for these systems were calculated and are presented in Table 3.2. The lattice parameters were calculated to be 24.55, 26.67, and 26.11 Å for the pure H2 phase, C6-GNP-dispersed H2 phase, and 10CB-GNP-dispersed H2 phase, respectively, which belong to the P6mm space group. This fact

along with the POM textures discussed previously supports our conclusion that this system exhibits a reverse hexagonal columnar phase (H2) even after the incorporation of the gold nanoparticles.

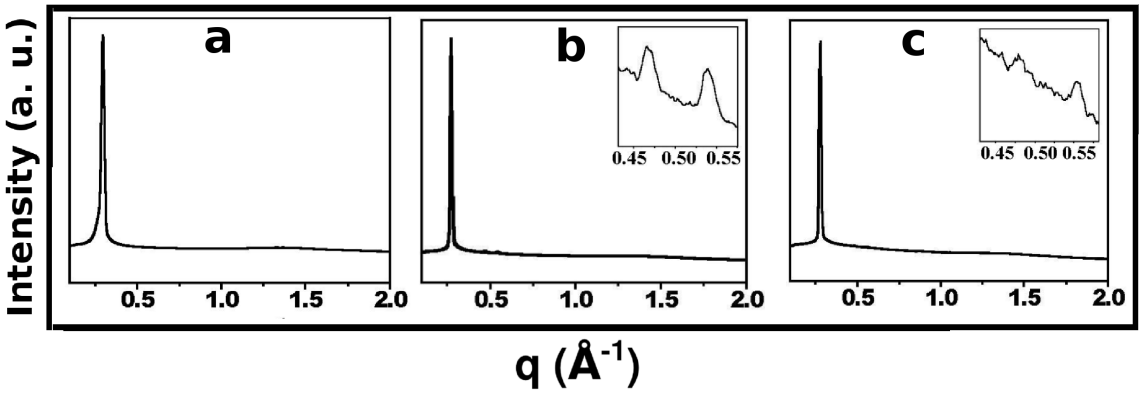

Figure 3.6: scattering vector vs. intensity plot obtained from the SAXS for a) pure AOT, b) C6-GNP/AOT and c) 10CB-GNP/AOT systems

Table 3.2: The *d* values in Å for the AOT system and 1 mg of GNP/AOT dispersion measured by SAXS at room temperature

	d_1	d_2	d_3
Pure AOT	21.26		
C6-GNP/AOT	23.1	13.33	11.61
10CB-GNP/AOT	22.61	13.01	11.33

The pure AOT shows only one peak while the dispersions show additional peaks in the ratio of of $1:\sqrt{3}:\sqrt{4}$. This indicates that the dispersions of GNPs enhance the liquid crystalline order of the AOT system. The *d* spacings of the dispersions have been observed to increase compared to the pure AOT system. The *d* value obtained for the pure AOT system is 21.26 Å which is in good agreement with the reported value in the literature [31, 33]. The addition of GNPs increased the *d* spacing for both the C6-GNP and the 10CB-GNP dispersions as seen in Table 3.2 and the maximum increase is observed in the C6-GNP dispersion where the *d* spacing is 23.10 Å. For the C6-GNPs due to the presence of the hydrophobic terminal groups, they can be accommodated within the hydrophobic surface of the reverse

hexagonal phase of AOT, which results in the increase in *d* spacing. For the 10CB-GNPs, there was a small increment in the *d* values to 22.61 Å.

Since the increment in *d* values is small, we conclude that the GNPs are present outside the columns of the H2 phase. Moreover, for the H2 phase, the outer surface of the columns is hydrophobic and the inner core is hydrophilic. The thiol stabilised GNPs being hydrophobic, will prefer to occupy the outer hydrophobic surface of the hexagonal columns. For the 10CB-thiolated nanoparticles due to its polar cyano group, the outer surface of these GNPs is less hydrophobic as compared to the C6-GNPs. This results in a weaker interaction between the terminal groups of GNPs and the outer surface of the H2 phase and a very small increment in the *d* values.

From the above studies, we have concluded that the nanoparticles are present outside the cylindrical micellar columns irrespective of the H1 or H2 phase used as the liquid crystalline medium. In the H1 phase, the GNPs prefer to stay outside the columns due to the freely available space between the columns which provides a net entropic gain. In the H2 phase the outer surface of the hexagonal columns are hydrophobic and this additional factor also prefer the nanoparticles to be present in the hydrophobic region. It is observed that in both the phases, the addition of GNPs has enhanced the hexagonal order of the liquid crystalline phase with additional Bragg peaks. These results indicate that the Triton X-100/water system and the AOT system provide a very good medium for the dispersion of nanoparticles which can be used as model systems for different applications.

3.3 Ionic conductivity studies of the H1 phase

Though the H1 phase of Triton X-100/water system is quite well known and its phase behaviour is well studied, there is little information on the ionic conductivity. For example, the ionic conductivity of many of the surfactant systems has been studied in the literature except for the nonionic surfactants which contain polyethoxy chains. Triton X-100 molecules have the polyethoxy chains, the groups that form part of conducting membranes and possess significant ionic conductivity.

The polyethoxy membranes are also finding importance in the proton exchange fuel cell devices as their ionic conductivity is quite high compared to other membranes. Eventhough

the polyethoxy chains can not form any self-organised structures in the aqueous medium like liquid crystals, their proton conductivity is very high in presence of other ions. A survey in the literature shows that the proton conducting nature of these chains have not been explored much.

This section describes our experimental results of ionic conductivity studies in the H1 phase of Triton X-100/water system, which show surprisingly high ionic conductivity. The effect of dispersion of different dopants is also discussed in the present section. The high ionic conductivity can be explained on the basis of Grotthus mechanism, which is based on the extended water chain network model. A similar mechanism has also been proposed to explain the high ionic conductivity of protein dispersions in aqueous solutions [34, 35, 36, 37] and for water inside the carbon nanotubes [38].

3.3.1 Experimental Section

Triton X-100 was obtained from Aldrich and was used as received. All the solutions were prepared using millipore water having a resistivity of 18 MΩ.cm. Urea was obtained from Rankem. The lyotropic hexagonal columnar liquid crystalline phase (H1 phase) was prepared following the method as described in the previous section that contains 42 weight% of Triton X-100 and 58 weight% of water. The dispersions of gold nanoparticles and urea were prepared using the same procedure as described in the previous section. The concentration of GNPs were restricted at low levels as at high concentration, due to the steric interactions, the phase was observed to be unstable. The ionic conductivity of these samples were measured while cooling from the isotropic phase using a lock-in-amplifier (Stanford Research Systems, model SR830). Two platinum foil electrodes in the parallel plate configuration were used as the electrodes for the conductivity measurements. A schematic representation of the measurement setup is depicted in Figure 3.7. The current across the resistor R was measured and from which the ionic conductivity of the H1 phase was calculated.

3.3.2 Results and discussion

Figure 3.8 shows the ionic conductivity of the H1 phase formed by the Triton X-100/water system as a function of frequency that was measured at room temperature. It can be noted that

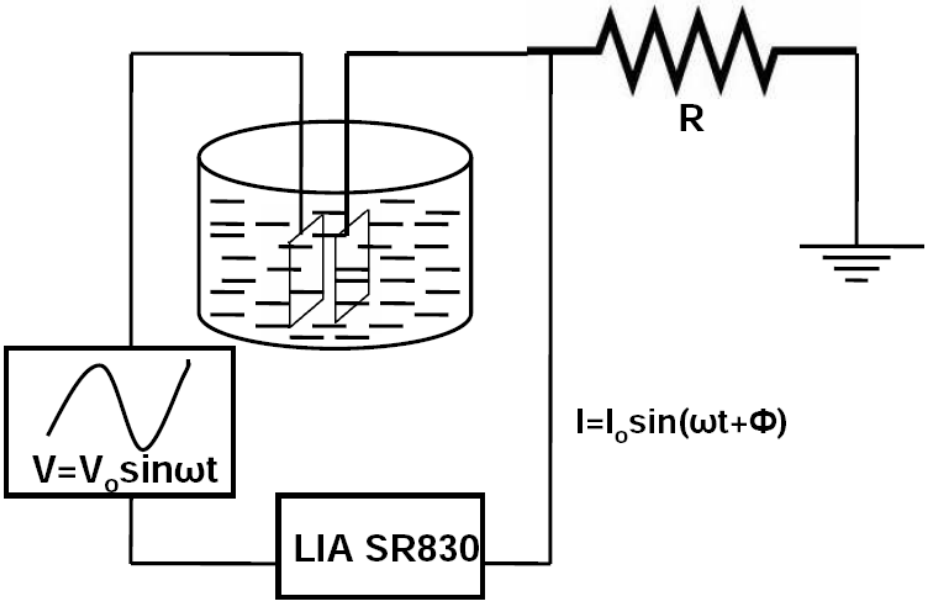

Figure 3.7: A schematic diagram showing the setup used for the measurement of ionic conductivity

the conductivity has a plateau region in the 500 Hz to 10 kHz. At higher frequencies, the ionic conductivity decreases significantly due to the slow relaxation effects. At frequencies below 500 Hz, there is a small decrease in the ionic conductivity. Based on these observations, we have measured the conductivity of these systems at a frequency of 2 kHz.

Figure 3.9 shows the ionic conductivity of the H1 phase as a function of temperature while cooling from the isotropic phase of the system. It is observed from the figure that the conductivity of the system is very high, of the order of several hundred μS/cm. This is contrary to the conductivity of pure water which is about 0.05 μS/cm. The phase transition from the H1 phase to the isotropic phase can be clearly observed in the conductivity vs. temperature plot of Figure 3.9 which occurs at 32 °C.

We have prepared aqueous solutions with different concentrations of Triton X-100, which is below the concentration corresponding to the formation of the liquid crystalline phase. The ionic conductivity of these samples are shown in Figure 3.10. It is observed that the ionic conductivity of these samples increases with the concentration of the surfactant. Since the pH of the solution is observed to be constant, the contribution from the dissolved CO_2 towards the conductivity can be ruled out. It also indicates the absence of any dissociation of the

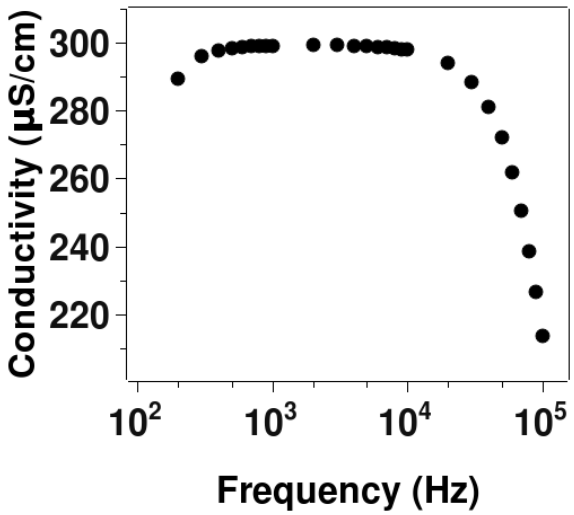

Figure 3.8: Ionic conductivity of the H1 phase of Triton X-100/water system as a function of frequency at room temperature

surfactants to form ionic species in the system, which in any case is not reasonable within the experimental conditions since it is a nonionic surfactant. These observations point to a different kind of mechanism, *ie* Grotthus mechanism which operates in these systems.

3.3.2.1 Grotthus Mechanism

The high ionic conductivity of water was first explained by Grotthus in the year 1806 [39]. According to the Grotthus mechanism, the proton conductivity arises due to the presence of different hydrated protons in the system. Among several solvated protons, the most prominent clusters are the hydronium ion H_3O^+, the Zundel cation, $H_5O_2^+$ and the Eigen cation $H_9O_4^+$. The H_3O^+ is just a protonated water molecule with pyramidal structure. Under normal conditions, one water molecule can form hydrogen bonds with 4 different water molecules, two using the hydrogen atoms and two using the oxygen atom. On the other hand, the H_3O^+ ion can form maximum three hydrogen bonds with other water molecules, two using the hydrogen atoms and one using the oxygen atom. In the Zundel cation, the proton is shared between two water molecules, while in the Eigen cation, three water molecules are present in the first solvation layer of the hydronium ion. Due to the presence of three solvated water molecules, the Eigen cation is more stable compared to the Zundel cation [40, 41, 42].

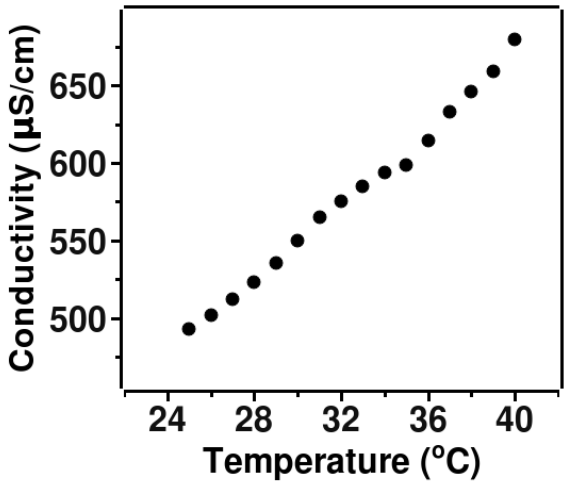

Figure 3.9: Ionic conductivity of the H1 phase of Triton X-100/water system as a function of temperature measured at different frequencies

The very high proton conductivity arises from the proton transport through these water clusters, *viz*, Zundel cations and Eigen cations. Eventhough different mechanisms have been proposed for the proton transfer pathways through these clusters, the most accepted mechanism is the E-Z-E pathway. Here, the proton transfer occurs from one oxygen atom to the other in an Eigen cation through the formation of an intermediate Zundel cation, as represented in Figure 3.11.

There are several speculations over the kinetics of the proton transfer mechanisms in these protonated water clusters. The rate limiting step in the proton transfer process may be either proton motion or the structural diffusion. Structural diffusion means the addition of water molecules to the solvation layer of the protonated clusters. Experimental results using deuterium showed that the isotropic effect is 1.4 instead of the expected value of 2 for the proton motion [40]. This indicates that the proton motion is not the rate limiting step. Since every water molecule can form 4 hydrogen bonds at a time as described above, the validity of structural diffusion process as the rate determining step may be ruled out. The NMR studies on proton hopping process indicate that the hydrogen-bond cleavage is the rate limiting step [43]. Moreover, the cleavage needs a reorientation of water molecules and under such a condition, the isotropic effect may be given by $\sqrt{m_D/m_H}$, where m_D is the atomic weight of deuterium (2) and m_H is atomic weight of hydrogen. This gives an isotropic effect value of $\sqrt{2}$ or 1.4, which is in agreement with the experimental results on the kinetics of the reaction

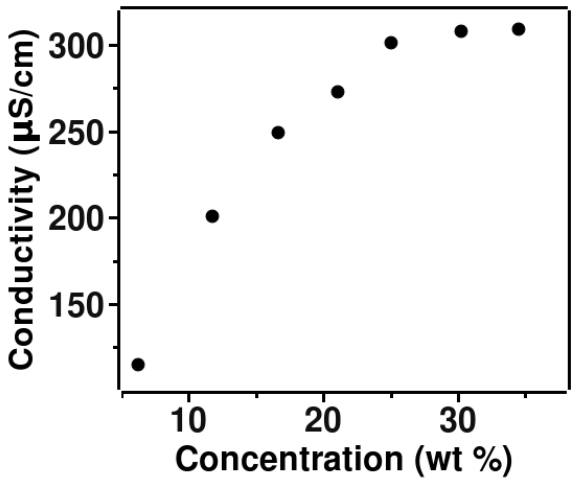

Figure 3.10: Ionic conductivity of the Triton X-100/water system as a function of the concentration of Triton X-100

[40].

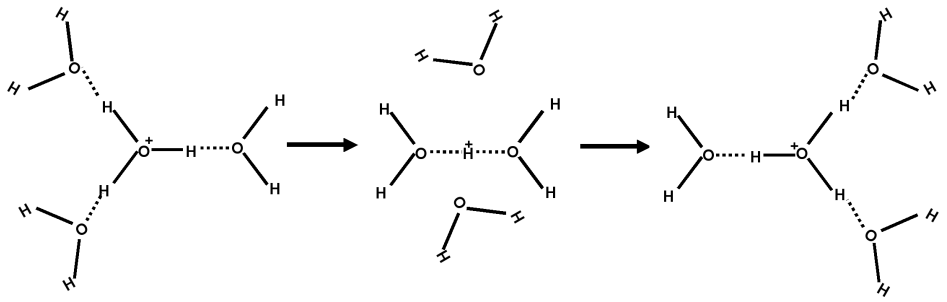

Figure 3.11: Schematic diagram of the proton transfer by Grotthus mechanism

In the liquid crystalline phase, due to the close packed arrangement of water molecules on the surface of the micelles, a well ordered network of hydrogen bonding water molecules is possible. This hydrogen bonding network provides a facile proton transfer pathway. Any release of free protons in the H1 phase is ruled out as the pH of the solution is constant irrespective of the concentration of the surfactant. The ionic conductivity shows a plateau at concentrations of Triton X-100 corresponding to the formation of columnar hexagonal phase as shown in Figure 3.10. This indicates the significant role of extended hydrogen-bond network in the ionic conductivity values. We have also observed that above this concentration, there is a very little increase in the conductivity with the increase in the concentration of the surfactant, which may be ascribed to the saturation of the hydrogen bonded network

formation.

The lyotropic columnar hexagonal liquid crystalline phase that is used in the present studies is formed by cylindrical micelles of Triton X-100 surfactant molecules in the aqueous medium. The surfactants are self-organised into the cylindrical micelles which are surrounded by water molecules. These water molecules, due to the hydrophilic-hydrophilic interactions with the polyethoxy chains, are strongly attached to the micelles. This is similar to the water molecules which are attached to the protein molecules in the biological systems. This provides a route for the formation of clusters of protonated water molecules like hydronium, Zundel and Eigen cations. The existence of similar water clusters has been proposed in a variety of systems like water inside carbon nanotubes and on the protein surface. Since these protonated water clusters are in close vicinity to each other on the micellar surface, proton transfer between these clusters are facile and hence the ionic conductivity increases. It has been proposed in the literature that such water clusters facilitate the transport of protons through the water-chains by Grotthus mechanism [34, 35, 36, 37].

For verifying the role of these cationic clusters in the ionic conductivity, we have measured the ionic conductivity of the H1 phase at different concentrations of urea. Urea is a well known reagent for the denaturation of protein systems by the distruction of hydrogen bonding network [44, 45]. Such materials are commonly known as chaotropic reagents. Similar effect of disruption of hydrogen bonded water network formed in the PEO chains is expected in the addition of urea. Figure 3.12 shows the ionic conductivity as a function of temperature for the different concentrations of urea. It is observed that the conductivity decreases as the concentration of urea increases. This indicates that the addition of urea disrupts the hydrogen-bonded networks, which is responsible for the decrease in the ionic conductivity. At lower concentrations of urea there is a negligible decrease in the conductivity while above 5 M concentration, it decreases drastically. It has been shown that 8 M urea is sufficient to denature proteins in aqueous solutions [45]. Our results are in agreement with these reports.

We have also studied the effect of addition of gold nanoparticles in the ionic conductivity of the H1 phase. Figure 3.13 shows the ionic conductivity as a function of temperature for the H1 phase of Triton X-100/water system before and after GNP dispersion. It is clear from the figure that the ionic conductivity has increased after GNP dispersion. The hexanethiolated gold nanoparticles have hydrophobic terminal groups, which are present in between

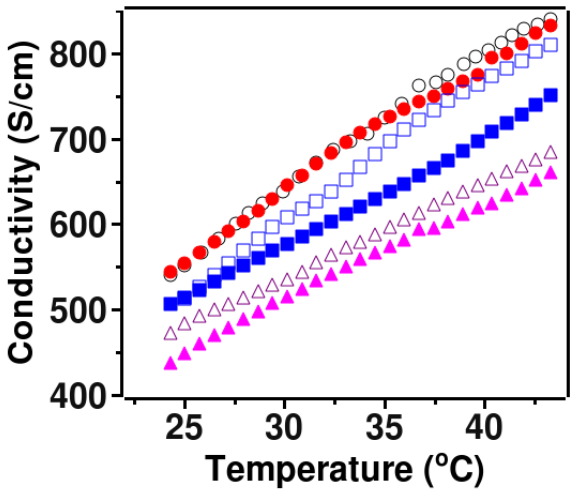

Figure 3.12: Ionic conductivity of the H1 phase as a function of temperature for Triton X-100/water system dispersed with different concentrations of urea, ○ (0 M), ● (0.5 M), □ (1 M), ■ (5 M), △ (8 M) and ▲ (9 M)

the columns and domain spaces as described in the previous section. As a result of this, the water molecules are aggregated more strongly to the micellar surface, which improves the hydrogen-bonded network and the ionic conductivity. This is in agreement with the SAXS studies described in the previous section, where we have shown that the *d* spacing of the GNP dispersed H1 phase is decreased compared to the pure H1 phase, which indicates a stronger water aggregation on the cylindrical micellar surface formed by the Triton X-100 surfactant.

The H1 phase provides a simple model for studying the behaviour of water clusters in different systems like on the protein surfaces. As described in chapter 2, the redox probes like ferrocyanide/ferricyanide and hexaammineruthenium molecules are less hydrated in the H1 phase as compared to the aqueous medium. These results are in agreement with the present model, as most of the water molecules are attached to the micellar surface, that leads to a higher ionic conductivity. As the concentration of the chaotropic agent increases, the hydrogen bonding network disrupts resulting in the lowering of proton conductivity, while addition of gold nanoparticles increases the hydrogen-bonded network and the ionic conductivity.

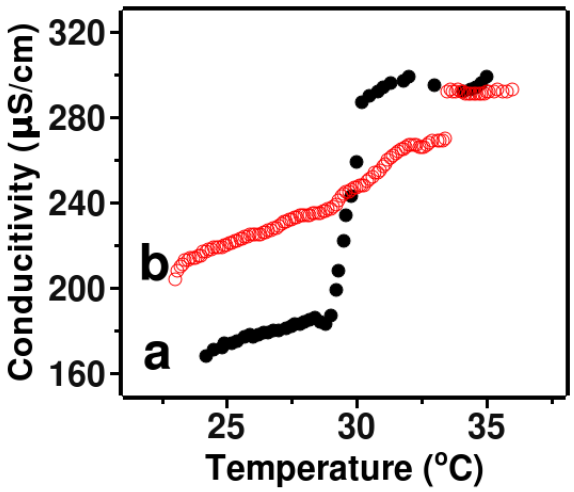

Figure 3.13: Ionic conductivity of a) the H1 phase of Triton X-100/water system and b) H1 phase dispersed with 1 mg hexanethiolated GNPs in 2 ml of Triton X-100/water system

3.4 Conclusion

The dispersion of thiol-protected gold nanoparticles in two columnar hexagonal systems are studied. The results show that the addition of nanoparticles at lower concentrations have retained the liquid crystalline phase, with an enhancement in the order within the phase. The SAXS studies show that the nanoparticles occupy the inter-domain space rather than inside the core of the cylindrical micelles.

From the conductivity studies of the H1 phase of the pure Triton X-100/water system and the dispersions, it is proposed that the system contains the protonated water clusters which are responsible for the high ionic conductivity. Proton conductivity is a complex process and clearly there are several issues which have to be addressed in order to fully understand the phenomenon of ionic conductivity in the liquid crystalline phase formed by nonionic surfactants. For example, a detailed study is necessary for establishing the different hydronium ions present in the system. This simple system may be used as a model system for the study of the proton transfer reaction mechanism and the structure of water on the protein surfaces.

Bibliography

[1] Goodby, *Handbook of Liquid Crystals*, John Wiley & Sons, London, 2nd edn., 2004.

[2] K. J. Bayer, *J. Colloid Interface Sci.*, 1982, **86**, 73.

[3] S. V. Ahir, P. G. Petrov and E. M. Terentjev, *Langmuir*, 2002, **18**, 9140.

[4] A. N. Galatanu, I. S. Chronakis, D. F. Anghel and A. Khan, *Langmuir*, 2000, **16**, 4922.

[5] V. Ganesh and V. Lakshminarayanan, *J. Colloid Interface Sci.*, 2005, **2**, 22.

[6] V. Ganesh and V. Lakshminarayanan, *Langmuir*, 2006, **22**, 1561.

[7] O. Regev and Thiruvenkadanathan, *Langmuir*, 2006, **22**, 2335.

[8] M.-H. Lee, S.-G. Oh, K.-D. Suh, D.-G. Kim and D. Sohn, *Colloid Surf. A*, 2002, **210**, 49.

[9] S. Nath, S. Praharaj, S. panigrahi, S. Basu and T. Pal, *Current Sci.*, 2007, **92**, 786.

[10] L. Wang, X. Chen, J. Zhan, Y. Chai, C. Yang, L. Xu, W. Zhuang and B. Jing, *J. Phys. Chem. B*, 2005, **109**, 3189.

[11] I. Gascon, J.-D. Marty, T. Gharsa and C. Mingotaud, *Chem. Mater.*, 2005, **17**, 5228.

[12] M.-E. Meyre, O. Lambert and C. Faure, *J. Mater. Chem.*, 2006, **16**, 3552.

[13] M.-E. Meyre, O. Lambert, B. Desbat and C. Faure, *Nanotechnol.*, 2006, **17**, 1193.

[14] L. Y. Wang, X. Chen, Y. C. Chai and J. C. Hao, *Colloids Surf. A*, 2007, **293**, 95.

[15] A. P. Herrera, O. Resto, J. G. Briano and C. Rinaldi, *Nanotechnology*, 2005, **16**, S618.

[16] N. R. Jana, L. A. Gearheart, S. O. OBare, C. J. Johnson, K. J. Edler, S. Mann and C. J. Murphy, *J. Mater. Chem.*, 2002, **12**, 2909.

[17] S. K. Ghosh, N. Sharma, M. Mandal, S. Kundu, K. Esumi and T. Pal, *Curr. Sci.*, 2003, **84**, 791.

[18] A. Longo, P. Calandra, M. P. Casaletto, C. Giordano, A. M. Venezia and V. T. Liveri, *Mater. Chem. Phys.*, 2006, **96**, 66.

[19] P. Calandra, C. Giordano, A. Longo and V. T. Liveri, *Mater. Chem. Phys.*, 2006, **98**, 494.

[20] J. Rogers and P. A. Winsor, *Nature*, 1967, **216**, 477.

[21] P. A. Winsor, *1968*, Chem. Rev., **68**, 1.

[22] K. Fontell, *1973*, J. Colloid Interface Sci., **44**, 318.

[23] L. Coppola, R. Muzzalupo, G. A. Ranieri and M. Terenzi, *Langmuir*, 1995, **11**, 1116.

[24] P. G. Petrov, S. V. Ahir and E. M. Terentjev, *Langmuir*, 2002, **18**, 9133.

[25] S. Kumar and S. K. Pal, *Liq. Cryst.*, 2005, **32**, 659.

[26] S. Kumar and V. Lakshminarayanan, *Chem. Commun.*, 2004, 1600.

[27] S. Kumar, S. K. Pal and V. Lakshminarayanan, *Mol. Cryst. Liq. Cryst.*, 2005, **434**, 251.

[28] M. Brust, M. Walker, D. Bethell, D. J. Schriffin and R. Whyman, *J. Chem. Soc. Chem. Commun.*, 1994, 801.

[29] Y. Song, T. Huang and R. W. Murray, *J. Am. Chem. Soc.*, 2003, **125**, 11694.

[30] V. Ganesh and V. Lakshminarayanan, *Electrochim. Acta*, 2004, **49**, 3561.

[31] S. T. Hyde, *Handbook of Applied Surface and Colloid Chemistry*, John Wiley & Sons Ltd., 2001.

[32] C. W. Bunn, *Chemical Crystallography An Introduction to Optical and X-ray Methods*, Clarendon Press, Oxford, 2nd edn., 1961.

[33] A. Ruggirellow and V. T. Liveri, *Chem. Phys.*, 2003, **288**, 187.

[34] B. Gabriel and J. Teissie, *Proc. Nat. Acad. Sci.*, 1996, **93**, 14521.

[35] R. Pomes and B. Roux, *Biophys. J.*, 1998, **75**, 33.

[36] R. M. Venable and R. W. Pastor, *J. Chem. Phys.*, 2002, **116**, 2663.

[37] O. Vendrell and H.-D. Meyer, *J. Chem. Phys.*, 2005, **122**, 104505.

[38] F. Zhu and K. Schulten, *Biophys. J.*, 2003, **85**, 236.

[39] C. J. D. Grotthuss, *Ann. Chim.*, 1806, **LVIII**, 54.

[40] N. Agmon, *Chem. Phys. Lett.*, 1995, **244**, 456.

[41] G. Corongiu, R. Kelterbaum and E. Kochanski, *J. Phys. Chem.*, 1995, **99**, 8038.

[42] J. T. Hynes, *Nature*, 1999, **397**, 565.

[43] S. Meiboom, *J. Chem. Phys.*, 1961, **34**, 375.

[44] G. Barone and C. Giancola, *Pure Appl. Chem.*, 1990, **62**, 57.

[45] B. J. Bennion and V. Daggett, *Proc. Nat. Acad. Sci.*, 2003, **100**, 5142.

Chapter 4

Electrical Conductivity Studies on the Discotic Liquid Crystals and its Composites

Liquid crystals, as mentioned earlier, are the intermediate phases between the crystalline and liquid phases. They have the orientational order of crystalline phases and the dynamic nature of liquid phases. The different properties of these phases have already been discussed in the chapter 1. The present chapter deals with the electrical conductivity studies on the thermotropic columnar liquid crystalline phases formed by triphenylene based discotic molecules and some of its composites. The discotic composites are prepared using two different acceptor systems, ferrocenium tetrafluoroborate and chloroauric acid. The composites were characterised using different techniques like POM, DSC, SAXS, spectral studies and cyclic voltammetry. The electrical conductivity of these composites were observed to be enhanced by several orders of magnitude compared to the pure discotic systems. The electrical conductivity studies of a series of pyridinium tethered triphenylene derivatives which form ionic liquid crystals are also part of this chapter.

4.1 Introduction

Columnar liquid crystalline phases are formed by the aggregation of disc like molecules which stack one over the other to form columns [1]. These columns can aggregate to form different phases like columnar rectangular, columnar hexagonal, columnar plastic and columnar oblique phases. Typically, these molecules consist of an aromatic core and flexible aliphatic chains. Several cores have been used for the synthesis of discotic molecules. The different strategies involved in the synthesis of molecules possessing columnar phases have been reviewed recently [2]. Some of the most studied electron rich discotic cores are benzene, naphthalene, anthracene, triphenylene, hexabenzocoronene and phthalocyanine. A typical electron deficient core is that of anthraquinone. Due to the strong π-π interaction between the cores, the typical core-core distance in the columnar phase is $\sim$0.35 nm. The column-column distance may be $\sim$2-4 nm depending on the length of the aliphatic substitution on the core groups. These alkyl chains should be of sufficient length in order to provide necessary flexibility for the discotic molecules to form columnar phases.

Due to the strong core-core and weak column-column interactions, the discotic molecules show a quasi-one-dimensional behaviour in the electrical conductivity. This one-dimensional conductivity has been suggested to be important for a variety of applications in the areas including solar cells [3], molecular electronics [4], photovoltaic cells [5], organic light emitting diodes (OLED) [6] and field effect transistors (FET) [7]. The efficiency of such devices depends on the band gap of the materials, which is typically about 4 eV for the discotic liquid crystals. This high band gap of the discotic molecules makes them behave as insulators under normal conditions. On the other hand, they show semiconducting behaviour on doping with either electron rich or electron deficient molecules into the supramolecular order of the liquid crystalline phase. The important point to be noted here is that the concentration of the dopant is critical in order that the liquid crystalline phase is not disrupted. At the same time, the amount of dopants should be sufficient enough to introduce electrons or holes into the liquid crystalline medium to increase the conductivity.

The conductivity of the pure discotic systems have been studied by several groups. Triphenylene, hexabenzocoronene and phthalocyanine based columnar phases are the most studied systems. Either the conductivity (σ) or the related charge carrier mobility ($\mu = \sigma/ne$) were

measured using different methods for these systems. For the measurement of mobility, two methods have been widely used in the literature. The first method is based on the time of flight (TOF) experiments [8, 9], while the second method is based on the pulse radiolysis-time resolved microwave conductivity (PR-TRMC) method [10, 11]. In the TOF method, the time taken by the excited charge carriers to travel a known distance is measured, from which the mobility is calculated using the following equation

$$\mu = \frac{d}{t_T F}$$

where d is the distance between the two electrodes and F is the applied electric field. The transit time t_T can be obtained at the intersection of the two tangents for the two relaxation processes in the current-time profile from the TOF experiment [9]. In the PR-TRMC method, a microwave radiation of particular power is irradiated on the sample, which generates charge carriers and hence the conductivity of the sample increases. The current response of the cell is measured as a function of time and from these values the mobility of the charge carries can be estimated [10]. TOF measures the long-range mobility of the sample which means that the mobility is averaged out over a large distance between the two electrodes which may be several microns, in a millisecond to microsecond time scale. On the other hand, the PR-TRMC measures the mobility over a small distance of the order of thickness of a few molecules in a time period of a few nanoseconds. Two points may be noted here. Due to the small distance involved, mobility values from PR-TRMC are more fundamental while TOF gives the bulk charge-carrier mobility. Secondly, due to the larger distance involved, the mobility obtained from TOF will be smaller than the values from PR-TRMC. This is due to the fact that the bulk of the sample will be disordered with multidomains and un-aligned columns that results in defect structures which will contribute to scattering of charge carriers. Therefore the defect contributions to the TOF experimental values is quite significant, while for the PR-TRMC the contributions from these defects will be less [12].

In our work, we have focused on the electrical conductivity measurements, which is related to charge carrier mobility by the formula $\sigma = ne\mu$ where σ is the conductivity, n is the charge carrier density, e is the charge of electrons and μ is the mobility of the charge carriers. The electrical conductivity studies provide information on the effect of doping in the transport properties of charge carriers. As a result of the very high band gap, the discotic

materials have very low electrical conductivity of the order of 10^{-12} S/m along the column and 10^{-15} S/m perpendicular to the column. One route to enhance the conductivity of these supramolecular systems is the addition of a small quantity of either electron donors or electron acceptors. This doping can introduce electrons or holes into the discotic matrix and as a result, the conductivity can be enhanced by several orders of magnitude. Trinitrofluorenone, TNF[13, 14], iodine[15], aluminium chloride, $AlCl_3$ [16, 17, 18], nitrosonium tetrafluoroborate, $NOBF_4$ [19] and gold nanoparticles [20, 21] are some of the most studied dopants in the columnar liquid crystalline matrix. These dopants at low concentrations retain the columnar phase with enhancement in the electrical conductivity by several orders of magnitude. For $AlCl_3$ and $NOBF_4$ doped systems, it has been shown that they form charge-transfer complexes with the discotic molecules. This results in the oxidation of the aromatic core of the discotic moiety with the formation of radical cations that enhances the electrical conductivity of the composites. For the $NOBF_4$ dopants, they may even intercalate within the column and can form a 1:1 complex [22]. These complexes have better liquid crystalline order compared to the pure systems, that results from the strong electron donor-acceptor interactions within the column due to the sandwich type structure. In other systems, the doping will increase the entropy of the system that reduces the temperature range of liquid crystalline phase and therefore at higher concentrations of the dopants, the liquid crystalline order collapses.

4.1.1 Mechanism of Electrical Conductivity

The quasi-one-dimensional conductivity on discotic liquid crystalline phases was first reported in 1985 using triphenylene based systems [23]. Further studies were carried out on several triphenylene derivatives and their composites, which indeed demonstrated that the conductivity of these supramolecular systems can be enhanced by several orders of magnitude [18, 24]. After this, a number of reports have appeared in the literature on the quasi-one-dimensional conductivity of the columnar phase formed by triphenylene, benzocoronene [25, 26, 27, 28, 29], phthalocyanine [12, 30] and perylene derivatives [31, 32, 33] either in their pure state or in the presence of dopants. In all these systems, it was shown that the electrical conductivity is very much higher in the columnar phase compared to the crystalline phase. In many systems, the low frequency ionic conductivity decreased again in

the isotropic phase. This clearly indicates that the conductivity in these systems is mainly governed by the columnar hexagonal arrangement of the disc-shaped molecules.

The ionic conductivity values are frequency dependent at higher frequency ranges, while being independent of frequency at lower frequency ranges. Boden *et al.* have shown that the conductivity at higher frequencies follows the form [16]

$$\sigma(\omega) = \sigma(0) + A\omega^{0.8}$$

The frequency independent part has been modelled by the Fickian diffusion, which is based on the concentration-independent Fick's law of diffusion, and can be expressed by the Nernst-Einstein equation given by [16]

$$\sigma(\omega) = \frac{ne^2}{kT} D(\omega)$$

where

$$D(\omega) = \frac{1}{2d} \Delta_{rms}^2 \lambda$$

with λ being the inverse of mean hopping time ($\lambda = 1/\bar{t}$) and Δ the mean hopping distance. This provides the frequency-independent conductivity at low frequencies where only the slowest motions, the non-localised or long-range hops, of the charge-carriers are dominated. In other words, the system is in the frozen state or the fully ordered state with single hopping rate between the sites. This diffusion was also observed to be independent of the carrier concentration [16].

Boden *et al.* have discussed the frequency dependency of the ionic conductivity in detail [16]. They have shown that the frequency independent conductivity observed at low frequencies originates from the charge-migration between the discotic columns of the domains, that are present due to the absence of perfect alignment of the columns. The frequency dependency of the conductivity arises from the following equation,

$$D(\omega) = \frac{\Delta_{rms}^2}{2d} \cdot \frac{i\omega(1 + i\omega/\lambda)^{-\nu-1}}{1 - (1 + i\omega/\lambda)^{-\nu-1}}$$

where Δ is the mean hopping distance, ν is an arbitrary parameter, d is the distance between neighbouring sites. Fitting of the experimental ionic conductivity data using this equation revealed the following points:

1) The frequency independent conductivity that dominates at low frequency region arises due

to the charge-migration between columns of different domains. Normally, these different domains are formed due to the imperfect alignment of the discotic columns.

2) The fitting parameters in the columnar hexagonal as well as in the isotropic phases are very close to each other, which indicates that the molecular stacks or the columns retain at least partially even in the isotropic phase.

3) For the frequency dependent conductivity at high frequencies, the best fitting value for ν is $\sim$0.8, which explains the $\omega^{0.8}$ dependency of the ionic conductivity at high frequencies. This is reported to be typical of hopping transitions with a distribution of hopping probabilities. For the columnar liquid crystalline systems, this originates from the disorder in the stacking of the disc-like molecules.

The conductivity of the system is related to the mobility (μ) of the charge-carriers by the relation $\sigma = ne\mu$, where n is the density of charge-carriers which can be estimated from the ESR measurements and e is the charge of electrons. The conductivity in the parallel and perpendicular directions are related to the mobility in the same manner [19]. The mean hopping time of charge-carriers within the column is related to the measured mobility by the equation

$$\tau = \frac{ed^2}{2kT\mu}$$

where d is the average separation between the aromatic cores within a column. For triphenylene derivatives, this corresponds to $\sim$0.35 nm.

The conductivity in the crystalline phase is very less, mainly due to the restricted charge-carrier migrations in the phase. The different carrier sites have frozen structure with defects. In the isotropic phase, the columns persist to some extent. The total hopping length is given by the length of the molecular stacks, which is $\sim$200 nm at a temperature close to the columnar-isotropic phase transition temperature. This length decreases as the temperature increases and the conductivity falls down. It may be noted however that close to the phase transition temperature, the conductivity may increase due to the facile temperature-dependent charge-carrier migration [16].

The conductivity perpendicular to the columns is more complex as the charge-carriers have to cross a longer distance. The typical core-core distance between adjacent columns in discotic systems is 2-4 nm and hence typical quantum-mechanical tunneling can not explain the observed conductivity. Inter-columnar charge-carrier transport at low temperatures may

take place through the defects or dislocations. At high temperature, the process may involve many-phonon assisted tunneling process [34]. Assuming the hopping rate is of the form

$$W_{\perp} \approx W_0 e^{-2\alpha\bar{R}}$$

where α is the inverse decay length of the wavefunction and $\bar{R} \approx 20$ Å is the column-column distance in the liquid crystalline phase for HAT6. Comparing this with the $W_{\parallel}$,

$$\sigma_{\parallel}/\sigma_{\perp} = W_{\parallel}/W_{\perp} \approx 10^6$$

The molecular diffusion coefficient perpendicular to the columns, $D_{\perp}$ is measured to be around 5×10^{-11} $m^2 s^{-1}$, which is comparable to the mobility of the charge-carriers perpendicular to the column. This indicates that the $\sigma_{\perp}$ may be dominated by the dislocations of these disc shaped molecules in between the adjacent columns which is ionic transport [35].

4.1.2 Role of the Electrodes

Boden *et al.* have studied the effect of electrode materials on the conductivity of discotic systems [36]. They have used indium tin oxide (ITO) electrodes as well as aluminium (Al) electrodes as symmetric and antisymmetric combinations. With a cell separation of about 5 μm and above, they have shown that the bulk resistance of the material dominates over the surface resistance and hence the influence of surface resistance can be neglected. In the bulk, under such a condition, the conductivity may be due to electron or the hole mobility. The hole mobility is temperature independent. The electron mobility follows the form

$$\mu_b^e \sim \mu_0 e^{-E_a/kT}$$

where E_a is the activation energy, and has values close to 0.5 V. In the symmetric ITO electrodes, ie. ITO/HAT6/ITO, it has been shown that hole conduction dominates due to the presence of intrinsic p-type impurities and a lower work function of ITO compared to HAT6. On the other hand, for the Al/HAT6/Al combination, the electron conduction is observed to be dominated.

Since the hole mobility is almost independent of temperature, the temperature dependency of the conduction at higher temperatures has to be either due to defect ionisation of

the trapped impurities or due to the external injection of charge carriers. Theoretical formulation of the defect ionisation would result $\sigma_{defect} \rightarrow 0$ as $T \rightarrow 0$. Experimentally it was observed that the conductivity levels off at low temperature instead of approaching zero. This means that the defect ionisation is not the dominant factor for the temperature dependency of conductivity. The experimental results can be explained on the basis of external injection of charge-carriers [36].

Some of the general trends in the conductivity of discotic liquid crystalline phase are as follows:

1. The conductivity in the columnar hexagonal phase is higher than that of crystalline and isotropic phases. In the crystalline phase the conductivity is less due to the defect structures at the electrode/discotic interface as well as in the bulk, that can not be cured. In the isotropic phase, the liquid crystalline order is collapsed. This results in the decrease in the mean free path, where the charge-carriers are trapped, and should normally lead to a decrease in conductivity.

2. As the chain length of the discotic molecules increases, the core-core distance increases which results in a lower coupling between the cores. It is also observed that the work function for the discotic system increases as the chain length increases. Due to these two reasons the conductivity decreases with increase in chain length.

3. The ionic conductivity shows a frequency-independent constant value at low frequencies and varies as $\omega^{0.8}$ at higher frequencies. The low frequency limiting value is attributed to the charge-migration between different columns or due to long-range hopping of charge-carriers while at high frequencies it is due to the charge-migration within the columns.

4.1.3 Alignment of Discotic Systems

The quasi-one-dimensional conductivity of the liquid crystalline phase originate from the stacking of the discs in columns and the transport of charge-carriers along these columns. Since the typical column length is only a few tens of nanometers while the separation between the electrodes is at least a few microns, the alignment of the discotic system is important for the observation of anisotropic conductivity. For the device applications, this alignment has a major role. For example, for the solar cell and photovoltaic cell applications, the

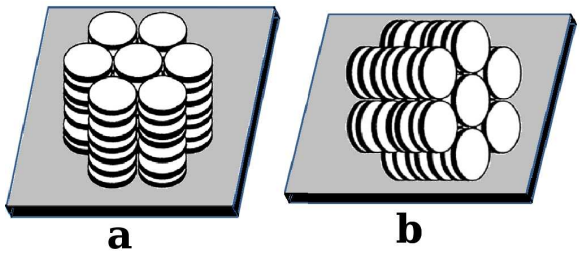

Figure 4.1: Schematic representation of a) homeotropic and b) homogeneous alignment

columns perpendicular to the surface is preferred while for the field effect transistor (FET) applications, the columns should be parallel to the surface. This means that all the columns should be aligned in the same direction so that the net carrier transport is a one-dimensional property. The alignment of the columns may be either parallel or perpendicular to the electrode surface as represented in the Figure 4.1. If the alignment of the columns is parallel to the surface, it is known as homogeneous alignment and in this case, the measurement of conductivity between the two electrodes gives the conductivity perpendicular to the columns ($\sigma_{\perp}$). On the other hand, if the columns are aligned perpendicular to the electrode surface, which is the homeotropic alignment, the conductivity parallel to the columns ($\sigma_{\parallel}$) can be measured between the electrodes.

Eventhough the alignment of calamitic liquid crystals are easy by the surface modifications or by the application of electric fields, these methods are not very effective for the alignment of discotic systems and several other methods have been proposed for this purpose [37]. One of the most common methods is the application of magnetic field. The discotic systems have negative magnetic susceptibility. Due to this, while cooling from the isotropic phase, the discs will align parallel to the field or the column axis will align perpendicular to the applied magnetic field. Hence applying a magnetic field perpendicular to the electrode surface will result in the homeotropic alignment of the sample [18]. Magnetic field of strength $\sim$2-5 T is observed to be sufficient for a nearly perfect alignment of the samples [16]. Similarly homogeneous alignment can be achieved by a magnetic field parallel to the electrode surface. Applying mechanical forces have been shown to align the discotic materials, especially for the highly viscous phases. The mechanical shear will align the columns perpendicular to the applied shear field [38, 39]. Alignment of liquid crystals by surface modification is a common method in calamitic liquid crystals, but is not a very successful

method for the discotic systems, although it has been shown that glass surfaces coated with electron rich molecules results in the homeotropic alignment [40]. Hexaphenol, mellitic acid, hexahydroxytriphenylene and rufigallol have been utilised for this purpose. A slow cooling of the discotic molecules from the isotropic phase in an ITO coated cell with a small cell thickness has shown to produce homeotropically aligned samples. This is one of the easiest and most common method for the alignment of discotic molecules. Hexaalkoxytriphenylenes can be homeotropically aligned easily using this method [8, 13, 14, 37, 41]. The typical cell thickness used for this purpose is $\sim$5 μm. In general, the aligned samples can be easily distinguished from a non-aligned sample using polarising optical microscopy. For an aligned sample, since the domains are all in the same direction, the sample will not show any birefringence whereas in the unaligned samples the birefringence originates from the defects from the different domains.

In the present chapter, we discuss the electrical conductivity measurements of triphenylene based columnar hexagonal liquid crystalline phases. The first part describes the ferrocenium doped HAT6 and HHTT composites, while the second part describes about the chloroauric acid-HAT6 composites. The composites were characterised using a variety of techniques and the electrical conductivity of these composites were observed to be enhanced by several orders of magnitude compared to the pure discotic systems. The last part of the chapter deals with the ac conductivity studies on ionic columnar hexagonal liquid crystals that are formed by pyridinium tethered triphenylene molecules.

4.2 Experimental Section

4.2.1 Chemicals

Two triphenylene derivatives, hexahexyloxytriphenylene (HAT6) and hexahexylthiotriphenylene (HHTT), which show columnar hexagonal phase, were used for the preparation of composites. The molecular structure of these two compounds are shown in Figure 4.2 and were synthesised by S. Kumar following the method described earlier [42]. The high purity dopants, ferrocenium tetrafluoroborate (FcTFB) was from Aldrich and chloroauric acid, $HAuCl_4$ was from Spectrochem and were used without further purification.

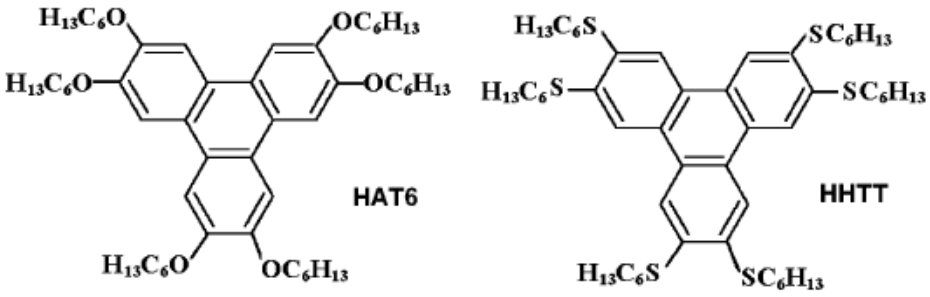

Figure 4.2: The molecular structure of HAT6 and HHTT

4.2.2 Preparation of the Composites

The discotic molecules were dissolved in dichloromethane, to which appropriate amount of dopants were added and sonicated for 5 minutes. A slow evaporation of the solvent with simultaneous stirring of the mixture resulted in the formation of the composites. Composites of different dopant-discotic ratios were prepared that includes 1 % FcTFB/HAT6, 10 % FcTFB/HAT6, 50 % FcTFB/HAT6 using HAT6 and FcTFB, 1 % FcTFB/HHTT, 10 % FcTFB/HHTT, 50 % FcTFB/HHTT using HHTT and FcTFB and 0.1 % $HAuCl_4$/HAT6, 1 % $HAuCl_4$/HAT6, and 5 % $HAuCl_4$/HAT6 using HAT6 and $HAuCl_4$.

4.2.3 Characterisation of the Composites

The composites were characterised using a variety of techniques like polarising optical microscopy, differential scanning calorimetry, small angle X-ray scattering, UV-visible spectroscopy, photoluminescence spectroscopy and electrical conductivity measurements. Polarising optical microscopy was carried out using Olympus POM instrument coupled with a Mettler heater. The samples were sandwiched between a glass-slide and a coverslip. The textures were imaged while cooling from the isotropic phase. The transition temperatures and associated enthalpy changes were determined by differential scanning calorimetry (DSC; Perkin-Elmer, model Pyris 1D) at a scan rate of 5 °C min^{-1} for both heating and cooling. The apparatus was calibrated using indium (156.6 °C) as a standard. Small-angle X-ray scattering studies were carried out using an X-ray diffractometer (Rigaku, UltraX 18) operating at 50 kV and 80 mA using Cu Kα radiation having a wavelength of 1.54 Å. Samples were

prepared by filling a capillary (Hampton Research, USA) with either the pure discotic systems or the composites and then sealed it. All scattering studies were carried out at 80 °C, and the diffraction patterns were collected on a two-dimensional Marresearch image plate. A model SD 2000 spectrophotometer (Ocean Optics, Dunedin, FL) or Perkin Elmer (USA) fitted with a tungsten lamp source and a cell having a path length of 1 cm was employed to measure the UV-visible absorbance spectra.

The DC conductivity studies of the samples were carried out in ITO-coated glass sandwich cells (10 mm$\times$5 mm area) with a thickness of either 60 μm or 4 μm. A schematic representation of the setup is shown in Figure 4.3. A Keithley picoammeter (model 480) along with a constant DC voltage source and a temperature controller was used for current measurements. The ionic conductivity measurements were conducted using a lock-in amplifier (Stanford Research Systems model SR830) at 1 kHz frequency on cooling from the isotropic phase. The frequency dependency for the conductivity of the composites were measured using the lock-in-amplifier at 80 °C, where the samples are in the liquid crystalline phase. A Howland constant current circuit, as shown in Figure 4.3 was used for the temperature measurements, where the terminals from the platinum thermal resistor were connected as the load resistance (LR). A precision operational amplifier (CA3140) was used in the circuits.

4.3 Results and Discussion

4.3.1 Discotic-Ferrocenium Composites

This section deals with the experimental results using the composites of FcTFB with the two discotic molecules *viz.* HAT6 and HHTT.

4.3.1.1 POM studies

Polarising optical microscopic studies provide an easy assessment of the different liquid crystalline phases formed by the materials. Figure 4.4 shows one of the polarising optical micrographic textures obtained for the 10 % FcTFB/HAT6, which is typical of the columnar hexagonal phase. A similar texture was also obtained for the other FcTFB composites. As is clear from the figure, all the composites retain the columnar hexagonal (Col_h) phase

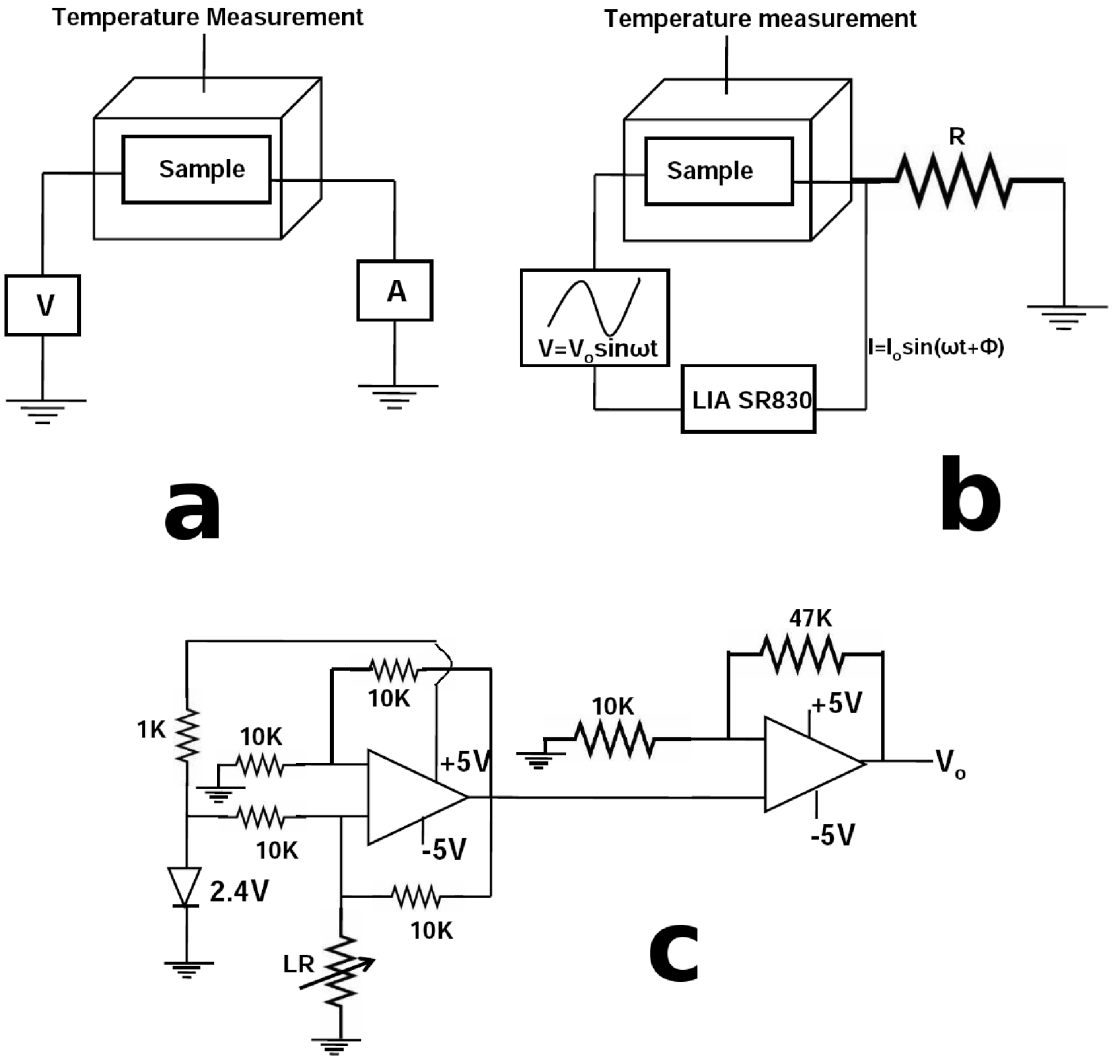

Figure 4.3: Schematic diagram of the experimental setup used for a) DC conductivity b) ac conductivity and c) temperature measurements. LR represents the load resistance from the platinum thermal resistor

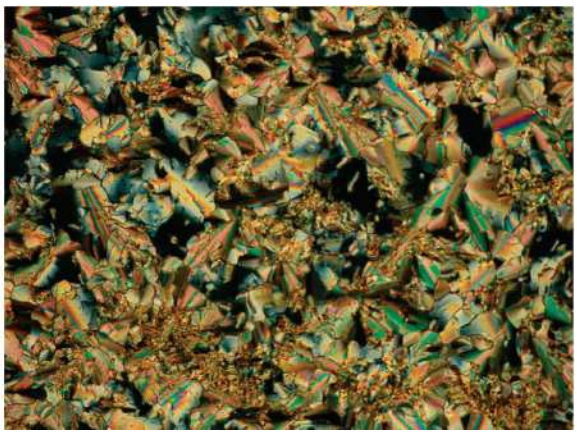

Figure 4.4: Polarising optical micrographic texture obtained for the 10 % FcTFB/HAT6 composite

of the pure discotic molecules. At very high concentrations of the dopant (for example, 50 % FcTFB) a phase separation was observed in both the discotic systems. The phase transition temperatures of the composites have been found to be a function of the ferrocenium concentration.

4.3.1.2 DSC studies

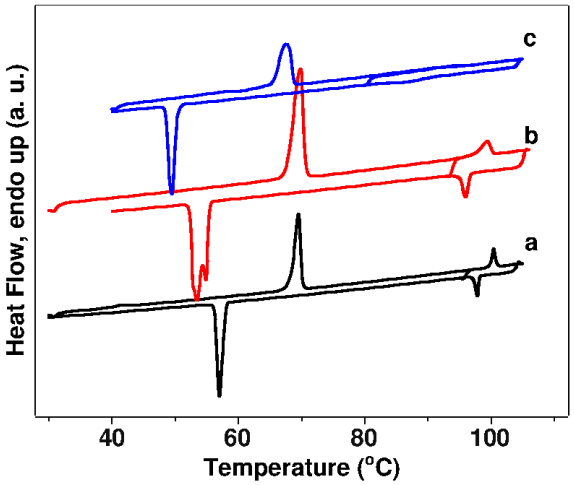

Figure 4.5: DSC traces for a) pure HAT6, and the composites b) 1 % FcTFB/HAT6 and c) 10 % FcTFB/HAT6

The composites were characterised by DSC analysis for the measurement of the phase transition temperatures and the enthalpies of the transitions. Figures 4.5 and 4.6 show

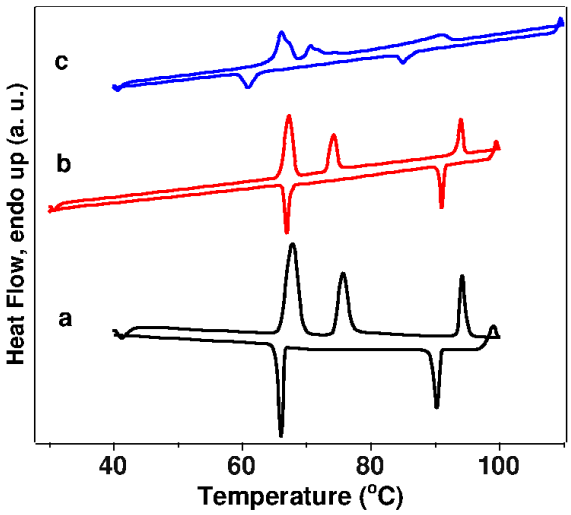

Figure 4.6: DSC traces for a) pure HHTT, and the composites b) 1 % FcTFB/HHTT and c) 10 % FcTFB/HHTT

the DSC traces for the pure discotic systems and the composites of HAT6 and HHTT, respectively. It is clear from the plots that the phase transition profiles are similar to the pure systems even after the addition of ferrocenium ions at low concentrations. It was observed that the Col_h phase becomes destabilised at very high concentrations of FcTFB, which is in accordance with the POM results. The phase transition temperatures were shifted to lower temperature and the enthalpy of the phase transition decreases with increasing dopant concentration. At very high concentration of the dopants, for example, 50 % FcTFB/HAT6, the Col_h phase was not observed. The highly electron-deficient ferrocenium ions form a charge-transfer complex with the electron-rich triphenylene core, as is evident from the UV-visible spectroscopic studies. The formation of the complex reduces the electron density in the columns. In addition, the steric hindrance of the ferrocenium ions is the major destabilising factor in the composite systems, eventhough charge-transfer complex formation of ferrocenium with the electron-rich triphenylene core may enhances the stability at lower concentrations. This is further supported by the fact that the enthalpy of the phase transition decreases with increasing ferrocenium concentration.

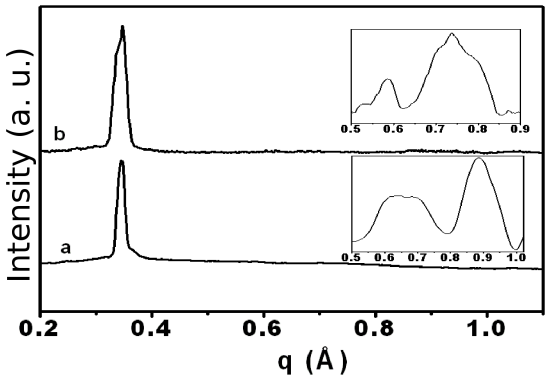

Figure 4.7: Scattering vector, q vs. intensity profiles obtained from small-angle X-ray scattering studies for (a) 10 % FcTFB/HAT6 and (b) 10 % FcTFB/HHTT composites. The insets show enlargements of the $1/\sqrt{3}$ and $1/\sqrt{4}$ peaks from the main plot

4.3.1.3 SAXS Studies

Small-angle X-ray scattering studies of the samples were carried out in 1 mm capillary tubes at 80 °C, and all of the scattering studies were performed during cooling from the isotropic phase. The SAXS patterns support our conclusions from the POM and DSC studies that 1 % and 10 % FcTFB composites with both HAT6 and HHTT systems retain the Col_h phase. The typical patterns obtained for the samples are shown in Figure 4.7. The *d* spacings calculated from the SAXS patterns are summarised in Table 4.1. The *d* values of 20.15 Å for HAT6 and 18.02 Å for HHTT as calculated from the SAXS patterns are in good agreement with the values reported in the literature [43]. The main scattering peak in the pattern shown here corresponds to the 2D plane having Miller indices of (1,0) of the Col_h phase. The other two peaks of lower intensity are shown in the inset of the figure. The ratio of the *d* values corresponding to the three peaks is $1:(1/\sqrt{3}):(1/\sqrt{4})$ which is typical for the hexagonal order. As is clear from the table 4.1, the doping of FcTFB in the discotic matrix has not disturbed the lattice parameters as there was a negligible change in the *d* spacing. We have shown that gold nanoparticles occupy the interdomain spacing without altering the *d* spacing of the columns in a discotic matrix [20]. In a similar manner, the ferrocenium molecules can occupy the interdomain spacing in the columnar architecture. The dopant, FcTFB may not occupy the intercolumnar spacing because of the relatively larger size of ferrocenium ions as compared to, for example, iodine [15]. This is supported by the *d* values, which is almost

the same even after the doping.

Table 4.1: The *d* spacing (in Å) for the Col_h phases of HAT6 and HHTT measured from the SAXS studies before and after doping

sample	pure	10% FcTFB
HAT6	20.15	18.16
HHTT	18.02	18.47

4.3.1.4 UV-visible Spectroscopy

UV-visible absorbance spectral studies of the pure samples and the composites were carried out in dichloromethane medium. The solution was sonicated for 5 min, and the absorbance of the solution was recorded immediately with pure dichloromethane as a reference. Figure 4.8 shows the absorbance spectra for different composites, in addition to those of pure FcTFB and ferrocene. It is clear from the figure that for the composites, there is a blue shift in the absorbance of the ferrocenium group, which is due to the formation of a charge-transfer complex. There is a shoulder peak in the 400-500 nm region. Since ferrocenium is a very strong electron acceptor, charge transfer from the electron-rich discotic molecules occurs, resulting in the formation of donor-acceptor pairs. Pure ferrocenium ions absorb at $\sim$600 nm, whereas pure ferrocene absorbs at $\sim$460 nm. In the present systems, a blue shift was observed in the absorption, which can be explained due to the charge transfer from triphenylene to ferrocenium ion in the composites. It is known that ferrocenium ions are unstable in an electron-rich environment such as highly polar solvents [44]. The extent of the blue shift was shown to be dependent upon the concentration of Fc^+ ion and the polarity of the solvent. In the present study, the absorbance had a larger blue shift at lower concentrations for both HAT6 and HHTT composites, as shown in the Figure 4.8. The 1 %, 10 % and 50 % FcTFB composites with HAT6 show absorbances at wavelengths of 358 nm, 362 nm, and 383 nm, respectively, whereas pure HAT6, absorbs at 277 nm [45]. This may be due to the fact that, at lower concentrations of Fc^+, complete charge transfer between the donor and acceptor molecules occurs. Similar behaviour was observed for the Fc^+/HHTT composites

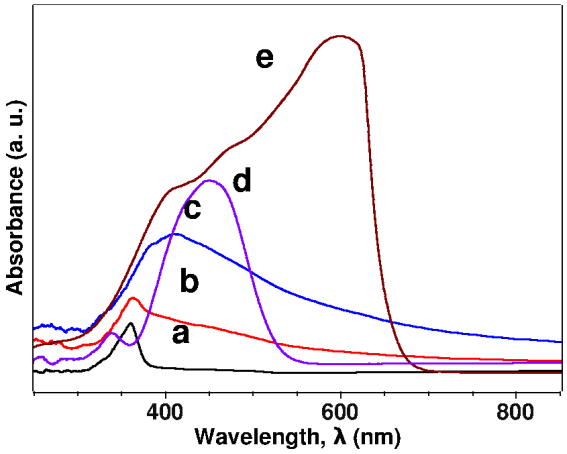

Figure 4.8: UV-visible absorbance spectra for a) 1 % FcTFB/HAT6, b) 10 % FcTFB/HAT6, c) 50 % FcTFB/HAT6, d) pure ferrocene and e) pure FcTFB

as well. The absorbance in ferrocenium species is a result of the charge transfer from the e_{1u} bonding ligand level to the empty e_{2g} metal level [46].

4.3.1.5 Conductivity Studies

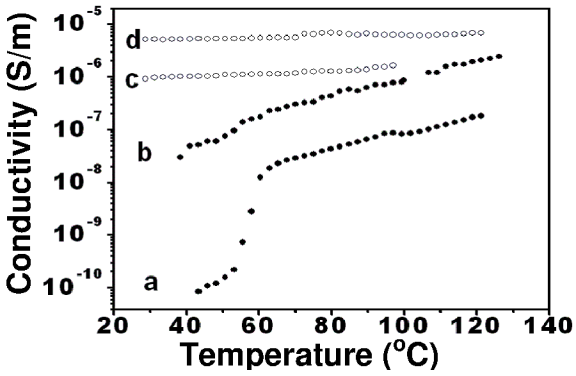

Figure 4.9: DC conductivity vs. temperature plots for a) 1 % FcTFB/HAT6 and b) 10 % FcTFB/HAT6 unaligned samples, c) 1 % FcTFB/HAT6 and d) 10 % FcTFB/HAT6 aligned samples

The DC conductivity studies of the composites were carried out in 60 μm thick ITO-coated glass sandwich cells. The conductivity measurements were also carried out using a 4 μm thickness cell. A slow cooling from the isotropic phase in the 4 μm cell results in the homeotropic alignment of the sample. This method of cooling from the isotropic phase

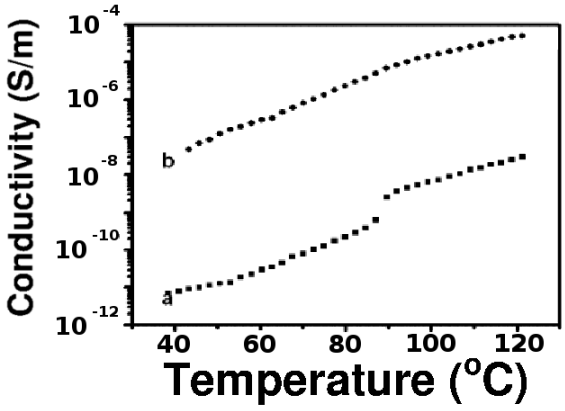

Figure 4.10: DC conductivity vs. temperature plots for a) 1 % FcTFB/HHTT and b) 10 % FcTFB/HHTT unaligned samples

in sandwiched cells has proven to be an effective method for the homeotropic alignment of discotic liquid crystals [34, 36, 37]. In the present study, the alignment was confirmed using polarising optical microscopy, where the aligned samples do not exhibit the characteristic birefringent textures. The conductivity values of both aligned and unaligned samples show a similar trend eventhough the aligned sample shows a larger electrical conductivity because of its facile electron transport through the well-aligned columns as compared to that of the unaligned sample.

The DC conductivity values of the samples were measured as a function of temperature while cooling from the isotropic phase. Figures 4.9 and 4.10 show the plots of conductivity as a function of temperature for the HAT6 and HHTT systems respectively, after doping. Both HAT6 and HHTT have very low DC conductivities in their pure state (of the order of 10^{-12} S/m) which is well below the accurate detection limit of our measurement system. There is a large increment in the conductivity values of the systems after doping. This can be explained by the charge transport that takes place after the addition of FcTFB to the discotic phase. It can be seen that the conductivity increases by several orders of magnitude after doping. The extent of increase depends up on the concentration of the dopant. A similar trend was observed for the aligned sample in the direction of column axis for the HAT6 system, as is obvious from Figure 4.9. The HHTT system also was found to exhibit similar behaviour as shown in Figure 4.10. The conductivity values of the HHTT composites were found to be higher than that of HAT6 composites, a trend similar to the higher conductivity

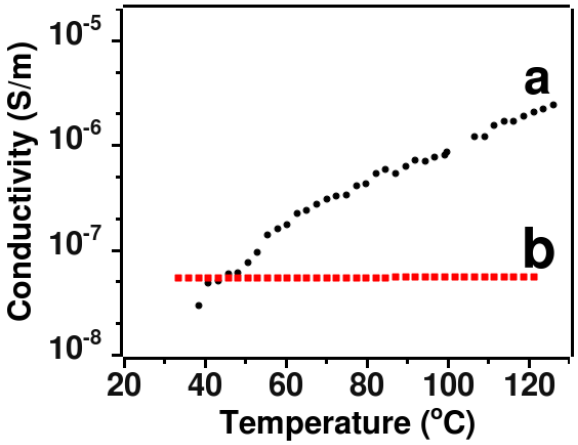

Figure 4.11: a) DC and b) ac conductivity plots for 10 % FcTFB/HAT6 on cooling from the isotropic phase

of HHTT over HAT6.

The ionic conductivity of the composites were studied by ac measurements for all of these samples. Figure 4.11 shows a plot for the comparison of ionic conductivity with the DC conductivity values for the 10 % FcTFB/HAT6 composite. From the graph, the ionic conductivity was found to be about 2 orders of magnitude less than the DC conductivity. This indicates that the mechanism operating in these systems is mainly electron transport rather than ion transport by the ferrocenium ions or the BF_4^- counterions. This is in accordance with the argument that the dopant ions will be trapped in between the alkyl chains of the discotic molecules in a frozen state and their contribution to the ionic conductivity will be less [16].

Ferrocene has an iron(II) ion sandwiched between the two cyclopentadienyl units, and this organometallic compound obeys the 18-electron rule [47]. On the other hand, the ferrocenium cation has 17 electrons and therefore acts as a strong electron acceptor. The a_{1g} molecular orbital of the ferrocenium ion has an unpaired electron, which explains its high electron-accepting nature. After the charge transfer from triphenylene, the composite forms an electron-hole pair, which enhances the DC conductivity of the composites. Even though the electron-accepting properties of ferrocenium have been well studied in different solvent systems, its behaviour in discotic liquid-crystalline systems is of greater interest as such systems form quasi-one-dimensional molecular wires.

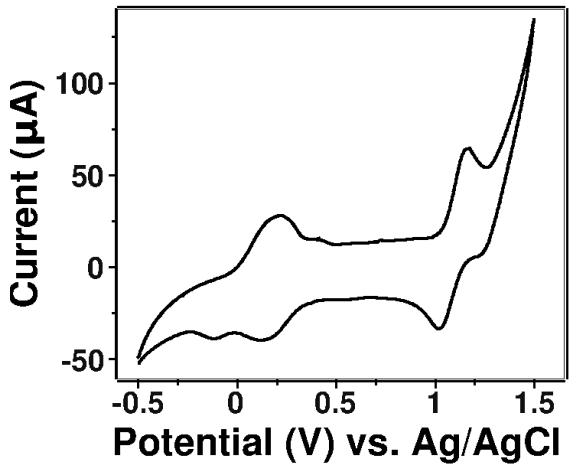

Figure 4.12: Cyclic voltammogram obtained for HAT6 in dichloromethane

We have calculated the mole fractions of the composites by taking 0.35 nm as the core-core distance and 18.3 Å as the *d* spacing for the discotic molecules. For 10 % FcTFB/HAT6 composition, the molar ratio of ferrocenium ions to discotic molecules was estimated to be about 1:3, which is much higher than the corresponding weight ratio. On the other hand, the volume fraction of ferrocenium ions to discotic molecules was calculated to be about 1:200 from the known molecular volumes of HAT6 and ferrocenium[48, 49]. This explains the fact that no significant change in the *d* spacing and no disruption of the hexagonal order occurs even after the doping of ferrocenium up to the extent of 10 %. For the 50 % composite, the molar ratio is too large, so that there is a disruption of the columnar phase.

From the cyclic voltammetry shown in Figure 4.12, we have calculated the oxidation potential of HAT6 to be -0.356 V vs. ferrocene/ferrocenium reference couple. The lower oxidation potential of HAT6 compared to ferrocene indicates that the electron transfer from HAT6 to the ferrocenium is energetically facile in the mixture and therefore their role as donor-acceptor pair. The electronic conductivity occurs by the hopping mechanism where the electron-rich triphenylene core donates an electron to the electron-deficient ferrocenium ion, thereby forming an electron-hole pair. The hopping conductivity of the electron-hole pair under the action of an applied DC electric field brings about the electronic conductivity. A very low dependence of the conductivity on temperature in the columnar phase supports the hopping mechanism as the dominant charge-carrier mechanism in the present systems. It has been reported that the electron tunneling mechanism depends more on the tempera-

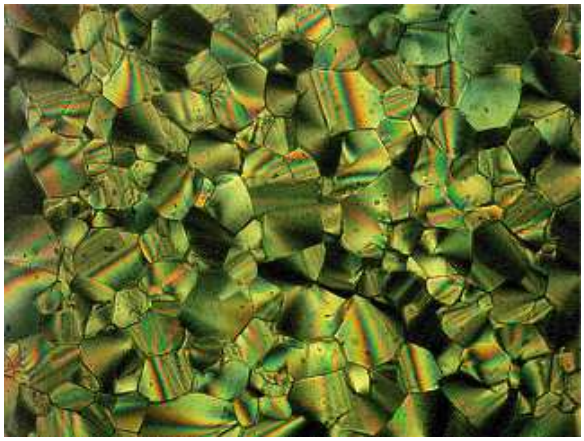

Figure 4.13: Polarising optical micrographic texture obtained for the composite 1 % $HAuCl_4$/HAT6 on cooling from the isotropic phase

ture while the hopping mechanism is weakly dependent on the temperature [36]. A similar mechanism was also reported in discotic liquid crystalline systems doped with TNF, iodine and gold nanoparticles [15, 20, 50].

4.3.2 Discotic-Chloroaurate Composites

This part describes the characterisation of HAT6-chloroaurate composites. As mentioned before, composites of three different ratios of $HAuCl_4$ with HAT6 were prepared, 0.1 % $HAuCl_4$/HAT6, 1 % $HAuCl_4$/HAT6 and 5 % $HAuCl_4$/HAT6. These composites were characterised using POM, DSC, SAXS, UV-visible spectra, photoluminescence spectra and conductivity studies.

4.3.2.1 POM Studies

Figure 4.13 shows the polarising optical micrographic texture obtained for the composite 1 % $HAuCl_4$/HAT6 and similar textures were obtained for other compositions also. The focal conic textures show that the composites retain the columnar hexagonal liquid crystalline phase. At high concentrations of $HAuCl_4$ (for example, the 5 % $HAuCl_4$/HAT6 composite), a phase separation was observed. We have noticed that higher concentration of $HAuCl_4$ leads to the total disruption of the liquid crystalline order.

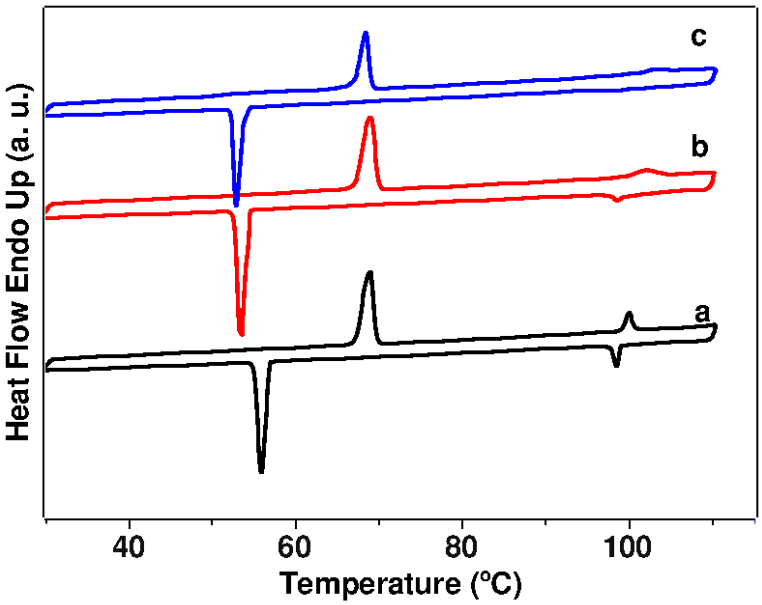

Figure 4.14: Differential scanning calorimetric traces for a) 0.1 % $HAuCl_4$/HAT6, b) 1 % $HAuCl_4$/HAT6 and c) 5 % $HAuCl_4$/HAT6

4.3.2.2 DSC Studies

The DSC traces as shown in Figure 4.14, show that the phase transition temperatures shift to lower temperature with increasing the dopant concentration. As expected, the enthalpy of the phase transition decreases as the dopant concentration increases. This is due to the fact that the dopants increase the entropy of the liquid crystalline phase and when its concentration is high, the liquid crystalline phase disrupts. Moreover, as the concentration of $HAuCl_4$ increases, the concentration of HAT6 radical cation also correspondingly goes up, which weakens the $\pi - \pi$ interaction within the column that acts as another major factor for the destabilisation of the liquid crystalline order. As clear from the figure, the enthalpies of phase transition is high for the pure HAT6 and for the composites up to the concentration of 1 % $HAuCl_4$/HAT6.

4.3.2.3 SAXS Studies

The liquid crystalline structure of the composites were further characterised by small-angle X-ray scattering (SAXS) studies. The studies were carried out in 0.7 mm diameter capillary tubes at 80 °C, while cooling from the isotropic phase. Figure 4.15 shows plot of intensity

vs. scattering vector for 0.1 % $HAuCl_4$/HAT6 and 1 % $HAuCl_4$/HAT6 composites. It is observed that the inter-columnar separation is not disturbed by the addition of the dopants at lower concentrations. The *d* values were calculated from the SAXS pattern using the equation

$$d = \frac{2\pi}{q}$$

The *d* values for the composites were similar to the values obtained for the pure HAT6 and with ferrocenium doping, which is already shown in the table 4.1. The *d* values follow the ratio $1:(1/(\sqrt{3}):(1/\sqrt{4})$ indicating that both the samples retain the columnar hexagonal order. It is clear that the addition of $HAuCl_4$ has not affected the *d* values and the columnar arrangement at lower concentration of the dopants in accordance with the POM and DSC studies.

4.3.2.4 Spectral Studies

UV-visible absorbance studies of all the composites were carried out in dichloromethane medium with pure dichloromethane as the reference sample. Figure 4.16 shows the spectra of 0.1 %, 1 % and 5 % $HAuCl_4$/HAT6 composites. The peaks at 430 nm, 580 nm, 630 nm and 830 nm are clear and can be attributed to the presence of HAT6 radical cation formed by the oxidation of HAT6 by $AuCl_4^-$ ions as shown below, which is similar to the oxidation of the discotic core by $AlCl_3$ reported earlier [45].

$AuCl_4^-$ + 2(HAT6) $\rightarrow$ $AuCl_2^-$ + 2$(HAT6)^+$ + 2Cl^-

The spectral bands described above, have been attributed to the symmetrically allowed transitions in the discotic molecules [42]. A strong band was observed at 360 nm and another peak at 280 nm. The peak at 280 nm is assigned to the electronic transitions in pure HAT6 molecule corresponding to a band gap of about 4.4 eV. It may be noted that these composites have absorption throughout the visible range.

Both photoluminescence (PL) emission and excitation spectra of the composites were taken in dichloromethane medium. First the emission spectra were taken at an excitation wavelength of 360 nm which is the highest intensity peak in the UV-vis spectra for the pure HAT6. The PL emission spectra are shown in Figure 4.17. The emissions were observed at three wavelengths, 383 nm, 406 nm and 433 nm. The intensity among these three was found

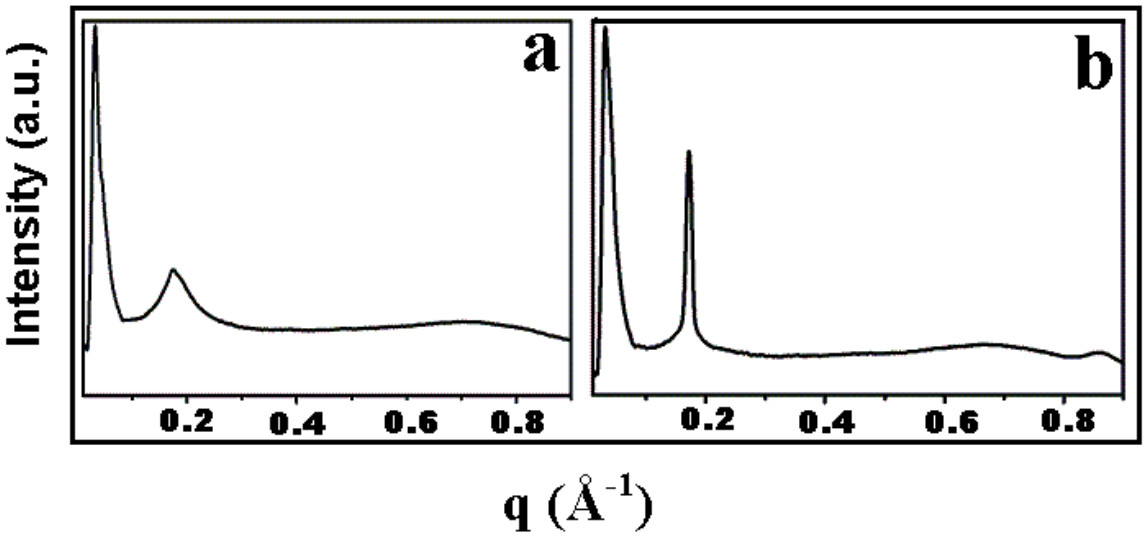

Figure 4.15: Intensity vs. scattering vector plot from the small-angle X-ray scattering studies for a) HAT6 b) 0.1 % $HAuCl_4$/HAT6 and c) 1 % $HAuCl_4$/HAT6

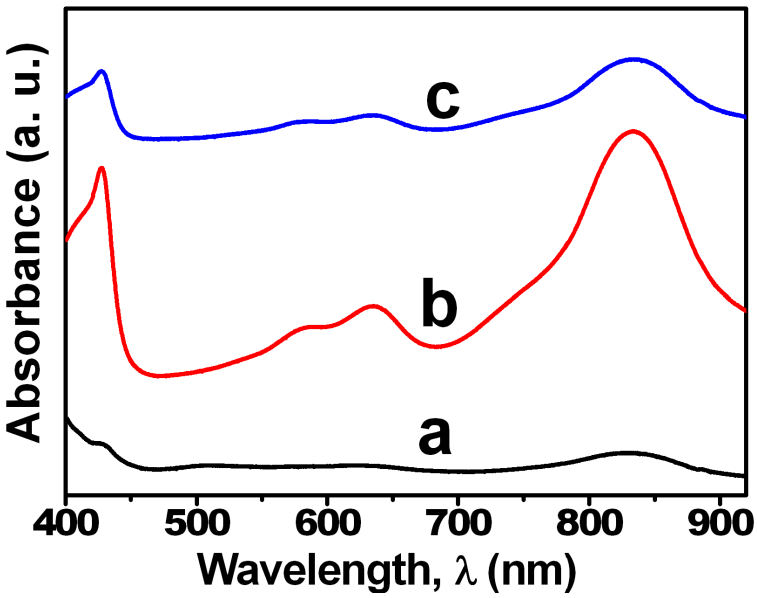

Figure 4.16: UV-visible spectra for the composites a) 0.1 % $HAuCl_4$/HAT6, b) 1 % $HAuCl_4$/HAT6 and c) 5 % $HAuCl_4$/HAT6. Absorbance is in arbitrary units

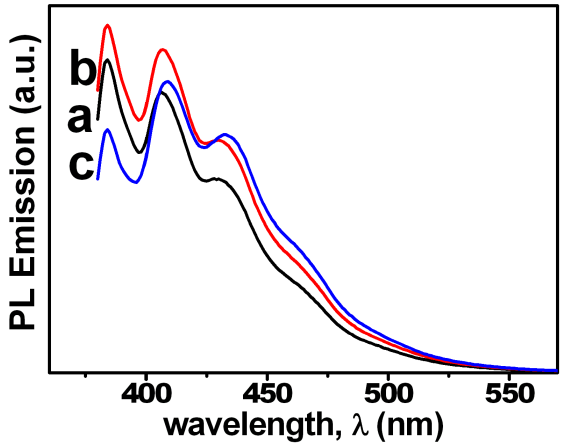

Figure 4.17: Photoluminescence emission spectra for excitation at 360nm for a) HAT6, b) 0.1 % $HAuCl_4$/HAT6 and c) 1 % $HAuCl_4$/HAT6

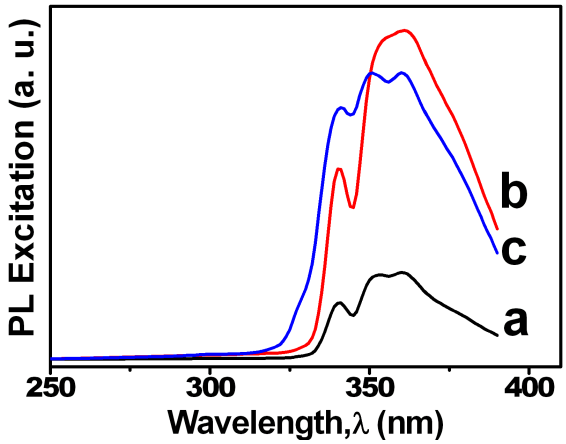

Figure 4.18: Photoluminescence excitation spectra for the emission at 406nm peak for a) HAT6, b) 0.1 % $HAuCl_4$/HAT6 and c) 1 % $HAuCl_4$/HAT6

to be highest for the 406 nm peak. The excitation spectra for the 406 nm band were taken and are shown in Figure 4.18. Three excitation wavelengths were observed at 361 nm, 353 nm, 340 nm and a weak shoulder band at 300 nm that correspond to a band gap of 3.43 eV, 3.51 eV, 3.64 eV and 4.08 eV. The peaks can be assigned to the $S_0 \rightarrow S_1$, $S_0 \rightarrow S_2$, $S_0 \rightarrow S_3$ and $S_0 \rightarrow S_4$ transitions. It has been shown that the photo-excitation spectral lines like $S_0 \rightarrow S_1$ and $S_0 \rightarrow S_2$ are symmetrically forbidden for the single discotic molecule, while the aggregation of the molecules makes them symmetrically allowed [51]. This indicates that there are small aggregates of the discotic molecules in the solution.

4.3.2.5 Conductivity Studies

Figure 4.19 shows the DC conductivity of the composites as a function of temperature while cooling from the isotropic phase. The electrical conductivity of pure HAT6 is about 10^{-12} S/m as mentioned in the previous section. The plots in Figure 4.19 show the variation of electrical conductivity with temperature for 0.1 % $HAuCl_4$/HAT6 and 1 % $HAuCl_4$/HAT6. It is observed that the conductivity increases by several orders of magnitude after the doping. This is similar to the ferrocenium composite with HAT6 which is explained in the previous section. It can be noted that there is a clear and significant change in the electrical conduc-

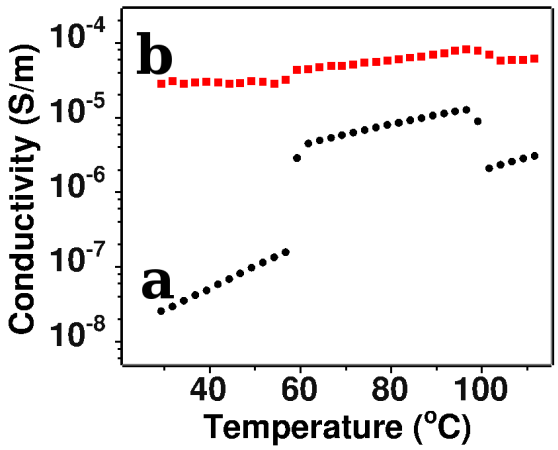

Figure 4.19: DC electrical conductivity plots for the composites a) 0.1 % $HAuCl_4$/HAT6 and b) 1 % $HAuCl_4$/HAT6 as a function of temperature

tivity at the temperatures corresponding to the phase transitions. The conductivity of the crystalline phase is very much lower than the columnar hexagonal phase. In the isotropic phase, the conductivity again decreases due to the disruption of the columns indicating that the major contribution of the conductivity comes from the columnar hexagonal order of the composites. Such a behaviour has not been reported for the DC conductivity in the literature earlier.

Figure 4.20 shows the ac conductivity of the composites as a function of temperature. The ac conductivity values are higher than the corresponding DC conductivity values. It has been previously observed that the addition of dopants like $AlCl_3$ and iodine increases the ionic conductivity of the columnar phase by about million times [16, 34]. The present systems show a similar trend in ionic conductivity with a simultaneous enhancement in the DC conductivity. Figure 4.21 shows a frequency independent ionic conductivity in the lower region while at high frequencies it increases rapidly. The conductivity follows a $\omega^{0.8}$ relation at high frequencies and this can be attributed to the hopping or tunneling mechanism of conductivity within the columns while the frequency-independent conductivity is attributed to the slowest transition rates due to the structural defects in the columns or hopping between different columns as discussed in section 4.1.1 [16, 35].

The DC conductivity enhancement can be attributed to the formation of radical cations with the retention of columnar phase that provides a facile transport of charge carriers along

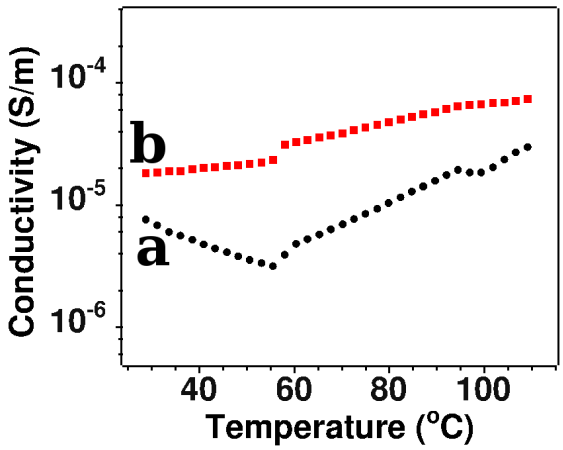

Figure 4.20: Ionic conductivity plots for the composites a) 0.1 % $HAuCl_4$/HAT6 and b) 1 % $HAuCl_4$/HAT6 as a function of temperature

the columns. The enhancement in the ac conductivity can be attributed either due to the presence of ionic dopants or due to the formation of radical cations in the discotic matrix. Previously, using $AlCl_3$/HAT6 composites, it has been proposed that the contribution of the counter ions to the ionic conductivity will be very less compared to the electronic migrations, since the counter ions will be almost frozen between the alkyl chains of the discotic molecules [16]. We have observed that doping with FcTFB has not increased the ionic conductivity even at higher concentrations of dopants eventhough they form charge-transfer complex with the discotic molecules. In the present system, the dopants form charge-transfer complex with the formation of radical cations of the discotic molecules. Comparing these observations, the very high ionic conductivity of the present composites can be attributed to the formation of HAT6 radical cations.

From the cyclic voltammetric studies as shown in Figure 4.12, the oxidation of HAT6 is observed to be at -0.356 V while for gold it is at 0.64 V vs. ferrocene/ferrocenium reference electrode. This shows that the formation of HAT6 radical cation is energetically favoured due to the reduction of Au^{3+} to Au^{+} ions. On the other hand, the absence of any surface plasmon band in the UV-vis spectra rules out the possibility of the complete reduction to gold nanoparticles, even though small clusters of gold may be formed due to the aggregation of gold atoms formed by disproportionating the Au^{+} ions.

The conductivity values of the $HAuCl_4$/HAT6 systems are comparable with conductivity

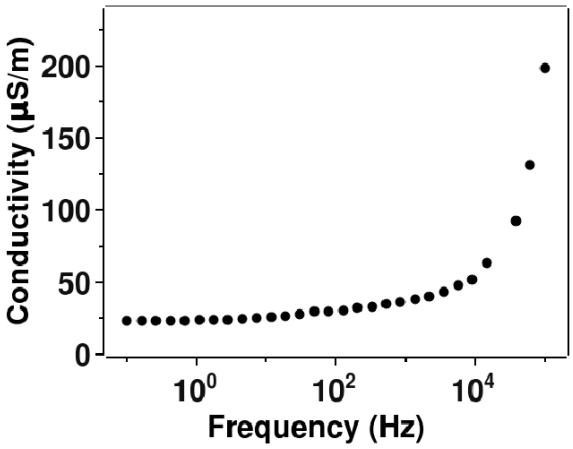

Figure 4.21: Ionic conductivity of the composite 1 % $HAuCl_4$/HAT6 as a function of frequency

of HAT6 composites doped with ferrocenium ions as described in the previous section. The values are also comparable with discotic systems doped with gold nanoparticles [20, 21]. The DC conductivity of discotic systems can be attributed to either hopping mechanism or to the electron tunneling mechanism. Due to the facile formation of the radical cations of HAT6 and a weak temperature dependence on the conductivity in the liquid crystalline phase, we have concluded that hopping mechanism rather than electron tunneling mechanism is responsible for the DC conductivity in $HAuCl_4$/HAT6 composites [36].

The $HAuCl_4$/HAT6 composites in the columnar hexagonal phase show a high ionic conductivity that is comparable to the DC conductivity values. Systems with very high electronic and ionic conductivity may provide several promising advantages over systems with only electronic or ionic conductivity. The photon absorption of the present system in the full visible region makes it an interesting candidate for the solar cell applications. A higher absorption in the near IR region of the photons is more promising as the sun emits a major flux in this region, which increases the external quantum efficiency for the solar cell and photovoltaic device applications [52, 53, 54]. Since the high conductivity of the present system originates from the columnar arrangement present in the columnar hexagonal phase under normal conditions, the system may find diverse applications and overcomes the major disadvantage of the quenching of charge carriers by moisture as observed in many other discotic systems.

The incerase in electrical conductivity of $HAuCl_4$/HAT6 systems after the addition of ferrocenium as well as tetrachloroaurate highlight several interesting aspects. They can be considered as model systems for the study of the interactions of donor-acceptor species. One can derive informations on interactions of other organometallic compounds in discotic systems, $\pi - \pi$ interactions between donor-acceptor moieties, and similar interactions. In the present systems, the dopants occupy the interdomain spacing as confirmed by the SAXS studies, and in this way they differ from many of the other reported dopants such as iodine or potassium, which occupy the intercolumnar space [15, 50].

4.4 Electrical Conductivity Studies of Ionic Liquid Crystals

This section deals with the ionic conductivity studies of a series of pyridinium tethered triphenylene based discotic liquid crystalline compounds. Eventhough the discotic systems are quasi-one-dimensional conductors with very low conductivity in their pure state, the conductivity can be enhanced by the addition of dopants into the columnar matrix as described in the previous sections. Other approaches to increase the conductivity of these materials are i) attachment of donor or acceptor molecules that may form intra-molecular charge-transfer complexes with the discotic molecules or ii) attachment of ionic groups in the side chains. In this section, we describe the second approach for the preparation of highly conducting discotic phases. Kato *et al.* have studied a series of pyridinium substituted phenyl derivatives with different spacer groups [39, 55, 56, 57]. They have shown that these ionic liquids form columnar hexagonal phase over a wide range of temperature and have studied the quasi-one-dimensional conductivity as a function of temperature. These ionic liquids possess very high ionic conductivity that are in the order of 10^{-2} S/m at temperatures close to the isotropic phase. The addition of $LiBF_4$ has shown to increase the $\sigma_{||}$ without significantly increasing the $\sigma_{\perp}$, which indicates that the lithium ions have occupied the centre ionic part of the columns, that also enhanced the liquid crystalline order [39]. This effectively increases the anisotropy in the conductivity. Here we describe the ionic conductivity of a series of pyridinium substituted triphenylene based discotic ionic liquid crystalline materials.

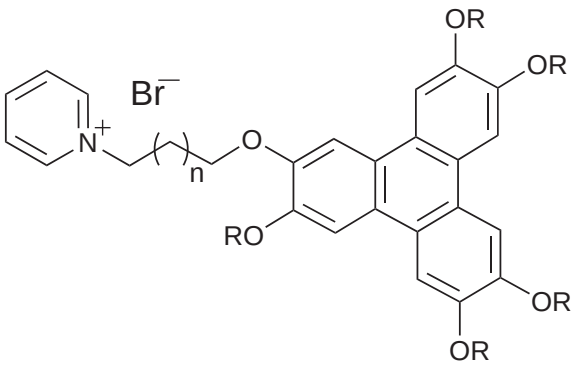

Figure 4.22: Structure of the pyridinium tethered triphenylene derivatives used for the conductivity studies

4.4.1 Experimental Section

The pyridinium tethered triphenylene molecules were synthesised by S. Kumar *et al.* and the synthesis and phase behaviour of these molecules have been reported previously [58]. The structure of these molecules are shown in the Figure 4.22 with the following alkyl chain lengths

C4Py: R=C_5H_{11}; n=2

C5Py: R=C_5H_{11}; n=3

C6Py: R=C_5H_{11}; n=4

C7Py: R=C_5H_{11}; n=5

C11Py: R=C_5H_{11}; n=9

In these CnPy compounds, the spacer group between triphenylene and pyridinium group used was alkyl chain length (n) with 4,5,6,7 and 11 carbon atoms. All these molecules show columnar hexagonal phase. The phase behaviour of C5Py is as follows:

On heating: SS 75.7 (6.3) SS 96.2(5) Col 112.2 (2) col 121.2 (2.4) I

On cooling: I 118.7 (2.3) col 107.4 (2) Col

where SS = solid state Col=columnar phase and I=isotropic phase. For the ionic conductivity studies, the sample was inserted between two ITO coated glass plates. The thickness of these conductivity cells were $\sim$60 μm while the area was $\sim$10 mm$\times$5 mm. The sample was inserted into the cell at the isotropic phase by the capillary action. The cells were then cooled, connected with the electrical contacts and used for the conductivity measurements.

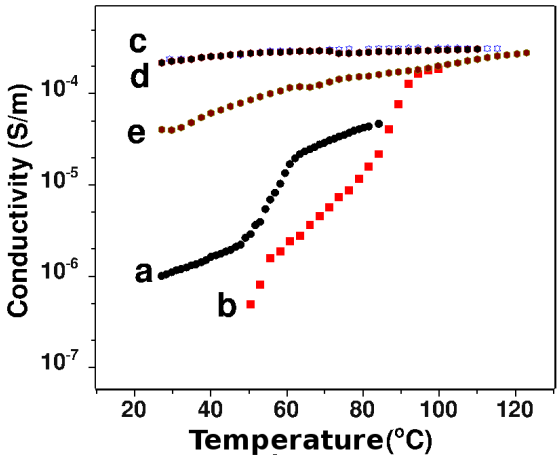

Figure 4.23: Ionic conductivity vs. temperature plots for the pyridinium tethered triphenylene derivatives

The ionic conductivity was measured using a temperature controller and a lock-in-amplifier (Stanford Research Systems, USA, model SRS 830) at 1 kHz frequency.

4.4.2 Results and Discussion

Figure 4.23 shows the plots of the variation of ionic conductivity with temperature for the above mentioned ionic liquid crystalline compounds. It is clear that the conductivity of these systems is very high in the liquid crystalline phase. In this phase, it can be seen that as the temperature increases, there is a sharp increase in the conductivity. The conductivity values are retained even in the isotropic phase. The conductivity of C4Py is less compared to the other homologous series. The conductivity is higher for C5Py especially in the columnar and isotropic phases. C6Py and C7Py shows very similar conductivity in the entire temperature range studied. For the C11Py with an alkyl spacer length of 11 carbon atoms, the conductivity decreases.

The samples C4Py and C5Py show a very high temperature dependent ionic conductivity in the liquid crystalline phase, which indicates a large contribution of electron mobility to the charge-migrations. The activation energy E_a for the electron mobility was calculated using the equations $\sigma = ne\mu$ and

$$\mu = \mu_0 e^{-E_a/kT}$$

A linear fit of the observed values of conductivity vs. inverse of temperature provide an

E_a value of 0.63 eV which is quite close to 0.5 eV as reported in the literature [39]. A higher value in the present system may be due to more substitutions in the side chains of the discotic core, which increases the core-core distance. In all other samples, the temperature dependence is less, which may be due to lesser involvement of electron mobility towards the charge-migration compared to the hole mobility. As the chain length increases, the core-core interaction decreases and the work function of the molecules increases. This increase in the core-core distance makes the electron tunneling process more difficult. This results in the lower electron mobility and the measured hole migration. Hopping conductivity may be favoured under such conditions through different vibrational couplings of the discotic molecules [16].

The conductivity increases with alkyl chain length of the spacer group from 4 to 7 carbon atoms while for C11Py with alkyl chain length of 11 carbon atoms, the conductivity decreases. It has been reported that the higher the chain length, the lower will be the core-core interaction since at higher core-core distance within a column there is more probability of defects in the stacking. This leads to a lower coupling strength between the cores, resulting in the decrease in conductivity. Moreover, the area occupied by each column on the surface will be more for molecules with higher chain length in the homeotropically aligned sample. This reduces the surface area available for the charge-injection to the discotic matrix, that contributes to a lower conductivity [36].

It is clear that the conductivity of these ionic liquids are several orders of magnitude higher than the same triphenylene cores without any pyridinium substitution. The conductivity of hexaalkoxytriphenylenes is of the order of 10^{-12} S/m while for the pyridinium tethered triphenylenes the conductivity is 10^{-6} S/m an enhancement by six orders of magnitude.

4.5 Conclusion

In this chapter, we have discussed the electrical conductivity studies of composites formed between discotic liquid crystals as donor and either ferrocenium tetrafluoroborate or chloroauric acid as dopants which act as acceptors. The presence of donor-acceptor pairs with the electron rich discotic molecules have been demonstrated. In the case of chloroaurate, the dopants oxidises the triphenylene core to form HAT6 radical cations which is con-

firmed by the UV-visible spectroscopy and cyclic voltammetry. These radical cations show significant absorbance throughout the visible and near IR region, indicating that these composites may act as potential candidates for solar cell applications. Both the dopants enhance the DC electrical conductivity of the composites by several orders of magnitude as compared to the pure discotic system. Interestingly the chloroaurate complex enhances the ionic conductivity of the systems to almost the same extent as that of DC conductivity. Eventhough both the dopants, FcTFB and $HAuCl_4$ enhance the conductivity by several orders of magnitude, the concentration levels of both the dopants are different. Chloroauric acid ($HAuCl_4$) is strong enough to enhance the conductivity even at a concentration as low as 0.1 % while 1 % FcTFB is necessary for a similar enhancement. It is also observed that even a 5 % doping of $HAuCl_4$ has an adverse effect on the phase behaviour of the discotic systems and therefore doping above this level has been found to disrupt the liquid crystalline phase. Doping with FcTFB, on the other hand, provides a better stability at least up to 10 %. Higher doping of FcTFB also results in the disruption of the liquid crystalline phase. The main reason for this behaviour is due to the fact that the $HAuCl_4$ is a more powerful oxidising agent than FcTFB, eventhough in both cases, the dopants form charge-transfer complexes with the discotic molecules, which is clear from the UV-visible spectral studies.

The ionic conductivity studies of the pyridinium tethered triphenylene based discotic liquid crystals have shown that the ac conductivity of these systems have been enhanced by several orders of magnitude as compared to the system without pyridinium moiety. This indicates that the ionic conductivity of the discotic systems can be enhanced by attaching ionic groups to the side chain of the aromatic core of the discotic molecules. The conductivity is shown to be due to electron mobility for lower chain lengths while for higher homologous series, hopping mechanism dominates.

Bibliography

[1] S. Chandrasekhar, B. K. Sadashiva and K. A. Suresh, *Pramana J. Phys.*, 1977, **9**, 471.

[2] S. Kumar, *Chem. Soc. Rev.*, 2006, **35**, 83.

[3] S. Segeyev, W. Pisula and Y. H. Greets, *Chem. Soc. rev.*, 2007, **36**, 1902.

[4] S. Laschat, A. Baro, N. Steinke, F. Giesselmann, C. hagele, G. Scalia, R. Judele, E. Kapatsina, S. Sauer, A. Schreivogel and M. Tosoni, *Angew. Chem. Int. Ed.*, 2007, **46**, 4832.

[5] L. S. Mende, A. Fechtenkotter, K. Mullen, E. Moons, R. H. Friend and J. D. Macken, *Science*, 2001, **293**, 1119.

[6] I. Seguy, P. Destruel and H. Bock, *Synth. Met.*, 2000, **111-112**, 15.

[7] W. Pisula, A. Menon, M. Stepputat, I. Lieberwirth, U. Kolb, A. Tracz, H. Sirringhaus, T. Pakula and K. Mullen, *Adv. Mater.*, 2005, **17**, 684.

[8] R. Azumai, M. Ozaki, H. Nakayama, T. Fujisawa, W. F. Schmidt and K. Yoshino, *Mol. Cryst. Liq. Cryst.*, 2001, **366**, 359.

[9] M. Kastler, F. Laquai, K. Mullen and G. Wegner, *Appl. Phys. Lett.*, 2006, **89**, 252103.

[10] J. M. Warman and A. M. V. de Craats, *Mol. Cryst. Liq. Cryst.*, 2003, **396**, 41.

[11] A. M. van de Craats, J. M. warman, M. P. de Haas, D. Adam, J. Sommerer, D. Haarer and P. Schuhmacher, *Adv. Mater.*, 1996, **8**, 823.

[12] H. Iino, J. Hanna, R. J. Bushby, B. Movaghar, B. J. whitaker and M. J. Cook, *Appl. Phys. Lett.*, 2005, **87**, 132102.

[13] V. S. K. Balaguruswamy, S. K. Prasad, S. Chandrasekhar, S. Kumar, M. Manickam and C. V. Yelamaggad, *Pramana J. Phys.*, 1999, **53**, 3.

[14] S. Chandrasekhar and V. S. K. Balagurusamy, *Proc. R. Soc. Lond. A*, 2002, **458**, 1783.

[15] G. B. M. Vaughan, P. A. Heiney, J. P. M. Jr. and A. B. S. III, *Phys. Rev. B*, 1992, **46**, 2787.

[16] N. Boden, R. J. Bushby and J. Clements, *J. Chem. Phys.*, 1993, **98**, 5920.

[17] N. Boden, R. J. Bushby and J. Clements, *J. Mater. Sci. Mater. Electronics*, 1994, **5**, 83.

[18] N. Boden, R. J. Bushby, J. Clements, M. V. Jesudason, P. F. Knowles and G. Williams, *Chem. Phys. Lett.*, 1988, **152**, 94.

[19] N. Boden, R. J. Bushby, A. N. Cammidge, J. Clements, R. Luo and K. J. Donavan, *Mol. Cryst. Liq. Cryst.*, 1995, **261**, 251.

[20] S. Kumar, S. K. Pal, P. S. Kumar and V. Lakshminarayanan, *Soft Matter*, 2007, **3**, 896.

[21] L. A. Holt, R. J. Bushby, S. D. Evans, A. Burgess and G. Seeley, *J. Appl. Phys.*, 2008, **103**, 063712.

[22] D. Markovitsi, H. Bengs and H. Ringsdorf, *J. Chem. Soc. Faraday Trans.*, 1992, **88**, 1275.

[23] L. Y. Chiang, J. P. Stokes, R. Safinya and A. N. Bloch, *Mol. Cryst. Liq. Cryst.*, 1985, **125**, 279.

[24] J. van Keulen, T. W. Warmerdam, R. J. M. Nolte and W. Drenth, *Recl. Trav. Chim.*, 1987, **106**, 534.

[25] J. P. Hill, W. Jin, A. Kosaka, T. Fukushima, H. Ischihara, T. Shimomura, K. Ito, T. Hashizume, N. Ishii and T. Aida, *Science*, 2004, **304**, 1481.

[26] Y. Yamamoto, T. Fukushima, W. Jin, A. Kosaka, T. Hara, T. Nakamura, A. Saeki, S. Seki, S. Tagawa and T. Aida, *Adv. Mater.*, 2006, **18**, 1297.

[27] J. Kirkpatrick, V. Marcon, K. Kremer, J. Nelson and D. Andrienko, *J. Chem. Phys.*, 2008, **128**, 094506.

[28] J. Kirkpatric, V. Marcon, K. Kremer, J. Nelson and D. Alendrienko, *Phys. Stat. Sol. B*, 2008, **245**, 835.

[29] T. Hara, K. Furukawa, T. Nakamura, Y. Yamamoto, A. Kosaka, W. Jin, T. Fukushima and T. Aida, *J. Phys. Soc. Jpn.*, 2008, **77**, 034710.

[30] H. Fujikake, T. Murashige, M. Sugibayashi and K. Ohta, *Appl. Phys. Lett.*, 2004, **85**, 3474.

[31] C. W. Struijk, A. B. Sieval, J. E. J. Dakhorst, M. van Dijk, P. Kimkes, R. B. M. Koehorst, H. Donker, T. J. Schaafsma, S. J. Picken, A. M. van de Craats, J. M. Warman, H. zuilhof and E. J. R. Sudhlter, *J. Am. Chem. Soc.*, 2000, **122**, 11057.

[32] A. M. van de Craats, N. Stutzmann, O. Bunk, M. M. Nielsen, M. Watson, K. Mullen, H. D. Chanzy, H. Sirringhaus and R. H. Friend, *Adv. Mater.*, 2003, **15**, 495.

[33] J. Y. Kim, I. J. Chaung, Y. C. Kim and J.-W. Yu, *Chem. Phys. Lett.*, 2004, **398**, 367.

[34] N. Boden, R. J. Bushby, J. Clements and B. Movaghar, *Phys. Rev. B*, 1995, **52**, 13274.

[35] E. K. Arikainen, N. Boden, R. J. Bushby, J. Clements, B. Movaghar and A. Wood, *J. Mater. Chem.*, 1995, **5**, 2161.

[36] N. Boden, R. J. Bushby, J. Clements and B. Movaghar, *J. Appl. Phys.*, 1998, **83**, 3207.

[37] S. H. Eichhorn, A. Adavelli, H. S. Li and N. Fox, *Mol. Cryst. Liq. Cryst.*, 2003, **397**, 47.

[38] H. Eichhorn, D. Wohrle and D. Pressner, *Liq. Cryst.*, 1997, **22**, 643.

[39] M. Yoshio, T. Mukai, H. Ohno and T. Kato, *J. Am. Chem. Soc.*, 2004, **126**, 994.

[40] C. Vauchier, A. Zann, P. Lebarny, J. C. Dubois and J. Billard, *Mol. Cryst. Liq. Cryst.*, 1981, **66**, 423.

[41] J. K. Vij, A. Kocot and T. S. Perova, *Mol. Cryst. Liq. Cryst.*, 2003, **397**, 231.

[42] S. Marguet, D. Markovitsi, P. Millie, H. Sigal and S. Kumar, *J. Phys. Chem. B*, 1998, **102**, 4697.

[43] I. Paraschiv, P. Delforterie, M. Giesbers, M. A. Posthumus, A. T. M. Marcelis, H. Zuilhof and E. J. R. Sudholter, *Liq. Cryst.*, 2005, **32**, 977.

[44] H. M. A. salman, M. R. Mahmoud, M. H. M. Abou-El-Wafa, U. M. Rabie and R. H. Crabtree, *Inorg. Chemm. Commun.*, 2004, **7**, 1209.

[45] N. Boden, R. J. Bushby, J. Clements and R. Luo, *J. Mater. Chem.*, 1995, **5**, 1741.

[46] Y. S. Sohn, D. N. Hendrickson and H. B. Gray, *J. Am. Chem. Soc.*, 1970, **92**, 3233.

[47] D. F. Shriver and P. W. Atkins, *Inorganic Chemistry*, Oxford University Press, New York, 3rd edn., 2004.

[48] F. Turpin, D. Guilon and R. Deschenaux, *Mol. Cryst. Liq. Cryst.*, 2001, **362**, 171.

[49] L. Frish, M. O. Vysotsky, V. Bohmer and Y. Cohen, *Org. Biomol. Chem.*, 2003, **1**, 2011.

[50] Y. Yamamoto, T. Fukushima, Y. Suna, N. Ishii, A. Saeki, S. Seki, S. Tagawa, M. Taniguchi, T. Kawai and T. Aida, *Science*, 2006, **304**, 1481.

[51] V. Duzhko, H. Shi, K. D. Singer, A. N. Semyonov and R. J. Twieg, *Langmuir*, 2006, **22**, 7947.

[52] G. Li, V. Shrotriya, J. Huang, Y. Yao, T. Moriarty, K. Emery and Y. Yang, *Nature Mater.*, 2005, **4**, 864.

[53] W. Ma, G. Yang, X. Gong, K. Lee and A. J. Heeger, *Adv. Mater.*, 2005, **15**, 1617.

[54] M. M. Weink, M. G. R. Turbiez, M. P. Struijk, M. Fonrodona and R. A. J. Janssen, *Appl. Phys. Lett.*, 2006, **88**, 153511.

[55] M. Yoshio, T. Kagata, K. Hoshino, T. Mukai, H. Ohno and T. Kato, *J. Am. Chem. Soc.*, 2006, **128**, 5570.

[56] M. Yoshio, T. Ichikawa, H. Shimura, T. Kagata, A. Hamasaki, T. Mukai, H. Ohno and T. Kato, *Bull. Chem. Soc. Jpn.*, 2007, **80**, 1836.

[57] H. Shimura, M. Yoshio, K. Hoshino, T. Mukai, H. Ohno and T. Kato, *J. Am. Chem. Soc*., 2008, **130**, 1759.

[58] S. Kumar and S. K. Pal, *Tetrahedron Lett.*, 2005, **46**, 4127.

Chapter 5

Self-Assembled Monolayers of Liquid Crystalline disulphides and Thiols on Gold Surface

Self-assembled monolayers (SAMs) are formed by the spontaneous adsorption of certain molecules on the surface resulting in the formation of a single layer of the molecules. SAMs of organic thiol molecules on the gold surface are of special interest due to their long-term stability and potential applications which have been described in chapter 1. The present chapter describes the formation and electrochemical characterisation of cyanobiphenyl attached disulphides and triphenylene functionalised thiols on gold surface, where the disulphides show nematic phase and the triphenylene thiols show columnar hexagonal phase in the bulk. The electron transfer barrier properties, double layer capacitance and the ionic permeability of these monolayer modified surfaces are discussed in this chapter.

5.1 Introduction

Molecular self-assembly on surfaces refers to the spontaneous adsorption of molecules on a solid surface [1, 2]. In general, adsorption processes involve either chemical or physical forces. An example of physical adsorption of long chain molecules is the formation of Langmuir monolayers, while the chemisorption is involved in the formation of self-assembled monolayers (SAMs) leading to a single layer of the molecules on the surfaces [2]. Due to the high stability of the thiol monolayers on the metal surface, they find a variety of applications in the field of biosensors, molecular electronics, nanolithography, corrosion inhibition etc. A general discussion on the properties and applications of SAMs has already been presented in the chapter 1.

Many interesting aspects of the monolayers can be revealed by the electrochemical characterisation of the monolayer modified electrodes. Due to the insulating hydrocarbon chain or similar organic groups of the monolayers, the electrode surface is not easily accessible by the electrolytes. This results in a blocking of electron transfer process between the electrode and the redox probes in the solution. For an ideally perfect monolayer, the redox reaction will be fully blocked even though due to the presence of pinholes and defects, there may be a small but significant Faradaic current. Due to this, the electrode exhibits a microelectrode array behaviour [1].

Monolayers with specific thiol molecules can be used for the selective permeability of certain molecules. On the other hand, terminally functionalised monolayers are used for the preconcentration of certain analyte molecules on the electrode surface, so that the detection limit of the analyte can be improved. Monolayers with terminal functional groups can be further functionalised with a variety of enzymes that have been widely used for the biosensor applications [3]. The adhesion of the molecules on the electrode can be improved by the modification of the surface with SAMs. For example, it has been shown that the adhesion of polyaniline on 4-aminothiophenol SAM is better compared to the adhesion on bare gold electrode [4].

In the present chapter we describe the following aspects of monolayers, *viz* the electron transfer barrier properties of the monolayers, the capacitance, permeability and disorganisation of the monolayers.

5.1.1 Double Layer Structure

The double layer structure of the electrode|electrolyte interface is the basis of all the electrochemical properties of the electrode surface. For a typical metal electrode in solution, the double layer consists of the Helmholtz layer and the diffuse layer. Under normal experimental conditions and low concentrations of the electrolyte, the Helmholtz layer dominates the interfacial capacitance values generally about 10 $\mu F/cm^2$ for a clean metal surface. When an insulating layer like SAMs of long chain alkanethiols is formed on the electrode surface, it constitutes the dielectric layer between the electrode surface and the electrolyte. The monolayer formed at the electrode|electrolyte interface is hydrophobic. Therefore, water molecules and ions near the interface do not permeate the dielectric film. The dielectric film formed by SAM increases the thickness of the interface and due to this, the interfacial capacitance decreases drastically. Moreover, it has been observed that the normal metal-electrolyte interfacial capacitance values are dependent on the electrode potential due to the presence of excess ions on the interface, while the capacitance values of monolayer modified electrodes are weakly dependent on the electrode potential [1].

Since the organic layer has a low dielectric constant and finite thickness, the double layer capacitance reduces significantly for the monolayer modified electrode according to the equation

$$C = \frac{\varepsilon_o \varepsilon_m}{d} A$$

where ε_0 and ε_m are the dielectric constant for the vacuum and the monolayer molecule respectively, d is the thickness of the monolayer and A is the area of the electrode. The capacitance value varies inversely with the alkyl chain length for a compact impermeable electrode. For short chain alkanethiol monolayers, the capacitance values are always greater than the expected value due to the higher permeability of the solution species through the monolayer. On the contrary, for the monolayers where the terminal groups are highly hydrophobic and are totally impermeable to ions and solvated molecules, there is a significant decrease in the capacitance due to the presence of hydrophobic gap between the monolayer modified surface and the hydrophilic electrolytic medium [5, 6].

5.1.2 Ionic Permeability

For a compact monolayer formed by normal alkanethiol monolayers, the molecules in the electrolytes are not capable of direct contact with the electrode. Under such conditions, as mentioned before, the double layer structure of the electrode|electrolyte interface changes and as a result, the double layer capacitance decreases. On the other hand, for monolayers modified with short chain thiols, where the organisation of the molecules are not perfect, the ions can reach the electrode surface through the pinholes and defects in the monolayer. The smaller the ions, the better they can permeate through the monolayer. As a result of this, the coverage of the monolayers calculated using the electrochemical methods will depend upon the size of the ions used.

5.1.3 Gold Oxide Stripping Analysis

The presence of pinholes and defects in the monolayer may be identified by the gold oxide stripping analysis. Here the gold electrode is cycled in perchloric acid solution. As shown in Figure 5.1, a gradual increase in the current during the positive potential scan is followed by a sharp rise at +1.2 V vs. SCE due to the formation of gold oxides on the surface. On the reverse potential sweep, these gold oxides on the metal surface are reduced to gold, which gives rise to the so-called stripping peak. For a pure gold surface, the integrated charge under this peak is measured to be 410 μC/cm^2 [7]. On the other hand, after the monolayer formation, the exposed area of the electrode towards the electrolyte decreases and hence the corresponding reverse peak. In this case, the gold oxide formation is due to the access of small OH^- ions through the pin holes, voids and defects. From the charge under this peak for the bare gold surface and for the monolayer modified electrode, the coverage of the monolayer on the metal surface can be calculated using the formula [7]:

$$\theta = 1 - \frac{Q_{SAM}}{Q_{Au}}$$

Where Q_{SAM} and Q_{Au} are the integrated area under the reverse peak for the SAM modified electrode and for the bare gold electrode respectively and θ is the surface coverage. Q_{SAM} corresponds to the charge value due to exposed gold to the electrolyte with the remaining region covered with the monolayer.

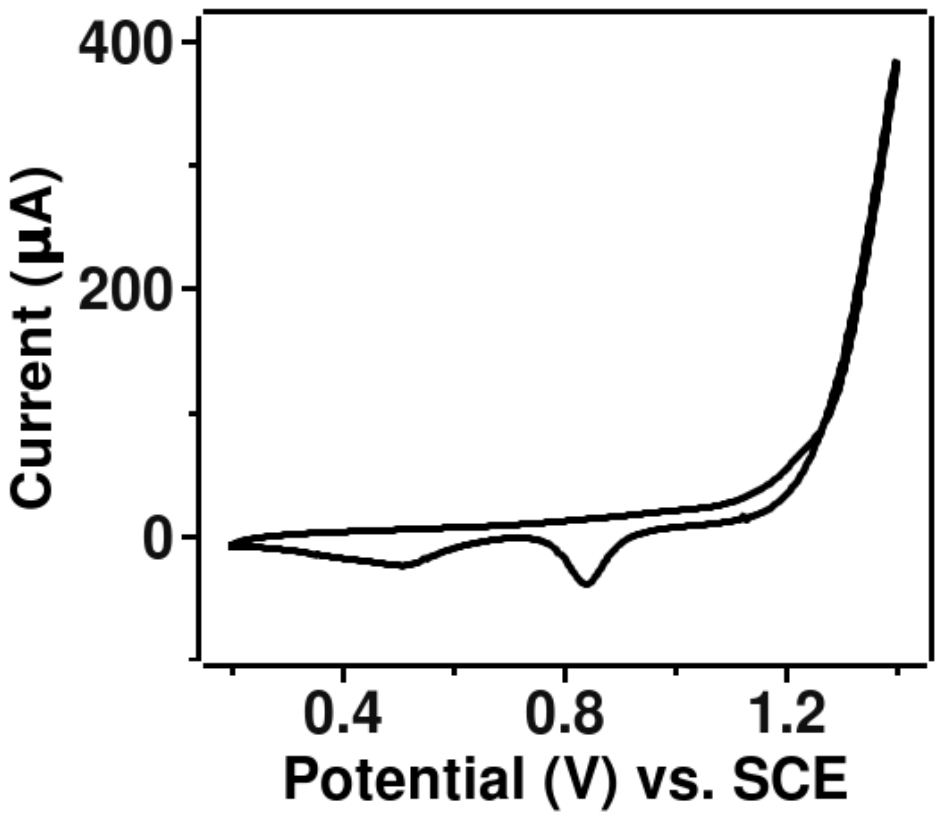

Figure 5.1: Cyclic voltammogram of bare gold electrode in 0.1 M $HClO_4$ showing the formation of gold oxide during the forwards sweep and the stripping of the gold oxide during the reverse sweep

5.1.4 Electron Transfer Barrier Properties

The SAMs introduce a compact insulating film between the metal electrode and the electrolyte. This prohibits the direct approach of the redox probes in the solution to the metal electrode, which means that the electron transfer between the electrode and the solution is totally inhibited in the presence of a perfect monolayer. As mentioned before, cyclic voltammetry and electrochemical impedance spectroscopy can be used to study the electron transfer blocking behaviour of these modified films. On a bare electrode, cyclic voltammogram shows a reversible redox reactions with a peak separation of 59/n mV in an n-electron redox process, as shown in Figure 5.2. On the other hand, on a modified electrode, the CV shows an irreversible behaviour with no peak formation, as shown in Figure 5.3.

Figure 5.4 shows the EIS data for a bare gold electrode and a monolayer modified elec-

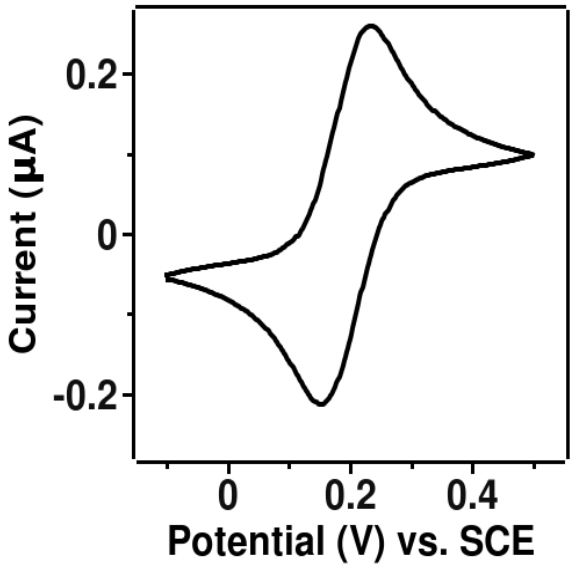

Figure 5.2: Cyclic voltammogram of 10 mM ferrocyanide/ferricyanide reaction on a bare gold electrode

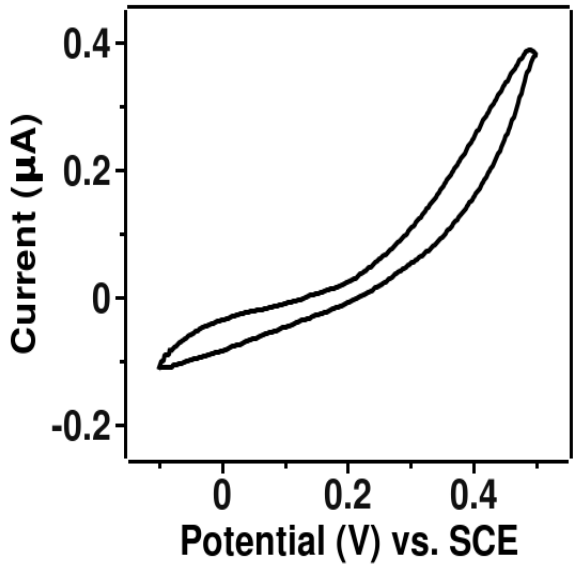

Figure 5.3: Cyclic voltammogram of 10 mM ferrocyanide/ferricyanide reaction on hexadecanethiol(HDT) monolayer modified gold electrode

trode in ferrocyanide/ferricyanide system. It can be seen that the bare gold electrode shows very small semicircle which indicates a facile electron transfer process between the electrode and the redox probe. On the other hand, the monolayer modified electrode as shown in Figure 5.5, shows a very large semicircle indicating that the electron transfer process on the modified electrode is inhibited due to the compact film formed on the surface. On the monolayer modified electrode, the hydrophobic-hydrophobic interactions between the alkyl chains of the thiol molecules lead to a compact impermeable monolayer film. This results in a very high charge-transfer resistance for the normally reversible redox system in the EIS studies. Therefore higher the charge-transfer resistance for the redox reaction, better will be the electron transfer barrier property of the film. This aspect will be discussed later in this chapter.

5.1.5 Disorganisation of Monolayers

The typical long chain alkanethiol monolayers show very high electron transfer barrier properties towards different redox probes under normal conditions. On the other hand, potential

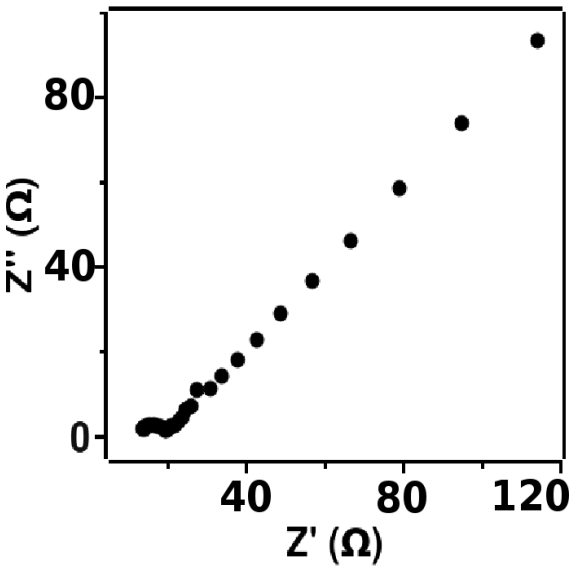

Figure 5.4: Electrochemical impedance spectroscopic plots for the 10 mM ferrocyanide/ferricyanide reaction on a bare gold electrode

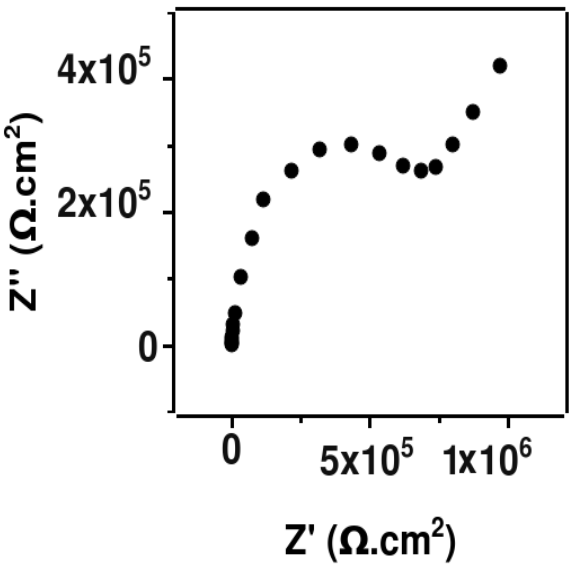

Figure 5.5: Electrochemical impedance spectroscopic plots for the 10 mM ferrocyanide/ferricyanide reaction on a hexadecanethiol(HDT) monolayer modified gold electrode

cycling in organic media disrupts the compact structure of these monolayers and results in the disorganisation of the monolayers forming voids. The driving force for the disorganisation is the van der Waals interaction between the alkyl or other hydrophobic chains with the hydrophobic part of the solvent or the redox probes. The disorganised monolayers facilitate the electron transfer between the metal electrode and the redox probe in the solution through the voids. A schematic representation of the disorganisation of the monolayers is shown in Figure 5.6. A disorganised monolayer also facilitates high permeability of ions through the monolayer, that results in the higher capacitance at the interface and lower charge-transfer resistance.

The present chapter deals with our experimental results on the characterisation of different monolayers on the gold surface. We have extensively used the electrochemical techniques like cyclic voltammetry and electrochemical impedance spectroscopy for the characterisation of the monolayer modified surfaces. Using these techniques, we have analysed the electron transfer barrier properties and also measured the double layer capacitance of the monolayer

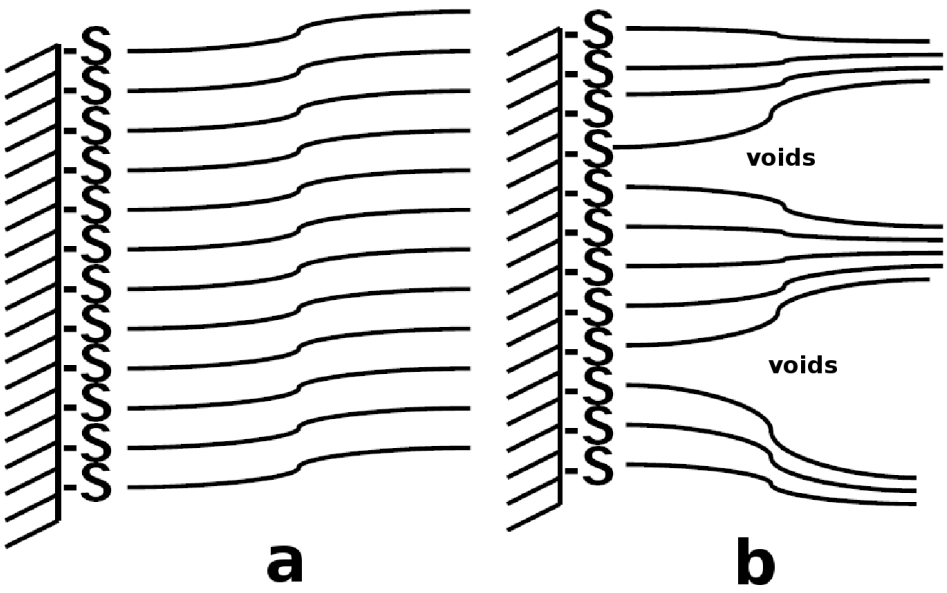

Figure 5.6: A schematic representation of a) compact and b) disorganised monolayer

modified electrodes. This chapter is divided into 2 sections. The section 5.3 deals with the electrochemical and surface characterisation of SAMs of rod-like disulphides and section 5.4 on the monolayers of discotic triphenylene functionalised thiols that show columnar hexagonal liquid crystalline phase in the bulk.

5.2 Experimental Section

Gold electrode: A gold sample of 99.99 % purity was obtained from Arora Mathey, India. Evaporated gold (about 100 nm thickness) on glass with chromium under layers (∼2-5 nm thickness) was used for the monolayer formation and later used for characterisation by electrochemical techniques and grazing angle FTIR spectroscopy. The evaporated gold substrate has been shown to have a very smooth surface with predominantly Au (111) orientation. These gold samples were used as strips of area about 0.25 cm^2 for the SAM formation. These strips were cleaned with piranha solution for 30 seconds (*Caution: Piranha solution is 1:3 v/v mixture of 30% H_2O_2: 96% con. H_2SO_4, which is highly reactive with organic compounds and storing in a closed container and exposure to direct contact should be avoided*), washed with distilled water and finally rinsed with millipore water and dried before the formation of SAMs.

SAM preparation: The thiols were dissolved in dichloromethane to form a 1 mM solution. The gold electrodes after the piranha treatment were immersed in the solution and kept for 12 hours for the SAM formation. The electrodes were then washed with dichloromethane to remove any physically adsorbed thiols on the surface. These electrodes were then cleaned with distilled water and finally rinsed with Millipore water and used for further characterisations.

Electrochemical characterisation: The cyclic voltammetric studies of the SAM modified electrodes were carried out using three different redox systems, namely 1 mM ferrocene, 10 mM ferrocyanide|ferricyanide and 1 mM hexaammineruthenium (II|III). Ferrocene, a hydrophobic redox probe was studied in a non-aqueous solvent, propylene carbonate with 0.1 M $LiClO_4$ acting as a supporting electrolyte in this medium. The other two redox probes were studied in aqueous solution. For potassium ferrocyanide|ferricyanide system, 1 M sodium fluoride (NaF) and for the hexaammineruthenium (II|III) system 0.1 M $LiClO_4$ were used as the supporting electrolytes. The cyclic voltammograms for the bare gold electrode were carried out in all these three redox systems for comparison at a scan rate of 50 mV/s. The electrochemical impedance studies were carried out at the half-peak potential of the redox system with an ac amplitude of 10 mV in a frequency range of 100 mHz to 100 kHz.

Instrumentation: Cyclic voltammetric studies were carried out using a potentiostat (EG&G model 263A) interfaced with a PC through GPIB (National Instruments). A conventional three electrode system was used for all the electrochemical characterisation, with a saturated calomel electrode (SCE) as the reference electrode and platinum foil as the auxiliary electrode. Either bare gold or the SAM modified electrodes were used as the working electrode. The electrochemical impedance spectroscopic studies (EIS) were performed using a Lock-in-Amplifier (Perkin Elmer Model 5210) along with the potentiostat interfaced to a PC. The EIS studies were carried out using Power Suite software (EG&G) and the equivalent circuit fitting by ZSimpWin software (EG&G). The FTIR spectrum of the monolayer-modified gold surface was carried out using Shimadzu FTIR model 8400 instruments at a grazing angle of 85° (FT-85, Thermo Spectra-Tech). The bare gold surface was used as a reference for the spectral studies.

5.3 Monolayers of Rod-like disulphides

Liquid crystalline materials have the orientational order of crystalline phase and the dynamic nature of liquid phase in the bulk under a definite temperature range. These mesogenic molecules, depending upon their orientation, may form different liquid crystalline phases like nematic, smectic and columnar phases that changes with temperature [8]. Self-assembled monolayers formed by these liquid crystalline materials are of great interest from the point of view of the orientation of the molecules on the surface [9]. There are several reports on the SAM formation of rod-like liquid crystalline materials on gold surface, especially of cyanobiphenyl thiols. Alloisio *et al.* have reported the 2-dimensional SAM formation on flat gold surface and 3-dimensional SAM formation on gold nanoparticles by diacetylenes functionalised disulphide [10]. They have shown that the nanoparticles stabilised by these disulphides are of two different sizes consisting of $\sim$4.5 nm and $\sim$21 nm in diameter. SAM formation by triphenylene substituted disulphides were studied in the literature using FTIR, quartz crystal microbalance (QCM) as well as AFM, where the studies show that the discotic cores lie in an edge-on configuration with respect to the gold surface [11]. The SAM formation of alkoxycyanobiphenyl thiols that show nematic phase in the bulk and its electrochemical characterisation have also been reported [12, 13].

In the present section, we describe the SAM formation by rod-like disulphides of alkoxycyanobiphenyl molecules that show a nematic phase in the bulk. The monolayers are characterised by electrochemical techniques like cyclic voltammetry (CV) and electrochemical impedance spectroscopy (EIS).

5.3.1 Experimental Section

The cyanobiphenyl based disulphide molecules were synthesised as reported earlier by S. Kumar *et al.* [14], where DSn represents 4'-{[n-({n-[(4'-Cyano[1,1'-biphenyl]-4yl)oxy]hexyl}-disulphanyl)hexyl]oxy}[1,1'-biphenyl]-4-carbonitrile, with n being the alkyl chain length. A schematic diagram showing the synthesis of these molecules is shown in Figure 5.7. The molecules with lower alkyl chains show a nematic liquid crystalline phase, while higher homologous compounds show a smectic A phase at higher temperature near 100 °C. The electrochemical studies like cyclic voltammetry (CV) and electrochemical

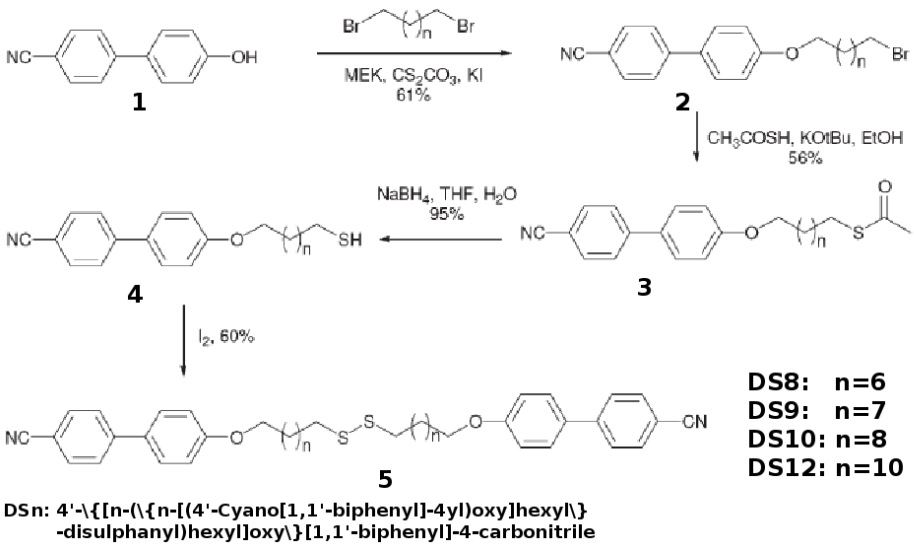

Figure 5.7: The scheme for the synthesis of the cyanobiphenyl based disulphide molecules

impedance spectroscopy (EIS) were carried out using two different redox systems, *viz.* ferrocyanide/ferricyanide and hexaammineruthenium(II/III) chloride systems. The EIS studies were performed at the half-peak potential of the corresponding redox system calculated from the CV studies.

5.3.2 Results and Discussion

5.3.2.1 Cyclic Voltammetry

Figure 5.8 shows the cyclic voltammograms of the monolayer modified electrodes in 10 mM ferrocyanide/ferricyanide system. The figure shows the CV for the bare gold electrode along with DS8, DS9, DS10 and DS12 modified electrodes. It is clear from the figure that the modified electrodes show a better blocking behaviour compared to the bare gold electrode. The electron transfer barrier property of the lower chain thiols is less and the blocking ability increases with increase in chain length. For the DS12 monolayer, the electron transfer process is almost fully blocked. It may be noted that the blocking behaviour of DS8 and DS9 modified electrodes are quite less as compared to the normal alkanethiol monolayer with similar chain lengths. The bulky cyanobiphenyl groups at the terminal positions of the monolayers prevents compact ordering of the monolayer on the surface, which results in a lower blocking ability.

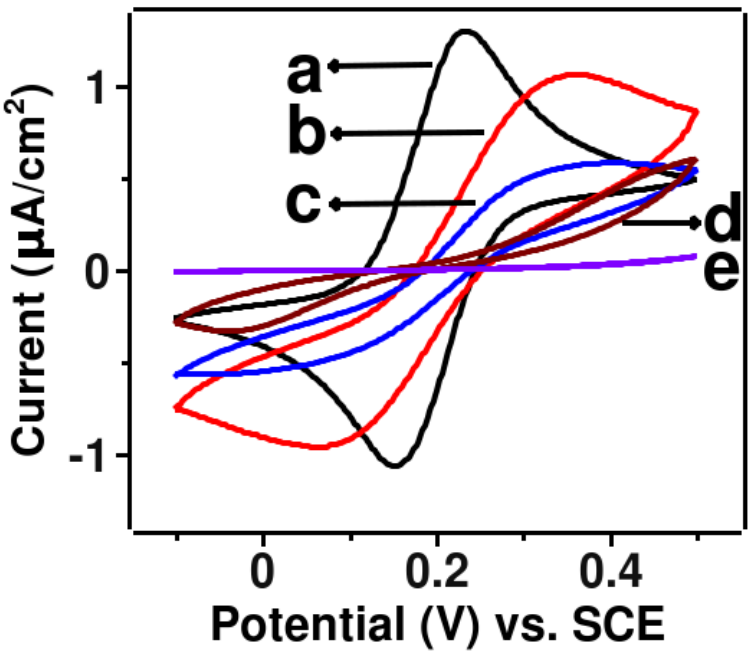

Figure 5.8: Cyclic voltammograms in ferrocyanide/ferricyanide using a) bare gold electrode and b) DS8, c) DS9, d) DS10 and e) DS12 modified electrodes

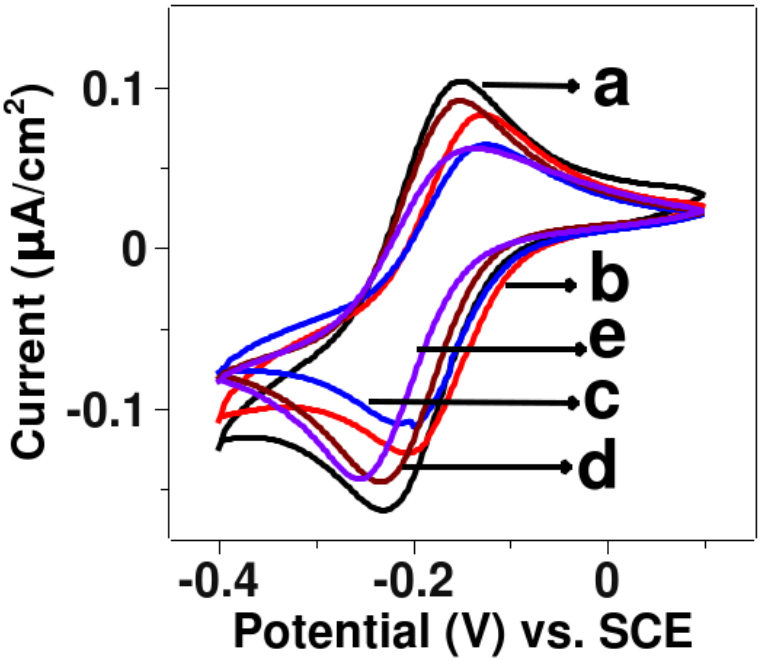

Figure 5.9: Cyclic voltammograms in hexaammineruthenium(II/III) using a) bare gold electrode and b) DS8, c) DS9, d) DS10 and e) DS12 modified electrodes

Figure 5.9 shows the cyclic voltammograms of the bare gold electrode and the different disulphide modified electrodes in 1 mM hexaammineruthenium (II/III) chloride solution. It is observed that the bare electrode as well as the modified electrodes show a facile redox reaction in this medium. It has been proposed earlier that hexaammineruthenium(II/III) undergoes an outer sphere electron transfer reaction and the reaction rate is less dependent on the solvent environment for the electron transfer to occur [15]. As a result, direct contact between the redox site and the electrode is not essential for the redox reaction to occur which means that the monolayer offers no hindrance to the redox reaction. A similar behaviour was observed previously on other monolayer modified electrodes [16].

5.3.2.2 Electrochemical Impedance Spectroscopy

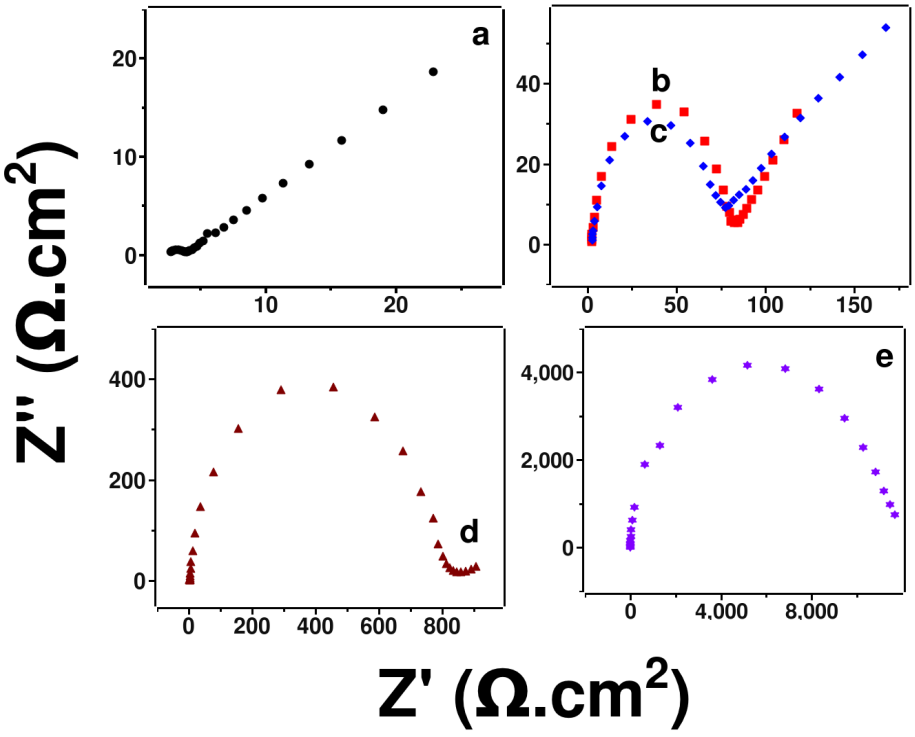

Figure 5.10: Real vs. imaginary plots from electrochemical impedance spectroscopy in ferrocyanide/ferricyanide system using a) bare gold electrode and b) DS8, c) DS9, d) DS10, and e) DS12 modified electrodes modified electrodes

We have carried out the electrochemical impedance studies in ferrocyanide/ferricyanide and hexaammineruthenium(II/III) redox systems using bare gold electrode as well as the dif-

Table 5.1: Values of the solution resistance (R_u), double layer capacitance (C_{dl}), charge-transfer resistance (R_{ct}), and Warburg impedance (Z_W) for the bare and DS SAM modified electrodes using ferrocyanide/ferricyanide reaction. *: R(CR) circuit was used for the fitting

	R_u (Ω)	C_{dl} (F/cm^2)	R_{ct} ($\Omega.cm^2$)	Z_W ($S.s^{1/2}.cm^2$)
BAu	67.05	2.31×10^{-6}	5.65	9.24×10^{-3}
HDT	952.1	3.53×10^{-8}	5.01×10^{5}	1.75×10^{-6}
DS8	12.81	2.44×10^{-6}	75.72	0.0233
DS9	14.32	1.78×10^{-6}	71.72	9.68×10^{-3}
DS10	14.33	1.97×10^{-6}	503.8	2.25×10^{-3}
DS12*	2.73	1.86×10^{-6}	1.03×10^{4}	-

ferent disulphide monolayer modified electrodes. Figure 5.10 shows the real vs. imaginary components of the impedance for the electrodes in ferrocyanide/ferricyanide redox system. The bare gold shows a very small semi-circle while the diameter of the semicircle increases with increasing chain length of the disulphide monolayer except in the case of DS9, where it is similar to that of DS8. The diameter of the semicircle corresponds to the charge-transfer resistance of the redox reaction. The impedance data were fitted using Randles equivalent circuit and the fitting parameters are presented in Table 5.1. From the table, it is observed that the R_{ct} values increase correspondingly and the redox reaction gets slower with the increase in chain length. This observation is in accordance with the CV results.

Figure 5.11 shows the impedance spectroscopic results for the bare gold and different DS modified electrodes in hexaammineruthenium(II/III) system and the fitting parameters using Randles equivalent circuit is presented in Table 5.2. Here the R_{ct} values are very less for all the modified electrodes, which is contrary to the results with the ferrocyanide/ferricyanide system. As discussed earlier, this is due to the outer sphere electron transfer reaction of the hexaammineruthenium system. The electron tunneling from the electrode surface to the redox site through the monolayer can also contribute to the low barrier properties [15]. Even though the R_{ct} values in general are less, they increase with the chain length of the molecules. As the chain length increases, the barrier to electron transfer also increases due to the better

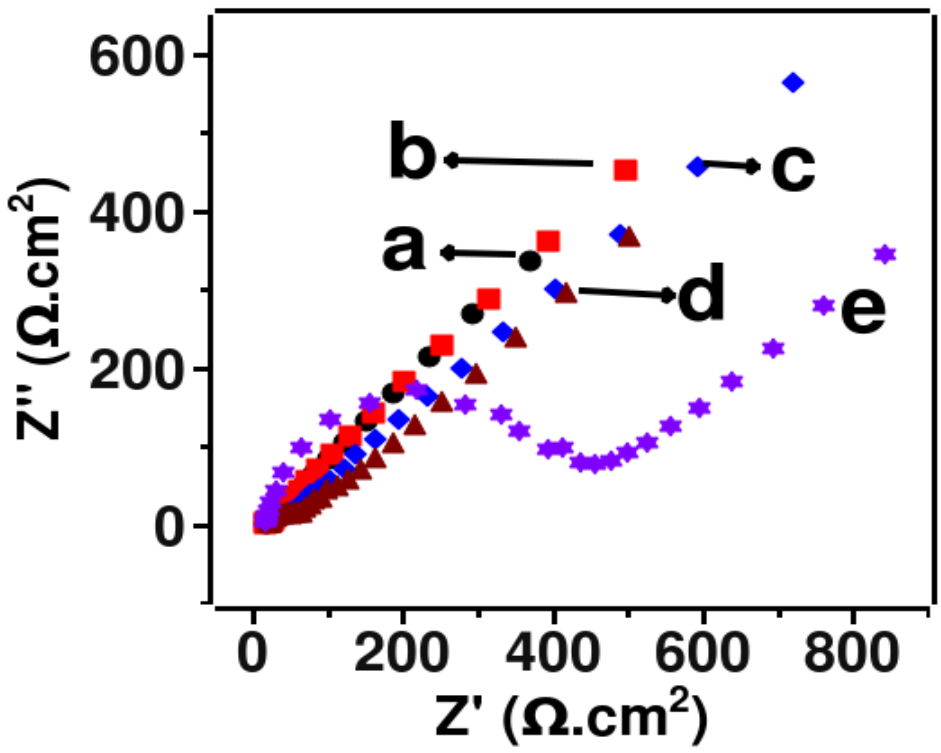

Figure 5.11: Real vs. imaginary plot from electrochemical impedance spectroscopy in hexaammineruthenium(II/III) system using a) bare gold electrode and b) DS8, c) DS9, d) DS10 and e) DS12 modified electrodes modified electrodes

packing of the monolayers which acts as an insulating layer between the electrode and the electrolyte.

We have observed that the barrier to electron transfer for the disulphide SAMs are less compared to alkanethiol SAMs of similar chain length. This shows that the packing of the monolayers are poor with the presence of a large number of pinholes and defects. These defects mainly arise due to the presence of bulky cyanobiphenyl terminal groups that are attached to the thiol molecules. The modified electrodes show very low impedance towards the redox reaction of hexaammineruthenium reaction irrespective of the chain length. This can be attributed to the fact that hexaammineruthenium undergoes an outer sphere reaction mechanism and the reaction may take place by through-bond tunneling of electrons between the electrode and the redox probes.

Table 5.2: Values of the solution resistance (R_u), double layer capacitance (C_{dl}), charge-transfer resistance (R_{ct}), and Warburg impedance (Z_W) for the bare and DS SAM modified electrodes using hexaammineruthenium(II/III) reaction

	R_u (Ω)	C_{dl} (F/cm^2)	R_{ct} (Ω.cm^2)	Z_W (S.s$^{1/2}$.cm^2)
BAu	69.64	1.59×10^{-6}	4.586	5.19×10^{-3}
HDT	3.47×10^{4}	3.55×10^{-8}	5.14×10^{5}	1.64×10^{-6}
DS8	76.13	5.4×10^{-7}	4.21	1.94×10^{-3}
DS9	102.9	1.49×10^{-6}	21	1.21×10^{-3}
DS10	93.72	1.99×10^{-6}	29.06	1.89×10^{-3}
DS12	126.5	1.61×10^{-6}	372.1	2×10^{-3}

5.3.2.3 Capacitance Measurements

The double layer capacitance values of the bare gold electrode as well as the SAM modified electrodes were measured by the electrochemical impedance spectroscopy in 1 M NaF solution. The capacitance was calculated from the imaginary part of the impedance using the equation [17]

$$C_{dl} = \frac{1}{\omega Z''}$$

Where C_{dl} is the double layer capacitance, ω the angular frequency (=2πf, f being the frequency) and Z'' is the imaginary part of the impedance. Table 5.3 represents the double layer capacitance values measured for the different disulphide SAM modified electrodes. The values indicate that the capacitance has decreased to a large extent for the modified electrodes compared to the bare gold electrode but not in proportion to the chain length of the molecules. It may be noted that the capacitance values of the modified electrodes are more or less of the same range for different chain lengths. This indicates that the double layer structure of all the monolayer modified electrodes is similar. Normally the double layer capacitance values of alkanethiol SAMs are <1 μF/cm^2 while for the disulphide SAMs presented here, the capacitance values are several μF/cm^2 [6]. This is due to the higher permeability of the ions through the monolayer, which originates from the less compact structure of the molecules on the surface.

Table 5.3: Double layer capacitance values for the bare gold surface and the disulphide monolayer modified surfaces in 1 M NaF calculated from electrochemical impedance spectroscopy

System	Capacitance (F/cm^2)
BAu	6.4×10^{-6}
DS8	1.34×10^{-6}
DS9	2.56×10^{-6}
DS10	1.98×10^{-6}
DS12	2.44×10^{-6}

In summary, we have presented the electrochemical characterisation of the cyanobiphenyl functionalised disulphide SAMs on gold surface. The SAM modified electrodes with lower chain length of the monolayer show lower barrier for electron transfer, which however increases with increase in chain length. In general, the barrier to electron transfer process is less compared to the alkanethiol monolayers, since the monolayers of disulphides are less compact owing to the bulky cyanobiphenyl groups at the terminal position. The double layer capacitance values of these monolayers are quite high due to the less compact monolayer and the presence of polar cyano groups.

5.4 Monolayers of Triphenylenethiols

As mentioned in the previous section, there are several reports on the SAM formation by rod-like molecules on the metal surfaces. On the other hand, there are very few reports on the monolayer studies using discotic liquid crystalline compounds. Allinson *et al.* have studied the SAMs formed by different triphenylene based thiols on the gold surface using ellipsometry and STM studies, where they have shown that depending on the number and position of the thiols, the monolayer can have either vertical or horizontal arrangement [18, 19]. They have also shown that the SAMs based on these discotic molecules are less hydrophobic compared to the alkanethiol SAMs [18, 19]. Owens *et al.* have described the STM imaging of triphenylene based thiol monolayers on gold surface, where they have reported that the

2-dimensional ordering of these discotic molecules were improved after dipping the monolayer in a saturated solution of TNF, due to the charge-transfer complex formation between the triphenylene and trinitrofluorenone (TNF) molecules [20]. Charra *et al.* have shown that the chiral ordering of SAMs of discotic molecules on the surface can be tuned by changing the chain length of alkoxy groups [21]. Yamada *et al.* showed the one-dimensional and hexagonal arrangement of discotic modified gold nanoparticles induced by changing the solvent polarity [22]. The orientation of such discotic molecules as monolayer on the metal surface has also been studied, where it has been shown that the triphenylene based monolayers may form either a face-on or an edge-on structure on the surface [11]. In the face-on configuration, the triphenylene cores are parallel to the electrode surface whereas in the edge-on configuration the cores are perpendicular to the electrode surface. Recently it was shown that triphenylene functionalised thiols can be used for the stabilisation of gold nanoparticles [23].

From the literature, we have observed that there are only some scattered reports on the electrochemical studies on the SAMs formed by discotic molecules even though a few reports are present on the self-organisation of such molecules on surfaces like HOPG or gold as described before. It is of great interest to study the electron transfer processes on the discotic molecules since they have very high one-dimensional conductivities and orientational order in the bulk. In this present work, we have carried out the electrochemical and FTIR characterisations of three different discotic triphenylene based thiols, having chain length of 6, 10 and 12 carbon atoms. These thiol modified SAMs were characterised by electrochemical methods like cyclic voltammetry, electrochemical impedance spectroscopy and capacitance measurements. The C_6TP thiol SAM shows very good blocking behaviour towards the redox reaction of ferrocyanide|ferricyanide system, while thiols with higher chain length (containing 10 and 12) show lower barrier properties. Using hexaammineruthenium(II/III) as a redox probe, all the modified electrodes show a very little blocking behaviour. In an organic solvent, we observe that due to disorganisation of the monolayers the electron transfer process is not inhibited significantly.

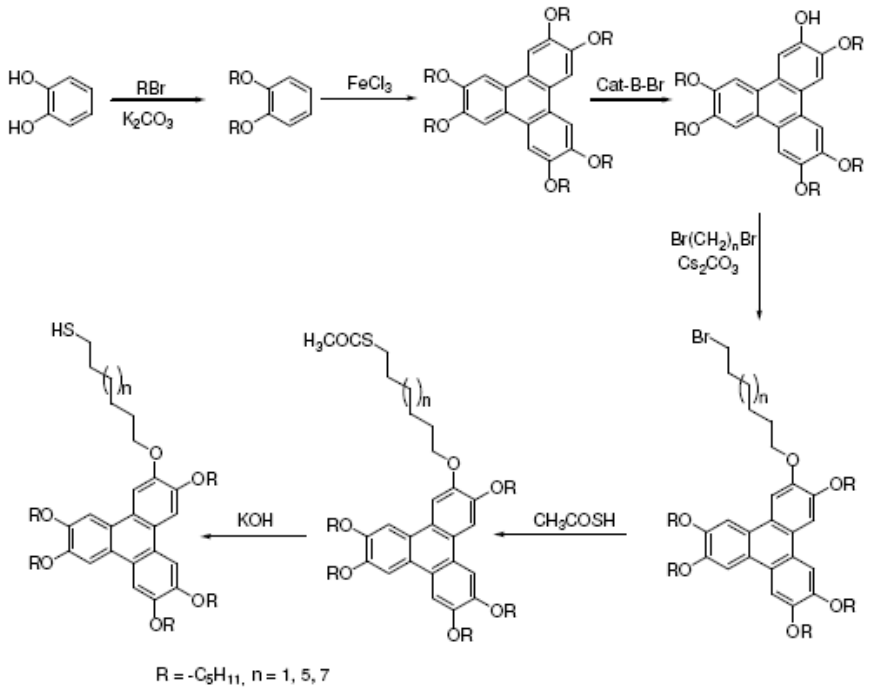

Figure 5.12: The scheme for the synthesis of the triphenylene-based thiol molecules

5.4.1 Experimental Section

Three triphenylene thiols having chain length of 6, 10 and 12 used in this study were provided by Prof. S. Kumar *et al.* and were synthesised by following the procedure as reported earlier [24, 23]. A schematic diagram of the synthesis of these molecules is shown in Figure 5.12. Dichloromethane (Rankem), potassium ferrocyanide (Loba), potassium ferricyanide (Qualigens), Sodium fluoride (S D fine-chem. limited), hexaammineruthenium (III) chloride (Alfa Aesar), ferrocene (Acros Organics), lithium perchlorate (Across organics) and ferrocenium tetrafluoroborate (Aldrich) were of analytical grade and used as received without further purification. Millipore water having a resistivity of 18 MΩ.cm was used for the preparation of all the aqueous solutions.

The monolayers were characterised using electrochemical techniques like cyclic voltammetry and electrochemical impedance spectroscopy and the experimental setup has been already described in the previous section. FTIR studies were carried out using Shimadzu FTIR model 8400 instruments at a grazing angle of 85° (FT-85, Thermo Spectra-Tech).

5.4.2 Results and Discussion

5.4.2.1 Cyclic Voltammetry

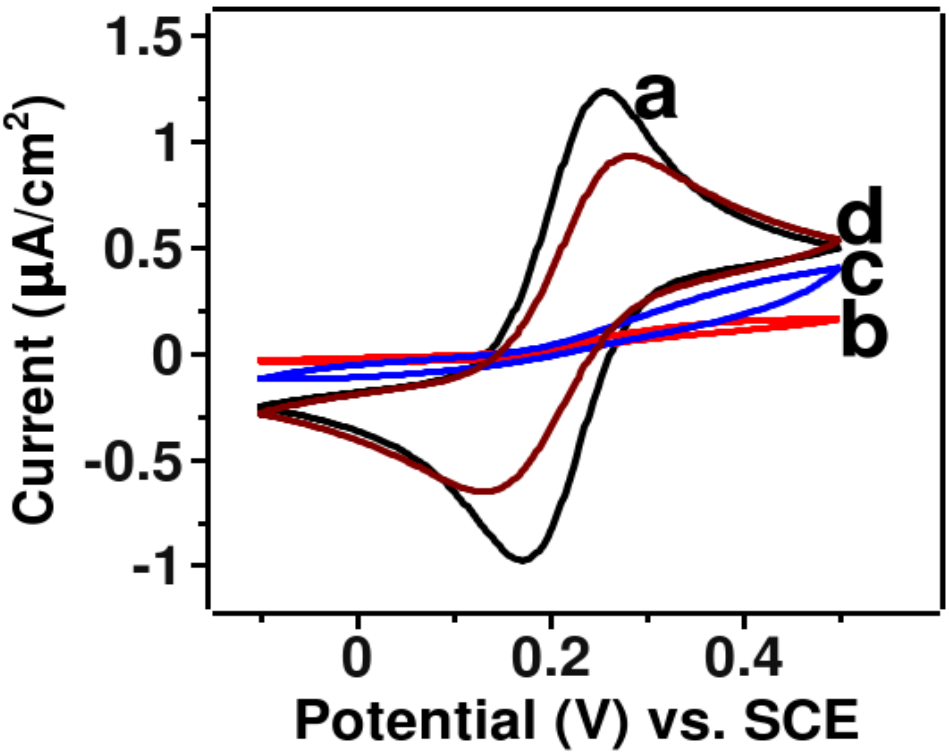

Figure 5.13: Cyclic voltammograms in 10 mM ferrocyanide/ferricyanide/1 M NaF/H_2O for a) bare electrode b) C_6TP, c) C_{10}TP and d) C_{12}TP modified electrodes

Figure 5.13(b-d) shows the cyclic voltammograms for the SAM-modified electrodes in 10 mM ferrocyanide/ferricyanide system containing 1 M NaF as the supporting electrolyte. The CV using the bare gold electrode is shown in Figure 5.13(a) for comparison. It can be seen from the figure 5.13(b) that the C_6TP has a better blocking property towards the ferrocyanide/ferricyanide system, while for C_{10}TP (Figure 5.13(c)) it is less and the C_{12}TP modified electrode (Figure 5.13(d)) behaves very similar to the bare gold electrode. This is contrary to the behaviour of typical alkanethiol SAM modified electrodes, where longer chain alkanethiol SAMs show better blocking behaviour to redox probes than shorter chain thiols. In alkanethiol monolayers, as the chain length increases, the packing will be more compact due to the hydrophobic-hydrophobic interaction among the hydrocarbon chains of the monolayers. In the present case, due to the π-π interaction of the discotic core, the

molecules can cluster together in different regions of the surface, which creates large number of voids within the monolayer surface as shown in Figure 5.14. This is more pronounced as the chain length of the thiol molecules increases due to higher flexibility of the alkyl chain of the thiol molecules. This allows the redox molecules to enter through the voids and undergo electron transfer reaction. A more quantitative study on these electron barrier properties based on the electrochemical impedance spectroscopy will be presented later in this chapter.

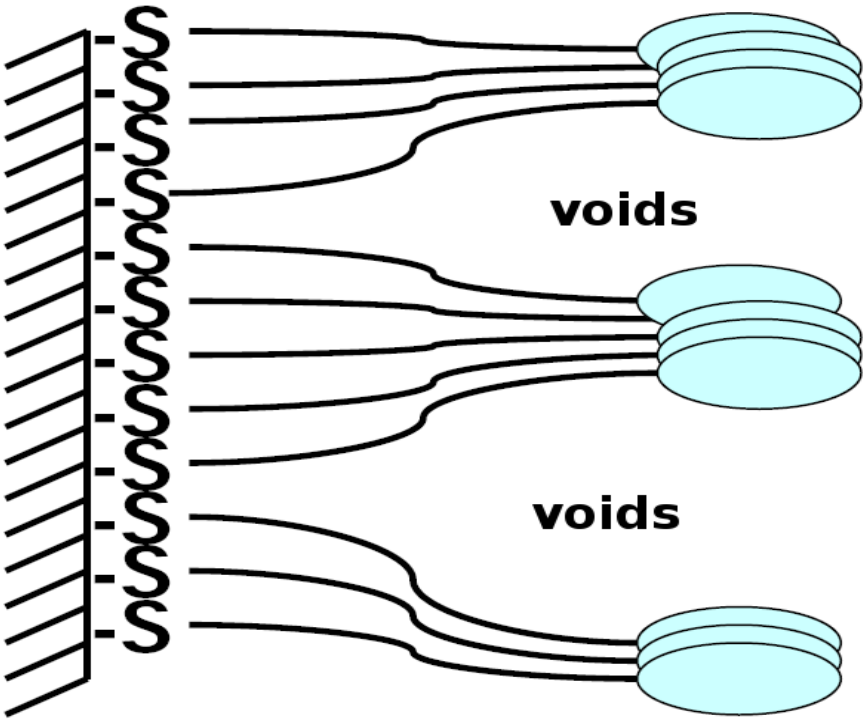

Figure 5.14: A schematic model of packing of the triphenylenethiols on the gold surface

The cyclic voltammetric studies of the monolayer modified electrodes in 1 mM hexaammineruthenium (II/III) system were carried out and the plots are shown in Figure 5.15(b-d). The cyclic voltammogram on the bare electrode is also shown for comparison as Figure 5.15(a). As can be observed from the plots, even though C_6TP and C_{10}TP modified electrodes show a good blocking behaviour towards the ferrocyanide/ferricyanide system (Figure 5.13(b-c)), all the three SAM modified electrodes show facile electron transfer towards the redox reaction of hexaammineruthenium (II/III) system (Figure 5.15(b-d)). A similar behaviour involving naphthalenethiol and alkanethiols was reported earlier [15, 16]. A further insight into this behaviour is provided in the following sections, where we discuss the results

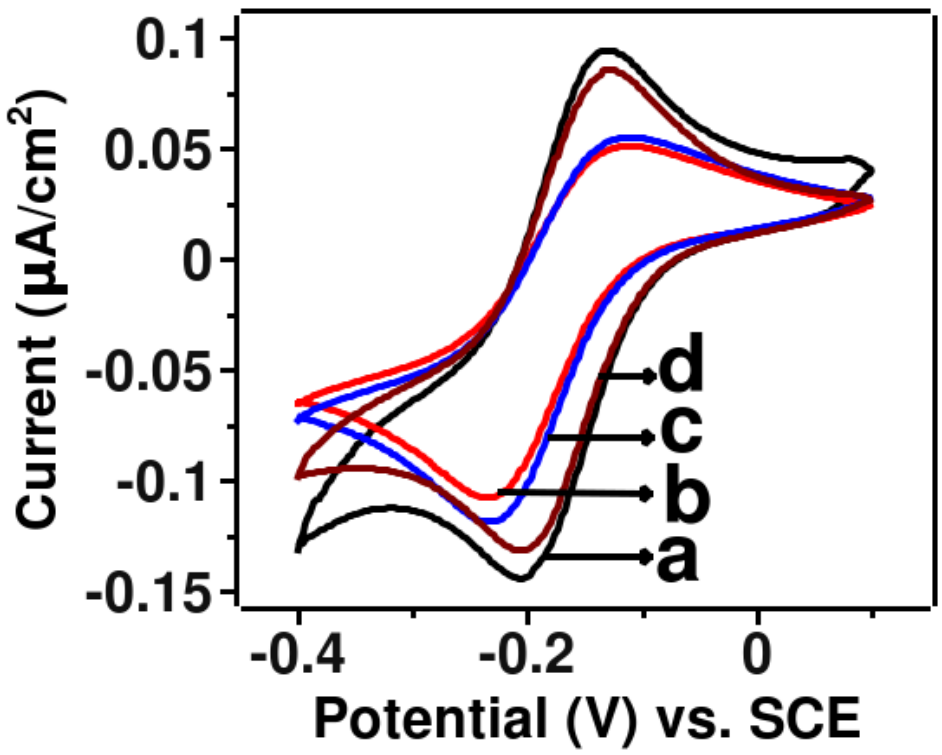

Figure 5.15: Cyclic voltammograms in 1 mM hexaammineruthenium(II/III)/0.1 M $LiClO_4/H_2O$ for a) bare electrode b) C_6TP, c) $C_{10}TP$ and d) $C_{12}TP$ modified electrodes

of the impedance spectroscopic studies to interpret the quantitative parameters of the redox reaction on the bare gold as well as on the SAM modified electrodes.

In order to study the effect of non-aqueous solvent on the blocking properties of the C_nTP SAM modified electrodes, the cyclic voltammetry in ferrocene system, a well-known redox probe in propylene carbonate medium was carried out. Figure 5.16 shows the cyclic voltammograms of bare gold and SAM modified electrodes when 1 mM ferrocene was used as the redox probe in propylene carbonate medium using 0.1 M $LiClO_4$ as the supporting electrolyte. As can be seen from the figure, all the three SAM modified electrodes show a facile redox reaction towards ferrocene. This can be attributed to the disorganisation of SAMs in the propylene carbonate medium. The disorganisation of the SAMs has been confirmed by cycling the same electrode modified with C6TP in 10 mM ferrocyanide/ferricyanide system, where the blocking ability is only partial, contrary to a freshly prepared monolayer surface, which has an excellent blocking ability. The electrode was annealed at 60 °C for 1 hour and the cyclic voltammetry was repeated in the 10 mM ferrocyanide/ferricyanide system for the

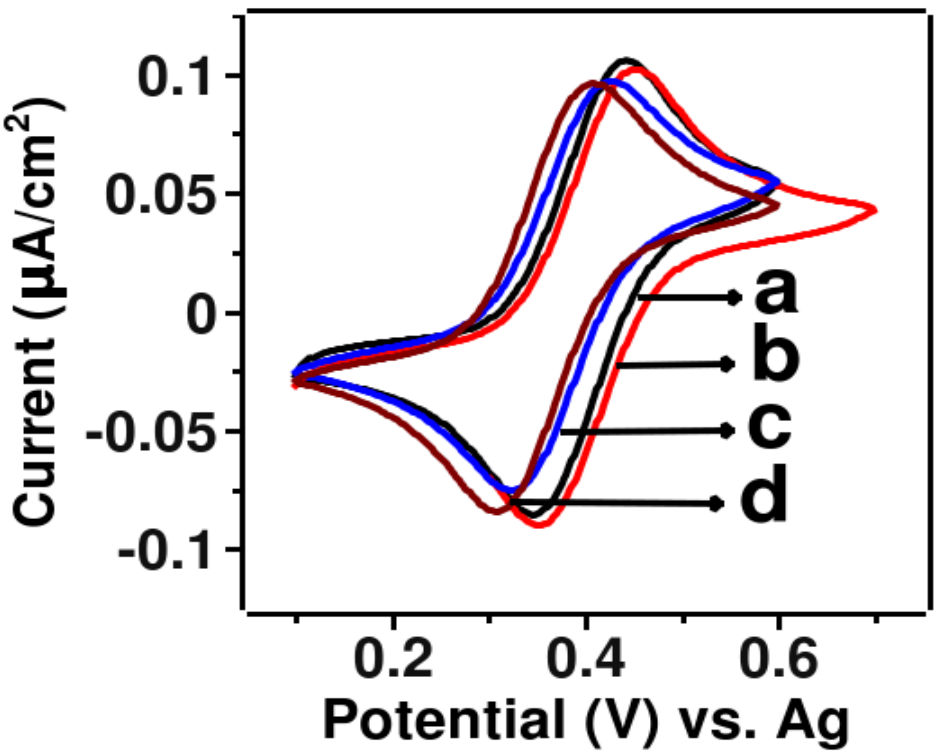

Figure 5.16: Cyclic voltammograms in 10 mM ferrocene/1 M $LiClO_4$/propylene carbonate for a) bare electrode b)C_6TP, c) C_{10}TP and d) C_{12}TP modified electrodes

same electrode. The better blocking property shown by this annealed electrode confirms the existence of the monolayer, which rules out any possibility of desorption of the monolayer from the gold surface. The annealing process removes the trapped solvent molecules and organises the monolayer by making it more compact. This results in a better blocking ability. Quantitative studies on the barrier properties of the modified electrodes have been carried out by electrochemical impedance spectroscopy which is discussed below.

5.4.2.2 Electrochemical Impedance Spectroscopy

The electrochemical impedance spectroscopic studies can be used to get a detailed information about the processes occurring at the interface like the double layer capacitance charging, kinetics of the redox reaction, diffusion of the ions towards the electrode surface etc. Such studies are of great interest for the monolayer modified electrodes. In the presence of the redox species, from the impedance studies, the kinetics of the redox reactions and therefore the barrier to electron transfer process can be calculated. In the present study, we have carried

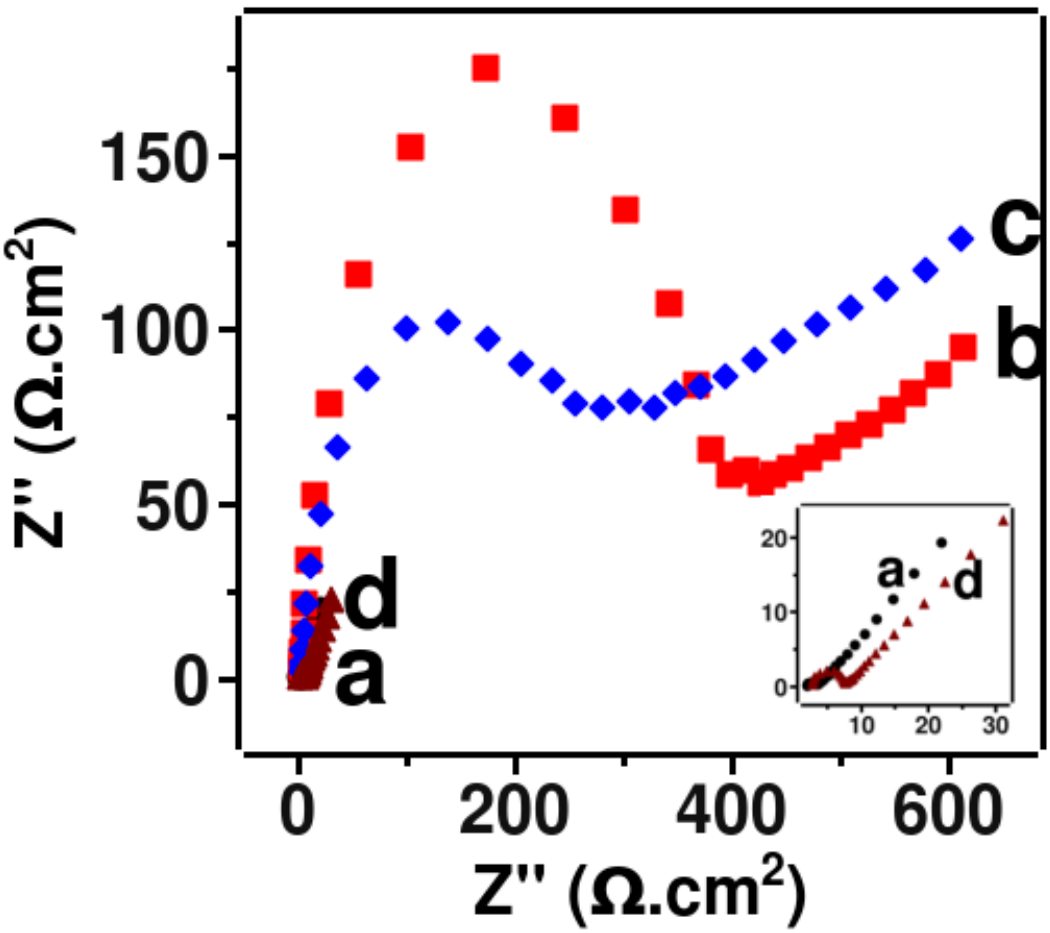

Figure 5.17: impedance plots in 10 mM ferrocyanide/ferricyanide/1 M NaF/H_2O for a) bare electrode b) C_6TP, c) C_{10}TP and d) C_{12}TP modified electrodes

Table 5.4: Values of the solution resistance (R_u, Ω), double layer capacitance (C_{dl}, F/cm^2), charge-transfer resistance (R_{ct}, Ω.cm^2), and Warburg impedance (Z_W, S.s$^{1/2}$.cm^2) for the bare and SAM modified electrodes using ferrocyanide/ferricyanide reaction

	R_u (Ω)	C_{dl} (F/cm^2)	R_{ct} (Ω.cm^2)	Z_W (S.s$^{1/2}$.cm^2)
BAu	13.59	1.48×10^{-5}	1.293	0.0475
C_6TP	17.7	8.32×10^{-7}	400.8	4.238×10^{-3}
C_{10}TP	17.08	1.34×10^{-6}	281	2.479×10^{-3}
C_{12}TP	11.01	5.26×10^{-6}	3.744	0.047225

out the impedance spectroscopic studies for all the three modified electrodes and for the bare gold electrode in three different redox systems at a potential corresponding to their formal potential calculated from the cyclic voltammetric studies.

Ferrocyanide/ferricyanide reaction: The impedance plots of the three SAM modified electrodes in 10 mM ferrocyanide/ferricyanide/ 1M NaF/H_2O system are shown in the Figure 5.17. The impedance plot for the bare gold electrode is also shown for comparison. We have observed from the plots that the C_6TP SAM modified electrode shows the highest blocking properties among the three modified electrodes. This is in accordance with the behaviour exhibited in the cyclic voltammetric studies. The plots were fitted with a modified Randles circuit containing the double layer capacitance, C_{dl} in parallel to a series combination of the charge transfer resistance R_{ct} and the Warburg impedance (Z_W). The solution resistance (R_u) was modeled in series to the above circuit. From the fitting of the plots we have calculated the charge-transfer resistance (R_{ct}) values for the ferrocyanide/ferricyanide reaction and the results are presented in Table 5.4. From the table, it can be seen that C_6TP and C_{10}TP thiols have higher R_{ct} values, which shows that the kinetics of the reaction is slower over these electrodes, a result in accordance with the cyclic voltammetric studies. For the C_{12}TP SAM, a very low R_{ct} value was observed, which shows that the reaction is highly facile on this modified electrode. This is also supported by cyclic voltammetric studies of the same system as shown in Figure 5.13, where higher current similar to behaviour of the bare gold electrode is observed. As stated before (section 5.4.2.1), this can be attributed to the clustering of the discotic molecules on the gold surface for higher chain length thiols, leaving large number of voids on the surface, through which the redox molecules can access the surface.

Hexaammineruthenium (II/III) system: The Nyquist plots of the impedance studies in 1 mM hexaammineruthenium (II/III) system are shown in Figure 5.18 using the SAM modified electrodes as well as the bare gold electrode. The R_{ct} values for the systems were calculated from the plots by fitting with the modified Randles circuit and are presented in Table 5.5. It can be seen from the table that the charge-transfer resistance values for these systems are very low, which means that the electron transfer process is not inhibited over the SAM modified electrode, a result in accordance with the cyclic voltammetric studies. The very low R_{ct} values for the redox system also imply that the monolayer does not block hexaammineruthenium electron transfer reaction unlike ferrocyanide reaction. This behaviour

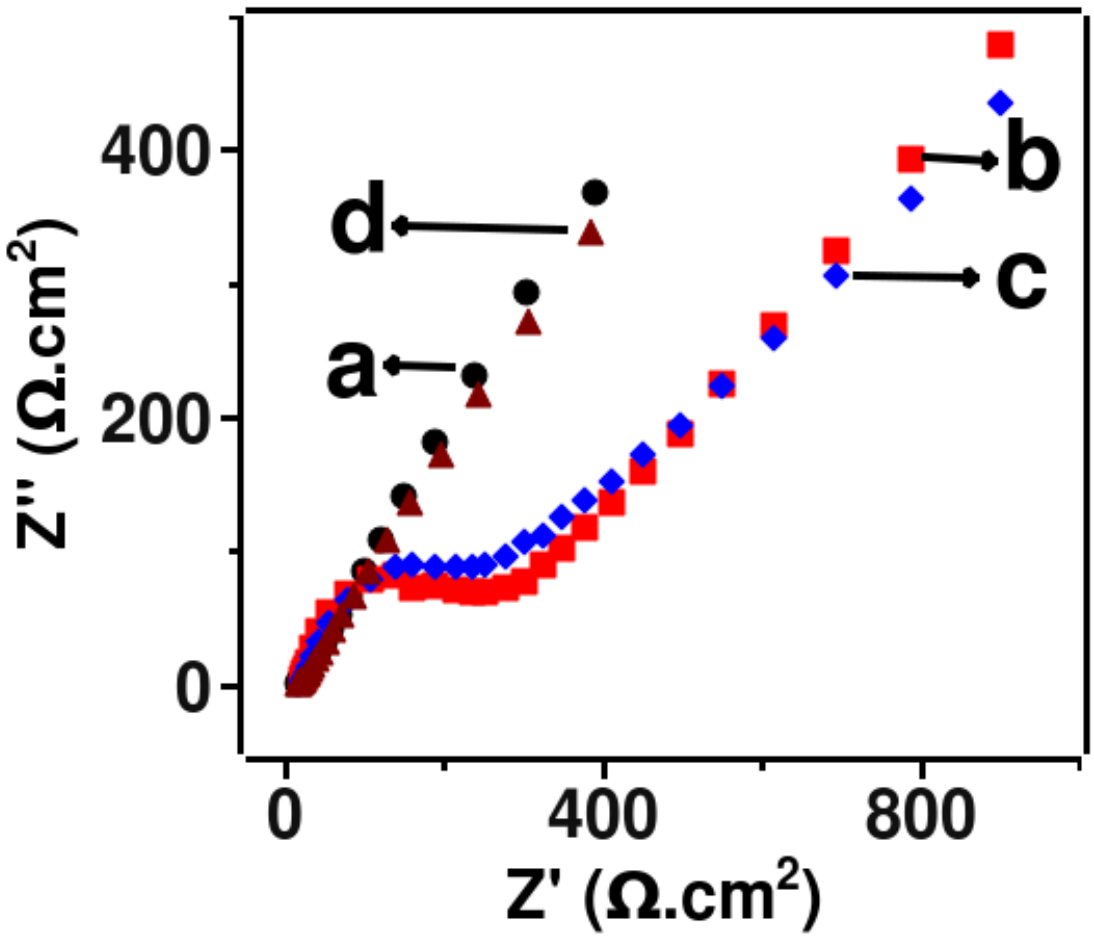

Figure 5.18: Impedance plots in 1 mM hexaammineruthenium(II/III)/0.1 M $LiClO_4/H_2O$ for a) bare electrode b) C_6TP, c) C_{10}TP and d) C_{12}TP modified electrodes

Table 5.5: Values of the solution resistance (R_u, Ω), double layer capacitance (C_{dl}, F/cm^2), charge-transfer resistance (R_{ct}, Ω.cm^2), and Warburg impedance (Z_W, S.s$^{1/2}$.cm^2) for the bare and SAM modified electrodes using hexaammineruthenium (II/III) reaction

	R_u (Ω)	C_{dl} (F/cm^2)	R_{ct} (Ω.cm^2)	Z_W (S.s$^{1/2}$.cm^2)
BAu	98.04	1.23×10^{-6}	1.95×10^{-3}	1.86×10^{-3}
C_6TP	123.9	1.36×10^{-6}	205.4	1.24×10^{-3}
C_{10}TP	124.8	1.36×10^{-6}	240.2	1.12×10^{-3}
C_{12}TP	80.75	2.94×10^{-6}	2.49	2.53×10^{-3}

is attributed to the outer-sphere electron-transfer mechanism followed by the ruthenium redox system as shown earlier [15]. In an electron transfer reaction following the outer-sphere mechanism, the redox species need not have to be in contact with the counter species, here the gold surface, and hence the monolayer has no significant effect on the electron transfer process.

Ferrocene system: Figure 5.19(a-d) show the Nyquist plots of the impedance spectra for 1 mM ferrocene system in propylene carbonate medium for the bare gold and the modified electrodes. The R_{ct} values for the reaction obtained by equivalent circuit fitting are shown in Table 5.6. It can be seen that the charge-transfer resistance values for these systems are very less in accordance with the cyclic voltammetric studies where it has been shown that the reaction is highly facile towards the ferrocene system. The results of the impedance studies support the fact that the SAMs of the C_nTP thiols disorganise in the propylene carbonate medium and therefore does not block the electron transfer process efficiently.

It is worth mentioning here that the molecules used for the monolayer studies contains a triphenylene group with attached alkoxy groups and thiol groups bound to the electrode surface. For the C_{12}TP, where the alkyl chain length is more, it is difficult for the molecule to have a perfect vertical orientation because of the bulky triphenylene groups on the top. Moreover the trace amounts of solvent and electrolyte species trapped between the monolayer molecules will also lead to a poor blocking behaviour of the electrodes.

The disorganisation of SAMs is exhibited normally only in the non-aqueous solutions. Since ferrocene is insoluble in water, we have carried out cyclic voltammetry and impedance studies using ferrocenium tetrafluoroborate, which is water soluble in order to probe the monolayer in aqueous medium. Figure 5.20 shows the typical cyclic voltammogram and the impedance plot in this medium using C_{12}TP modified electrode. It has been observed that the redox reaction of Fc^+ species is blocked on the SAM modified electrode in aqueous medium as compared to the ferrocene reaction in propylene carbonate medium. This clearly shows that the disorganisation of the SAMs is a direct consequence of the cycling in the organic solvent. The above results confirm that the C_{12}TP SAM is better organised in aqueous medium than in the propylene carbonate.

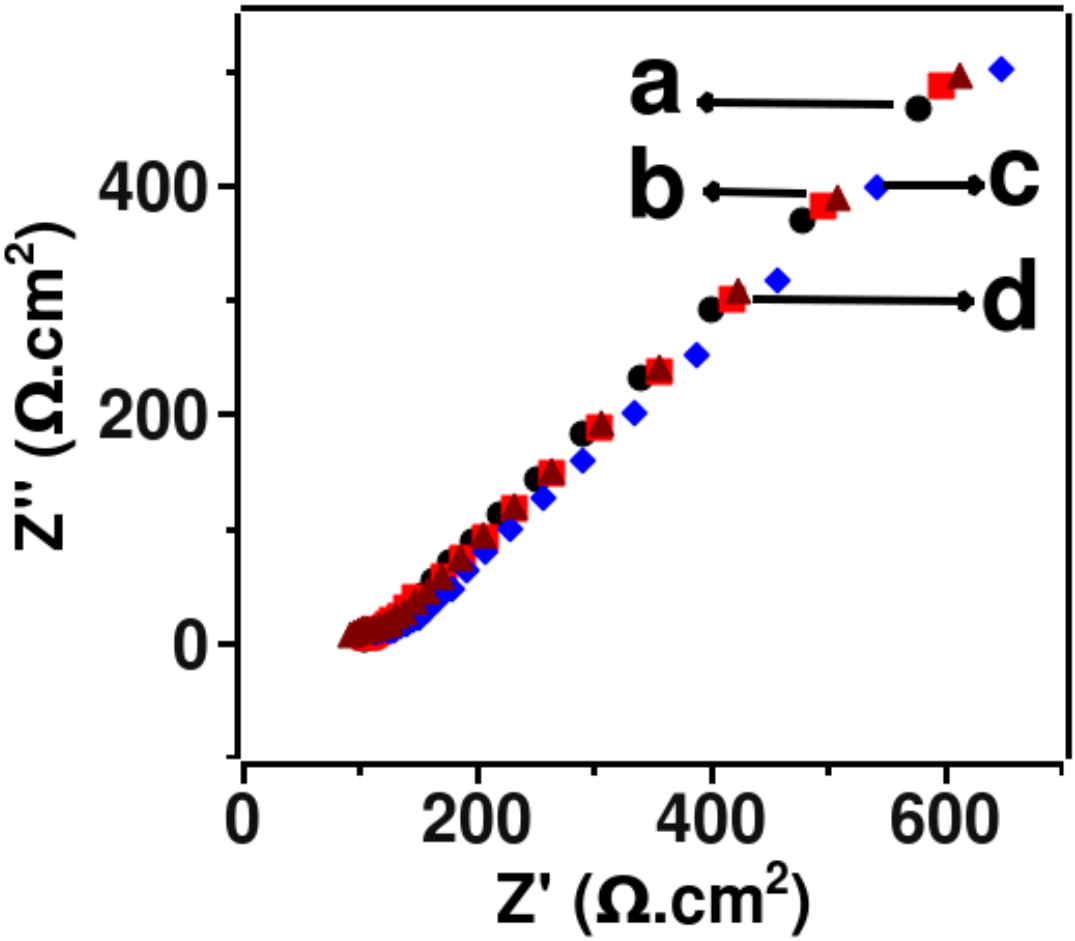

Figure 5.19: Impedance in 10 mM ferrocene/1 M $LiClO_4$/propylene carbonate for a) bare electrode b)C_6TP, c) C_{10}TP and d) C_{12}TP modified electrodes

Table 5.6: Values of the solution resistance (R_u, Ω), double layer capacitance (C_{dl}, F/cm^2), charge-transfer resistance (R_{ct}, Ω.cm^2), and Warburg impedance (Z_W, S.s$^{1/2}$.cm^2) for the bare and SAM modified electrodes using ferrocene reaction

	R_u (Ω)	C_{dl} (F/cm^2)	R_{ct} (Ω.cm^2)	Z_W (S.s$^{1/2}$.cm^2)
BAu	411.5	1.34×10^{-5}	6.32	2.37×10^{-3}
C_6TP	419	7.7×10^{-6}	7.21	2.25×10^{-3}
C_{10}TP	422	2.72×10^{-6}	16.69	2.12×10^{-3}
C_{12}TP	438.8	2.92×10^{-6}	21.34	1.78×10^{-3}

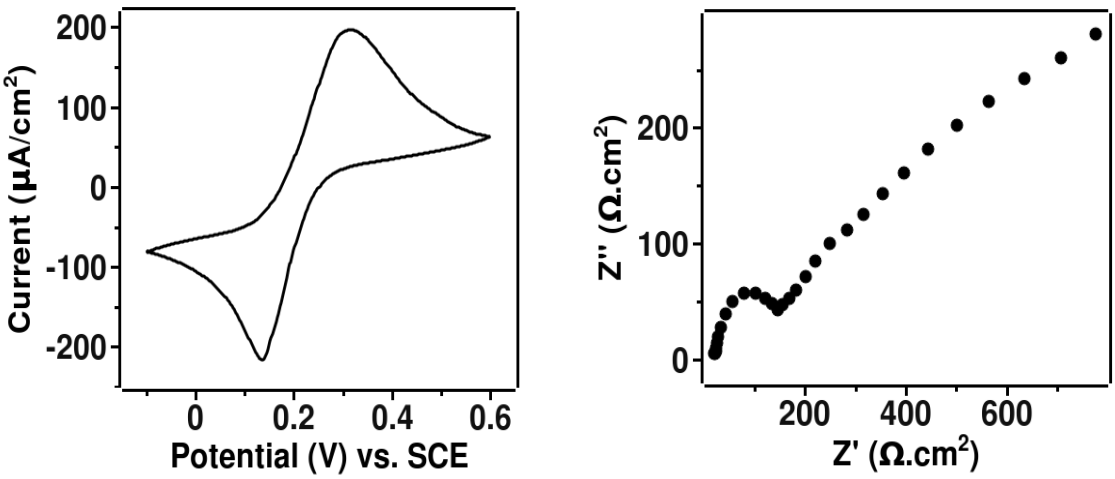

(a) CV (b) EIS

Figure 5.20: cyclic voltammogram and impedance plot in 10 mM ferrocenium tetrafluoroborate/0.1 M NaF/H_2O for the C_{12}TP modified gold electrode

5.4.2.3 Capacitance Measurements

Table 5.7 shows the double layer capacitance values measured for the SAM modified electrodes using EIS. As expected, the capacitance for the bare gold is highest among these systems. The C_6TP and C_{10}TP SAM modified electrodes show a lower capacitance values, due to the formation of monolayer. In contrast, the C_{12}TP thiol SAM shows a higher capacitance than the other two thiols, but it is lower than the value for bare gold. The higher capacitance is due to the very poor organisation of the thiol over the gold surface. The ions and solvent molecules enter through the monolayer thereby effectively increasing the dielectric constant and reducing the monolayer thickness resulting in an increase in the interfacial capacitance. These results are in agreement with the cyclic voltammetric studies in the presence of redox probes, where we have observed that SAMs formed by C_6TP and C_{10}TP thiols have better blocking properties compared to bare gold electrode and C_{12}TP SAM modified electrode. The lower capacitance for the C_6TP and C_{10}TP modified electrodes can be further explained due to the hydrophobic nature of the electrodes. In these cases, due to the better orientation of the molecules, the highly hydrophobic alkyl chains make the outer surface of the monolayer more hydrophobic and less permeable to ions. A more compact monolayer has a lower dielectric constant and therefore lower double layer capacitance. It has been reported that the

Table 5.7: Double layer capacitance values for the bare gold surface and the monolayer modified surfaces in 1 M NaF calculated from electrochemical impedance spectroscopy

System	Capacitance (F/cm^2)
BAu	7.10×10^{-6}
C_6TP	1.22×10^{-6}
C_{10}TP	1.02×10^{-6}
C_{12}TP	3.25×10^{-6}

triphenylene based thiol monolayers exhibit more hydrophilic surface compared to normal alkanethiol SAM modified surfaces and hence higher capacitance values [18, 19].

5.4.2.4 Gold Oxide Stripping Analysis

Gold oxide stripping analysis provides a qualitative picture about the coverage of the SAM over the gold surface. The modified electrode was cycled in 0.1 M $HClO_4$ solution in a potential window of 0.2 V to 1.4 V vs. SCE. During the forward sweep, the gold surface is oxidised and on the reverse scan, it is reduced to Au, as represented in Figure 5.21. The charge measured by integrating the reverse peak provides information about the amount of gold oxide reduced which is a measure of the surface area of the gold exposed to the electrolyte. Therefore from the ratio of the charge value with that of the bare gold surface, the coverage of the thiol on the gold surface can be estimated using the equation

$$\theta = 1 - \frac{Q_{SAM}}{Q_{Au}}$$

Where Q_{SAM} and Q_{Au} are the integrated area under the reverse peak for the SAM modified electrode and for the bare gold electrode respectively and θ is the surface coverage. Q_{SAM} corresponds to the charge value due to exposed gold to the electrolyte with the remaining region covered with the monolayer. It has been reported that the surface area for the bare gold surface corresponds to a charge of 410 $\mu C/cm^2$ [7].

For the C_6TP the surface coverage is measured to be 0.595 while for the C_{10}TP and C_{12}TP the values are 0.615 and 0.692 respectively. The surface coverage values obtained by

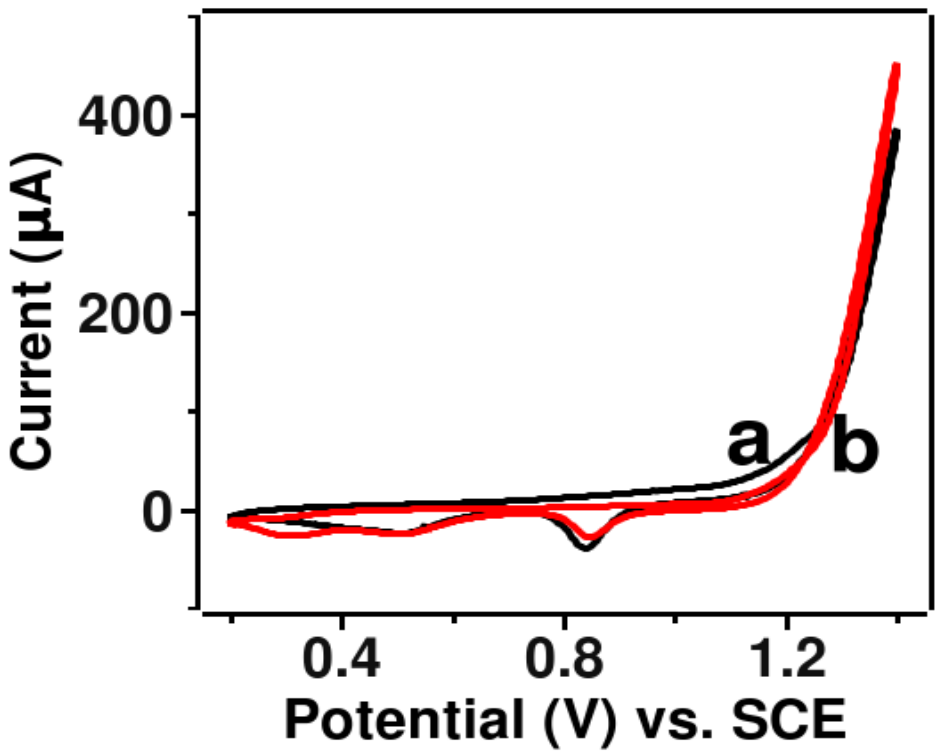

Figure 5.21: Cyclic voltammograms of a) bare gold electrode and b) C6TP modified electrode in 0.1 M $HClO_4$

this method are contrary to the cyclic voltammetric and impedance studies in the presence of redox probes like ferrocyanide/ferricyanide system. Moreover the coverage values calculated by this method varies significantly from that calculated from the impedance in the presence of redox probes. The coverage of the monolayer on the surface is given by

$$\theta = 1 - \frac{R'_{ct}}{R_{ct}}$$

where R'_{ct} and R_{ct} are being the charge transfer resistance on the bare gold and the SAM modified electrodes. For example, for the C_6TP modified surface, the impedance calculation gives coverage of 0.996 and for C_{10}TP and C_{12}TP the values are 0.995 and 0.655 respectively. The lesser coverage values obtained from the stripping analysis is due to the better permeability of the smaller ions , in this case OH^- ions, through the monolayer surface.

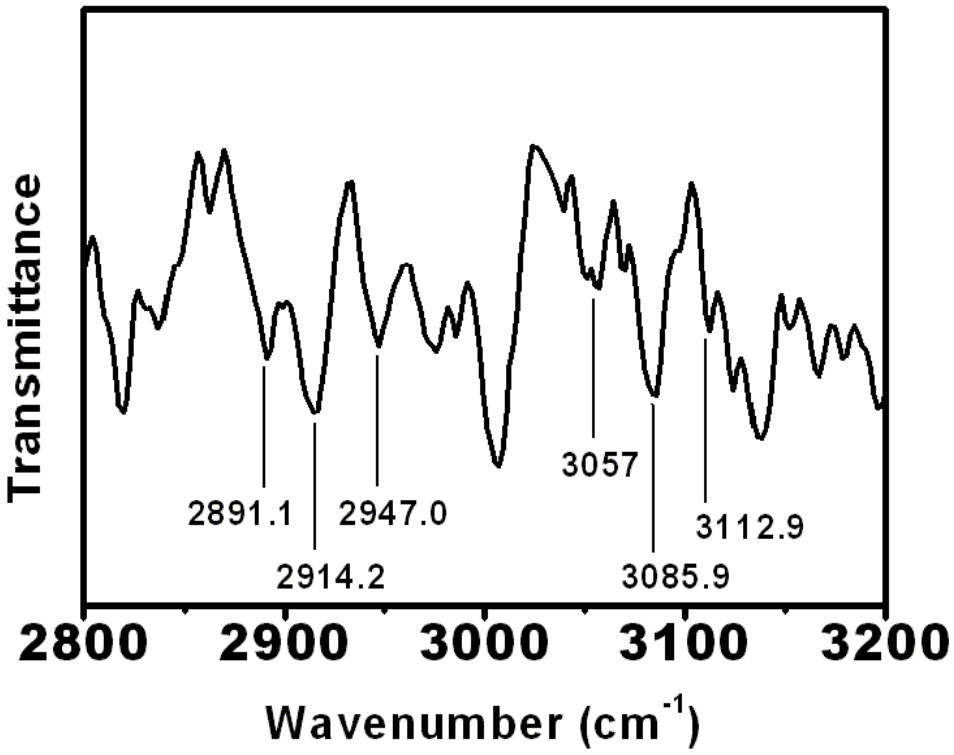

Figure 5.22: Grazing-angle FTIR spectroscopic profile for the C_6TP modified gold electrode

5.4.2.5 Grazing Angle Fourier Transform Infrared Spectroscopy

Figure 5.22 shows the GA-FTIR spectrum of the C_6TP SAM over the gold surface. Bare gold surface was used as a reference to get the spectra of the SAM modified sample. From the spectra, the peaks at 1625 and 1701 cm^{-1} are attributed to the aromatic core of triphenylene. Peaks at 2891, 2914, and 2947 are due to the asymmetric stretching vibrations of CH_2 groups. Peaks at wave numbers of 3057, 3085 and 3114 cm^{-1} are due to the symmetric stretching vibrations of the CH_2 groups. The absence of any S-H vibrations in the spectra shows that all the thiols are adsorbed by chemisorption forming Au-S bonding as expected for any thiol monolayer over the gold surface.

In summary, the monolayers of three triphenylene-based thiols with different chain lengths have been formed on the gold surface and are characterised by electrochemical and FTIR analysis. The lower chain thiols show better barrier properties for the electron transfer to the redox probes in the solution, which is contrary to the typical alkanethiol monolayers.

5.5 Conclusion

The self-assembled monolayers of cyanobiphenyl based thiols have been formed and were characterised using electrochemical techniques like cyclic voltammetry and electrochemical impedance spectroscopy. The studies show that the coverage of these monolayers on the evaporated gold surface is less when compared to that of alkanethiol SAMs of similar chain length. This is due to the poor packing of the bulky cyanobiphenyl groups that are present as the terminal groups. The electron transfer barrier properties of higher homologous series of these monolayers are better than the lower chain thiols. This is similar to the trend in the alkanethiol monolayers and arises due to the better organisation of the aliphatic chains on the surface after adsorption. The capacitance values of these monolayers are higher compared to the alkanethiol SAMs, which is due to the terminal polar cyano groups which allow ions to enter into the film and the poor organisation due to repulsion among negatively charged polar cyano groups.

The self-assembled monolayers of triphenylene substituted thiols on the gold surface and their electrochemical behaviour indicate that the electron transfer barrier properties of these thiols decrease with the chain length. This is contrary to the behaviour of typical alkanethiol monolayers. We attribute this to the cluster formation of the triphenylene core on several regions of the monolayer surface which creates large number of pinholes and defects. As the chain length increases, the interaction of the triphenylene cores on the surface also increases due to the flexibility of these molecules on the surface. This leads to the lowering of electron transfer barrier properties. The capacitance values of these modified electrodes are in general very high compared to the typical alkanethiol monolayers.

Bibliography

[1] H. O. Finklea, *Encyclopedia of analytical Chemistry*, John Wiley & Sons Ltd, Chichester.

[2] A. Ulmann, *An introduction to ultrathin organic films from Langmuir-Blodgett to self-assembly*, Academic Press, San Diago, CA, 1991.

[3] N. K. Chaki and K. Vijayamohanan, *Biosensors and Bioelectronics*, 2002, **17**, 1.

[4] S. Abasi and C. Shannon, *Electrochim. Acta*, 2005, **50**, 2967.

[5] U. K. Sur and V. Laksminarayanan, *J. Colloid Interface Sci.*, 2002, **254**, 410.

[6] U. K. Sur and V. Laksminarayanan, *Pramana J. Phys.*, 2003, **61**, 361.

[7] S. Trasatti and O. Petril, *Pure Appl. Chem.*, 1991, **63**, 711.

[8] Goodby, *Handbook of Liquid Crystals*, John Wiley & Sons, London, 2nd edn., 2004.

[9] C. T. Imrie and G. R. Luckhrust, *Handbook of Liquid Crystals*, Wiley-VCH, Weinheim, Vol. 2B edn., 1998.

[10] M. Alloisio, A. Demartini, C. Cuniberti, G. Petrillo, S. Thea, E. Giorgetti, A. Giusti and G. Dellepiane, *J. Phys. Chem. C*, 2007, **111**, 345.

[11] H. Schonherr, F. J. B. Kremer, S. Kumar, J. A. Rego, H. Wolf, H. Ringsdorf, M. Jaschke, H.-J. Butt and E. Bamberg, *J. Am. Chem. Soc.*, 1996, **118**, 13051.

[12] V. Ganesh, S. K. Pal, S. Kumar and V. Lakshminarayanan, *J. Colloid Interface Sci.*, 2006, **296**, 195.

[13] V. Ganesh, S. K. Pal, S. Kumar and V. Lakshminarayanan, *Electrochim. Acta*, 2007, **52**, 2987.

[14] S. K. Pal, V. A. Raghunathan and S. Kumar, *Liq. Cryst.*, 2007, **34**, 135.

[15] V. Ganesh and V. Lakshminarayanan, *J. Phys. Chem. B*, 2005, **109**, 16372.

[16] V. Ganesh and V. Lakshminarayanan, *Langmuir*, 2006, **22**, 1561.

[17] R. Greef, R. Peat, L. M. Peter, D. Pletcher and J. Robinson, *Instrumental Methods in Electrochemistry*, Ellis Horwood Ltd., Chichester, Great Britain, 1990.

[18] H. Allinson, N. Boden, R. J. Bushby, S. D. Evans and P. S. Martin, *Mol. Cryst. Liq. Cryst.*, 1997, **303**, 273.

[19] N. Boden, R. J. Bushby, P. S. Martin, S. D. Evans, R. W. Owens and D. A. Smith, *Langmuir*, 1999, **15**, 3790.

[20] R. Owens and D. A. Smith, *Mol. Cryst. Liq. Cryst.*, 1999, **329**, 383.

[21] F. Charra and J. Cousty, *Phys. Rev. Lett.*, 1998, **80**, 1682.

[22] M. Yamada, Z. Shen and M. Miyake, *Chem. Commun.*, 2006, 2569.

[23] S. Kumar, S. K. Pal, P. S. Kumar and V. Lakshminarayanan, *Soft Matter*, 2007, **3**, 896.

[24] S. Kumar, S. K. Pal and V. Lakshminarayanan, *Mol. Cryst. Liq. Cryst.*, 2005, **434**, 251.

Chapter 6

Summary and Future Works

In this chapter we summarise the significant results and conclusions derived from the work described in the previous chapters. We also present here the scope for future investigations based on the outcome of our studies. Broadly, the thesis works can be classified as follows:

1. Electrochemical studies of redox probes in the columnar hexagonal phase of Triton X-100/water system.

2. Studies on dispersion of thiol-protected gold nanoparticles in the columnar hexagonal phase (H1 phase) of Triton X-100/water system and the reverse columnar hexagonal phase (H2 phase) of AOT.

3. Ionic conductivity studies of the H1 phase of Triton X-100/water system and the effect of different dopants on the ionic conductivity in these systems.

4. The electrical conductivity studies of the discotic liquid crystalline materials and the effect of addition of ferrocenium and chloroaurate dopants into the discotic matrix.

5. Self-assembled monolayers formed by rod-like cyanobiphenyl substituted disulphides and discotic triphenylene tethered thiols on gold surface and their electrochemical characterisation.

1. Electrochemical studies of redox probes in the columnar hexagonal phase of Triton X-100/water system

We have studied the electron transfer processes of a variety of redox probes in the columnar hexagonal phase of Triton X-100/water system. The polarising optical microscopic (POM) and small angle X-ray scattering (SAXS) studies revealed that the H1 phase of the Triton X-100/water system is retained even after the addition of the redox probes and the supporting electrolytes. The cyclic voltammetric studies show that the half-peak potential of the redox probes have shifted significantly in the H1 phase compared to the solvent phase. The nature and extent of the potential shifts have been explained on the basis of the interaction between the redox probe and the surrounding H1 phase. For the hexaammineruthenium (II/III) redox system, we have observed a negligible shift in the half-peak potential, which has been attributed to the outer-sphere electron transfer process in this system. On the other hand, the diffusion coefficient values of all the redox probes were found to be lower in the H1 phase than in the solvent phase. The extent of decrease was observed to be dependent on the interaction of the redox probes with the liquid crystalline system.

2. Dispersion of thiol-protected gold nanoparticles in the H1 phase and H2 phase

Hexanethiol and 10-CB thiol protected gold nanoparticles were dispersed in the lyotropic columnar hexagonal phase (H1 phase) of Triton X-100/water system and in the reverse columnar hexagonal phase (H2 phase) of AOT system. POM and SAXS studies were utilised for the characterisation of the dispersions. POM studies showed that the addition of gold nanoparticles did not disturb the liquid crystalline structure of these two systems. The SAXS studies have confirmed that the dispersions retain the liquid crystalline characteristics. Infact it was observed that the addition of gold nanoparticles have actually improved the columnar order in these two liquid crystalline systems with additional peaks in the SAXS, corresponding to the different lattice planes. The lattice parameters derived from SAXS studies are not altered by the addition of the nanoparticles.

3. Ionic conductivity studies of the H1 phase of Triton X-100/water system

We have observed that the ionic conductivity of the H1 phase of Triton X-100/water system is very high eventhough it is constituted of a non-ionic surfactant. The unexpectedly high ionic conductivity in the phase has been explained on the basis of Grotthus mechanism, according to which the ionic conductivity originates from the proton transfer between different

protonated water clusters like Zundel cations and Eigen cations. On the surface of the micelles of the Triton X-100/water system, the water molecules are arranged very close to each other and hence the proton transfer between the clusters is facile resulting in a very high ionic conductivity. We have observed that the addition of urea, a well known chaotropic agent decreases the ionic conductivity in contrast to that of of gold nanoparticles which enhance the ionic conductivity. These observations are in good agreement with the Grotthus mechanism of conductivity.

4. Electrical conductivity studies on the discotic liquid crystalline composites

We have studied the effect of dopants on the phase behaviour and the electrical conductivity of discotic liquid crystalline materials. For these studies, we have used ferrocenium tetrafluoroborate and chloroaurate as dopants in hexahexyloxytriphenylene and hexahexylthiotriphenylene which are the discotic molecules. The composites of different concentrations of the dopants were prepared with the discotic molecules. The POM, DSC and SAXS studies revealed that when the concentration of the dopants are low, they do not alter the columnar structure of the discotic molecules. The UV-visible spectral studies show that the ferrocenium ions form charge-transfer complex with the electron rich discotic molecules while the chloroaurate oxidises the triphenylene core of the discotic molecules resulting in the formation of triphenylene radical cations. Both the dopants enhance the DC conductivity of the discotic phase by almost million times while the chloroaurate-discotic composites show very high ionic conductivity due to the formation of radical cations. The chloroaurate-discotic composites show a significant absorption in the entire visible and NIR regions, which indicates that these composites can find potential applications in the field of solar cells. The DC conductivity of these composites were observed to decrease in the isotropic phase indicating that the observed high conductivity is due to the quasi-one-dimensional nature of the columnar hexagonal phase.

5. Self-assembled monolayers of liquid crystalline disulphides and thiols on gold surface

We have formed self-assembled monolayers of two liquid crystalline compounds on the gold surface *viz* the rod-like cyanobiphenyl functionalised disulphides and the discotic triphenylene based thiols. These monolayer modified surfaces were characterised using electrochemical techniques like cyclic voltammetry and electrochemical impedance spectroscopy.

The studies show that the cyanobiphenyl substituted disulphides inhibit the electron transfer process for the ferrocyanide|ferricyanide reaction, while allowing the hexaammineruthenium(II/III) reaction to take place through the monolayer film. The facile electron transfer in the hexaammineruthenium(II/III) has been explained on the basis of outer-sphere electron transfer reaction mechanism. Electrochemical impedance spectroscopic studies have revealed that the barrier offered for electron transfer process by these monolayers are lower than that of typical alkanethiol monolayers. This is attributed to the loose packing of the monolayers which are formed owing to the bulky cyanobiphenyl groups at the terminal positions. The higher chain disulphide modified monolayers offer higher barrier to electron transfer process owing to better organisation of the monolayers on the surface due to hydrophobic-hydrophobic interactions. On the other hand, the triphenylenethiol modified monolayers show poor blocking behaviour and the barrier to electron transfer process decreases for higher chain length. This has been explained on the basis of the disorganised structure of the longer chain length monolayers resulting from the $\pi - \pi$ interaction between the electron rich triphenylene cores that leads to clustered packing, leaving out many voids on a polycrystalline gold surface.

Scope For Future Studies

In chapter 2, we have discussed the electron transfer reactions of several redox probes in the lyotropic columnar hexagonal liquid crystalline phase (H1 phase) of Triton X-100/water system. We have observed significant shifts in the half-peak potentials and large reduction in the diffusion coefficient of the redox probes in the H1 phase as compared to the solvent phase. At the same time, we have shown that the redox probes follow linear diffusion characteristics irrespective of the columnar arrangement of the cylindrical micelles near the electrodes. This provides a general basis for the study of several biological electron transfer reactions as the systems presented here can mimic the biological environment.

In chapter 3, we have discussed the dispersion of thiol-protected gold nanoparticles in the H1 phase of Triton X-100/water system and in the H2 phase of AOT, where we have shown that the dispersion of nanoparticles into the columnar phase does not alter the liquid crystalline phase behaviour. Such composites can be studied for several applications includ-

ing the targeted drug delivery. The interaction of the terminal groups of the ligands attached to the nanoparticles with the surfactant and the water molecules on the surface of the micelle plays a significant role on the *d* spacing of these dispersions as discussed in the chapter 3. Further studies have to be carried out for a better understanding of these phenomena. For example, the phase diagram of the nanoparticle-Triton X-100-water systems may be of fundamental interest for a better understanding of the behaviour of such dispersions.

The ionic conductivity of the H1 phase of Triton X-100/water system shows a surprisingly high ionic conductivity even though the constituent materials are non-ionic in nature. Interestingly, similar observations have been made on some protein surfaces as well as inside of the carbon nanotubes. A detailed experimental studies have to be carried out in this field, and the system that we presented here may become a model system for these experiments. In this context, the existence of different protonated water clusters needs to be probed and the kinetics of the proton transfer reactions have to be studied in detail.

The chapter 4 describes the electrical conductivity studies of the discotic liquid crystalline composites. We have shown that the electrical conductivity of the discotic materials can be enhanced by several orders of magnitude while the composites still retain the liquid crystalline order. The absorption of the chloroaurate-discotic composites over the entire visible and NIR region make them potential candidates for the solar cell applications. For this purpose the photocurrent measurements have to be carried out and should be compared with other solar cell devices. The efficiency of such solar absorbers can also be studied. The discotic-ferrocenium composite reported here opens a new area of discotic-organometallic composites of donor-acceptor couples. A study of similar composites with other organometallic compounds may lead to some novel composite materials with several interesting properties.

The self-assembled monolayers of disulphides, as described in the chapter 5, show that the electron transfer barrier properties of these modified electrodes are significantly lower than typical alkanethiol monolayers. This has been attributed to loose organisation owing to the bulky cyanobiphenyl groups at the terminal positions. Such monolayers can be further analysed using scanning tunneling microscopy and atomic force microscopy to establish the orientation of these molecules on the gold surface. The triphenylene thiols show abnormal behaviour in the electron transfer process as the blocking ability decreases with increase in

the chain length. This counterintuitive behaviour has been attributed to the formation of clusters by $\pi - \pi$ interaction between the triphenylene cores. Further surface studies using *in situ* scanning tunneling microscopy and atomic force microscopy are necessary for a clear understanding of this behaviour. Moreover, such clusters on the electrode surface may exhibit some interesting properties as triphenylenes are well know for their quasi-one-dimensional electron transport in the bulk phase and therefore may be good candidate materials for molecular electronics.